Title

Modulation of Electronic Structures and Magnetic Properties of Metal—Organic Solids

Author

Park, Jesse G

Publication Date

2021

Peer reviewed|Thesis/dissertation

Modulation of Electronic Structures and Magnetic Properties of Metal–Organic Solids

by

Jesse G. Park

A dissertation submitted in partial satisfaction of the

requirements for the degree of

Doctor of Philosophy

in

Chemistry

in the Graduate Division

of the

University of California, Berkeley

Committee in charge:

Professor Jeffrey R. Long, Chair
Professor Jeffrey B. Neaton
Professor Christopher J. Chang

Summer 2021

Modulation of Electronic Structures and Magnetic Properties of Metal–Organic Solids

Jesse G. Park

Abstract

Modulation of Electronic Structures and Magnetic Properties of Metal–Organic Solids

by

Jesse G. Park

Doctor of Philosophy in Chemistry

University of California, Berkeley

Professor Jeffrey R. Long, Chair

Chapter 1 provides an introduction to charge transport and magnetism in coordination solids. Metal–organic frameworks bear structures that offer intrinsic porosity, vast chemical and structural programmability, and tunability of electronic properties. As such, metal–organic frameworks offer a desirable chemical platform to realize and modulate long-ranged magnetic order and charge transport, offering numerous applications in low-density magnets, magnetic separation, quantum sensing, spintronics, and battery electrodes. Development of strategies towards designing metal–organic electronic conductors and magnets have been successful and benefitted largely from a bottom-up approach by adopting insights from molecular coordination chemistry. Selected examples describing these efforts are also described in this Chapter.

Chapter 2 discusses the isolation of the mixed-valence framework materials, $Fe(Tri)_2(BF_4)_x$ (Tri^- = 1,2,3-triazolate; x = 0.09, 0.22, and 0.33), obtained from the stoichiometric chemical oxidation of the poorly-conductive iron(II) framework $Fe(Tri)_2$, and find that the conductivity increases dramatically with iron oxidation level. Notably, the most oxidized variant, $Fe(Tri)_2(BF_4)_{0.33}$, displays a room-temperature conductivity of 0.3(1) S/cm, which represents an increase of eight orders of magnitude from that of the parent material and is one of the highest conductivity values reported among three-dimensional metal–organic frameworks. Detailed characterization of $Fe(Tri)_2$ and the $Fe(Tri)_2(BF_4)_x$ materials via powder X-ray diffraction, Mössbauer spectroscopy, IR, and UV-vis-NIR diffuse reflectance spectroscopies reveals that the high conductivity arises from intervalence charge transfer between mixed-valence low-spin $Fe^{II/III}$ centers. Further, Mössbauer spectroscopy indicates the presence of a valence-delocalized $Fe^{II/III}$ species in $Fe(Tri)_2(BF_4)_x$ at 290 K, one of the first such observations for a metal–organic framework. The electronic structure of valence-pure $Fe(Tri)_2$ and the charge transport mechanism and electronic structure of mixed-valence $Fe(Tri)_2(BF_4)_x$ frameworks are discussed in detail.

Chapter 3 presents the ligand substitution on the $Fe(Tri)_2$ to tune the ligand field around Fe^{II} ions and the bulk material electronic structure. Detailed structural, magnetic, and spectroscopic characterizations suggest that $Fe(MeTri)_2$ ($MeTri^-$ = 4-methyl-1,2,3-triazolate) is a rare example of 3D metal–organic framework that undergoes spin crossover. Spin-crossover materials undergo reversible changes in their electronic structure in response to external stimuli, and as such are of

interest for potential applications including data storage and optical switching devices. The characteristic spin-crossover temperature for $Fe(MeTri)_2$ occurs at ~265 K, more than 200 K lower than the corresponding temperature in the parent material $Fe(Tri)_2$, highlighting the utility of simple linker functionalization in modulating the functional properties of this new subclass of 3D spin-crossover materials.

Chapter 4 details the metal substitution on the $Fe(Tri)_2$ to modify the electronic and magnetic properties. In particular, a mixed-valence chromium(II/III) triazolate compound exhibits itinerant ferromagnetism and a magnetic order at T_C = 225 K, representing the highest ferromagnetic ordering temperature yet observed in a metal–organic framework. The itinerant ferromagnetism proceeds via a double-exchange mechanism, resulting in a barrierless charge transport below T_C and a large negative magnetoresistance of 23% at 5 K. These observations suggest applications for double-exchange-based coordination solids in the emergent fields of magnetoelectrics and spintronics.

Table of Contents

Acknowledgement

First, I thank my parents, Soyeon Kim and Changwoo Park. My mom is a selfless woman who has dedicated her life to raising her sons with indescribable love and care. After her marriage after graduating from a university with a master's degree, my parents came to US for graduate studies. Soon after I was born, my mom decided to postpone her study and focus on raising me for many reasons now I am starting to understand. Growing up, I moved between schools in Korea and US multiple times as my parents thought it is important for me to get exposed to different cultures and language. While my dad stayed in Korea to support my family, my mom, who rarely spoke English, was brave enough to always travel together with her sons. While I grew mature from my experiences, I was a person of mixed culture and language and often seen as a foreigner in both countries. In every moment of difficulty and confusion, it was through my mom's love that I was able to always bring myself together and stay strong. On the other hand, my dad is a brave and respectable man. I am always amazed when I hear about his stories pursuing graduate studies and financially supporting my mom and his two sons. If I were him, I would have probably starved myself to death. Even when his whole family traveled to US for a long time, my dad lived alone in Korea never failing to keep balance in his jobs and family. My dad is extremely family oriented and taught me all the valuable manners and values for maintaining a healthy family. At the same time, my dad has been highly influential on encouraging me to be engaged and curious about nature, which helped me tremendously during my research. When I was young, I remember my dad showing me liquid nitrogen to freeze random things and letting me take Litmus papers home to test the acidity of rainfalls. However, my uncontrollable curiosity has sometimes led me to do many stupid things in my life, but dad rarely punished me if they were not of bad intentions. I thank my dad for his patience and keeping me in his family until this day.

I have had many influential mentors growing up. Starting in a college, Dr. Priest was my academic advisor and an insightful mentor in my personal life who got me in love with studying organic chemistry, introduced me to different scientific novels, taught me how to communicate with professors, provided advice regarding academic and personal issues outside office hours, and suggested joining the Harris research group. While working for Dave, I found chemical research to be highly enjoyable. It was fascinating to transform classroom knowledge in inorganic chemistry into synthesizing new transition metal coordination compounds that not only show beautiful colors but also diverse magnetic properties(!). Working in the Harris group as an undergraduate research assistant, I was welcomed and given trust that I was eventually allowed to pursue an independent research with my own research topic. When I was discouraged from research, I remember Dave telling me that regardless of the performance, if I try hard and learn something new each day, I should be proud of myself. During the times of mental hardship, Dave listened to my concerns and kindly offered to help whenever I needed it. I thank Dave for his countless support during my undergraduate and graduate studies. In the Harris group, I also met two fascinating post-docs, Dr. Ie-Rang Jeon and Dr. John Anderson. They taught me a large portion of my current synthetic techniques and research habits. I thank Ie-Rang and John for all the research advice and knowledge that constitute me today. I am also thankful to have met Prof. Christopher Chang, Prof. Richard Anderson, Prof. John Arnold, and Prof. Jeffrey Neaton during my qualifying exam. I learned to think critically and communicate effectively during discussions with other scientists. Most importantly, graduate school requires ceaseless speculation, learning, and endurance, and Prof. Jeffrey Long provided patience and encouragements for me to find a good balance and keep focused on research. Before coming to Berkeley, I was used to spending

time alone and learning from textbooks, and I lacked ability to communicate science. When preparing for presentations at group meetings, I used to prepare scripts and memorize them word-by-word. Jeff provided feedbacks and suggestions to help me improve with making effective slides, giving presentations, and answering questions. I was able to improve tremendously in the graduate school, thanks to Jeff's encouragements and trust. Jeff also genuinely congratulates and rewards his students for their work. During a holiday party, Jeff taught me to make the best gin tonic. Since then, it has become one of my favorite drinks. I thank Jeff for all his support during my graduate study and giving me an opportunity to work in a group of talented scientists.

I am thankful to have met excellent co-workers while working in the Long group. Prof. Fernande Grandjean and Prof. Gary Long were my first Mössbauer collaborators on my first paper in the Long group. I am often appalled by looking back at my first several drafts on the manuscript. However, they kindly provided thorough scientific and grammatical edits not just limited on the Mössbauer section but also on overall manuscript. I learned a lot, and I am also thankful for the valuable discussions through emails and from their visits to Berkeley. During my fourth year in Berkeley, I had a chance to travel to Oak Ridge National Laboratory with a neutron diffraction collaborator, Prof. Mark Green. During our free time, Mark told me fascinating stories on traveling different countries, gaining a faculty position at a university at a young age, Girl with Balloon by Banksy, and so on. I thank Mark for traveling together and teaching me neutron diffraction. I thank my computational collaborators, Brianna Collins and Prof. Jason Goodpaster, for welcoming my visit at University of Minnesota and having discussions on computational methods and electronic structure calculations. I also thank Prof. Rodolphe Clérac for insightful discussions on spin-crossover materials and discussions on magnetic coordination solids.

The Long group consists of talented, hard-working students and scientists. First, I thank my year-mates. Soon after joining the Long group, Daniel Lussier became my close friend. We had countless conversations supporting each other during stressful moments. Dan has now become an expert in actinide chemistry, and I am happy and look forward to your groundbreaking results soon open to the world. I enjoyed eating Thai food, going to the animal farms, and taking care of Mössbauer instrument with Job Chakarawet. Michael Ziebel have been an inspiring and talented scientist protecting our conductivity subgroup teammate against the outnumbering students of molecular magnetism. I thank Collin Gould for his help with organic chemistry and awesome presentations on single-molecule magnets. Henry Jiang is an IR expert in the Long group. It was fun to talk about computer games and how old we are now and no longer have functional fingers to compete with youngsters. Ari Turkiewicz is the most humorous among my year-mates and his works on incorporating metal clusters in MOFs truly inspired me. Lucy Darago and Michael Aubrey helped me get started in the lab and served as my mentors on magnetism and conductivity in MOFs. Julia Oktawiec taught me all about Rietveld refinements. Ever Velasquez always took beautiful SEM images of my MOFs, and I enjoyed talking to him while traveling to the SEM facility across the campus from Lewis Hall. I thank Hiroyasu Furukawa and David Jaramillo for spending time and happily teaching me everything about gas adsorption in MOFs. Ryan Murphy is my Juul friend, and it was always inspiring to discuss frustrated magnetism with him. Alexandre Vincent, Kennedy McCone, Hyunchul Kwon, and Danh Ngo are other talented members in conductivity and magnetism subgroup. I look forward to their awesome scientific discoveries.

Last but not least, I would like to thank all my friends including Morgan Seidel, Richard Kwon, Michael Shin, and Kyunjun Park, my brother Joseph Park, my partner Soomin Woo who is always there for me, my beautiful dog Cola, and those who I couldn't mention. Everyone has shaped me into who I am right now and thank you for supporting me during my time in Berkeley.

Dedicated to my parents, Changwoo and Soyeon

Chapter 1: Introduction to Charge Transport and Magnetism in Coordination Solids

1.1 Introduction

With a global shift towards a zero-carbon economy and emerging green technologies, the development of high-performance magnets and electrical conductors has become ever more important. For instance, the intermetallic solid-state materials $Nd_2Fe_{14}B$ and $SmCo_5$ remain the best permanent magnets, with exceptional magnetic coercivity and remanent magnetization.[1-3] However, the production of these rare-earth magnets is largely limited by the shortage on supply from mostly China and environmental hazards associated with rare-earth mining and processing.[4] Indeed, the United States Department of Energy has included rare-earth minerals as critical materials for national security and has initiated the Rare Earth Alternatives in Critical Technologies program to develop cost-effective alternatives to rare-earth magnets.[5,6] Furthermore, improvements on the magnetic properties of these solid-state materials have been limited by the intrinsic challenges associated with their top-down, empirical syntheses.

As an alternative, metal–organic frameworks are an interesting class of materials in which metal ions or clusters are bridged by organic linkers to form a crystalline lattice with permanent porosity.[7] The building blocks of metal–organic frameworks can be easily substituted to access a wide range of crystal structures and to tune chemical and physical properties.[8-12] Through judicious choice of metal ion and organic linker from a tremendous library of coordination complexes and organic molecules, metal–organic frameworks offer an ideal platform to develop multifunctional materials with various intriguing properties, such as long-range magnetic order,[13,14] spin crossover,[15-18] and charge transport,[19-21] offering numerous applications in memory storage, spintronics, magnetoelectrics, displays, and batteries. Furthermore, metal–organic frameworks that are responsive to the insertion of gases, solvents, ions, and other small molecules may find applications in magnetic and chemiresistive sensing and separation media.[22-27]

Despite these promising applications, the vast majority of metal–organic frameworks are electronic insulators and lack long-range magnetic order. However, tremendous success has recently been made on the development of conductive and magnetic metal–organic frameworks.[19,21] In 2009, the first conductive metal–organic framework, $Cu[Cu(pdt)_2]$ (pdt = 2,3-pyrazinedithiolate), was discovered.[28] Since then, the field has grown rapidly in the last decade, with multiple reports of metal–organic frameworks that now exhibit metallic conductivities. Similarly, numerous strategies have been developed for synthesizing magnetic coordination solids. The first molecule-based ferromagnets $[Cp^*_2M^{III}](TCNE)^{-\bullet}$ (M^{II} = Mn^{III}, Fe^{III}; Cp^{*-} = pentamethylcyclopentadienyl anion; TCNE = tetracyanoethylene) were shown to exhibit magnetic order up to 8.8 K.[29-31] Now, coordination solids that exhibit magnetic order beyond room-temperature include $V(TCNE)_x \cdot yCH_2Cl_2$ ($x \approx 2$; $y \approx 0.5$) and $Cr(pz)_2 \bullet 0.7LiCl$ (pz = pyrazine).[32,33]

The dissertation is dedicated to the design and synthesis of magnetic and conductive metal–organic frameworks using insights learned from molecular coordination chemistry with a bottom-up approach. Further, demonstrates that metal and ligand substitution is a viable strategy to tune electronic structures and physical properties. Chapter 1 provides a general overview of electronic conductivity and magnetism and highlights previous efforts to synthesize conductive and magnetic coordination solids with selected examples.

1.2 Electronic Conductivity of Metal-Organic Frameworks

General overview of conductivity

The electrical resistance, *R*, describes the opposition to the electrical current flowing through an object, described by the Ohm's law:

$$R = \frac{V}{I}; G = \frac{1}{R} = \frac{I}{R} \quad (1)$$

where *V* is voltage and *I* is current. The conductance, *G*, is a reciprocal of the resistance and has the unit of Siemen (S), which is the inverse of Ohm (Ω^{-1}). The resistivity, ρ, is the resistance normalized for the sample dimension and specific to the physical composition of the material:

$$\rho = R\frac{A}{l}; \sigma = \frac{1}{\rho} = \frac{l}{RA} \quad (2)$$

where *A* is the cross-sectional area and *l* is the length of the sample. The resistivity and conductivity have the units of Ω cm and S cm^{-1}, respectively. In an anisotropic system with non-uniform current and electric field, Equation 2 must be modified to a more general form:

$$\rho = \frac{E}{J}; \sigma = \frac{1}{\rho} = \frac{J}{E} \quad (3)$$

where *E* and *J* are the magnitude of electric field vector and the current density vector at a particular position in a material, respectively. Indeed, under a constant electric field and current, they will adopt a scalar quantity, defined as

$$E = \frac{V}{l}; J = \frac{I}{A} \quad (4)$$

Substituting Equation 4 into Equation 3,

$$\rho = \frac{VA}{lI}; \ \sigma = \frac{lI}{VA} \quad (5)$$

Now, applying Ohm's law to Equation 5 yields the identical expression to Equation 2. At a certain position and time, the current density of a charge carrier is described as

$$j = qnv \quad (6)$$

where *j* is the current density vector, *q* is the fundamental charge of a charge carrier, n is the volumetric density, *v* is the average drift velocity of charge carriers. Under a constant electric field, drift velocity of a charge carrier is related to its mobility, μ, as shown in Equation 7:

$$v = \mu E \quad (7)$$

Finally, using Equations 3, 6, and 7, the total conductivity of a material can be expressed using Equation 8:

$$\sigma = \sum qn\mu \quad (8)$$

Overview of efforts to design conductive metal–organic frameworks

Metal–organic frameworks such as $Zn_4O(bdc)_3$ (bdc^{2-} = 1,4-benzenedicarboxylate), known as MOF-5[34] and shown in Figure 1.1, are typically synthesized as electronic insulators. Most of them are constructed by using closed-shell organic ligands and metal ions that are poor sources of charge carriers. Furthermore, maintaining crystallinity and porous structures of metal–organic frameworks relies on the reversible binding of hard metal ions and ligands, resulting in the ionic electronic structure that further limits the charge carrier mobility.[35-37] As evident from Equation 8, the lack of charge carrier concentration and mobility results in the low electronic conductivity that is typical of metal–organic frameworks.

Despite the challenges, tremendous efforts have been made towards synthesizing electronically conductive metal–organic frameworks by utilizing synthetic tunability and unique pore structures.[19-21] For instance, metal–organic frameworks based on various redox-active ligands such as tetrathiafulvalene, anthracene, naphthalene, and naphthalenediimide provide efficient through-space charge-transport pathways from π–π stacking interactions between the linkers.[38-43] Furthermore, it was also shown that the electronic conductivity of an insulating metal–organic framework can also be tuned via post-synthetic incorporation of redox-active guest molecules into the framework cavity.[44-47] In one example, incorporation of tetracyanoquinodimethane molecules into Cu paddlewheel metal–organic frameworks was proposed to increase the number of charge carriers and transport pathways.[46,47] The major successes in the synthesis of conductive metal–organic frameworks were made possible through utilizing strong d–π conjugation with covalent bonds between metal ions and ligands that feature delocalized π systems.[48-57] For instance, a two-dimensional framework $Cu_3(bht)$ (bht^{6-} = benzenehexathiolate) constructed from square-planar Cu^{II} ions bridged by bht^{6-} ligands was shown to exhibit a metallic conductivity of 2,500 S cm^{-1} and a high charge mobility of ~100 $cm^2\ V^{-1}\ s^{-1}$.[55-57] Interestingly, $Cu_3(bht)$ undergoes a magnetic phase transition to a superconducting state below 0.25 K.[57]

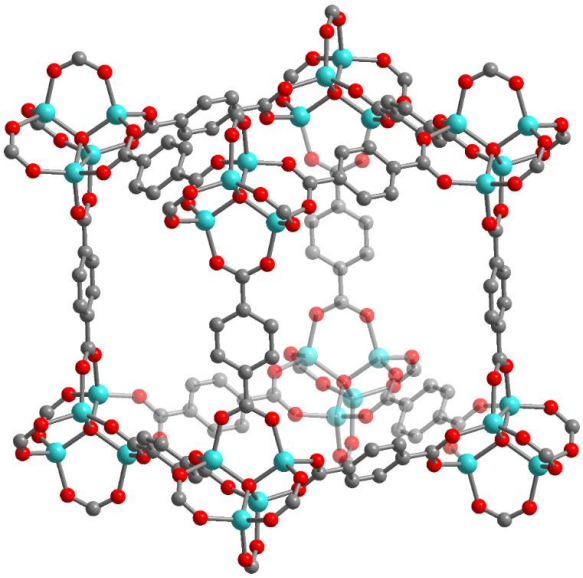

Figure 1.1. Crystal structure of MOF-5, $Zn_4O(bdc)_3$, adapted from ref. 34. Cyan, red, blue, and gray spheres represent Zn, O, N, and C atoms, respectively; H atoms are omitted for clarity.

1.3 Mixed-Valence in Coordination Solids

Mixed-valence

Mixed-valence compounds consist of metals or ligands that exist in more than one formal oxidation state, often featuring electronic coupling and electron transfer, or intervalence charge transfer (IVCT), between the mixed-valence centers.[58-60] Depending on the degree of electronic coupling, mixed-valence compounds can be classified according to the classification scheme devised by Robin and Day and further analyzed using a two-state model by Hush and co-workers.[61,62]

Class I mixed-valence systems lack electronic coupling between mixed-valence centers and exhibit charge-localized sites. Class II systems feature different optical and electronic properties from increased electronic coupling. An energy coordinate diagram for a symmetric mixed-valence system may be described as Figure 1.2. While the mixed-valence centers remain valence-trapped in the ground state, the electrons can be transferred over a barrier with the activation energy given as

$$E_a = \frac{\lambda}{4} - H_{ab} + \frac{{H_{ab}}^2}{\lambda} = \frac{(\lambda - 2H_{ab})^2}{4\lambda}$$

where λ is the reorganization energy and H_{ab} is the electronic coupling parameter. Class II systems adopt H_{ab} value of $0 < H_{ab} < \lambda/2$ with the ground state described by a double-well potential. With strong electronic coupling ($H_{ab} > \lambda/2$), Class III systems feature a ground state with a single energy minimum, corresponding to full electron delocalization where each mixed-valence center adopts an average, intermediate oxidation state. Characteristic intense intervalence charge transfer absorption bands can be observed in the mid-infrared, near-infrared, and visible regions of the optical spectra.

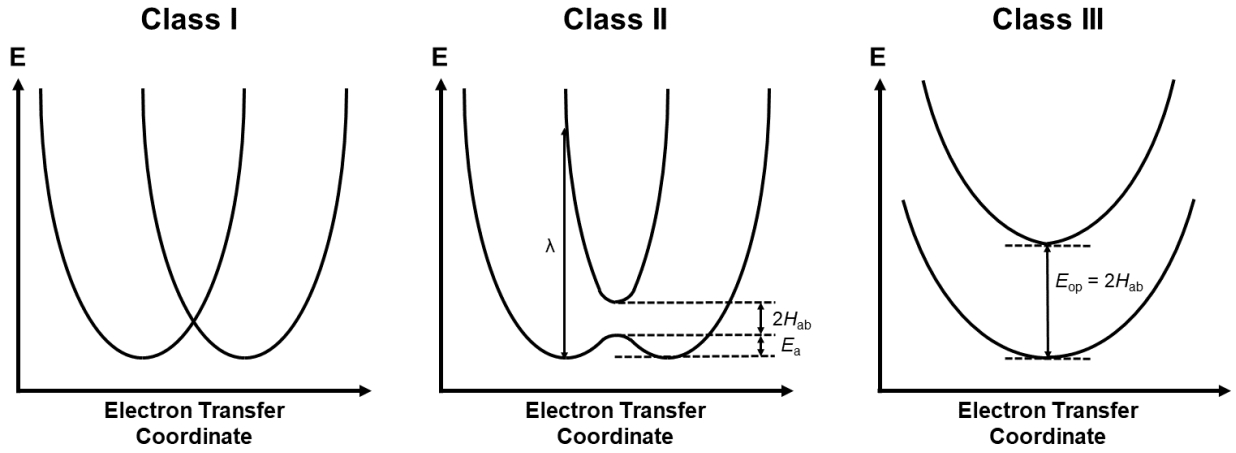

Figure 1.2. Energy-coordinate diagrams for symmetric Class I, II, and III mixed-valence systems. λ is the reorganization energy, E_{op} is the absorption band maximum for the intervalence charge transfer transition, H_{ab} is the electronic coupling parameter, and E_a is the energy barrier to electron transfer.

While mixed-valence compounds are prevalent in nature, the Cruetz-Taube complex, $[(NH_3)_5Ru(pz)Ru(NH_3)_5]^{5+}$ (pz = pyrazine), was the first synthetic mixed-valence complex to be

reported (Figure 1.3).[63,64] The Cruetz-Taube ion consists of two $Ru^{II/III}$ ions with octahedral coordination geometry bridged by a pz ligand and 10 amine molecules completing the coordination sphere. Metal-ligand bond distances are similar for both $Ru^{II/III}$ ions, suggesting valence delocalization with each Ru ion having a fractional oxidation state of +2.5. The Cruetz-Taube complex exhibits a strong intervalence charge transfer absorption in the near-infrared region of the absorption spectrum, and the Cruetz-Taube complex can be classified as a borderline Class II-III mixed-valence system from the Hush analysis. This remarkable valence delocalization can be attributed to the combination of strong orbital overlap between $Ru^{II/III}$ $4d_\pi$ and pz π^* orbitals and the small reorganization energy required for the intervalence charge transfer as the result of the mixed-valence low-spin $d^{5/6}$ electronic configuration and the symmetric coordination sphere of $Ru^{II/III}$ ions.

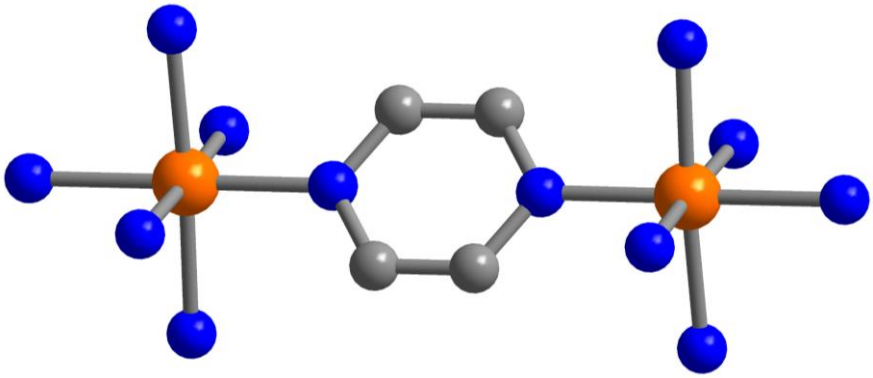

Figure 1.3. Crystal structure of the Cruetz-Taube complex, $[(NH_3)_5Ru(pz)Ru(NH_3)_5]^{5+}$, adapted from ref. 65. Orange, blue, and gray spheres represent Ru, N, and C atoms, respectively; H atoms and counterions are omitted for clarity.

Extending mixed-valence chemistry to metal–organic frameworks

Design insights derived from molecular complexes can be employed to construct extended coordination solids with closely spaced mixed-valence metal centers and favorable intervalence charge transfer, thereby engendering bulk electronic conductivities.[21,66] For instance, post-synthetic reduction of $Fe_2(BDP)_3$ (BDP^{2-} = 1,4-benzenedipyrazolate) using potassium naphthalenide affords $K_xFe_2(BDP)_3$ ($0<x<2$).[67,68] Notably, $Fe_2(BDP)_3$ consists of one-dimensional chains of octahedral Fe^{III} chains bridged by μ^2-pyrazolate ligands. The post-synthetic reduction results in mixed-valence $Fe^{II/III}$ ions with the insertion of potassium ions in the framework cavity for charge-balance (Figure 1.4).[68,69] Analogous to the Cruetz-Taube complex, $K_xFe_2(BDP)_3$ ($0<x<2$) comprises mixed-valence $Fe^{II/III}$ ions with a symmetric coordination environment and low-spin $d^{5/6}$ electronic configuration, giving rise to a small reorganizational energy and favorable intervalence charge transfer. Furthermore, strong hybridization of $Fe^{II/III}$ $3d_\pi$ and pyrazolate π^* orbitals can provide an efficient one-dimensional charge transport pathway. Reduction of half of the Fe^{III} ions yields delocalized charge carriers, with the material $K_{0.98}Fe_2(BDP)_3$ shown to exhibit a peak charge mobility of μ_e = 0.84 $cm^2\ V^{-1}\ s^{-1}$ and an estimated single-crystal four-contact conductivity of $\sim 7\times10^2$ S/cm at 300 K—nearly 10,000-fold increased conductivity compared to that of the parent $Fe_2(BDP)_3$ framework (9.6×10^{-3} S/cm). This large increase highlights that post-synthetic redox chemistry to engender mixed-valence centers and strong intervalence charge transfer is a promising approach for modification of electronic structures and conductivities of

extended coordination solids with a variety of charge transport pathways, as also exemplified by other previous reports.[21,66]

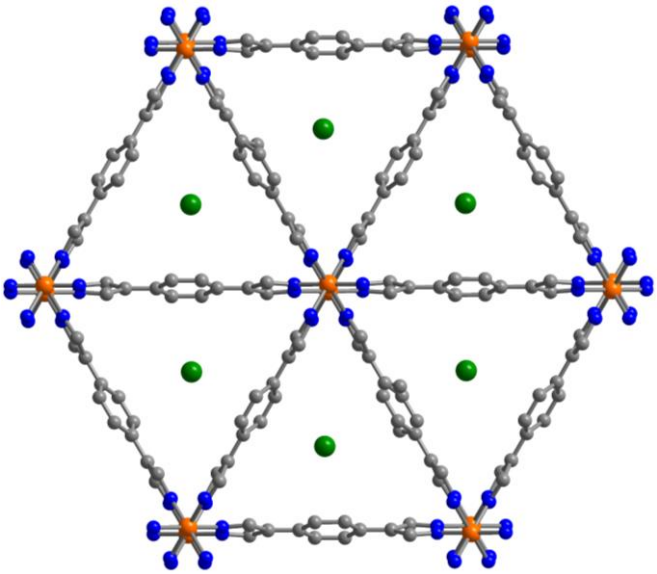

Figure 1.4. Crystal structure of $K_xFe_2(BDP)_3$ ($0<x\leq2$), adapted from ref. 69. Orange, green, blue, and gray spheres represent Fe, K, N, and C atoms, respectively; H atoms are omitted for clarity.

While metal-based mixed-valence is prevalent in solid-state materials and molecular compounds, extended coordination solids offer a fascinating platform to access ligand-based mixed-valence and investigate the resulting bulk properties.[19,21,70-79] For instance, numerous efforts have utilized ligand-centered mixed-valence to synthesize conductive metal–organic frameworks, such as reports on ferric semiquinoid frameworks.[76-79] In particular, the three-dimensional framework $(NBu_4)_2Fe_2(dhbq)_3$ ($dhbq^{2-/3-}$ = 2,5-dioxidobenzoquinone/1,2-dioxido-4,5-semiquinone) is constructed by octahedral high-spin Fe^{III} ions bridged by $dhbq^{n-}$ ligands (Figure 1.5).[79,80] During the synthesis, two of the three $dhbq^{2-}$ ligands undergo a spontaneous reduction by Fe^{II} ions to form mixed-valence $dhbq^{2-/3-}$ ligands. Furthermore, two NBu_4^+ cations per formula unit are inserted in the framework cavity for charge balance. As the result of the ligand mixed-valence, $(NBu_4)_2Fe_2(dhbq)_3$ was shown to exhibit an appreciable electronic conductivity of 0.16(1) S cm^{-1} at 298 K. Post-synthetic reduction of $(NBu_4)_2Fe_2(dhbq)_3$ using sodium naphthalenide resulted in the reduction of $dhbq^{2-}$ to $dhbq^{3-}$ ligands and yields $Na_{0.9}(NBu_4)_2Fe_2(dhbq)_3$. As expected, the reduced framework exhibits a decreased electronic conductivity of 0.0062(1) S Scm^{-1} at 298 K due to the lack of ligand-centered mixed-valence.

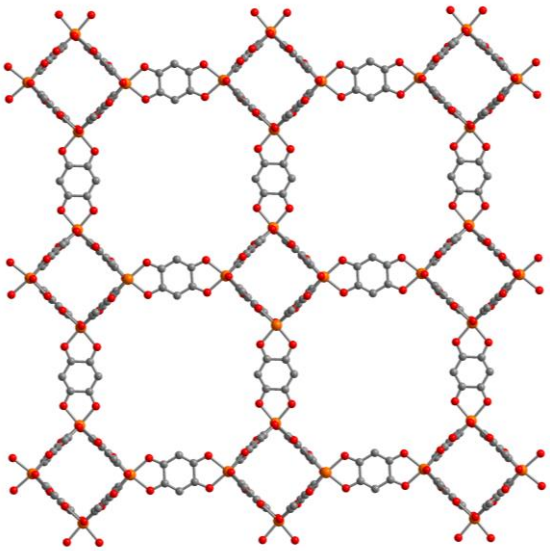

Figure 1.5. Crystal structure of $(NBu_4)_2Fe_2(dhbq)_3$, adapted from ref. 79. Orange, red, and gray spheres represent Fe, O, and C atoms, respectively; H atoms and NBu_4^+ cations are omitted for clarity.

Polarons

The electronic structures of many conductive mixed-valence metal–organic frameworks can be described by small polarons. A polaron is a localized charge carrier within a potential well in a dielectric crystal through polarization or displacement of the surrounding lattice ions.[81-87] As such, a polaron can be envisioned as a charge carrier surrounded by a polarized cloud of phonons. The strength of the electron-phonon coupling determines the width of the polarized cloud or the depth of the potential well, which can distinguish small and large polarons. Transport of small polarons within a crystal carries a lattice distortion. In other words, diffusion of small polarons proceed through phonon-assisted tunneling or hopping. The mobility of small polarons are reduced compared to the free charge carriers and exhibit a positive dependence on temperature. In contrast, large polarons have a large effective mass that reduces scattering from phonon fields to maintain coherent transport and high mobility. Therefore, large polarons resemble free charge carriers with their mobilities having negative dependences on temperature.

Variable-temperature conductivity measurements can be used to understand the electronic structure of a material consisting of small polarons. In crystalline systems where small polarons form impurity mid-gap states of uniform distribution and similar energy, the thermally activated hopping of charge carriers would occur between the nearest-neighboring states with a constant value for an activation process. The temperature dependence of electronic conductivity in such systems follows the Arrhenius equation for nearest-neighbor hopping:

$$\sigma(T) = \sigma_0 e^{-(\frac{E_a}{k_b T})}$$

where σ_0 is the pre-exponential factor and E_a is the activation energy. In many other systems including amorphous semiconductors and doped conductive polymers, the impurity mid-gap states may acquire a random distribution of position and energy. In this case, charge transport would no longer follow the Arrhenius behavior with a constant activation energy. At high temperatures,

thermal energy allows various phonon modes that can assist a hopping process between the nearest-neighbor mid-gap states of a large energy difference. At low temperatures, the phonon modes freeze out, and the charge carrier can only hop between mid-gap states of similar energies with a larger hopping distance. The variable-temperature conductivity data can be modelled using an equation for variable-range hopping:

$$\sigma(T) = \sigma_0 e^{-(\frac{T_a}{T})^z}$$

with

$$z = \frac{1}{1+d}$$

where *d* is the dimensionality of the charge transport, and with

$$\sigma_0 = e^2 N(E_F) R v_{ph}$$

where $N(E_F)$ is the density of states at the Fermi energy, *R* is the average hopping distance, and v_{ph} is typical phonon frequency, and with

$$T_0 = \frac{(8\alpha)^3}{9\pi k N(E_F)}$$

where α is inverse localization length. For a three-dimensional system, the temperature dependent variable-range hopping conductivity equation transforms into Mott's variable-range hopping equation with the conductivity proportional to $T^{-1/4}$.[88]

1.4 Magnetic Exchange in Coordination Compounds

Goodenough–Kanamori rules

The dominant type of magnetic exchange in coordination solids consisting of paramagnetic metal centers bridged by diamagnetic ligands is superexchange coupling. According to the Goodenough–Kanamori rules, the strength and sign of magnetic interaction is determined by the orientation and degeneracy of the interacting metal and ligand orbitals.[89-91] Consider a case of a linear M^{n+}–O^{2-}–M^{n+} fragment, where two equivalent metals with half-filled d_σ orbitals are bridged by a single oxygen atom. If an unpaired electron in the left metal ion has a spin-up configuration, then any partially transferred electron density from the O p orbital must have a spin-down configuration according to the Pauli exclusion principle, thus leaving spin-up electron density in the right metal ion. The unpaired electron of the right metal ion will have a spin-down configuration, leading to an anti-parallel alignment—or antiferromagnetic coupling—of the metal-centered electronic spins. A parallel alignment—or ferromagnetic coupling—is also possible through superexchange when the M–O–M angle is 90°. In this case, two metal-based d_σ orbitals overlap with two orthogonal O p orbitals. When the left metal has spin-up unpaired electrons, the first O p orbital will donate spin-down electron density, leaving an "excess" spin-up electron density. Spin correlation within the O ligand favors a parallel spin-up alignment of the electronic spin on the second O p orbital. As such, this second p orbital will donate spin-down electron

density and yield a spin-up configuration for the unpaired electrons on the right metal ion. The Goodenough–Kanamori rules also states that the superexchange between a metal ion with half-filled orbitals and a metal ion with empty or filled orbitals will be ferromagnetic. While this generalized scheme is useful for explaining the magnetism of many solids with simple chemical structures, such as metal oxides and Prussian Blue analogues, accurately and precisely predicting the magnetic properties of other coordination solids is challenging. For example, a deviation in a metal–ligand bond angle can lead to competing antiferromagnetic and ferromagnetic interactions.

Spin-polarization mechanism

The magnetic properties of many conductive and magnetic coordination solids that feature paramagnetic metal ions bridged by organic ligands with conjugated π systems may be understood by the spin-polarization mechanism.[92-96] In systems with strong overlap between metal d_π and ligand p_π orbitals, an electronic spin of an atom can polarize the electron cloud on the nearest-neighbor atoms such that they acquire an antiparallel alignment of the spins. For instance, a spin-polarization mechanism is responsible for inducing antiferromagnetic and ferromagnetic interactions between metal ions bridged by pyrazine and pyrimidine, respectively. More generally, the magnetic interactions between metal ions bridged by even and odd numbers of atoms are antiferromagnetic and ferromagnetic, respectively.

1.5 Designing High Temperature Metal–Organic Magnets

Strong superexchange via short bridging ligands

Analogues of the pigment Prussian blue have been targeted and extensively studied as potential room-temperature bulk magnets.[13,14] The parent compound Prussian blue, $Fe_4[Fe(CN)_6]_3{\cdot}xH_2O$, is historically the first synthetic coordination solid that was widely used in a number of paints and fabrics for its deep blue color.[97-100] Prussian blue has a cubic framework structure with alternating low-spin Fe^{II} and high-spin Fe^{III} ions bridged by cyanide ligands (Figure 1.6). In the idealized structure, Fe^{II} and Fe^{III} ions are coordinated to the carbon and nitrogen atoms of the cyanide ligands, respectively. As a ligand, cyanide is a good π-acceptor with low-lying π* orbitals that can accept electron density from metal ions via back-bonding, thereby facilitating a relatively strong magnetic coupling between the paramagnetic metal ions via a superexchange mechanism.[13,14] While Prussian blue ferromagnetically orders below 5.6 K,[101,102] substitution of the metal ions can dramatically improve the magnetic ordering temperature in the analogous compounds.[13,14,103-107] The exchange interaction between metal ions through a cyanide bridge can be estimated to be either ferromagnetic or antiferromagnetic if the interacting spins belong to the orbitals of the same or different symmetry, respectively. Intuitively, the strongest antiferromagnetic superexchange may be expected from the nearest-neighboring metal ions having t_{2g}^3-t_{2g}^3 electronic configurations. Furthermore, the exchange coupling constant, *J*, between the nearest neighbor metal centers, M and M´, can be calculated by using the approximate mean-field expression derived from the Langevin, Weiss, and Néel equation:[108]

$$T_c = \frac{\sqrt{z_M z_{M'}}|J|\sqrt{xS_M(S_M+1)S_{M'}(S_{M'}+1)}}{3k_B}$$

where T_c is the magnetic ordering or correlation temperature, *z* is the number of nearest neighbors, *S* is the local spin on each metal center, and k_B is the Boltzmann constant. Indeed, various Prussian blue analogues have been synthesized and shown to exhibit high magnetic ordering temperatures.

In particular, $KV[Cr(CN)_6]\cdot 2H_2O$ exhibits a ferrimagnetic ordering temperature of T_N = 376 K from strong antiferromagnetic coupling between V^{II} and Cr^{III} ions, with a computationally determined exchange coupling constant of J = –241 cm^{-1}.[103,105] Efforts to further increase the magnetic ordering temperature in Prussian blue analogues, include utilizing 4d and 5d late transition metals in combination with early 3d transition metals to enhance exchange coupling.[109-112]

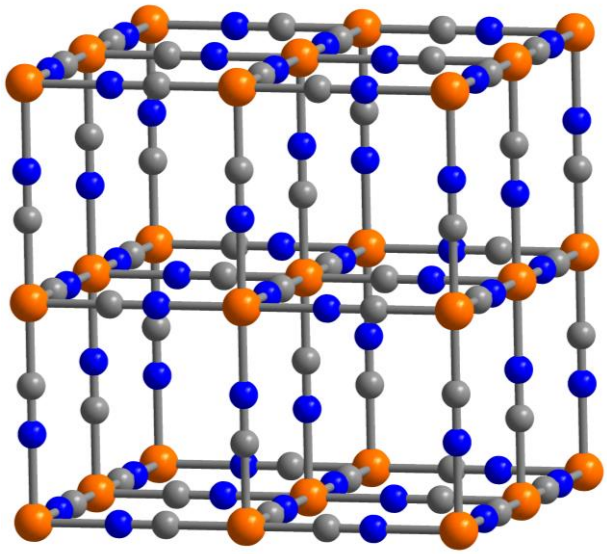

Figure 1.6. Idealized crystal structure of Prussian blue adapted from ref. 100. Orange, blue, and gray spheres represent Fe, N, and C atoms, respectively.

Direct exchange via paramagnetic bridges

Substitution of diamagnetic linkers with paramagnetic organic ligands can lead to increased magnetic ordering temperatures in metal–organic magnets. For instance, paramagnetic metal ions can engage in direct magnetic exchange with the spin-carrying ligand orbitals, leading to a further enhanced magnetic interaction or communication between the spin centers compared to the systems that rely on relatively weak superexchange coupling. Indeed, many examples of radical-bridged dinuclear transition metal compounds have been shown to exhibit strong magnetic exchange couplings, as high as –900 cm^{-1}.[113-115] The large library of molecular examples containing organic radical bridges can serve as basis for designing metal–organic magnets with high magnetic ordering temperatures. Furthermore, metal–organic magnets consisting of large paramagnetic organic ligands are highly desirable for their synthetic tunability and modular chemical, electronic, and magnetic structures.

Tremendous efforts have been dedicated to synthesizing organonitrile radical-bridged compounds such as tetracyanoethylene (TCNE)[13,14,32,116-126] and tetracyanoquinodimethane (TCNQ)[13,14,23,24,127-130] ligands. In particular, TCNE features low-lying π^* orbitals and can thus accept an electron to form the $TCNE^{-\bullet}$ radical anion. The first structurally characterized metal–TCNE magnet was the two-dimensional compound $[Fe(TCNE)(MeCN)_2](FeCl_4)$, which consists of layers of octahedral Fe^{II} ions equatorially bridged by μ_4-$TCNE^{-\bullet}$ radical anions (Figure 1.7).[125] This compound exhibits a metastable antiferromagnetic ordering below 90 K due to the interlayer antiferromagnetic coupling between ferrimagnetic $[Fe(TCNE)(MeCN)_2]$ layers, with

antiferromagnetic interactions between Fe^{II} and μ_4-$TCNE^{-\bullet}$ radical spins. At 50 K, this two-dimensional Fe-TCNE compound exhibits magnetic hysteresis with a coercive field of 1730 Oe.

Similarly, the ability to facilitate strong magnetic interactions with $TCNE^{-\bullet}$ radical anions was further confirmed by the room-temperature magnet $V(TCNE)_x \cdot yCH_2Cl_2$ ($x \approx 2$; $y \approx 0.5$) with the experimentally accessible ferrimagnetic ordering temperature of $T_{Nexp} \sim 370$ K, due to thermal decomposition.[32,131-136] Furthermore, chemical vapor deposition techniques can be utilized to yield a high-quality thin film of $V(TCNE)_x$ ($x \approx 2$) that exhibits a theoretical ferrimagnetic ordering temperature of $T_N \sim 600$ K and coherent magnon transport.[137,138] While $V(TCNE)_x \cdot yCH_2Cl_2$ ($x \approx 2$; $y \approx 0.5$) is amorphous, the chemical structure of the material is proposed to be similar to that of a related material $Mn(TCNE)_{1.5}(I_3)_{0.5} \cdot 0.5THF$ (Figure 1.7).[126,131] In contrast to most of the three-dimensional metal–TCNE compounds that exhibit dimerization of $TCNE^{-\bullet}$ during crystallization to form diamagnetic $[C_4(CN)_8]^{2-}$ linkers within the framework lattice, $Mn(TCNE)_{1.5}(I_3)_{0.5} \cdot 0.5THF$ consists of octahedral Mn^{II} ions bridged by six different, fully radical $TCNE^{-\bullet}$ anions. The compound $Mn(TCNE)_{1.5}(I_3)_{0.5} \cdot 0.5THF$ exhibits ferrimagnetically orders below $T_N = 171$ K, and the presence of long-range magnetic order was confirmed through ac magnetic susceptibility measurements. This ferrimagnetic order can be attributed to direct antiferromagnetic coupling between Mn^{II} ions and $TCNE^{-\bullet}$ radical anions. Similarly, numerous studies including X-ray absorption spectroscopy, conductivity, magnetic studies have been performed to understand the electronic structure and the origin of high magnetic ordering temperature of $V(TCNE)_x \cdot yCH_2Cl_2$.[139-142] While $V(TCNE)_x \cdot yCH_2Cl_2$ has octahedral V^{II} ions also bridged by six $TCNE^{-\bullet}$ anions, the diffuse 3d orbitals of V^{II} compared to that of Mn^{II} can form a stronger metal-ligand orbital overlap and engage in a stronger metal-radical magnetic exchange, ultimately leading to the observed high magnetic ordering temperature.

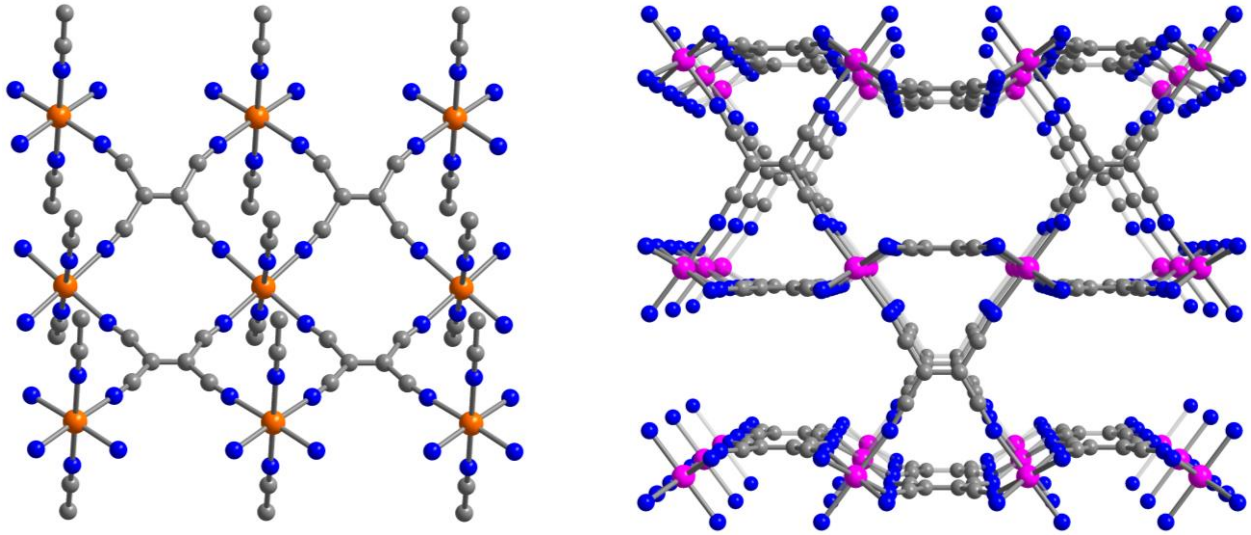

Figure 1.7. Crystal structure of $[Fe(TCNE)(MeCN)_2](FeCl_4)$ (left) and $Mn(TCNE)_{1.5}(I_3)_{0.5} \cdot 0.5THF$ (right) adapted from ref. 125 and 126, respectively. Orange, pink, blue, and gray spheres represent Fe, Mn, N, and C atoms, respectively; H atoms, THF molecules, and counterions are omitted for clarity.

The recent a report of $Cr(pz)_2 \cdot 0.7LiCl$ (pz = pyrazine) prepared through post-synthetic chemical reduction of *trans*-$CrCl_2(pz)_2$ highlights the efforts of utilizing paramagnetic linkers to

engender high-temperature magnetic order in metal–organic magnets.[33,143,144] The parent *trans*-$CrCl_2(pz)_2$ framework features two-dimensional sheets consisting of octahedral Cr^{III} ions equatorially bridged by pz linkers, with the terminal coordination sites completed by Cl^- anions (Figure 1.8). During the synthesis of *trans*-$CrCl_2(pz)_2$, spontaneous reduction of half of the neutral pz linkers to radical anions by Cr^{II} ions during synthesis results in the ligand mixed-valence. As the result, *trans*-$CrCl_2(pz)_2$ exhibits a room-temperature electronic conductivity of 32 mS/cm and ferrimagnetic order below ~55 K due to an antiferromagnetic direct exchange between spins on Cr^{III} $3d_\pi$ and $pz^{-\bullet}$ π^* orbitals. In contrast, $Cr(pz)_2 \cdot 0.7LiCl$ consists of four $pz^{-\bullet}$ radical anions bridging square planar Cr^{II} ions to form two-dimensional sheets and intercalated LiCl salts within the layers. Notably, $Cr(pz)_2 \cdot 0.7LiCl$ holds the record magnetic ordering temperature of T_N = 515 K among any structurally characterized metal–organic magnets. Compared to the parent *trans*-$CrCl_2(pz)_2$ compound, the large increase in the magnetic ordering temperature can be attributed to the increased number of spin centers and metal-ligand pairings engaged in the direct magnetic exchange and strong hybridization of metal and ligand orbitals. Furthermore, the magnetic anisotropy of square planar Cr^{II} ions and the two-dimensional bulk structure of $Cr(pz)_2 \cdot 0.7LiCl$ contributes to the observation of a large coercivity of 0.75 T at 300 K.

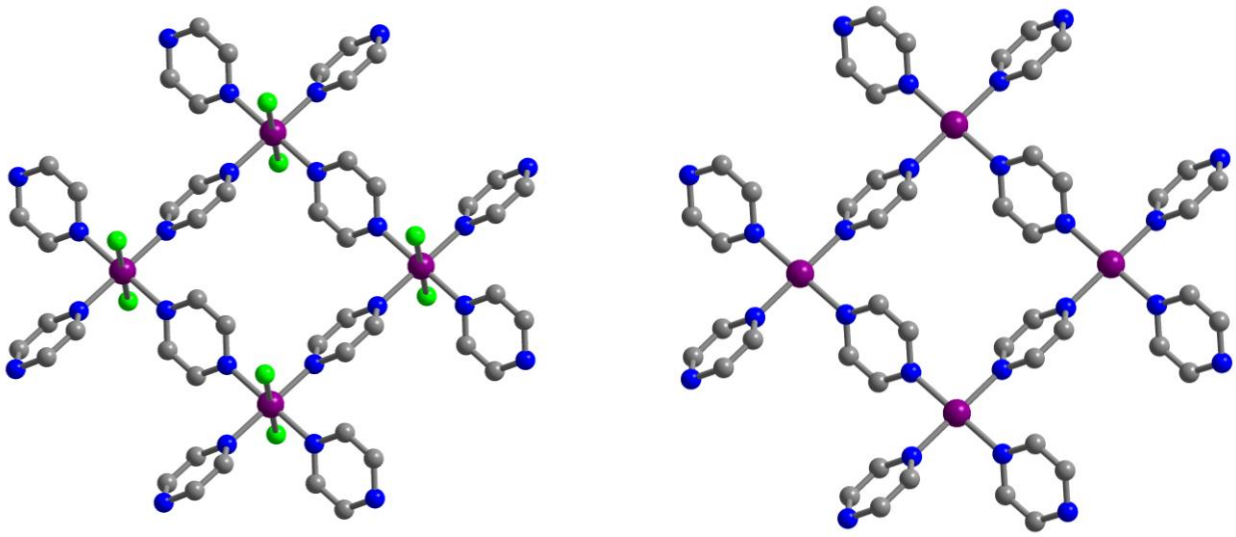

Figure 1.8. Crystal structure of *trans*-$CrCl_2(pz)_2$ (left) and $Cr(pz)_2 \cdot 0.7LiCl$ (right) adapted from ref. 143 and 33, respectively. Purple, neon green, blue, and gray spheres represent Cr, Cl, N, and C atoms, respectively; H atoms and counterions are omitted for clarity.

Ferromagnetism via itinerant charge carriers

The third promising, yet much less investigated, strategy for designing a metal–organic magnet with a high magnetic ordering temperature is via itinerant magnetism. In fact, many solid-state materials with high magnetic ordering temperatures are based on this mechanism.[145] For instance, in 1951, Zener developed the double-exchange mechanism to explain the high temperature ferromagnetism and metallic conductivity in the mixed-valence manganese perovskites $La_{(1-x)}A_xMnO_3$ (A^{2+} = Ca, Sr, Ba).[146-148] As shown in Figure 1.9, mixed-valence $Mn^{III/IV}$ ions have partially filled e_g orbitals that are strongly hybridized with the 2p orbitals of the bridging O^{2-} anion. When a spin-up electron is transferred between e_g orbitals, it is more energetically favorable for other d electrons in the half-filled t_{2g} orbitals to be aligned parallel to the itinerant spin-up electron, in accordance with Hund's rule. This leads to the simultaneous observation of

ferromagnetism and barrierless electron transfer. Double exchange is responsible for the colossal magnetoresistance observed in the manganese perovskites, and they have been heavily investigated for spintronics applications.[149-153]

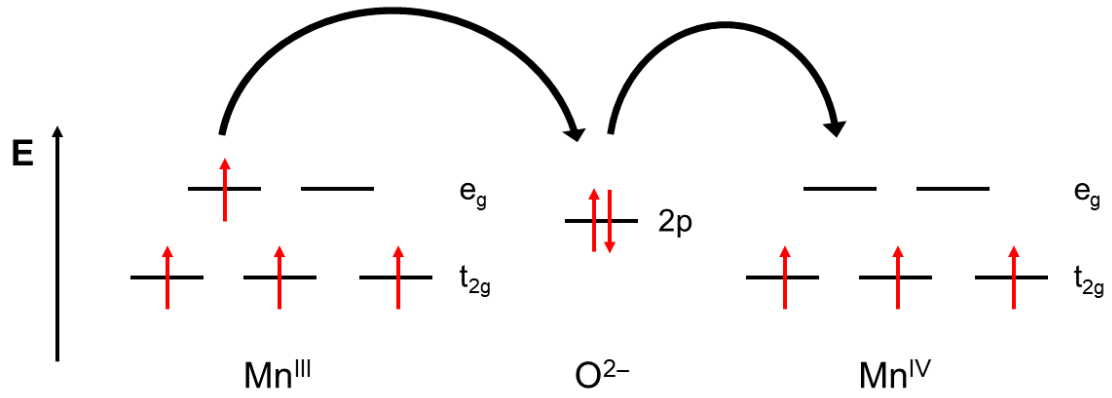

Figure 1.9. Double-exchange mechanism in mixed-valence manganese perovskites. Each manganese ion features an octahedral coordination environment, in which the energies of the 3d orbitals are split into t_{2g} and e_g sets. Red and black arrows depict electrons and path of electron transfer, respectively.

While the double-exchange phenomenon is commonly observed in many solid-state materials such as magnetite, cobaltite, and Heusler alloys, it is a much rarer occurrence in molecular compounds and coordination solids with organic bridging ligands.[154-159] Indeed, double exchange in metal–organic magnets is highly desirable for simultaneously allowing high magnetic ordering temperature and the use of various diamagnetic organic linker. Double exchange in a molecular complex consisting of an organic bridge was first observed in a mixed-valence divanadium imidazolate complex, $[(PY5Me_2)_2V_2(\mu\text{-}5,6\text{-dmbzim})]^{4+}$ ($PY5Me_2$ = 2,6-*bis*(1,1,-*bis*(2-pyridyl)ethyl)pyridine; 5,6-dmbzim$^-$ = 5,6-dimethylbenzimidazolate) (Figure 1.10).[160] Upon an oxidation of the valence-pure $[(PY5Me_2)_2V_2(\mu\text{-}5,6\text{-dmbzim})]^{3+}$, $[(PY5Me_2)_2V_2(\mu\text{-}5,6\text{-dmbzim})]^{4+}$ acquires mixed-valence $V^{II/III}$ ions with $d^{2/3}$ electronic configurations. Importantly, the complex features symmetric, compact, and conjugated imidazolate ligands that link the mixed-valence $V^{II/III}$ ions. Also, strong overlap of diffuse V t_{2g} and imidazolate π^* ligand orbitals provide an efficient platform for a favorable intervalence charge transfer. This mixed-valence divanadium imidazolate complex exhibits optical spectroscopic properties consistent with Class II/III mixed-valence and magnetic data supporting high spin S=5/2 ground state with an electron exchange parameter of B = 122 cm^{-1}.

The complex $[(Me_3TPyA)_2Fe_2(L)]^{3+}$ (Me_3TPyA = tris((6-methyl-2-pyridyl)-methyl)amine; LH_2 = 2,5-di(2,6-dimethylanilino)-3,6-dibromo-1,4-benzoquinone) provided the second example of double exchange through an organic ligand between mixed-valence metal centers (Figure 1.10).[161] The mixed-valence $[(Me_3TPyA)_2Fe_2(L)]^{3+}$ complex is obtained through a chemical oxidation of one of the Fe^{II} ions in $[(Me_3TPyA)_2Fe_2(L)]^{2+}$. Similar to $[(PY5Me_2)_2V_2(\mu\text{-}5,6\text{-dmbzim})]^{4+}$, the double-exchange mechanism in $[(Me_3TPyA)_2Fe_2(L)]^{3+}$ yields Class II/III mixed-valence and is responsible for the stabilization high spin S = 9/2 ground state. Interestingly, $[(Me_3TPyA)_2Fe_2(L)]^{3+}$ also exhibits single-molecule magnet behavior below 5 K, with a relaxation barrier of U_{eff} = 14(1) cm^{-1}. While the obtained electron exchange parameter of B = 69(4) cm^{-1} is significantly smaller than that of the mixed-valence divanadium imidazolate complex,

$[(Me_3TPyA)_2Fe_2(L)]^{3+}$ exhibits the largest metal-metal separation of 8.029(4) Å yet observed in any double-exchange molecular compounds.

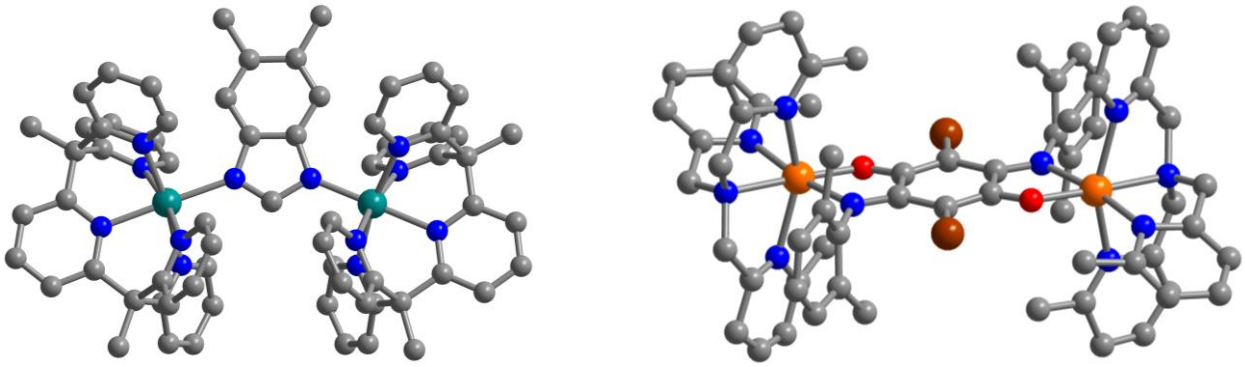

Figure 1.10. Crystal structures of $[(PY5Me_2)_2V_2(\mu\text{-}5,6\text{-dmbzim})]^{3+}$ (left) and $[(Me_3TPyA)_2Fe_2(L)]^{3+}$ (right) adapted from ref. 160 and 161, respectively. Orange, teal, brown, red, blue, and gray spheres represent Fe, V, Br, O, N, and C atoms, respectively; H atoms are omitted for clarity.

1.6 References

(1) Croat, J. J.; Herbst, J. F.; Lee, R. W.; Pinkerton, F. E. *J. Appl. Phys.* **1984**, *55*, 2078.
(2) Sagawa, M.; Fujimura, S.; Togawa, N. *J. Appl. Phys.* **1984**, *55*, 2083.
(3) Strnat, K.; Hoffer, G.; Olson, J.; Ostertag, W.; Becker, J. J. *J. Appl. Phys.* **1967**, *38*, 1001.
(4) de Boer, M. A.; Lammertsma, K. *ChemSusChem* **2013**, *6*, 2045.
(5) U.S. Department of Energy, *Critical Materials Strategy*, **2011**.
(6) "Research Funding for Rare Earth Free Permanent Magnets", ARPA-E, **2011**. https://arpa-e.energy.gov/technologies/programs/react.
(7) Yaghi, O. M.; O'Keeffe, M.; Ockwig, N. W.; Chae, H. K.; Eddaoudi, M.; Kim, J. *Nature* **2003**, *423*, 705.
(8) Brozek, C. K.; Dincă, M. *Chem. Soc. Rev.* **2014**, *43*, 5456.
(9) Deria, P.; Mondloch, J. E.; Karagiaridi, O.; Bury, W.; Hupp, J. T.; Farha, O. K. *Chem. Soc. Rev.* **2014**, *43*, 5896.
(10) Kim, M.; Cahill, J. F.; Su. Y.; Prather, K. A.; Cohen, S. M. *Chem. Sci.* **2012**, *3*, 126.
(11) Liu, C.; Luo, T.-Y.; Feura, E. S.; Zhang, C.; Rosi, N. L. *J. Am. Chem. Soc.* **2015**, *137*, 10508.
(12) Yin, Z.; Wan, S.; Yang, J.; Kurmoo, M.; Zeng, M.-H. *Coord. Chem. Rev.* **2019**, *378*, 500.
(13) Dechambenoit, P.; Long, J. R. *Chem. Soc. Rev.* **2011**, *40*, 3249.
(14) Thorarinsdottir, A. E.; Harris, T. D. *Chem. Rev.* **2020**, *120*, 8716.
(15) Murray, K. S.; Kepert, C. J. *Top. Curr. Chem.* **2004**, *233*, 195.
(16) Garcia, Y.; Niel, V.; Muñoz, M. C.; Real, J. A. *Top Curr. Chem.* **2004**, *233*, 229.
(17) Ni, Z.-P.; Liu, J.-L.; Hoque, M. N.; Liu, W.; Li, J.-Y.; Chen, Y.-C.; Tong, M.-L. *Coord. Chem. Rev.* **2017**, *335*, 23.
(18) Grzywa, M.; Röß-Ohlenroth, R.; Muschielok, C.; Oberhofer, H.; Blachowski, A.; Żukrowski, J.; Vieweg, D.; Krug von Nidda, H.-A.; Volkmer, D. *Inorg. Chem.* **2020**, *59*, 10501.
(19) Sun, L.; Campbell, M. G.; Dincă, M. *Angew. Chem. Int. Ed.* **2016**, *55*, 3566.

(20) Medina, D. D.; Mähringer, A.; Bein, T. *Isr. J. Chem.* **2018**, *58*, 1089.
(21) Xie, L. S.; Skorupskii, G.; Dincă, M. *Chem. Rev.* **2020**, *120*, 8536.
(22) Kaye, S. S.; Choi, H. J.; Long, J. R. *J. Am. Chem. Soc.* **2008**, *130*, 16921.
(23) Kosaka, W.; Liu, Z.; Zhang, J.; Sato, Y.; Hori, A.; Matsuda, R.; Kitagawa, S.; Miyasaka, H. *Nat. Commun.* **2018**, *9*, 5420.
(24) Zhang, J.; Kosaka, W.; Kitagawa, Y.; Miyasaka, H. *Nat. Chem.* **2021**, *13*, 191.
(25) Campbell, M. G.; Sheberla, D.; Liu, S. F.; Swager, T. M.; Dincă, M. *Angew. Chem. Int. Ed.* **2015**, *54*, 4349.
(26) Smith, M. K.; Mirica, K. A. *J. Am. Chem. Soc.* **2017**, *149*, 16759.
(27) Aubrey, M. L.; Kapelewski, M. T.; Melville, J. F.; Oktawiec, J.; Presti, D.; Gagliardi, L.; Long, J. R. *J. Am. Chem. Soc.* **2019**, *141*, 5005.
(28) Kobayashi, Y.; Jacobs, B.; Allendorf, M. D.; Long, J. R. *Chem. Mater.* **2010**, *22*, 4120.
(29) Miller, J. S.; Calabrese, J. C.; Epstein, A. J.; Bigelow, R. W.; Zhang, J. H.; Reiff, W. M. *J. Chem. Soc., Chem. Commun.* **1986**, 1026.
(30) Miller, J. S.; Calabrese, J. C.; Rommelmann, H.; Chittipeddi, S. R.; Zhang, J. H.; Reiff, W. M.; Epstein, A. J. *J. Am. Chem. Soc.* **1987**, *109*, 769.
(31) Yee, G. T.; Manriquez, J. M.; Dixon, D. A.; McLean, R. S.; Groski, D. M.; Flippen, R. B.; Narayan, K. S.; Epstein, A. J.; Miller, J. S. *Adv. Mater.* **1991**, *3*, 309.
(32) Manriquez, J. M.; Yee, G. T.; McLean, R. S.; Epstein, A. J.; Miller, J. S. *Science* **1991**, *252*, 1415.
(33) Perlepe, P.; Oyarzabal, I.; Mailman, A.; Yquel, M.; Platunov, M.; Dovgaliuk, I.; Rouzières, M.; Négrier, P.; Mondieig, D.; Suturina, E. A.; Dourges, M.-A.; Bonhommeau, S.; Musgrave, R. A.; Pedersen, K. S.; Chernyshov, D.; Wilhelm, F.; Rogalev, A.; Mathonière, C.; Clérac, R. *Science*, **2020**, *370*, 587.
(34) Li, H.; Eddaoudi, M.; O'Keeffe, M.; Yaghi, O. M. *Nature* **1999**, *402*, 276.
(35) Yaghi, O. M.; O'Keeffe, M.; Ockwig, N. W.; Chae, H. K.; Eddaoudi, M.; Kim, J. *Nature* **2003**, *423*, 705.
(36) Hendon, C. H.; Tiana, D.; Walsh, A. *Phys. Chem. Chem. Phys.* **2012**, *14*, 13120.
(37) Feng, L.; Wang, K.-Y.; Day, G. S.; Ryder, M. R.; Zhou, H.-C. *Chem. Rev.* **2020**, *120*, 13087.
(38) Su, J.; Hu, T.-H.; Murase, R.; Wang, H.-Y.; D'Alessandro, D.; Kurmoo, M.; Zuo, J.-L. *Inorg. Chem.* **2019**, *58*, 3698.
(39) Park, S. S.; Hontz, E. R.; Sun, L.; Hendon, C. H.; Walsh, A.; Van Voorhis, T.; Dincă, M. *J. Am. Chem. Soc.* **2015**, *137*, 1774.
(40) Chen, D.; Xing, H.; Su, Z.; Wang, C. *Chem. Commun.* **2016**, *52*, 2019
(41) Ogihara, N.; Ohba, N.; Kishida, Y. *Sci. Adv.* **2017**, *3*, e1603103.
(42) Haider, G.; Usman, M.; Chen, T.-P.; Perumal, P.; Lu, K.-L.; Chen, Y.-F. *ACS Nano*, **2016**, *10*, 8366.
(43) Qu, L.; Iguchi, H.; Takaishi, S.; Habib, F.; Leong, C. F.; D'Alessandro, D. M.; Yoshida, T.; Abe, H.; Nishibori, E.; Yamashita, M. *J. Am. Chem. Soc.* **2019**, *141*, 6802.
(44) Kung, C.-W.; Otake, K.; Buru, C. T.; Goswami, S.; Cui, Y.; Hupp, J. T.; Spokoyny, A. M.; Farha, O. K. *J. Am. Chem. Soc.* **2018**, *140*, 3871.
(45) Goswami, S.; Ray, D.; Otake, K.; Kung, C.-W.; Garibay, S. J.; Islamoglu, T.; Atilgan, A.; Cui, Y.; Cramer, C. J.; Farha, O. K.; Hupp, J. T. *Chem. Sci.* **2018**, *9*, 4477.
(46) Talin, A. A.; Centrone, A.; Ford, A. C.; Foster, M. E.; Stavila, V.; Haney, P.; Kinney, R. A.; Szalai, V.; El Gabaly, F.; Yoon, H. P.; Léonard, F.; Allendorf, M. D. *Science* **2014**, *343*, 66.

(47) Schneider, C.; Ukaj, D.; Koerver, R.; Talin, A. A.; Kieslich, G.; Pujari, S. P.; Zuilhof, H.; Janek, J.; Allendorf, M. D.; Fischer, R. A. *Chem. Sci.* **2018**, *9*, 7405.
(48) Sheberla, D.; Sun, L.; Blood-Forsythe, M. A.; Er, S.; Wade, C. R.; Brozek, C. K.; Aspuru-Guzik, A.; Dincă, M. *J. Am. Chem. Soc.* **2014**, *136*, 8859.
(49) Dou, J. H.; Sun, L.; Ge, Y.; Li, W.; Hendon, C. H.; Li, J.; Gul, S.; Yano, J.; Stach, E. A.; Dincă, M. *J. Am. Chem. Soc.* **2017**, *139*, 13608.
(50) Dong, R.; Han, P.; Arora, H.; Ballabio, M; Melike, K.; Zhang, Z.; Shekhar, C.; Alder, P.; St. Petkov, P.; Erbe, A.; Mannsfeld, S. C. B.; Felser, C.; Heine, T.; Bonn, M.; Feng, X.; Cánovas, E. *Nat. Mater.* **2018**, *17*, 1037.
(51) Day, R. W.; Bediako, D. K.; Rezaee, M.; Parent, L. R.; Skorupskii, G.; Arguilla, M. A.; Hendon, C. H.; Stassen, I.; Gianneschi, N.; Kim, P.; Dincă, M. *ACS Cent. Sci.* **2019**, *5*, 1959.
(52) Jia, H.; Yao, Y.; Zhao, J.; Gao, Y.; Luo, Z.; Du, P. *J. Mater. Chem. A.* **2018**, *6*, 1188.
(53) Meng, Z.; Aykanat, A.; Mirica, K. A. *J. Am. Chem. Soc.* **2019**, *141*, 5, 2046.
(54) Yang, C.; Dong, R.; Wang, M.; St. Petkov, P.; Zhang, Z.; Wang, M.; Han, P.; Ballabio, M; Br äuninger, S. A.; Liao, Z.; Zhang, J.; Schwotzer, F.; Zschech, E.; Klauss, H.-H.; Cánovas, E; Kaskel, S.; Bonn, M.; Zhou, S.; Heine, T.; Feng, X. *Nat. Commun.* **2019**, *10*, 3260.
(55) Huang, X.; Sheng, P.; Tu, Z.; Zhang, F.; Wang, J.; Geng, H.; Zou, Y.; Di, C.; Yi, Y.; Sun, Y.; Wu, W.; Zhu, D. *Nat. Commun.* **2015**, *6*, 7408.
(56) Jin, Z.; Yan, J.; Huang, X.; Xu, W.; Yang, S.; Zhu, D.; Wang, J. *Nano Energy* **2017**, *40*, 376.
(57) Huang, X.; Zhang, S.; Liu, L.; Yu, L.; Chen, G.; Xu, W.; Zhu, D. *Angew. Chem. Int. Ed.* **2018**, *57*, 146.
(58) Demadis, K. D.; Hartshorn, C. M.; Meyer, T. J. *Chem. Rev.* **2001**, *101*, 2655.
(59) Brunschwig, B. S.; Creutz, C.; Sutin, N. *Chem. Soc. Rev.* **2002**, *31*, 158.
(60) D'Alessandro, D. M.; Keene, F. R. *Chem. Soc. Rev.* **2006**, *35*, 424.
(61) Robin, M. B.; Day, P. *Adv. Inorg. Chem. Radiochem.* **1967**, *10*, 247.
(62) Hush, N. S. *Prog. Inorg. Chem.* **1967**, *8*, 391.
(63) Cruetz, C.; Taube, H. *J. Am. Chem. Soc.* **1969**, *91*, 3988.
(64) Creutz, C.; Taube, H. *J. Am. Chem. Soc.* **1973**, *95*, 1086.
(65) Fürholz, U.; Joss, S.; Bürgi, H.-B.; Ludi, A. *Inorg. Chem.* **1985**, *24*, 943.
(66) Murase, R.; Leong, C. F.; D'Alessandro, D. M. *Inorg. Chem.* **2017**, *56*, 14373.
(67) Herm, Z. R.; Wiers, B. M.; Mason, J. A.; van Baten, J. M.; Hudson, M. R.; Zajdel, P.; Brown, C. M.; Masciocchi, N.; Krishna, R.; Long, J. R. *Science* **2013**, *340*, 960.
(68) Aubrey, M. L.; Wiers, B. M.; Andrews, S. C.; Sakurai, T.; Reyes-Lillo, S. E.; Hamed, S. M.; Yu, C.-J.; Darago, L. E.; Mason, J. A.; Baeg, J.-O.; Grandjean, F.; Long, G. J.; Seki, S.; Neaton, J. B.; Yang, P.; Long, J. R. *Nat. Mater.* **2018**, *17*, 625.
(69) Biggins, N.; Ziebel, M. E.; Gonzalez, M.; Long, J. R. *Chem. Sci.* **2020**, *11*, 8196.
(70) Kato, R.; Kobayashi, H.; Kobayashi, A. *J. Am. Chem. Soc.* **1989**, *111*, 5224.
(71) Heintz, R. A.; Zhao, H.; Ouyang, X.; Grandinetti, G.; Cowen, J.; Dunbar, K. R. *Inorg. Chem.* **1999**, *38*, 1444.
(72) Neufeld, A. K.; Madsen, I.; Bond, A. M.; Hogan, C. F. *Chem. Mater.* **2003**, *15*, 3573.
(73) Zhang, Z.; Zhao, H.; Kojima, H.; Mori, T.; Dunbar, K. R. *Chem. Eur. J.* **2013**, *19*, 3348.
(74) Kambe, T.; Sakamoto, R.; Hoshiko, K.; Takada, K.; Miyachi, M.; Ryu, J.-H.; Sasaki, S.; Kim, J.; Nakazato, K.; Takata, M.; Nishihara, H. *J. Am. Chem. Soc.* **2013**, *135*, 2462.

(75) Kambe, T.; Sakamoto, R.; Kusamoto, T.; Pal, T.; Fukui, N.; Hoshiko, K.; Shimojima, T.; Wang, Z.; Hirahara, T.; Ishizaka, K.; Hasegawa, S.; Liu, F.; Hishihara, H. *J. Am. Chem. Soc.* **2014**, *136*, 14357.
(76) Jeon, I.-R.; Negru, B.; Van Duyne, R. P.; Harris, T. D. *J. Am. Chem. Soc.* **2015**, *137*, 15699.
(77) Degayner, J. A.; Jeon, I.-R.; Sun, L.; Dincă, M.; Harris, T. D. *J. Am. Chem. Soc.* **2017**, *139*, 4175.
(78) Ziebel, M. E.; Darago, L. E.; Long, J. R. *J. Am. Chem. Soc.* **2018**, *140*, 3040.
(79) Darago, L. E.; Aubrey, M. L.; Yu, C. J.; Gonzalez, M. I.; Long, J. R. *J. Am. Chem. Soc.* **2015**, *137*, 15703.
(80) Abrahams, B. F.; Hudson, T. A.; McCormick, L. J.; Robson, R. *Cryst. Growth Des.* **2011**, *11*, 2717.
(81) Franchini, C.; Reticcioli, M.; Setvin, M.; Diebold, U. *Nat. Rev. Mater.* **2021**, doi: 10.1038/s41578-021-00289-w
(82) Alexandrov, A. S.; Devreese, J. T. *Advances in Polaron Physics*; Springer: New York, **2010**.
(83) Bredas, J. L.; Street, G. B. *Acc. Chem. Res.* **1985**, *18*, 309.
(84) Roth, S.; Carroll D. *One-Dimensional Metals: Conjugated Polymers, Organic Crystals, Carbon Nanotubes and Graphene*; Wiley-VHC: Singapore, **2015**.
(85) Launay, J.-P.; Verdaguer, M. *Electrons in Molecules: From Basic Principles to Molecular Electronics*; Oxford University Press: Oxford, **2013**.
(86) Roth, S.; Bleier, H.; Pukashi, W. *Faraday Discuss. Chem. Soc.* **1989**, *88*, 223.
(87) Ruth, S. *Hopping Transport in Solids*; Pollak, M. Ed.; Elsevier: Amsterdam, **1991**, 3, 517.
(88) Mott, N. F. *Philos. Mag.* **1969**, *19*, 835.
(89) Goodenough, J. B. *Magnetism and the Chemical Bond*; Wiley: New York, **1963**.
(90) Kanamori, J. *J. Phys. Chem. Solids* **1959**, *10*, 87.
(91) Coey, J. M. D. *Magnetism and Magnetic Materials*; Cambridge University Press: Cambridge, U.K., **2009**.
(92) McConnell, H. M. *J. Chem. Phys.* **1963**, *39*, 1910.
(93) Kollmar, C.; Kahn, O. *J. Chem. Phys.* **1993**, *98*, 453.
(94) Oshio, H.; Ichida, H. *J. Phys. Chem.* **1995**, *99*, 3294.
(95) Lloret, F.; De Munno, G.; Julve, M.; Cano, J.; Ruinz, R.; Caneschi, A. *Angew. Chem. Int. Ed.* **1998**, *37*, 135.
(96) Broderick, W. E.; Hoffman, B. M. *J. Am. Chem. Soc.* **1991**, *113*, 6334.
(97) Sharpe, A. G. *The Chemistry of Cyano Complexes of the Transition Metals*; Academic Press, **1976**.
(98) Simonov, A.; De Baerdemaeker, T.; Boström, H. L. B.; Gómez, M. L. R.; Gray, H. J.; Chernyshov, D.; Bosak, A.; Bürgi, H.-B.; Goodwin, A. L. *Nature* **2020**, *578*, 256.
(99) Jaffe, A.; Long, J. R. *Nature* **2020**, *578*, 222.
(100) Buser, H. J; Schwarzenbach, D.; Petter, W.; Ludi, A. *Inorg. Chem.* **1977**, *16*, 2704.
(101) Mayoh, B.; Day, P. *J. Chem. Soc., Dalton Trans.* **1976**, 1483.
(102) Herren, F.; Fischer, P.; Ludi, A. Hälg, W. *Inorg. Chem.* **1980**, *19*, 956.
(103) Ruiz, E.; Rodríguez-Fortea, A.; Alvarez, S.; Verdaguer, M. *Chem. Eur. J.* **2005**, *11*, 2135.
(104) Sugimoto, M.; Yamashita, S.; Akutsu, H.; Nakazawa, Y.; DaSilva, J. G.; Kareis, C. M.; Miller, J. S. *Inorg. Chem.* **2017**, *56*, 10452.
(105) Holmes, S. M.; Girolami, G. S. *J. Am. Chem. Soc.* **1999**, *121*, 5593.
(106) Garde, R.; Villain, F.; Verdaguer, M. *J. Am. Chem. Soc.* **2002**, *124*, 10531.

(107) Mallah, T.; Thiébaut, S.; Verdaguer, M.; Veillet, P. *Science* **1993**, *262*, 1554.
(108) Néel, L. *Ann. Phys.* **1948**, *3*, 137.
(109) Sieklucka, B.; Podgajny, R.; Pinkowicz, D.; Nowicka, B.; Korzeniak, T.; Balanda, M.; Wasiutyński, T.; Pelka, R.; Makarewicz, M.; Czapla, M.; Rams, M.; Gawel, B.; Lasocha, W. *CrystEngComm* **2009**, *11*, 2032.
(110) Podgajny, R.; Pinkowicz, D.; Korzeniak, T.; Nitek, W.; Rams, M.; Sieklucka, B. *Inorg. Chem.* **2007**, *46*, 10416.
(111) Beauvais, L. G.; Long, J. R. *J. Am. Chem. Soc.* **2002**, *124*, 2110.
(112) Wang, X.-Y.; Avendaño, C.; Dunbar, K. R. *Chem. Soc. Rev.* **2011**, *40*, 3213.
(113) Demir, S.; Jeon, I.-R.; Long, J. R.; Harris, T. D. *Coord. Chem. Rev.* **2015**, *289*, 149.
(114) Jeon, I.-R.; Park, J. G.; Xiao, D. J.; Harris, T. D. *J. Am. Chem. Soc.* **2013**, *135*, 16845.
(115) DeGayner, J.; Jeon, I.-R.; Harris, T. D. *Chem. Sci.* **2015**, *6*, 6639.
(116) Olson, C.; Heth, C. L. Lapidus, S. H.; Stephens, P. W.; Halder, G. J. Pokhodnya, K. *J. Chem. Phys.* **2011**, *135*, 024503.
(117) Pokhodnya, K. I.; Dokukin, V.; Miller, J. S. *Inorg. Chem.* **2008**, *47*, 2249.
(118) Lapidus, S. H.; McConnell, A. C.; Stephens, P. W.; Miller, J. S. *Chem. Commun.* **2011**, *47*, 7602.
(119) Zhang, J.; Ensling, J.; Ksenofontov, V.; Gütlich, P.; Epstein, A. J.; Miller, J. S. *Angew. Chem. Int. Ed.* **1998**, *37*, 657.
(120) Pokhodnya, K. I.; Petersen, N.; Miller, J. S. *Inorg. Chem.* **2002**, *41*, 1996.
(121) Her, J.-H.; Stephens, P. W.; Pokhodnya, K. I.; Bonner, M.; Miller, J. S. *Angew Chem. Int. Ed.* **2007**, *46*, 1521.
(122) McConnell, A. C.; Shurdha, E.; Bell, J.; Miller, J. S. *J. Phys. Chem. C* **2012**, *116*, 18952.
(123) Raebiger, J. W.; Miller, J. S. *Inorg. Chem.* **2002**, *41*, 3308.
(124) Gordon, D. C.; Deakin, L.; Arif, A. M.; Miller, J. S. *J. Am. Chem. Soc.* **2000**, *122*, 290.
(125) Pokhodnya, K. I.; Bonner, M.; Her, J.-H.; Stephens, P. W.; Miller, J. S. *J. Am. Chem. Soc.* **2006**, *128*, 15592.
(126) Stone, K. H.; Stephens, P. W.; McConnell, A. C.; Shurdha, E.; Pokhodnya, K. I.; Miller, J. S. *Adv. Mater.* **2010**, *22*, 2514.
(127) Motokawa, N.; Miyasaka, H.; Yamashita, M.; Dunbar, K. R. *Angew. Chem. Int. Ed.* **2008**, *47*, 7760.
(128) Clérac, R.; O'Kane, S.; Cowen, J.; Ouyang, X.; Heintz, R.; Zhao, H.; Bazile, M. J.; Dunbar, K. R. *Chem. Mater.* **2003**, *15*, 1840.
(130) Motokawa, N.; Matsunaga, S.; Takaishi, S.; Miyasaka, H.; Yamashita, M.; Dunbar, K. R. *J. Am. Chem. Soc.* **2010**, *132*, 11943.
(131) Miller, J. S. Polyhedron 2009, 28, 1596.
(132)Turnbull, M. M.; Sugimoto, T.; Thompson, L. K. Molecule-based Magnetic Materials:
(133) Theory, Techniques and Applications; ACS Publications: Washington D.C., **1996**.
(134) Pokhodnya, K. I.; Pejakovic, D.; Epstein, A. J.; Miller, J. S. *Phys. Rev. B* **2001**, *63*, 174408.
(135) Brinckerhoff, W. B.; Zhang, J.; Miller, J. S.; Epstein, A. J. *J. Mol. Cryst. Liq. Cryst.* **1995**, *272*, 195.
(136) Pokhodnya, K. I.; Epstein, A. J.; Miller, J. S. *Adv. Mater.* **2000**, *12*, 410.
(137) Yu, H.; Harberts, M.; Adur, R.; Lu, Y.; Hammel, P. C.; Johnston-Halperin, E.; Epstein, A. J. *Appl. Phys. Lett.* **2014**, *105*, 012407.

(138) Harberts, M.; Lu, Y.; Yu, H.; Epstein, A. J.; Johnston-Halperin, E. *J. Vis. Exp.* **2015**, *101*, e52891.
(139) de Jong, M. P.; Tengstedt, C.; Kanciurzewska, A.; Carlegrim, E.; Salaneck, W. R.; Fahlman, M. *Phys. Rev. B* **2007**, *75*, 064407.
(140) Du, G.; Joo, J.; Epstein, A. J.; Miller, J. S. *J. Appl. Phys.* **1993**, *73*, 6566.
(141) Raju, N. P.; Savrin, T.; Prigodin, V. N.; Pokhodnya, K. I.; Miller, J. S.; Epstein, A. J. *J. Appl. Phys.* **2003**, *93*, 6799.
(142) Yoo, J.-W.; Edelstein, R. S.; Lincoln, D. M.; Raju, N. P.; Xia, C.; Pokhodnya, K. I.; Miller, J. S.; Epstein, A. J. *Phys. Rev. Lett.* **2006**, *97*, 247205.
(143) Pedersen, K. S.; Perlepe, P.; Aubrey, M. L.; Woodruff, D. N.; Reyes-Lillo, S. E.; Reinholdt, A.; Voigt, L.; Li, Z.; Borup, K.; Rouzières, M.; Samohvalov, D.; Wilhelm, F.; Rogalev, A.; Neaton, J. B.; Long, J. R.; Clérac, R. *Nat. Chem.* **2018**, *10*, 1056.
(144) Murphy, R. A.; Long, J. R.; Harris, T. D. *Commun. Chem.* **2021**, *4*, 70.
(145) Kübler, J. *Theory of Itinerant Electron Magnetism*; Oxford University Press: New York, **2000**.
(146) Zener, C. *Phys. Rev.* **1951**, *82*, 403.
(147) Goodenough, J. B. *Phys. Rev.* **1955**, *100*, 564.
(148) de Gennes, P. G. *Phys. Rev.* **1960**, *118*, 141.
(149) von Helmolt, R.; Wecker, J.; Holzapfel, B.; Schultz, L.; Samwer, K. *Phys. Rev. Lett.* **1993**, *71*, 2331.
(150) Jin, S.; Tiefel, T. H.; McCormack, M.; Fastnacht, R. A.; Ramesh, R.; Chen, L. H. *Science* **1994**, *264*, 413.
(151) Haghiri-Gosnet, A. M.; Renard, J. P. *J. Phys. D: Appl. Phys.* **2003**, *36*, R127.
(152) Bibes, M.; Barthelemy, A. *IEEE Trans. Electron Devices* **2007**, *54*, 1003.
(153) Felser, C.; Fecher, G. H.; Balke, B. *Angew. Chem. Int. Ed.* **2007**, *46*, 668.
(154) Jonker, G. H.; Van Saten, J. H. *Physica* **1953**, *19*, 120.
(155) Rosencwaig, A. *Phys. Rev.* **1969**, *181*, 946.
(156) Buschow, K. H. J.; van Engen, P. G. *J. Magn. Magn. Mater.* **1981**, *25*, 90.
(157) Briceño, G.; Chang, H.; Sun, X.; Schultz, P. G.; Xiang, X.-D. *Science*, **1995**, *270*, 273.
(158) Korotin, M. A.; Anisimov, V. I.; Khomskii, D. I.; Sawatzky, G. A. *Phys. Rev. Lett.* **1998**, *80*, 4305.
(159) Şaşıoğlu, E.; Sandratskii, L. M.; Bruno, P. *Phys. Rev. B* **2008**, *77*, 064417.
(160) Bechlars, B.; D'Alessandro, D. M.; Jenkins, D. J.; Iavarone, A. T.; Glover, S. D.; Kubiak, C. P.; Long, J. R. *Nat. Chem.* **2010**, *2*, 362.
(161) Gaudette, A. I.; Jeon, I.-R.; Anderson, J. S.; Grandjean, F.; Long, G. J.; Harris, T. D. *J. Am. Chem. Soc.* **2015**, *137*, 12617.

Chapter 2: Charge Delocalization and Bulk Electronic Conductivity in the Mixed-Valence Metal–Organic Framework Fe(1,2,3-triazolate)$_2$(BF_4)$_x$

This chapter includes published contents

2.1 Introduction

Metal–organic frameworks are modular, three-dimensional network solids constructed from metal ions and rigid, polytopic organic linkers.[1] This modularity can endow metal–organic frameworks with impressive porosities, surface chemistry, and chemical stability,[2] and, consequently, these frameworks are being extensively investigated for applications ranging from gas separations and storage to drug delivery.[3] Within the past decade, engendering bulk electronic conductivity in metal–organic frameworks has also become of interest as a means of extending their potential application as battery electrode materials, electrochemical sensors, and electrocatalysts.[4]

However, many of the features that render metal–organic frameworks advantageous as porous storage and separation materials also present a challenge to their application in electronic devices that require high conductivity. Indeed, the characteristically low crystal densities of metal–organic frameworks imply large distances between atoms along most lattice vectors. Such materials inherently favor electronic structures with particularly weak band dispersion because valence orbital overlap (an *ad hoc* indicator of bulk dispersion) diminishes exponentially with interatomic distance.[5] Thus, charge carriers in metal–organic frameworks can generally be expected to have extremely large effective masses yielding local electronic structures of a near-molecular nature.[6] Indeed, to date there have been only a few literature examples of metal–organic frameworks that exhibit both permanent porosity and a high electronic conductivity.[7]

Among many notable efforts to increase charge transport in these materials, one attractive strategy is the development of frameworks consisting of either repeating mixed-valence, redox-active metal centers or redox-active linkers.[8,9] The use of mixed-valency can at a minimum locally improve charge mobility on neighboring atoms; in most mixed-valence frameworks, the electronic substructures are indeed localized and may reasonably be described as small polarons, akin to an isolated Marcus-type coupling interaction.[10] Nonetheless, with a contiguous path along at least one dimension of the framework lattice, the resulting hopping-type charge mobility can still engender a relatively high conductivity.[10a,11] For instance, a ferric semiquinoid-quinoid framework was recently shown to exhibit a three-dimensional conductivity of 0.16 S/cm, arising from a combination of ligand-based mixed-valence supported by 3*d*-π orbital interactions through bridging iron(III) centers.[9g] Likewise, a number of other frameworks have been found to be conductive owing to charge delocalization across mixed-valence ligand centers.[9]

Metal-centered mixed-valence has been extensively investigated in many solid state systems, such as iron oxides, iron sulfides, iron cyanides, Prussian Blue compounds, manganese perovskites, and titanates, to name a few.[12] In addition, mixed-valence first-row transition metal coordination solids have been shown to exhibit electronic delocalization.[13] Engendering high electronic conductivity in three-dimensional metal–organic frameworks by taking advantage of metal-centered valence delocalization may thus hold promise. However, early examples of such frameworks have typically displayed conductivity values much lower than frameworks with ligand-centered charge carriers, and thus there is likely much room for improvement.[7g,8]

In pursuit of promising systems with the potential for exhibiting metal-centered mixed-valence, we identified the framework $Fe(tri)_2$ (tri^- = 1,2,3-triazolate), a previously reported material with an intriguing electronic structure arising from octahedrally-coordinated Fe^{II} centers bridged by π-acidic azolate ligands (Figure 2.1).[8c] Previously, $Fe(tri)_2$ was reported to exhibit an intrinsic conductivity of 7.7×10^{-5} S/cm, which further increased to 1.0×10^{-3} S/cm following vapor diffusion of I_2 through the material. This reported conductivity for the as-synthesized $Fe(tri)_2$

is surprisingly high, given the closed-shell nature of low-spin iron(II) and the triazolate linker, as noted elsewhere.[7g,14] As such, Fe(tri)$_2$ was determined to be an excellent candidate for exploring the relationship between metal-centered mixed-valence and conductivity in a porous solid.

Herein, we present the rigorous air-free synthesis of Fe(tri)$_2$, together with its mixed-valence derivatives, Fe(tri)$_2$(BF$_4$)$_x$ (x = 0.09, 0.22, and 0.33), obtained through post-synthetic stoichiometric oxidation reactions. Physical characterization then enables insight into the charge transport behavior underlying the impressive enhancement in the conductivity of these materials with increasing oxidation level.

2.2 Experimental Information

General Considerations. Unless otherwise noted, all manipulations were carried out in an argon atmosphere in an Mbraun MB200MOD glovebox. Glassware was oven-dried at 150 °C for at least 4 h and allowed to cool in an evacuated glove box antechamber prior to use. Dimethylformamide (DMF), acetonitrile (MeCN), and dichloromethane were dried using a commercial solvent purification system made by JC Meyer Solvent Systems and stored over 3- or 4-Å molecular sieves prior to use. Anhydrous FeCl$_2$ beads (99.9% purity) were purchased from Sigma-Aldrich. The 1,2,3-triazole ligand (98% purity) was purchased from VWR International LLC, deoxygenated with three freeze-pump-thaw cycles, and stored over 4-Å molecular sieves prior to use. The synthesis of Fe(tri)$_2$ was carried out using a modification of the previously reported procedure.[8c] Instead of performing the reaction in an evacuated sealed tube, it was carried out in an Ar-filled glovebox using 20-mL vials. Thianthrenium tetrafluoroborate was synthesized as previously described.[15] Carbon, hydrogen, and nitrogen elemental analyses were obtained from the Microanalytical Laboratory at the University of California, Berkeley. Inductively-coupled plasma atomic emission spectrometry (ICP-AES) analysis for iron and boron were obtained from Galbraith Laboratories, Inc.

Synthesis of Fe(1,2,3-triazolate)$_2$(BF$_4$)$_{0.33}$. A purple solution of thianthrenium tetrafluoroborate (0.158 g, 0.520 mmol) in 10 mL of MeCN was added to neat pink crystalline powder Fe(tri)$_2$ (0.200 g, 1.04 mmol) and the mixture was stirred at 25 °C for 16 h. The resulting suspension was filtered to yield a light brown powder. The powder was washed by soaking in two successive 15-mL aliquots of MeCN for 24 h, and was then dried under reduced pressure (13 μbar) at 120 °C for 48 h to yield 0.222 g (97% yield) of product as a brown microcrystalline solid. Anal. Calcd for FeC$_4$H$_4$N$_6$B$_{0.33}$F$_{1.32}$: C, 21.78; H, 1.83; N, 38.09. Found: C, 21.78; H, 1.78; N, 37.6. ICP-AES Found: Fe:B, 1:0.33.

Synthesis of Fe(1,2,3-triazolate)$_2$(BF$_4$)$_x$ (x = 0.025, 0.05, 0.09, 0.22). Similar procedures were followed as above. See Supporting Information for details.

2.3 Results and Discussion

Synthesis and Characterization of Fe(tri)$_2$. The synthesis of Fe(tri)$_2$ was carried out in 20-mL vials in a glovebox under an Ar atmosphere, in a modification of the previously reported procedure.[8c] Special caution was taken during the synthesis and handling of Fe(tri)$_2$, as even slight air-exposure or the use of a partially oxidized FeCl$_2$ source led to the isolation of an orange or light brown colored powder, instead of the pale pink powder characteristic of the valence-pure phase. Successful synthesis of phase-pure Fe(tri)$_2$ was confirmed by powder X-ray diffraction

analysis,[8c,16] and Le Bail refinement of the diffraction data enabled identification of the space group as $Fd\bar{3}m$ and resulted in a lattice parameter of a = 16.6423(6) Å.

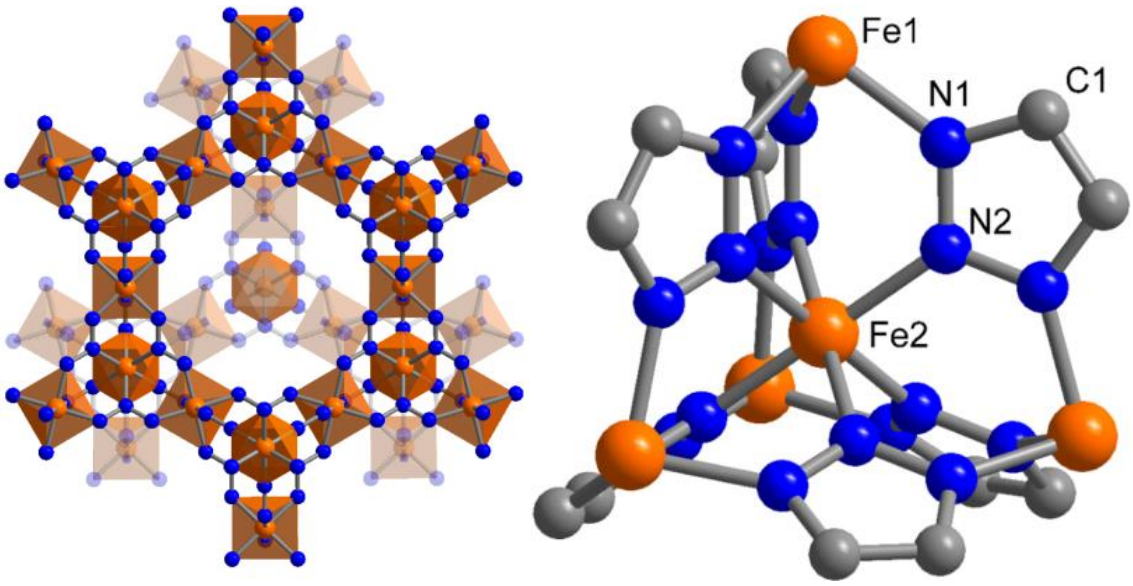

Figure 2.1. The Fe–N sublattice (left) and a tetrahedral secondary building unit of $Fe(tri)_2$ (right). Orange, blue, and grey spheres represent Fe, N, and C atoms, respectively; H atoms have been omitted for clarity.

The structure of activated $Fe(tri)_2$ was obtained by Rietveld refinement of the synchrotron powder X-ray diffraction pattern (see Figure S2.6) and is composed of octahedral Fe^{II} centers bridged by μ_3-1,2,3-triazolate ligands (Figure 2.1). Here, two crystallographically-distinct Fe^{II} centers form tetrahedral pentanuclear repeat units that share vertices to form a diamondoid structure type. A single, adamantane-like cage of the structure is depicted in Figure 2.1. The Fe1–N1 and Fe2–N2 distances, where Fe1 and Fe2 correspond to the tetrahedral corner and center iron(II) sites, respectively, are 1.961(2) and 1.977(3) Å, consistent with Fe–N distances for compounds with low-spin Fe^{II} ions and strong-field ligands.[17] Metal–organic frameworks exhibiting low-spin Fe^{II} centers are quite rare in the literature, although there have been several reports suggesting that triazolate-based ligands can stabilize low-spin octahedral Fe^{II} centers in zero-,[18] one-,[19] and three-dimensional[20] coordination compounds.

Slow-Scan Cyclic Voltammetry of $Fe(tri)_2$. Slow-scan cyclic voltammetry experiments were carried out to investigate the redox behavior of $Fe(tri)_2$. This technique has been commonly used to characterize redox-active intercalation solids.[21] By observing the current response arising from scanning potentials with sufficiently slow rates, it is possible to probe the process of bulk ion insertion into a solid. In addition, a precise stoichiometry of the entire active material can be determined by current integration.

By using the equipment described in the Supporting Information, a slow-scan cyclic voltammogram (CV) of $Fe(tri)_2$ was obtained (Figure 2.2). Oxidation and reduction processes occur between 2.9-3.3 and 2.6-3.2 V vs $Li^{0/+}$ with corresponding charge capacities of 30.8 and 28.2 mAh/g, respectively. The oxidative feature most likely corresponds to oxidation of the Fe^{II} centers to Fe^{III} and the voltage composition profile obtained for $Fe(tri)_2$ between 2.6 and 3.4 V suggests that $Fe(tri)_2(BF_4)_x$ can be oxidized quasi-reversibly from x = 0 to x = 0.22 with an efficiency of

92% (Figure S2.2). The predicted stoichiometry is lower than expected for complete oxidation of the Fe^{II} centers that would correspond to $x = 1$, potentially owing to the small pore size of $Fe(tri)_2$, which may limit BF_4^- ion insertion.

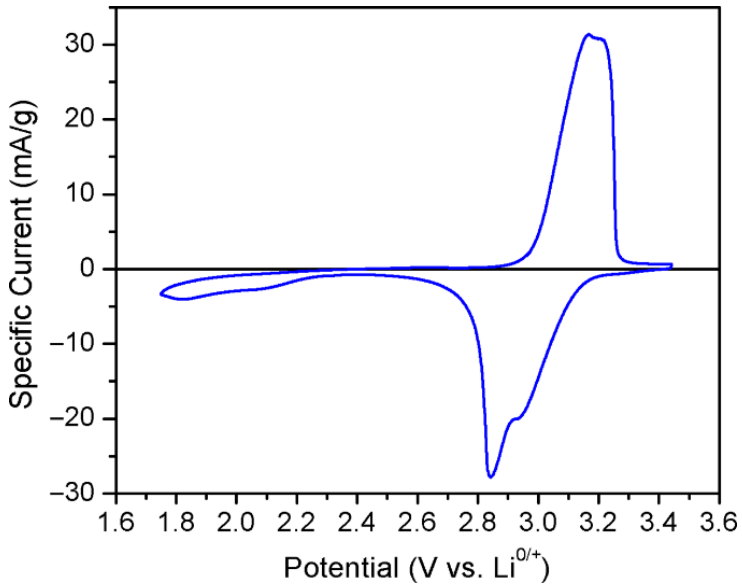

Figure 2.2. Slow-scan cyclic voltammogram of $Fe(tri)_2$ collected at a scan rate of 50 μV/s in an electrolyte solution of 1 M $LiBF_4$ in propylene carbonate. Lithium was used as a reference and counter electrode.

Scheme 2.1. Post-synthetic chemical oxidation of $Fe(tri)_2$ with thianthrenium tetrafluoroborate.

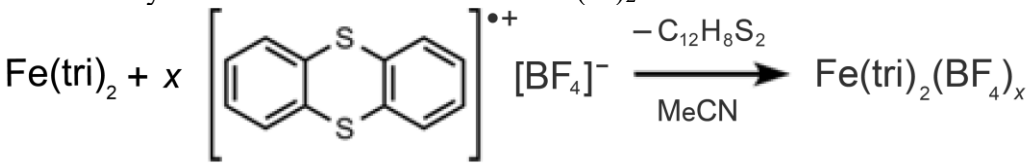

Chemical Oxidation of $Fe(tri)_2$. Motivated by the quasi-reversible $Fe^{II/III}$ redox features observed in the slow scan CV of $Fe(tri)_2$, we performed stoichiometric chemical oxidations of the framework using thianthrenium tetrafluoroborate in MeCN (Scheme 2.1). Reaction of $Fe(tri)_2$ with 0.1, 0.25, and 0.5 equivalents of the oxidant resulted in isolation of light brown, brown, and dark brown microcrystalline powders, respectively. For the products isolated using 0.1 and 0.25 equivalents of oxidant, ICP-AES analysis revealed Fe:B ratios of 1:0.09 and 1:0.22, respectively, indicating near-stoichiometric conversions. However, when 0.5 equivalents of oxidant were added, the solution was observed to retain the purple color of unreacted thianthrenium tetrafluoroborate even after the reaction had proceeded for 16 h, suggesting that oxidation of $Fe(tri)_2$ did not go to completion. Indeed, analysis of the product isolated from this reaction via ICP-AES revealed a Fe:B ratio of only 1:0.33, consistent with a sub-stoichiometric oxidation. We note that $x = 0.33$ is the stoichiometry expected if each adamantyl-like pore within the framework structure is filled with a single BF_4^- ion.

Brunauer Emmet-Teller (BET) surface areas of 230, 70, and 50 m^2/g were calculated for the activated $Fe(tri)_2(BF_4)_x$ materials with $x = 0.09$, 0.22, 0.33, respectively, using N_2 adsorption

data collected at 77 K (Figure S2.3). Here, the diminishing surface areas are consistent with the increasing presence of charge-balancing BF_4^- anions in the pores relative to the parent $Fe(tri)_2$ framework, which exhibits a BET surface area of 370 m^2/g. The very low surface area determined from a type II isotherm of $Fe(tri)_2(BF_4)_{0.33}$ suggests that the compound is essentially non-porous, consistent with the lack of any calculated accessible surface area (see Table S2.1), and therefore that N_2 adsorption occurs solely on the outer surfaces of the crystallites. Both ICP-AES and N_2 adsorption isotherm data indicate that the pore size of $Fe(tri)_2$ precludes counteranion insertion beyond 0.33 equivalents and therefore further oxidation.

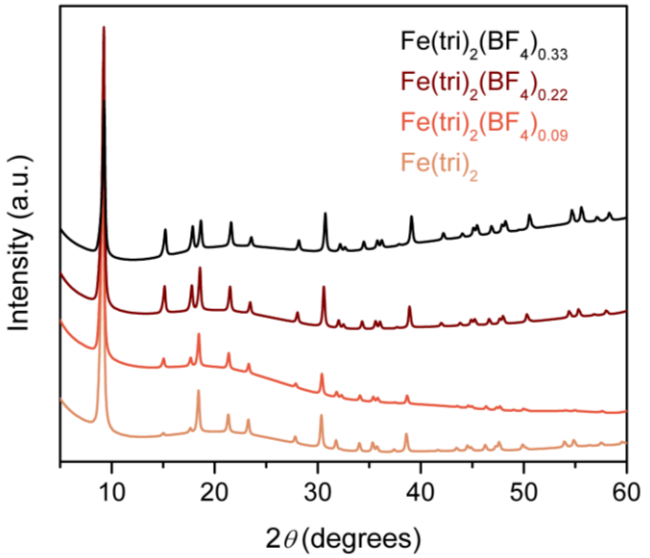

Figure 2.3. Powder X-ray diffraction patterns for $Fe(tri)_2$ and $Fe(tri)_2(BF_4)_x$ obtained with a wavelength of 1.5418 Å.

Characterization of the activated $Fe(tri)_2(BF_4)_x$ (x = 0.09, 0.22, 0.33) materials using powder X-ray diffraction revealed that the parent framework structure is maintained upon oxidation, with no evidence of decomposition (Figure 2.3). Le Bail refinement of the diffraction patterns yielded lattice parameters of a = 16.6136(7), 16.5140(5), and 16.4368(5) Å for x = 0.09, 0.22, and 0.33, respectively, indicating a contraction of the unit cell upon chemical oxidation (Table S2.2). A plot of lattice constants vs x follows a nearly linear trend that is qualitatively consistent with Vegard's law (Figure S2.5), implying that each $Fe(tri)_2(BF_4)_x$ material behaves as a single phase with a homogenous distribution of BF_4^- ions.

The crystal structures of activated $Fe(tri)_2(BF_4)_{0.33}$ at 300 and 100 K determined by Rietveld refinement using synchrotron powder X-ray diffraction patterns (see Figures S2.7 and S2.8) are shown in Figures S2.9 and S2.10, respectively, and reflect a slight contraction of the unit cell with decreasing temperature (See Table S2.3 for the fit parameters). However, the significant structural distortion that would be anticipated to accompany charge localization is not apparent. Comparing the structures of $Fe(tri)_2$ and $Fe(tri)_2(BF_4)_{0.33}$ obtained at 300 K, a small decrease occurs in the Fe1–N1 distance from 1.961(2) to 1.938(3) Å, as expected for a partial oxidation of low-spin iron(II) to low-spin iron(III).[17] In contrast, the Fe2–N2 distance changes only negligibly (i.e., within error) from 1.977(3) to 1.971(3) Å, suggesting that oxidation occurs primarily at the corner Fe1 sites. Given that the two unique iron sites experience similar ligand fields based upon the

Mössbauer spectrum of $Fe(tri)_2$ (vida infra), the apparent preferential oxidation at the Fe1 site may result from the geometrical constraints imposed at the iron ions, with low-spin iron(III) favoring the corner Fe1 site due to a greater freedom there to distort away from an ideal octahedral coordination geometry. A slight contraction of the unit cell and the corresponding supertetrahedra occurs upon framework oxidation, as is evidenced by a decrease in the Fe1···Fe1 separation from 5.8869(4) to 5.8263(8) Å. Difference Fourier maps generated from the $Fe(tri)_2(BF_4)_{0.33}$ diffraction data also indicated the presence of charge-balancing BF_4^- ions, with a single ion present in the pores of the framework. These BF_4^- ions refine to full occupancy, again suggesting that oxidative insertion of further BF_4^- ions is not possible in $Fe(tri)_2$.

Mössbauer Spectroscopy. The ^{57}Fe Mössbauer spectra of $Fe(tri)_2$ and $Fe(tri)_2(BF_4)_x$ obtained at 290 K are shown in Figure 2.4 (see Table S2.4 for the corresponding fitting parameters). At 290 K, $Fe(tri)_2$ exhibits a single component spectrum that was best fit with a narrow symmetric quadrupole doublet with a linewidth, Γ, of 0.267(5) mm/s, an isomer shift, δ, of 0.385(1) mm/s, and a small quadrupole splitting, ΔE_Q, of 0.084(7) mm/s. Each of these parameters are consistent with the presence of low-spin iron(II)[12c] in a highly symmetric pseudo-octahedral nitrogen coordination environment. Although the measured linewidth is similar to the calibration linewidth of the spectrometer, the two inequivalent crystallographic iron(II) sites in $Fe(tri)_2$ are not resolved in the spectrum. This absence suggests that the two iron(II) sites in $Fe(tri)_2$ experience very similar ligand fields.

The 290 K Mössbauer spectra of $Fe(tri)_2(BF_4)_x$ also exhibit very similar narrow quadrupole doublet components that are assigned to the Fe2 low-spin iron(II) site (Figure 2.4, red lines; the corresponding hyperfine parameters are given in Table S2.4). However, an additional absorption at approximately −0.1 mm/s clearly begins to grow in as x increases. This absorption was fit as part of a symmetric doublet (Figure 2.4, blue lines) and the corresponding hyperfine parameters are given in Table S2.4. For all values of x, the isomer shift of this component is smaller than that of the red component, which suggests that the blue component can be assigned to the Fe1 intermediate valence iron(II/III) ion. The percent areas of the blue quadrupole doublets were found to be 16.2(5), 50.8(6), and 66.67 % for x = 0.09, 0.22, and 0.33, respectively, in reasonable agreement with twice the expected iron(III) stoichiometry (based upon the empirical formula for each material). Hence, at 290 K the blue doublets are assigned to valence averaged low-spin iron(II/III) sites, between which the delocalized electron is averaged on the Mössbauer timescale of $\sim 10^{-8}$ s[22] (corresponding to the period of the precession of the iron-57 nuclear quadrupole moment within its electron electric field gradient). For x = 0.22 and 0.33, Mössbauer spectra collected at various temperatures down to 5 K (vida infra), reveal that this feature persists down to 150 and 100 K, respectively.

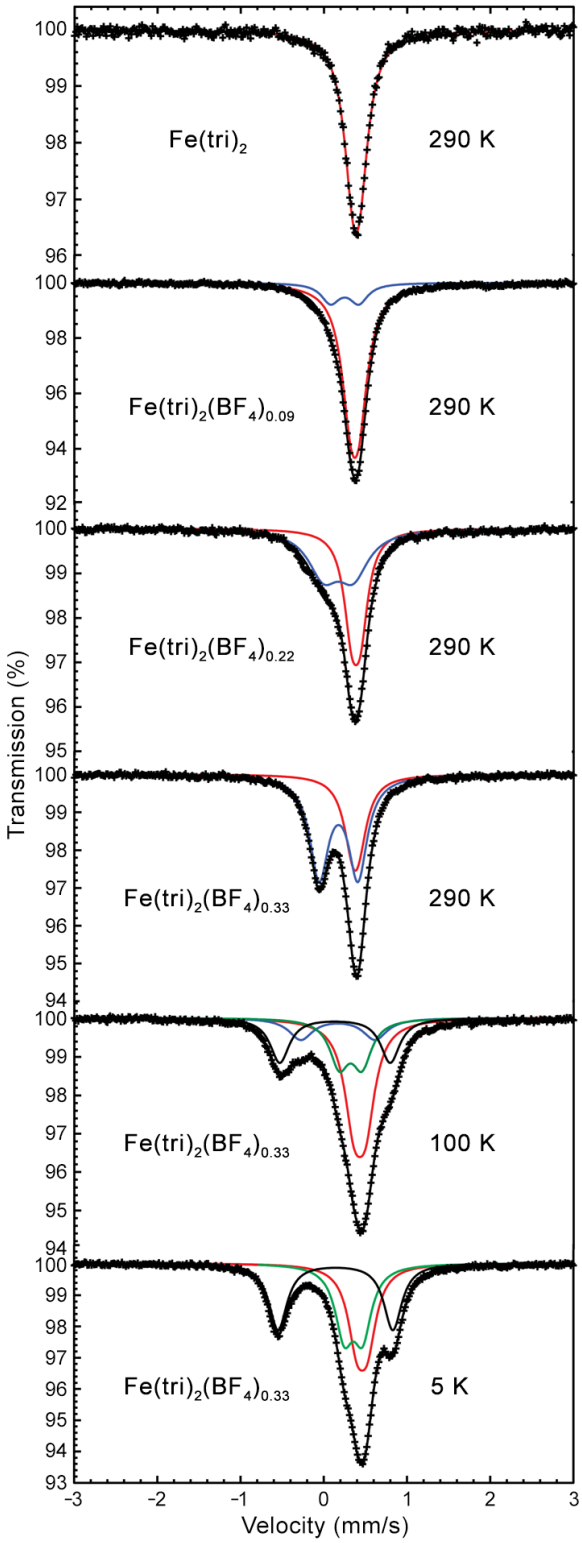

Figure 2.4. Mössbauer spectra of $Fe(tri)_2$ and $Fe(tri)_2(BF_4)_x$ obtained at the indicated temperatures. The component doublets correspond to low-spin iron(II) (red trace), valence-delocalized low-spin iron(II/III) (blue trace), localized low-spin iron(II) (green trace), and localized low-spin iron(III) (black trace).

A consideration of the structural data obtained from powder X-ray diffraction studies suggests this valence averaging most likely occurs over the four Fe1 tetranuclear vertices that surround the central Fe2 crystallographic site at a distance of 5.8263(8) Å (see the right portion of Figure 2.1). Additionally, from an examination of the triazolate ligand resonance structures, it is clear that electronic coupling between the two N1 sites via π-3d orbital conjugation would be preferable over coupling between N1 and N2, despite the closer corresponding Fe1···Fe2 distance. At room temperature, these valence-averaged Fe1 sites are indistinguishable by crystallography and Mössbauer spectroscopy. Furthermore, since the Fe1 centers occupy shared vertices in the extended structure, they are likely responsible for promoting charge mobility between adjacent supertetrahedra and ultimately throughout the entire crystal. While such delocalization behavior has been observed previously in minerals and molecular compounds containing mixed-valence $Fe^{II/III}$ centers, this is a rare example of such an observation in a metal–organic framework.[12,13]

To further support the above assignments and investigate the electron delocalization, Mössbauer spectra were also obtained for $Fe(tri)_2(BF_4)_{0.22}$ and $Fe(tri)_2(BF_4)_{0.33}$ at various temperatures between 5 and 295 K (see Figure S2.11 and Figure 2.4, respectively, and Table S2.4 for the corresponding fit parameters). At 5 K, no electron delocalization is expected and the Mössbauer spectra of both $Fe(tri)_2(BF_4)_{0.22}$ and $Fe(tri)_2(BF_4)_{0.33}$ were accordingly fit with three doublets: one assigned to the static, low-spin iron(II) site, Fe2 (red trace), and two assigned to the portion of the Fe1 sites that are low-spin iron(II) and low-spin iron(III) at some point on the Mössbauer time scale (green and black traces, respectively). These assignments assume that Fe2 has a static valence and does not participate in the electron delocalization. At 5 K, the sum of the percent areas of the green and black doublets is equal to the percent area of the blue doublet at 290 K, which strongly supports electron localization at 5 K. In contrast, the observation of the blue doublet at 290 K strongly supports electron delocalization at 290 K for $x = 0.22$ and 0.33.

The Mössbauer spectra of $Fe(tri)_2(BF_4)_{0.22}$ at 150 and 200 K and of $Fe(tri)_2(BF_4)_{0.33}$ at 100 K are more complex, as is revealed in the absorption profile around −0.5 mm/s (Figure S2.11 and Figure 2.4, respectively). At these temperatures, the spectra were fit with four quadrupole doublets: the narrow red doublet assigned to the Fe2 low-spin iron(II) site, green and black doublets assigned to valence localized Fe1 low-spin iron(II) and iron(III) sites, and the blue doublet assigned to valence averaged Fe1 low-spin iron(II/III). For $x = 0.22$, the percent area of the valence average blue doublet increases from 15% at 150 K to 51% at 295 K, indicating increased valence delocalization with increasing temperature. Indeed, the variable-temperature conductivity behavior of $Fe(tri)_2(BF_4)_x$ material (vida infra) may be closely correlated to this temperature dependent valence-localization observed in the Mössbauer spectra of $x = 0.22$ and 0.33. Additional discussion of the Mössbauer spectra, including the temperature and the x dependence of the spectral parameters, can be found in the Supporting Information.

Magnetic Properties of $Fe(tri)_2(BF_4)_{0.33}$. Variable-temperature dc magnetic susceptibility data were collected in order to investigate the possibility of magnetic ordering in $Fe(tri)_2(BF_4)_{0.33}$. Under an applied magnetic field of 1 T, the 300 K value of the molar magnetic susceptibility (χ_M) times T is 0.406 emu·K/mol, significantly higher than the value of 0.124 emu·K/mol expected for 0.33 equivalents of low-spin ($S = 1/2$) iron(III) per mole of framework (Figure S2.12). We attribute this difference to substantial contributions from higher-spin excited states, and the field-dependence of the $\chi_M T$ product is consistent with such contributions (Figure S2.12). With decreasing temperature, $\chi_M T$ decreases gradually from 300 to 20 K and abruptly below 20 K to reach a value of 0.105 emu·K/mol at 3 K. Such behavior is suggestive of antiferromagnetic interactions between low-spin Fe^{III} centers and, indeed, a Curie-Weiss fit to a plot of $1/\chi_M$ versus

T in the high-temperature regime (Figure S2.13) yielded a Curie constant of $C = 0.514$ emu·K/mol and a Weiss temperature of $\theta = -80.9$ K, consistent with a dominant antiferromagnetic interaction. However, no long-range magnetic ordering was observed down to 3 K (see Figure S2.14).

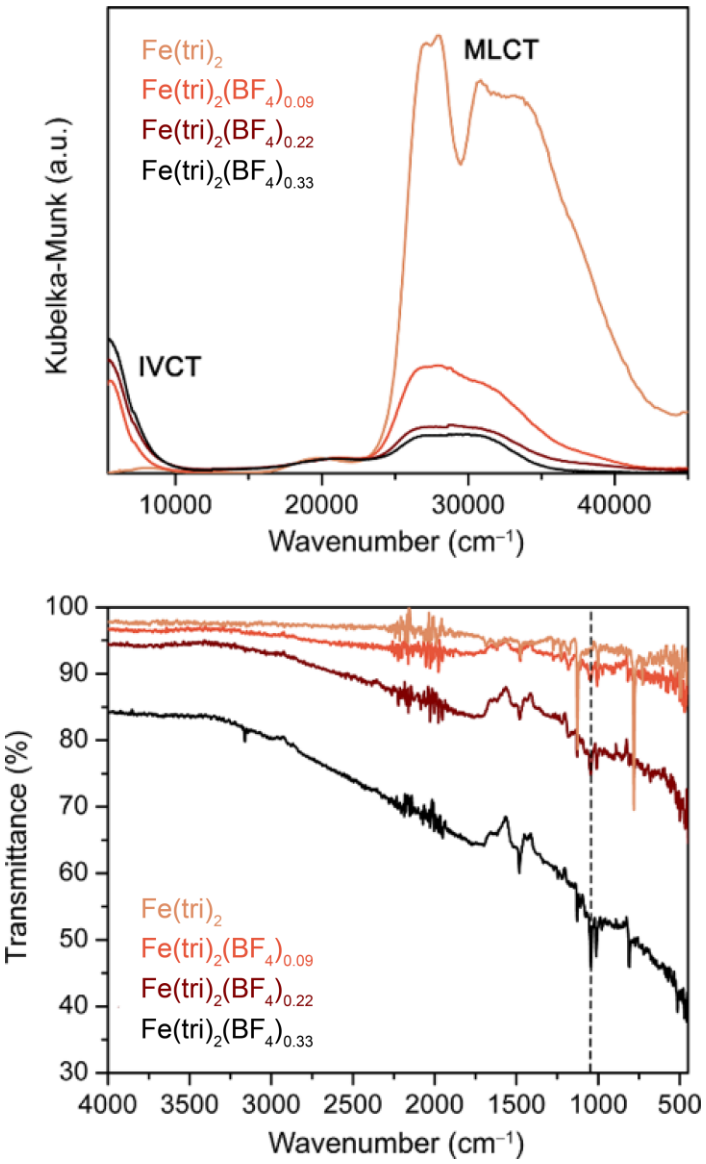

Figure 2.5. Diffuse reflectance UV-vis-NIR (top) and infrared spectra (bottom) of $Fe(tri)_2$ and $Fe(tri)_2(BF_4)_x$. The diffuse reflectance spectra were normalized to the intensity of the weak d–d transition band. The infrared peak corresponding to a stretching mode of BF_4^- is shown with a dashed line.

UV-Vis-NIR Diffuse Reflectance Spectroscopy. UV-Vis-NIR diffuse reflectance spectra of $Fe(tri)_2(BF_4)_x$ ($x = 0.0, 0.09, 0.22, 0.33$) are shown at the top of Figure 2.5. A weak absorption band in the spectrum for $Fe(tri)_2$ at $\nu_{max} = 19{,}900$ cm^{-1} is assigned to a low-spin Fe^{II} d–d transition, and with increasing oxidation and the introduction of Fe^{III} centers into the framework this band shifts to higher energies. Note that the $Fe(tri)_2(BF_4)_x$ spectra in Figure 2.5 were normalized to the

d–d transition intensity of $Fe(tri)_2$ for ease of comparison, as this spectral feature remains similar across the four compounds, in contrast to the intensity changes in the other bands.

Although $Fe(tri)_2$ exhibits no significant absorption in the near-IR region, substantial broad absorption bands are apparent between 5,000 and 10,000 cm^{-1} and increase in relative intensity with oxidation in $Fe(tri)_2(BF_4)_x$. These features can be attributed to an intervalence charge transfer (IVCT) transition between iron(II/III) centers, but due to the detection limit of the UV-vis-NIR instrument, the diagnostic low-energy edge of the IVCT absorption could not be observed.[23] We speculate that the IVCT bands of $Fe(tri)_2(BF_4)_x$ extend out to the mid-IR region, as suggested in Figure 2.5.

The UV-vis-NIR spectrum of $Fe(tri)_2$ also exhibits broad, intense absorption bands at higher ν_{max} values of 27,200 and 31,000 cm^{-1}, which we assign to metal-to-ligand charge transfer (MLCT) transitions.[18a] With increasing oxidation, the MLCT bands substantially decrease in intensity relative to the d-d transitions. Whereas the increasing relative intensity of IVCT transition is consistent with an increasing charge carrier density with oxidation, a decreasing relative intensity of MLCT transition results from a decreasing concentration of Fe^{II} centers that participate in the π back-bonding.

Infrared Spectroscopy. The IR spectra of $Fe(tri)_2$ and $Fe(tri)_2(BF_4)_x$ collected under a N_2 atmosphere also exhibit remarkably different features (Figure 2.5, bottom). The IR spectrum of $Fe(tri)_2$ displays a flat baseline with sharp features corresponding to discrete vibrational modes arising primarily from the triazolate ligand. In contrast, the IR spectrum of $Fe(tri)_2(BF_4)_{0.09}$ features a broad absorption band in the mid-IR region that becomes stronger with increasing oxidation to x = 0.22 and 0.33. This absorption most likely originates from low-lying electronic excitations extending into the mid-IR region of the spectrum. A strong absorption of this type that increases with decreasing photon energy may suggest an optical band gap approaching zero. However, because band dispersion in the $Fe(tri)_2$ system is expected to be low, the origin of the feature is perhaps better described as a nearly continuous distribution of localized mid-gap states.[13a,14,24] Indeed, similar features have been observed in the IR spectra of polaronic materials, such as charge transfer salts[25] and mixed-valence, pyrazine-bridged $Ru^{II/III}$ and $Os^{II/III}$ porphyrinate coordination solids.[13a] While these broad band absorptions may mask the original vibrational modes present for $Fe(tri)_2$, a discernible new feature is observed at 1,044 cm^{-1}, corresponding to a stretching mode of BF_4^-.[26] As expected, the relative intensity of this peak increases with increasing degree of oxidation and increasing BF_4^- content of a material.

Electronic Conductivity of $Fe(tri)_2$. By using ac impedance spectroscopy, two-contact electronic conductivity was measured on a pressed pellet of $Fe(tri)_2$ in a screw cell with polished copper electrode contacts (Figure S2.15). The resulting Nyquist impedance plot was fit with a model circuit (Figure S2.16) to estimate the dc conductivity. In contrast to the previously reported electronic conductivity of 7.7×10^{-5} S/cm for $Fe(tri)_2$, we obtained a much lower value of less than 7×10^{-9} S/cm. Estimation of the dc conductivity by an *I-V* sweep (±32.7 V/cm) resulted in an ohmic response and a similarly low value of 1×10^{-10} S/cm (Figure S2.17). This low conductivity is more consistent with that expected for a valence-pure material containing octahedral iron(II) ions with a low-spin $t_{2g}^6e_g^0$ electron configuration, ions that are separated by large distances (Fe1⋯Fe1 = 5.8869(4) Å). We suspect that the reported conductivity of 7.7×10^{-5} S/cm was measured not on pure $Fe(tri)_2$ but rather on a partially oxidized sample, as the previous study reported $Fe(tri)_2$ to be air stable and therefore did not follow the rigorous air-free procedures employed herein. A recent report suggesting trace Fe^{III} impurities in $Fe(tri)_2$ also supports this conclusion.[14] Additionally, the measured conductivities for samples of $Fe(tri)_2$ oxidized with small

quantities (0.025 and 0.05 equiv) of thianthrenium tetrafluoroborate display a significant increase in conductivity (see Table S2.5, Figure 2.6 inset, and Figure S2.18). Indeed, even oxidizing just 2.5% of the iron(II) centers to iron(III) is sufficient to explain the previously reported conductivity values.

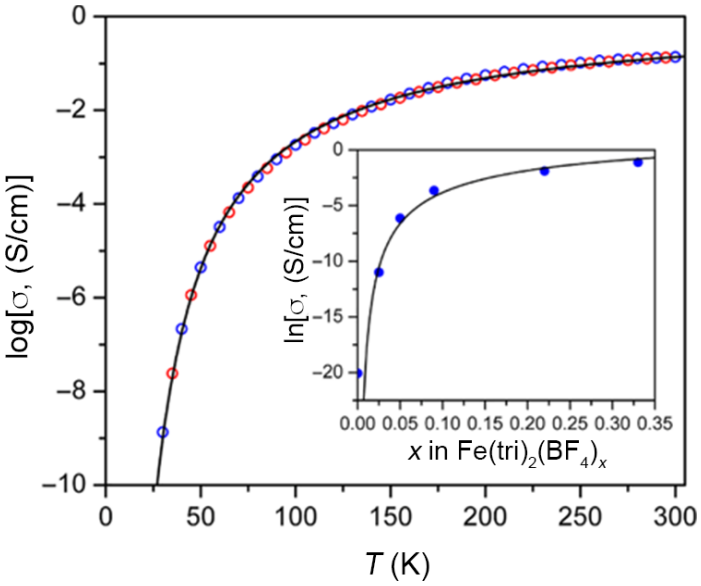

Figure 2.6. Variable-temperature conductivity data for $Fe(tri)_2(BF_4)_{0.33}$. Blue and red circles represent measurements taken during cooling and warming, respectively. An Arrhenius fit to the data, as described in the Supporting Information, is shown by the black curve. (Inset) Plot of room-temperature conductivities versus x in $Fe(tri)_2(BF_4)_x$ (blue circles) and a fit for the doping dependence of conductivity for polaronic Mott insulators (black line). The fit parameters are discussed in the Supporting Information.

Two-contact, dc electronic conductivities were also measured on pressed pellets of $Fe(tri)_2(BF_4)_x$. Room temperature conductivities of 0.03(2), 0.2(1), and 0.3(1) S/cm were measured for x = 0.09, 0.22, and 0.33, respectively, and were found to be ohmic within ±8.9 V/cm of an open circuit (Table S2.5, Figure S2.18). This increase in conductivity with oxidation level is also consistent with our Mössbauer and UV-vis-NIR spectroscopy data. In particular, the increasing intensities of the valence-averaged feature in the 290 K Mössbauer spectra and the IVCT bands suggest an increasing carrier concentration with oxidation that engenders a bulk electronic conductivity, possibly accompanied by an increase in carrier mobility.

As shown in the inset of Figure 2.6 and described in the Supporting Information, the room-temperature conductivity values of $Fe(tri)_2(BF_4)_x$ (x = 0.025-0.33) were fit to a model describing the doping dependence of conductivity for Mott insulators with polaronic hopping transport.[10,27] This model derives from Mott's formula for the temperature dependence of the conductivity for variable-range hopping transport (Equation 1, d is dimensionality):

$$\sigma(T) = \sigma_0 e^{-(\frac{T_0}{T})^{\frac{1}{1+d}}} \qquad (1)$$

Both the σ_0 and T_0 parameters are dependent on the electron density of states at the Fermi level, $N(E_F)$, according to the following proportionalities:

$$\sigma_0 \propto N(E_F) \qquad (2)$$

and

$$T_0 \propto \frac{\alpha^3}{N(E_F)} \quad (3)$$

where α^{-1} is the localization length. If oxidation leads to stoichiometric creation of mid-gap states, $N(E_F)$ should be proportional to x and therefore:

$$ln(\sigma) \propto x^{-(\frac{1}{1+d})} \quad (4)$$

The satisfactory fit of the doping dependence of the conductivity is consistent with a polaronic hopping-based transport model and an increase in carrier concentration upon oxidation of the Fe^{II} centers. To the best of our knowledge, the observed conductivity of 0.3(1) S/cm for $Fe(tri)_2(BF_4)_{0.33}$ is among the highest for three-dimensionally conducting metal–organic frameworks; the iron(III) semiquinoid-quinoid framework is reported to display a conductivity of 0.16(1) S/cm.[9g] In addition, it is worth highlighting that a near 10^8 enhancement in conductivity has been achieved simply through the stoichiometric oxidation of a closed-shell type, insulating metal–organic framework.

Variable-temperature conductivity measurements were performed on $Fe(tri)_2(BF_4)_{0.33}$ over the temperature range of 30-300 K, as shown in Figure 6, and the data exhibit a trend that is consistent with that observed in the variable-temperature Mössbauer spectra. For example, the conductivity is highest at the highest temperature measured, 300 K, the same temperature at which the valence-delocalized feature observed in the Mössbauer spectra displays its maximum percent area. Upon decreasing the temperature, the conductivity decreases gradually and then rapidly below 90 K. Similarly, the Mössbauer spectrum of $Fe(tri)_2(BF_4)_{0.33}$ obtained at 100 K exhibits a decrease in the intensity of the valence-delocalized $Fe^{II/III}$ doublet concomitant with the emergence of new Fe^{II} and Fe^{III} features, indicating a localization of the charges responsible for the observed conductivity. Thus, the decreased conductivity at low temperature likely results of low hopping frequencies of localized charge carriers. The conductivity data suggest that complete localization of charge carriers occurs near or below 30 K, consistent with the disappearance of the valence-delocalized feature in the Mössbauer spectrum for this material at 5 K.

The variable-temperature conductivity data for $Fe(tri)_2(BF_4)_{0.33}$ were fit assuming an Arrhenius temperature dependence to determine the activation energy for charge hopping, as is shown in Figure 2.6 and S2.19. However, fitting the data with a single line revealed that the ln(σ) vs 1/T plot is not perfectly linear, indicating that the activation energy changes with temperature. It was possible instead to fit the high and low temperature data independently to extract activation energy values of 57.1 and 52.3 meV, respectively, with a crossover between these two regimes occurring at ~90 K. These activation energies are relatively small compared to other conductive MOFs (which display values typically on the order of 0.1-1 eV),[7g] likely due to factors such as the strong electronic coupling between low-spin iron centers mediated by the diffuse empty π* orbitals of the triazolate ligand and the highly isotropic crystal structure. The existence of two temperature regimes with distinct activation energies for $Fe(tri)_2(BF_4)_{0.33}$ likely originates from the valence localization behavior characterized at low temperature by Mössbauer spectroscopy (vida supra and Table S2.4). The observed contraction of the unit cell with decreasing temperature (see Table S2.3), and the corresponding decrease in iron-iron distances, may also contribute to the observed decrease in activation energy at ~90 K.

2.4 Conclusions and Outlook

The foregoing results demonstrate that the $Fe(tri)_2$ framework, although previously reported[8c] to be air-stable and moderately conductive, is in fact extremely sensitive to oxidation and in pure form exhibits very low conductivity that is consistent with the insulating behavior expected for low-spin octahedral iron(II) ions bridged by 1,2,3-triazolate linkers. This work thus serves to emphasize that special caution is imperative when handling and studying the conductivity of redox-active metal–organic frameworks, because even small valence impurities can result in a drastic enhancement of conductivity. We have also shown that the conductive frameworks $Fe(tri)_2(BF_4)_x$ (x = 0.09, 0.22, 0.33) can be readily obtained via stoichiometric chemical oxidation of $Fe(tri)_2$, and that these materials exhibit enhancements in conductivity up to eight orders of magnitude over that of the parent framework. Further, $Fe(tri)_2(BF_4)_{0.33}$ exhibits an electronic conductivity of 0.3(1) S/cm, which is one of the highest values reported to date for a three-dimensional metal–organic framework. The electronic conductivities notably derive from a high degree of charge delocalization between octahedral low-spin iron(II) and iron(III) centers, as revealed by Mössbauer spectroscopy. Ongoing studies will seek to examine other metal-triazolate frameworks, as well as how linker donor atoms may be varied to further enhance the conductivity of oxidized variants of $Fe(tri)_2$ through the use of substituted 1,2,3-triazolates.

2.5 Acknowledgement

This research was supported by NSF award number DMR-1611525, with the exception of the measurement and analysis of the magnetic data, which were supported by the Nanoporous Materials Genome Center of the U.S. Department of Energy, Office of Basic Energy Sciences, Division of Chemical Sciences, Geosciences and Biosciences under Award No. DE-FG02-17ER16362. Powder X-ray diffraction data were collected at Beamline 17-BM at the Advanced Photon Source, a U.S. Department of Energy Office of Science User Facility, operated by Argonne National Laboratory. Use of the Advanced Photon Source at Argonne National Laboratory was supported by the U.S. Department of Energy, Office of Science, Office of Basic Energy Sciences, under Contract No. De-AC02-06CH11357. We thank the National Science Foundation Graduate Research Fellowship Program for providing support for J.G.P, J.O., and L.E.D., Rodolfo Torres-Gavosto, Michael Ziebel, and Dr. Hiroyasu Furukawa for helpful discussions and experimental assistance, and Dr. Katie R. Meihaus for editorial assistance.

2.6 References

(1) Yaghi, O. M..; O'Keeffe, M.; Ockwig, N. W.; Chae, H. K.; Eddaoudi, M.; Kim, J. Reticular Synthesis and the Design of New Materials. *Nature* **2003**, *423*, 705.
(2) Burtch, N. C.; Jasuja, H.; Walton, K. S. Water Stability and Adsorption in Metal-Organic Frameworks. *Chem. Rev.* **2014**, *114*, 10575.
(3) For selected reviews, see the following: (a) Li, J.-R.; Kuppler, J. J.; Zhou, H.-C. Selective Gas Adsorption and Separation in Metal-Organic Frameworks. *Chem. Soc. Rev.* **2009**, *38*, 1477. (b) Sculley, J.; Yuan, D.; Zhou, H.-C. The Current Status of Hydrogen Storage in Metal-Organic Frameworks-Updated. *Energy Environ. Sci.* **2011**, *4*, 2721. (c) Sumida, K.; Rogow, D. L.; Mason, J. A.; McDonald, T. M.; Bloch, E. D.; Herm, Z. R.; Bae, T.-H.; Long, J. R. Carbon Dioxide Capture in Metal-Organic Frameworks. *Chem. Rev.* **2012**, *112*, 724. (d) Furukawa, H.; Cordova, K. E.;

O'Keeffe, M.; Yaghi, O. M. The Chemistry and Applications of Metal-Organic Frameworks. *Science* **2013**, *341*, 974. (e) Wu, M.-X.; Yang, Y.-W. Metal-Organic Framework (MOF)-Based Drug/Cargo Delivery and Cancer Therapy. *Adv. Mater.* **2017**, *29*, 1606134.
(4) (a) Morozan, A.; Jaouen, F. Metal Organic Frameworks for Electrochemical Applications. *Energy Environ. Sci.* **2012**, *5*, 9269. (b) Zhang, Z.; Awaga, K. Redox-Active Metal-Organic Frameworks as Electrode Materials for Batteries. *MRS Bull.* **2016**, *41*, 883. (c) Liao, P.-Q.; Shen, J.-Q.; Zhang, J.-P. Metal-Organic Frameworks for Electrocatalysis. *Coord. Chem. Rev.* [Online early access]. DOI: 10.1016/j.ccr.2017.09.001. Published Online: September 20, 2017.
(5) Cox, P. A. *The Electronic Structure and Chemistry of Solids*; Oxford University Press: New York, **2005**.
(6) Hendon, C. H.; Tiana, D.; Walsh, A. Conductive Metal-Organic Frameworks and Networks: Fact or Fantasy? *Phys. Chem. Chem. Phys.* **2012**, *14*, 13120.
(7) (a) Kobayashi, Y.; Jacobs, B.; Allendorf, M. D.; Long, J. R. Conductivity, Doping, and Redox Chemistry of a Microporous Dithiolene-Based Metal-Organic Framework. *Chem. Mater.* **2010**, *22*, 4120. (b) Narayan, T. C.; Miyakai, T.; Seki, S.; Dincă, M. High Charge Mobility in a Tetrathiafulvalene-Based Microporous Metal-Organic Framework. *J. Am. Chen. Soc.* **2012**, *134*, 12932. (c) Sun, L; Miyakai, T.; Seki, S.; Dincă, M. Mn_2(2,5-disulfhydrylbenzene-1,4-dicarboxylate): A Microporous Metal-Organic Framework with Infinite $(-Mn-S-)_\infty$ Chains and High Intrinsic Charge Mobility. *J. Am. Chen. Soc.* **2013**, *135*, 8185. (d) Talin, A. A.; Centrone, A.; Ford, A. C.; Foster, M. E.; Stavila, V.; Haney, P.; Kinney, R. A.; Szalai, V.; Gabaley, F. E.; Yoon, H. P.; Léonard, F.; Allendorf, M. D. Tunable Electrical Conductivity in Metal-Organic Framework Thin-Film Devices. *Science* **2014**, *343*, 66. (e) Sun, L.; Hendon, C. H.; Minier, M. A.; Walsh, A.; Dincă, M. Million-Fold Electrical Conductivity Enhancement in Fe_2(DEBDC) versus Mn_2(DEBDC) (E = S, O). *J. Am. Chen. Soc.* **2015**, *137*, 6164. (f) Park, S. S.; Hontz, E. R.; Sun, L.; Hendon, C. H.; Walsh, A.; Van Voorhis, T.; Dincă, M. Cation-Dependent Intrinsic Electrical Conductivity in Isostructural Tetrathiafulvalene-Based Microporous Metal-Organic Frameworks. *J. Am. Chen. Soc.* **2015**, *137*, 1774. (g) Sun, L.; Campbell, M. G.; Dincă, M. Electrically Conductive Porous Metal-Organic Frameworks. *Angew. Chem. Int. Ed.* **2016**, *55*, 3566.
(8) For metal mixed-valency: (a) Takaishi, S.; Hosoda, M.; Kajiwara, T.; Miyasaka, H.; Yamashita, M.; Nakanish, Y.; Kitagawa, Y.; Yamaguchi, K.; Kobayashi, A.; Kitagawa, H. Electroconductive Porous Coordination Polymer $Cu[Cu(pdt)_2]$ Composed of Donor and Acceptor Building Units. *Inorg. Chem.* **2009**, *48*, 9048. (b) D'Alessandro, D. M.; Kanga, J. R. R.; Caddy, J. S. Towards Conducting Metal-Organic Frameworks. *Aust. J. Chem.* **2011**, *64*, 718. (c) Gándara, F.; Uribe-Romo, F. J.; Britt, D. K.; Furukawa, H.; Lei, L.; Cheng, R.; Duan, X.; O'Keeffe, M.; Yaghi, O. M. Porous, Conductive Metal-Triazolates and Their Structural Elucidation by the Charge-Flipping Method. *Chem. Eur. J.* **2012**, *18*, 10595. (d) D'Alessandro, D. M. Exploiting Redox Activity in Metal-Organic Frameworks: Concepts, Trends and Perspectives. *Chem. Commun.* **2016**, *52*, 8957. (e) Murase, R.; Leong, C. F.; D'Alessandro, D. M. Mixed Valency as a Strategy for Achieving Charge Delocalization in Semiconducting and Conducting Framework Materials. *Inorg. Chem.* **2017**, *56*, 14373. (f) Xie, L. S.; Sun, L.; Wan, R.; Park, S. S.; DeGayner, J. A.; Hendon, C. H.; Dincă, M. Tunable Mixed-Valence Doping towards Record Electrical Conductivity in a Three-Dimensional Metal-Organic Framework. *J. Am. Chem. Soc.* [Online early access]. DOI: 10.1021/jacs.8b03604. Published Online: May 28, 2018. (g) Aubrey, M. L.; Wiers, B. M.; Andrews, S. C.; Sakurai, T.; Reyes-Lillo, S. E..; Hamed, S. M.; Yu, C.-J. Y.; Darago, L. E.; Mason, J. A.; Baeg, J.-O.; Grandjean, F.; Long, G. J.; Seki, S.; Neaton, J. B.; Yang, P.; Long, J. R. Electron Delocalization and Charge Mobility as a Function of Reduction in a Metal-Organic

Framework. *Nat. Mater.* [Online early access]. DOI: 10.1038/s41563-018-0098-1. Published Online: June 4, 2018.
(9) For ligand mixed-valency: (a) Kato, R.; Kobayashi, H.; Kobayashi, A. Crystal and Electronic Structures of Conductive Anion-Radical Salts, (2,5-R_1R_2-DCNQI)$_2$Cu (DCNQI = *N*,*N*'-Dicyanoquinonediimine; R_1, R_2 = CH_3, CH_3O, Cl, Br). *J. Am. Chem. Soc.* **1989**, *111*, 5224. (b) Heintz, R. A.; Zhao, H.; Ouyang, X.; Grandinetti, G.; Cowen, J.; Dunbar, K. R. New Insight into the Nature of Cu(TCNQ): Solution Routes to Two Distinct Polymorphs and Their Relationship to Crystalline Films That Display Bistable Switching Behavior. *Inorg. Chem.* **1999**, *38*, 144. (c) Neufeld, A. K.; Madsen, I.; Bond, A. M.; Hogan, C. F. Phase, Morphology, and Particle Size Changes Associated with the Solid-Solid Electrochemical Interconversion of TCNQ and Semiconducting CuTCNQ (TCNQ = Tetracyanoquinodimethane). *Chem. Mater.* **2003**, *15*, 3573. (d) Zhang, Z.; Zhao, H.; Kojima, H.; Mori, T.; Dunbar, K. R. Conducting Organic Frameworks Based on a Main-Group Metal and Organocyanide Radicals. *Chem. Eur. J.* **2013**, *19*, 3348. (e) Kambe, T.; Sakamoto, R.; Hoshiko, K.; Takada, K.; Miyachi, M.; Ryu, J.-H.; Sasaki, S.; Kim, J.; Nakazato, K.; Takata, M.; Nishihara, H. π-Conjugated Nickel Bis(dithiolene) Complex Nanosheet. *J. Am. Chem. Soc.* **2013**, *135*, 2462. (f) Kambe, T.; Sakamoto, R.; Kusamoto, T.; Pal, T.; Fukui, N.; Hoshiko, K.; Shimojima, T.; Wang, Z.; Hirahara, T.; Ishizaka, K.; Hasegawa, S.; Liu, F.; Nishihara, H. Redox Control and High Conductivity of Nickel Bis(dithiolene) Complex π-Nanosheet: A Potential Organic Two-Dimensional Topological Insulator. *J. Am. Chem. Soc.* **136**, *41*, 14357. (g) Darago, L. E.; Aubrey, M. L.; Yu, C. J.; Gonzalez, M. I.; Long, J. R. Electronic Conductivity, Ferrimagnetic Ordering, and Reductive Insertion Mediated by Organic Mixed-Valence in a Ferric Semiquinoid Metal-Organic Framework. *J. Am. Chem. Soc.* **2015**, *137*, 15703. (h) Jeon, I.-R.; Negru, B.; Van Duyne, R. P.; Harris, T. D. A 2D Semiquinone Radical-Containing Microporous Magnet with Solvent Induced Switching from T_c = 26 to 80 K. *J. Am. Chem. Soc.* **2015**, *137*, 15699. (i) DeGayner, J. A.; Jeon, I.-R.; Sun, L.; Dincă, M.; Harris, T. D. 2D Conductive Iron-Quinoid Magnets Ordering up to T_c = 105 K via Heterogenous Redox Chemistry. *J. Am. Chem. Soc.* **2017**, *139*, 4175. (j) Ziebel, M. E.; Darago, L. E.; Long, J. R. Control of Electronic Structure and Conductivity in Two-Dimensional Metal-Semiquinoid Frameworks of Titanium, Vanadium, and Chromium. *J. Am. Chem. Soc.* **2018**, *140*, 3040.
(10) (a) Roth, S.; Carroll D. One-Dimensional Metals: Conjugated Polymers, Organic Crystals, Carbon Nanotubes and Graphene; Wiley-VCH: Singapore, **2015**. (b) Launay, J.-P.; Verdaguer, M. Electrons in Molecules: From Basic Principles to Molecular Electronics; Oxford University Press: Oxford, **2013**.
(11) Epstein, A. J.; Rommelmann, H.; Abkowitz, M.; Gibson, H. W. Frequency Dependent Conductivity of Polyacetylene. *Mol. Cryst. Liq. Cryst.* **1981**, *77*, 81.
(12) (a) Litterst, F. J.; Amthauer, G. Electron Delocalization in Ilvaite, a Reinterpretation of Its ^{57}Fe Mössbauer Spectrum. *Phys. Chem. Miner.* **1984**, *10*, 250. (b) Prassides, K. *Mixed Valency Systems: Applications in Chemistry, Physics and Biology*; Springer: Netherlands, **1991**. (c) Grandjean, F.; Samain, L.; Long, G. J. Characterization and Utilization of Prussian Blue and Its Pigments. *Dalton Trans.* **2016**, *45*, 18018.
(13) (a) Collman, J. P.; McDevitt, J. T.; Leidner, C. R.; Yee, G. T.; Torrance, J. B.; Little, W. A. Synthetic, Electrochemical, Optical, and Conductivity Studies of Coordination Polymers of Iron, Ruthenium, and Osmium Octaethylporphyrin. *J. Am. Chem. Soc.* **1987**, *109*, 4606. (b) Ding, X.-Q.; Bominaar, E. L; Bill, E.; Winkler, H.; Trautwein, A. X.; Druëke, S.; Chaudhuri, P.; Wieghardt, K. Mössbauer and Electron Paramagnetic Resonance Study of the Double-Exchange and Heisenberg-Exchange Interactions in a Novel Binuclear Fe(II/III) Delocalized-Valence

Compound. *J. Chem. Phys.* **1990**, *92*, 178. (c) Narvor, N. L.; Toupet, L.; Lapinte, C. Elemental Carbon Chain Bridging Two Iron Centers: Syntheses and Spectroscopic Properties of $[Cp^*(dppe)Fe\text{-}C_4\text{-}FeCp^*(dppe)]^{n+}\bullet n[PF_6]^-$. X-Ray Crystal Structure of the Mixed Valence Complex (n = 1). *J. Am. Chem. Soc.* **1995**, *117*, 7129. (d) Behera, J. N.; D'Alessandro, D. M.; Soheilnia, N.; Long, J. R. Synthesis and Characterization of Ruthenium and Iron-Ruthenium Prussian Blue Analogues. *Chem. Mater.* **2009**, *21*, 1922. (e) Gaudette, A. I; Jeon, I.-R.; Anderson, J. S.; Grandjean, F.; Long, G. J.; Harris, T. D. Electron Hopping through Double-Exchange Coupling in a Mixed-Valence Diiminobenzoquinone-Bridged Fe_2 Complex. *J. Am. Chem. Soc.* **2015**, *137*, 12617. (f) Ma, X.; Lin, C.-S.; Zhu, X.-Q.; Hu, S.-M.; Shen, T.-L.; Wu, X.-T. An Unusually Delocalized Mixed-Valence State of a Cyanidometal-Bridged Compound Induced by Thermal Electron Transfer. *Angew. Chem. Int. Ed.* **2017**, *56*, 1605.

(14) Sun, L.; Hendon, C. H.; Park, S. S.; Tulchinsky, Y.; Wan, R.; Wang, F.; Walsh, A.; O'Keeffe, M.; Dincă, M. Is Iron Unique in Promoting Electrical Conductivity in MOFs? *Chem. Sci.* **2017**, *8*, 4450.

(15) Boduszek, B.; Shine, H. J. Preparation of Solid Thianthrene Cation Radical Tetrafluoroborate. *J. Org. Chem.* **1988**, *53*, 5142.

(16) Zhou, X.-H.; Peng, Y.-H.; Du, X.-D.; Zuo, J.-L.; You, X.-Z. Hydrothermal Syntheses and Structures of Three Novel Coordination Polymers Assembled From 1,2,3-Triazolate Ligands. *Cryst. Eng. Comm.* **2009**, *11*, 1964.

(17) (a) Gütlich, P.; Garcia, Y.; Goodwin, H. A. Spin Crossover Phenomena in Fe(II) Complexes. *Chem. Soc. Rev.* **2000**, *29*, 419. (b) Nihei, M.; Shiga, T.; Maeda, Y.; Oshio, H. Spin Crossover Iron(III) Complexes. *Coord. Chem. Rev.* **2007**, *251*, 2606.

(18) (a) Vos, G.; Le Febre, R. A.; De Graaff, R. A. G.; Haasnoot, J. G.; Reedijk, J. Unique High-Spin-Low-Spin Transition of the Central Ion in a Linear, Trinuclear Iron(II) Triazole Compound. *J. Am. Chem. Soc.* **1983**, *105*, 1682. (b) Biswas, S.; Tonigold, M.; Kelm, H.; Krüger, H.-J.; Volkmer, D. Thermal Spin-Crossover in the $[M_3Zn_6Cl_6L_{12}]$ (M = Zn, Fe^{II}; L = 5,6-Dimethoxy-1,2,3-Benzotriazolate) System: Structural, Electrochemical, Mössbauer, and UV-Vis Spectroscopic Studies. *Dalton Trans.* **2010**, *39*, 9851.

(19) (a) Kahn, O.; Martinez, C. J. Spin-Transition Polymers: From Molecular Materials Toward Memory Devices. *Science* **1998**, *279*, 44. (b) Grosjean, A.; Daro, N.; Kauffmann, B.; Kaiba, A.; Létard, J.-F; Guionneau, P. The 1-D Polymeric Structure of the $[Fe(NH_2trz)_3](NO_3)_2\bullet nH_2O$ (with n = 2) Spin Crossover Compound Proven by Single Crystal Investigations. *Chem. Commun.* **2011**, *47*, 12382.

(20) Reed, D. A.; Xiao, D. J.; Gonzalez, M. I.; Darago, L. E.; Herm, Z. R.; Grandjean, F.; Long, J. R. Reversible CO Scavenging via Adsorbate-Dependent Spin State Transitions in an Iron(II)-Triazolate Metal-Organic Framework. *J. Am. Chem. Soc.* **2016**, *138*, 5594.

(21) (a) Aurbach, D.; Levi, M. D.; Levi, E.; Teller, H.; Markovsky, B.; Salitra, G.; Heider, U.; Heider, L. Common Electroanalytical Behavior of Li Intercalation Processes into Graphite and Transition Metal Oxides. *J. Electrochem. Soc.* **1998**, *145*, 3024. (b) Levi, M. D.; Salitra, G.; Markovsky, B.; Teller, H.; Aurbach, D.; Heider, U.; Heider, L. Solid-State Electrochemical Kinetics of Li-Ion Intercalation into $Li_{1-x}CoO_2$: Simultaneous Application of Electroanalytical Techniques SSCV, PITT, and EIS. *J. Electrochem. Soc.* **1999**, *146*, 1279. (c) Fey, G. T.-K.; Yo, W.-H.; Chang, Y.-C. Electrochemical Characterization of $Li_xNi_yCo_{1-y}O_2$ Electrodes in a 1 M $LiPF_6$ Solution of the Ethylene Carbonate-Diethyl Carbonate. *J. Power Sources* **2002**, *105*, 82.

(22) Ingalls, R. Electric-Field Gradient Tensor in Ferrous Compounds. *Phys. Rev.* **1964**, *133*, A787.

(23) (a) Demadis, K. D; Hartshorn, C. M.; Meyer, T. The Localized-to-Delocalized Transition in Mixed-Valence Chemistry. *J. Chem. Rev.* **2001**, *101*, 2655. (b) Brunschwig, B. S.; Creutz, C.; Sutin, N. Optical Transitions of Symmetrical Mixed-Valence Systems in the Class II-III Transition Regime. *Chem. Soc. Rev.* **2002**, *31*, 168. (c) D'Alessandro, D. M.; Keene, F. R. Current Trends and Future Challenges in the Experimental, Theoretical, and Computational Analysis of Intervalence Charge Transfer (IVCT) Transitions. *Chem. Soc. Rev.* **2006**, *35*, 424.
(24) (a) Wooten, F. *Optical Properties of Solids*; Academic: New York, **1972**. (b) Torrance, J. B. *Chemistry and Physics of One-Dimensional Metals*; Keller, H. J., Ed.; Plenum: New York, **1977**.
(25) Tanner, D. B.; Jacobsen, C. S.; Garito, A. F.; Heeger, A. J. Infrared Studies of the Energy Gap in Tetrathiofulvalence-Tetracyanoquinodimethane (TTF-TCNQ). *Phys. Rev. B* **1976**, *13*, 3381.
(26) (a) Brown, D. H.; Nuttall, R. H.; McAvoy, J.; Sharp, D. W. A. Pyridine, γ-Picoline, and Quinoline Complexes of Transition Metal Perchlorates and Tetrafluoroborates. *J. Chem. Soc. A*, **1966**, 892. (b) Reedijk, J. Pyrazoles and Imidazoles as Ligands. II. Coordination Compounds of N-methyl Imidazole with Metal Perchlorates and Tetrafluoroborates. *Inorg. Chim. Acta* **1969**, *3*, 517. (c) Holbrey, J. D.; Seddon, K. R. The Phase Behavior of 1-Alkyl-3-Methylimidazolium Tetrafluoroborates; Ionic Liquids and Ionic Liquid Crystals. *J. Chem. Soc., Dalton Trans.* **1999**, 2133.
(27) (a) Roth, S.; Bleier, H.; Pukachi, W. Charge Transport in Conducting Polymers. *Faraday Discuss. Chem. Soc.* **1989**, 88, 223. (b) Roth, S. *Hopping Transport in Solids*; Pollak, M. Ed.; Elsevier: Amsterdam, **1991**, *3*, 517.

Chapter 2 Supporting Information

S2.1 Additional Experimental Data

Synthesis of Fe(1,2,3-triazolate)$_2$(BF$_4$)$_{0.22}$. A purple solution of thianthrenium tetrafluoroborate (0.0788 g, 0.260 mmol) in MeCN (10 mL) was added to the neat pink crystalline powder Fe(tri)$_2$ (0.200 g, 1.04 mmol) and the suspension was stirred at 25 °C for 16 h. The resulting suspension was filtered to yield a light brown powder. The powder was washed by soaking in MeCN for 24 h (2 × 15 mL) and then dried under reduced pressure (13 μbar) at 120 °C for 48 h to yield 0.208 g of brown powder (95%). Anal. Calcd for $FeC_4H_4N_6B_{0.22}F_{0.88}$: C, 22.76; H, 1.91; N, 39.82. Found: C, 22.4; H, 2.21; N, 38.4. ICP-AES Found: Fe:B, 1:0.22.

Synthesis of Fe(1,2,3-triazolate)$_2$(BF$_4$)$_{0.09}$. The same procedure as above was followed for the synthesis of Fe(1,2,3-triazolate)$_2$(BF$_4$)$_{0.09}$ with Fe(tri)$_2$ (0.200 g, 1.04 mmol), thianthrenium tetrafluoroborate (0.0303 g, 0.100 mmol), and MeCN (10 mL) to afford 0.204 g of brown powder (98%). Anal. Calcd for $FeC_4H_4N_6B_{0.09}F_{0.36}$: C, 24.05; H, 2.02; N, 42.07. Found: C, 23.79; H, 2.12; N, 40.29. ICP-AES Found: Fe:B, 1:0.09.

Synthesis of Fe(1,2,3-triazolate)$_2$(BF$_4$)$_{0.05}$. The same procedure as above was followed for the synthesis of Fe(1,2,3-triazolate)$_2$(BF$_4$)$_{0.05}$ with Fe(tri)$_2$ (0.200 g, 1.04 mmol), thianthrenium tetrafluoroborate (0.0158 g, 0.052 mmol), and MeCN (10 mL) to afford 0.191 g of brown powder (94% yield). Anal. Calcd for $FeC_4H_4N_6B_{0.05}F_{0.2}$: C, 24.47; H, 2.05; N, 42.81. Found: C, 24.67; H, 2.12; N, 42.51.

Synthesis of Fe(1,2,3-triazolate)$_2$(BF$_4$)$_{0.025}$. The same procedure as above was followed for the synthesis of Fe(1,2,3-triazolate)$_2$(BF$_4$)$_{0.025}$ with Fe(tri)$_2$ (0.200 g, 1.04 mmol), thianthrenium tetrafluoroborate (0.0788 g, 0.026 mmol), and MeCN (10 mL) to afford 0.192 g of brown powder (95% yield). Anal. Calcd for $FeC_4H_4N_6B_{0.025}F_{0.1}$: C, 24.75; H, 2.08; N, 43.29. Found: C, 25.06; H, 1.90; N, 43.42.

From our synthetic experience with metal triazolate systems, we believe that a slight mismatch in the elemental analysis data of x = 0.22 and 0.09 is most likely from defects, also supported by the elemental analysis data of other metal triazolates.[1] Indeed, data may be fitted well by considering metal/ligand vacancies.

Powder X-ray Diffraction Data Collection and Rietveld Refinement. Samples were packed into 1.0 mm borosilicate glass capillary tubes and flame-sealed for measurements. Diffraction data were collected during an overnight scan in the 2θ range of 3-60° with 0.02° steps using a Bruker AXS D8 Advance diffractometer equipped with Cu-Kα radiation (λ = 1.5418 Å), a Lynxeye linear position-sensitive detector, and mounting the following optics: Göbel mirror, fixed divergence slit (0.6 mm), receiving slit (3 mm), and secondary beam Soller slits (2.5°). The X-ray generator was set at 40 kV and 40 mA.

A standard peak search, followed by indexing via the Single Value Decomposition approach,[2] as implemented in the software package TOPAS-Academic,[3] yielded the approximate

unit cell dimensions. Precise unit cell dimensions were determined by performing a structureless Le Bail refinement in the software package TOPAS-Academic.

For Rietveld refinements of structural models, high-resolution X-ray powder diffraction data was collected at Beamline 17-BM-B at the Advanced Photon Source (APS) at Argonne National Laboratory. Diffraction patterns were collected between 300 and 100 K with a wavelength of 0.45241(4) Å. The previously reported crystal structure of the isostructural $Cd(tri)_2$,[4] with Cd(II) ions replaced by Fe(II) ions, was used as a starting structural model for Rietveld refinements of $Fe(tri)_2$ and $Fe(tri)_2(BF_4)_{0.33}$. Prior to the refinement, precise unit cell parameters were obtained by Le Bail fitting implemented in TOPAS-Academic. During the refinement of the $Fe(tri)_2(BF_4)_{0.33}$ patterns, difference Fourier maps were generated. Positive electron densities in the shape of a tetrahedral molecule were observed in the pores, suggesting the presence of unaccounted for $[BF_4]^-$ anions. Boron and fluorine atoms were placed at the corresponding coordinates of the observed electron densities. Upon the introduction of $[BF_4]^-$ anions, a large improvement of the refinement parameters was observed.

For both $Fe(tri)_2$ and $Fe(tri)_2(BF_4)_{0.33}$, hydrogen atoms were placed on calculated positions, assuming a fixed aromatic C–H distance of 1.09 Å. In the final stage of the refinements, all atomic positions (with the exception of special positions and the atomic coordinates of the H atom) and thermal and unit cell parameters were fully refined and convoluted with the sample and instrument parameters and Chebyshev background polynomials. Calculated diffraction patterns for the final structural models of $Fe(tri)_2$ and $Fe(tri)_2(BF_4)_{0.33}$ are in excellent agreement with the experimental diffraction pattern as is seen in the Rietveld refinement plots in Figure S2.4-2.6 and the crystallographic details reported in Table S2.2.

Surface Area Measurement and Calculation. Samples were transferred in an N_2-filled glovebox to a pre-weighed analysis tube and capped with a Transeal. The samples were then transferred to a Micromeritics Smart VacPrep instrument, evacuated, and heated to 120 °C at 5 °C per minute for 3 days, at which the pressure was stabilized at 13 μbar. N_2 isotherms at 77 K were measured using UHP-grade gas sources. For the determination of surface areas, the Langmuir and BET methods were applied using the adsorption branches of the N_2 isotherms, assuming a N_2 cross-sectional area of 16.2 $Å^2$/molecule; BET areas were calculated in the pressure range with values of $v(P_0\text{-}P)$ increasing with P/P_0, according to the method reported by Walton and Snurr.[5] We would like to propose that the apparent lack of porosity in $x = 0.22$ material most likely results from the $[BF_4]^-$ distribution in the pores, a distribution that may prevent N_2 access to the pores. CO_2 adsorption isotherm data at 195 K was collected for $x = 0.22$ material and is shown in Figure S2.23. The BET surface area was calculated to be 70 m^2/g, which is consistent with the value obtained from the N2 adsorption data.

The theoretical surface area of $Fe(tri)_2(BF_4)_{0.33}$ was calculated using the open-source software Zeo++ version 0.3[6] accessible through Lawrence Berkeley Laboratory (LBNL) and the crystal structure of $Fe(tri)_2(BF_4)_{0.33}$ was refined from the high-resolution powder X-ray diffraction data collected at 300 K. A probe of radius of 1.2 Å was used to calculate the accessible surface area. Non-accessible surface area corresponds to the surface area inside inaccessible pockets.

Electrochemical Methods. Materials were characterized electrochemically in an argon-filled glovebox. A custom built, airtight three-electrode cell was constructed using a ½ inch diameter Swagelok PFA union tee and Ti current collectors. Lithium metal was smeared onto the counter and reference electrodes and polished to a mirror finish. Working electrodes were prepared by

drop casting a suspension of 60 wt% sample, 30 wt% conductive carbon Super P (Alfa Aesar), and 10 wt% PVDF (Sigma Aldrich) onto carbon cloth discs (Fuel Cell Earth). Cells were assembled with 1 M $LiBF_4$ propylene carbonate electrolyte solution soaked quartz fiber separating the electrodes. Slow-scan cyclic voltammograms were collected at 50 μV/s using a Bio-Logic VMP-3 multipotentiostat fitted to an argon glovebox. Data were analyzed with EC-Lab v10.41 software package from Bio-Logic.

Mössbauer Spectroscopy. Zero-field, Fe-57 Mössbauer spectra were recorded in a constant acceleration spectrometer (See Co., Edina, MN) between room temperature and 5 K in a Janis Research Co. cryostat (Willmington, MA). Prior to the measurement, the spectrometer was calibrated at 295 K with α-iron foil. The $Fe(tri)_2$ framework was gently ground and mixed homogenously with boron nitride for dilution of the iron concentration to 2 wt%. Approximately 50 mg of powder mixture was placed in a nylon washer and sealed between multiple layers of commercially available Scotch tape under an inert atmosphere, prior to introduction into the spectrometer in air, to avoid oxidation of the air-sensitive compound.

All the Mössbauer spectra were fitted with Lorentzian symmetric quadrupole doublets. In some cases, the absence of sharp features in the experimental spectra limited the number of adjustable parameters. Hence, to avoid overparametrization of the fits, some parameters were constrained to be equal, such as the linewidths of the three or four components in the complex low-temperature fits. Further, the percent areas of the components were constrained to expected reasonable values in these low-temperature fits. Finally, in a few cases, some hyperfine parameters were fixed at reasonable values, without any detectable loss in the quality of the fit. All fits are characterized by reduced χ^2 values that are slightly less than one.

The temperature dependence of the spectral parameters of $Fe(tri)_2(BF_4)_{0.22}$ is shown in Figure S2.21. As expected, the isomer shift of the valence average blue doublet is intermediate between the isomer shifts of the valence localized green and black doublets.[7] As expected from the second-order Doppler shift, all isomer shifts decrease with increasing temperature. The solid lines are the result of a Debye model for a solid[8,9] and yield Mössbauer temperatures, Θ_M, of 905(101), 456(107), and 447(46) K, for the red, green, and black doublets. A Mössbauer temperature of 450(100) K was estimated for the blue doublet. These temperatures are characteristic of the high-energy phonons in the vibrational spectrum of the iron ions. The Fe2 static, low-spin iron(II) site exhibits a larger Θ_M than the "dynamic" Fe1 low-spin iron(II) site and low-spin iron(III) site. Most likely the presence of a shared electron between the two Fe1 sites ions leads to a decrease in phonon energy, i.e., to a less rigid structural environment.

In $Fe(tri)_2(BF_4)_{0.22}$ the quadrupole splitting, ΔE_Q, of both low-spin iron(II) doublets, the red and green components, are essentially independent of temperature, as expected, because there is no valence contribution to ΔE_Q from the t_{2g}^6 electronic configurations of these iron(II) ions; the observed ΔE_Q results solely from a lattice contribution to the electric field gradient, a contribution that typically exhibits little temperature dependence. The observed ΔE_Q of the valence averaged blue doublet is intermediate between that of the valence localized green and black doublets.

The logarithm of the absorption area was fit with the Debye model for a solid and yields a Debye temperature, Θ_D, of 225(15) K. The difference between the Debye and Mössbauer temperatures[8,9] results from the different phonon-energy ranges probed by these two temperatures. It is quite usual to observe Θ_M that are two or three times the Θ_D value. It should be noted that, the Θ_M and Θ_D values of the static Fe2 site observed herein for $Fe(tri)_2(BF_4)_{0.22}$ are very similar to those observed in another metal organic framework containing both iron(II) and iron(III) ions,

namely $K_xFe_2(BDP)_3$, where BDP^{2-} is 1,4-benzenedipyrazolate.[10] In conclusion, the temperature dependence of the Mössbauer spectral parameters of $Fe(tri)_2(BF_4)_{0.22}$ strongly supports the analysis of the remaining spectra.

The compositional dependence of the 290 K Mössbauer spectral parameters of $Fe(tri)_2(BF_4)_x$ is shown in Figure S2.22. The red Fe2 low-spin iron(II) site isomer shift and quadrupole splitting are independent of *x*, an independence that confirms that the Fe2 site does not participate in the electron delocalization. There is a small dependence on *x* for the blue valence average doublet, a dependence that may be related to small changes in the crystallographic structure with *x*. Finally, the percent area of the blue doublet increases with increasing *x*, in agreement with an increase in conductivity.

Pressed Pellet Room-Temperature Conductivity Measurements. Electrical conductivity of the sample pressed with the home-built copper screw cell (Figure S2.15) was determined through both the *I-V* measurements and electrochemical impedance spectroscopy using a Bio-Logic VMP-3 multipotentiostat fitted into an argon atmosphere glovebox. Data were analyzed with the EC-Lab v10.41 software package from Bio-Logic. *I-V* profiles were collected for a ±1 V voltage window and fitted with Ohm's law, $V = I \cdot R$, where *V* is the voltage, *I* is the current, and *R* is the resistance. Resistance and volume of the pressed-pellets were used to calculate the conductivity, σ, of the sample by using the equation, $\sigma = L/(R \cdot A)$, where *L* and *A* are thickness and contact area of a cylindrical pellet, respectively. For impedance measurements, unless otherwise noted, all data was collected at 250 mV AC and 0 V DC bias with a frequency sweep range of 1 MHz to 1 Hz with sampling 15 points per decade, averaging 10 measurements per frequency. Data were fit to a model circuit in Figure S2.16, assuming electrons are the only mobile species, as $[BF_4]^-$ anions do not have mobility in dry pressed-pellets.

Pressed Pellet Variable-Temperature Conductivity Measurements. In an argon atmosphere glovebox, a sample was pressed into a pellet using a home-built copper screw cell (Figure S2.15). The screw cell was sealed using a Torr Seal@ low vapor pressure epoxy which makes an airtight seal. Conductivity measurements were performed in a Quantum Design MPMS2 SQUID magnetometer equipped with a cryostat. A standard sample rod was modified to accommodate two 26 AWG silver coated copper cables sealed at the top of the rod with an air tight Swagelok fitting and a Torr Seal@ low vapor pressure epoxy. The sample cell was attached to the SQUID rod and introduced into the SQUID chamber. A Bio-Logic SP200 potentiostat was used to collect *I-V* profiles at different temperatures for a ±1 V voltage window. To obtain an activation energy for a charge transport, variable-temperature conductivity data were fit to the Arrhenius equation, $\sigma = \sigma_0 \cdot e^{-(\frac{Ea}{k_B T})}$, where σ is the conductivity, σ_0 is the pre-exponential factor, E_a is the Arrhenius activation energy, k_B is the Boltzmann constant, and *T* is the temperature.

To fit the compositional dependence of the conductivity of $Fe(tri)_2(BF_4)_x$, the following equation was used,[11]

$$\ln(\sigma) = c \cdot \left(\frac{x}{x_{sat}}\right)^{-\left(\frac{1}{1+d}\right)} + \ln(\sigma_{sat})$$

where *c* is a unitless constant, *x* is the doping level in $Fe(tri)_2(BF_4)_x$, x_{sat} is the saturation level for redox doping, *d* is the dimensionality, and σ_{sat} is the saturation conductivity. Because of the small number of doping levels, five, it is necessary to reduce the number of adjustable parameters, four, in the above equation. First, the simplest model was chosen by fixing the dimensionality, *d*, equal

to one. Because c and x_{sat} are two factors of a product, they are 100 % correlated and cannot be simultaneously and unequivocally determined. Because c and σ_{sat} are parts of two terms in a sum, they are also highly correlated. Hence, it is imperative to fix one of these three parameters. Because the oxidation of $Fe(tri)_2$ is saturated through the insertion of 0.33 BF_4^- anion, x_{sat} was fixed equal to 0.33. With these assumptions, c and σ_{sat} refine to –3.7(2) and 19(11) S/cm, respectively, with a correlation coefficient of –0.908. If the oxidation of $Fe(tri)_2$ can be achieved with a smaller anion than BF_4^-, x_{sat} is expected to be greater than 0.33.

Because of the 100 % correlation between c and x_{sat}, all fits, with x_{sat} fixed between 0.33 and 1.0, show the same goodness of fit with c varying between –3.7(2) and –2.1(1) and with σ_{sat} always equal to 19(11) S/cm. Indeed, the low precision on the adjusted parameters can only be improved by additional measurements at different doping levels.

Magnetic Measurements. A sample was prepared by adding crystalline powder of $Fe(tri)_2(BF_4)_{0.33}$ (43.7 mg) to a 5 mm i.d. / 7 mm o.d. quartz tube containing a raised quartz platform. Solid eicosane was added both to cover the sample to prevent crystallite torqueing and to provide good thermal contact between the sample and the cryostat. The tube was fitted with a Teflon sealable adapter, evacuated on a Schlenk line, and flame-sealed under static vacuum. The solid eicosane was then briefly melted in a water bath held at 40 °C. Magnetic susceptibility measurements were performed using a Quantum Design MPMS-XL SQUID magnetometer. Diamagnetic corrections were applied to the data using Pascal's constants to give χ_D = −0.00008826 emu/mol ($Fe(tri)_2(BF_4)_{0.33}$) and χ_D = –0.00024306 emu/mol (eicosane).

Other Physical Measurements. UV-visible-NIR diffuse reflectance spectra were collected using a CARY 5000 spectrophotometer interfaced with Varian Win UV software. The samples were held in a Praying Mantis air-free diffuse reflectance cell. Barium sulfate powder was used as a non-adsorbing matrix. The Kubelka-Munk conversion (F(R) versus wavenumber) of the raw diffuse reflectance spectrum (R versus wavenumber) was obtained by applying the formula $F(R) = (1 - R)^2/2R$.

Thermogravimetric analysis (TGA) was performed on a TA Q5000 instrument in a flow of dinitrogen at a heating rate of 2 °C/min between 26 and 540 °C. A suspension of sample powder in hexane was transferred via pipette to a pre-weighed pan in an argon glovebox. The pan containing a suspension was kept inside a vial. As soon as the vial was taken out of an argon glovebox, it was cooled to 77 K using a liquid nitrogen bath. Prior to starting a measurement, the pan containing a sample in a frozen hexane matrix was quickly transferred to the TGA instrument.

Infrared spectra were collected on a Perkin Elmer Spectrum FT-IR/FT-FIR spectrometer with an attenuated total reflectance accessory (ATR) with a home-built N_2 glove bag attachment for air-sensitive compounds.

Table S2.1. Calculated surface areas of $Fe(tri)_2(BF_4)_x$ (x = 0 and 0.33) from N_2 adsorption isotherm data and crystal structures.

Surface Area	$Fe(tri)_2$	$Fe(tri)_2(BF_4)_{0.33}$
Langmuir / m^2g^{-1}	562	240
BET / m^2g^{-1}	370	50
Calculated Accessible / m^2g^{-1}	557[1]	0
Calculated Non-accessible / m^2g^{-1}	–	129

Table S2.2. Structureless Le Bail refinement fit parameters to room-temperature powder X-ray diffraction patterns of $Fe(tri)_2(BF_4)_x$ (x = 0, 0.09, 0.22, and 0.33).

Compound	$Fe(tri)_2$	$Fe(tri)_2(BF_4)_{0.09}$	$Fe(tri)_2(BF_4)_{0.22}$	$Fe(tri)_2(BF_4)_{0.33}$
Crystal system	Cubic			
Space group	*Fd*–3*m*			
a / Å	16.6423(6)	16.6136(7)	16.5140(5)	16.4368(5)
R_p / %	1.347	1.885	1.361	1.296
R_{wp} / %	0.897	1.404	0.899	0.886
V / Å^3	4609.4(5)	4585.6(6)	4503.6(4)	4440.7(4)
GOF	4.114	4.629	4.140	4.032

Table S2.3. Rietveld structure refinement parameters to variable-temperature high resolution powder X-ray diffraction patterns of $Fe(tri)_2(BF_4)_x$ (x = 0, 0.33).

Compound	$Fe(tri)_2$	$Fe(tri)_2(BF_4)_{0.33}$	
Temperature	300 K	100 K	300 K
Crystal system	Cubic	Cubic	Cubic
Space group	*Fd*–3*m*	*Fd*–3*m*	*Fd*–3*m*
a / Å	16.65075(17)	16.4500(3)	16.4794(3)
R_p / %	2.731	4.286	4.325
R_{wp} / %	3.914	6.100	6.334
V / Å^3	4616.38(14)	4451.4(3)	4475.4(3)
GOF	2.368	3.445	3.571

Table S2.4. Temperature Dependence of the Mössbauer Spectral Parameters.[a]

Complex	*T*, K	δ, mm/s[b]	ΔE_Q, mm/s	Γ, mm/s	*Area, %*	*Area* (%ε), mm/s	Assignment
$Fe(tri)_2$	290	0.385(1)	0.084(7)	0.267(5)	100	1.65(1)	Fe2, LS Fe(II)
$Fe(tri)_2(BF_4)_{0.09}$	290	0.371(2)	0.101(5)	0.269(2)	83.8(5)	3.63(1)	Fe2, LS Fe(II)
		0.25(1)	0.34(3)	0.269(2)	16.2(5)	-	Fe1, Fe(II/III)
$Fe(tri)_2(BF_4)_{0.22}$	295	0.388(4)	0.07(2)	0.24(2)	49(2)	1.520(1)	Fe2, LS Fe(II)
		0.17	0.3	0.448	51(2)	-	Fe1, Fe(II/III)
	290	0.382(1)	0.105(3)	0.227(5)	49.2(6)	-	Fe2, LS Fe(II)
		0.17	0.356(6)	0.448	50.8(6)	-	Fe1, Fe(II/III)
	200	0.41(2)	0.09(3)	0.29(1)	50	2.44(2)	Fe2, LS Fe(II)
		0.23(3)	0.53(6)	0.29(1)	18	-	Fe1, Fe(II/III)
		0.32(4)	0.20(7)	0.29(1)	16		Fe1, LS Fe(II)
		0.09(5)	0.77(9)	0.29(1)	16		Fe1, LS Fe(III)
	150	0.416(4)	0.101(9)	0.291(5)	50	2.60(1)	Fe2, LS Fe(II)
		0.270(9)	0.64	0.291(5)	15	-	Fe1, Fe(II/III)
		0.37(1)	0.16(2)	0.291(5)	17.5	-	Fe1, LS Fe(II)
		0.10	0.8	0.291(5)	17.5	-	Fe1, LS Fe(III)
	100	0.44(1)	0.03(9)	0.343(9)	50	2.79(2)	Fe2, LS Fe(II)
		0.40(3)	0.12(6)	0.343(9)	25	-	Fe1, LS Fe(II)
		0.13(1)	0.86(2)	0.343(9)	25	-	Fe1, LS Fe(III)
	75	0.443(2)	0.03(4)	0.341(2)	50	2.92(1)	Fe2, LS Fe(II)
		0.376(4)	0.12(1)	0.341(2)	25	-	Fe1, LS Fe(II)
		0.140(4)	0.922(8)	0.341(2)	25	-	Fe1, LS Fe(III)
	50	0.447(1)	0.004(20)	0.340(1)	50	2.980(5)	Fe2, LS Fe(II)
		0.385(2)	0.096(6)	0.340(1)	25	-	Fe1, LS Fe(II)
		0.140(2)	0.967(4)	0.340(1)	25	-	Fe1, LS Fe(III)
	25	0.439(4)	0.03(3)	0.326(6)	50	3.05(2)	Fe2, LS Fe(II)
		0.39(1)	0.14(3)	0.326(6)	25	-	Fe1, LS Fe(II)
		0.140(6)	1.04(1)	0.326(6)	25	-	Fe1, LS Fe(III)
	5	0.441(3)	0.08(1)	0.318(5)	50	3.17(1)	Fe2, LS Fe(II)
		0.386(7)	0.18(2)	0.318(5)	25	-	Fe1, LS Fe(II)
		0.143(4)	1.088(8)	0.318(5)	25	-	Fe1, LS Fe(III)
$Fe(tri)_2(BF_4)_{0.33}$	290	0.375(6)	0.07(1)	0.264(4)	33.33	3.39(1)	Fe2, LS Fe(II)
		0.173(3)	0.466(6)	0.272(2)	66.67	-	Fe1, Fe(II/III)
	100	0.43	0.139(2)	0.28	43(1)	4.65(1)	Fe2, LS Fe(II)
		0.167(4)	0.89(1)	0.35	13.2(4)	-	Fe1, Fe(II/III)
		0.320(2)	0.273(3)	0.28	22.0(3)	-	Fe1, LS Fe(II)
		0.132(2)	1.337(3)	0.28	22.0(3)	-	Fe1, LS Fe(III)
	5	0.460(2)	0.128(2)	0.263(2)	34	5.28(1)	Fe2, LS Fe(II)
		0.354(2)	0.219(3)	0.263(2)	33	-	Fe1, LS Fe(II)
		0.140(1)	1.380(1)	0.263(2)	33	-	Fe1, LS Fe(III)

[a]Statistical fitting uncertainties are given in parentheses; the true errors may be twice as large. The absence of an uncertainty indicates that the parameter was constrained to the value given. [b]The isomer shifts are given relative to α-iron foil measured at 290 K.

Table S2.5. Summary of room-temperature conductivities of $Fe(tri)_2(BF_4)_x$ (x = 0, 0.025, 0.05, 0.09, 0.22, and 0.33).

x	0	0.025	0.05	0.09	0.22	0.33
Contact Area (cm^2)	0.054(1)	0.055(1)	0.055(1)	0.059(1)	0.058(1)	0.056(1)
Pellet Thickness (cm)	0.153(2)	0.102(2)	0.103(2)	0.174(2)	0.152(2)	0.098(2)
Conductivity (S/cm)	1×10^{-10}	2×10^{-5}	2×10^{-3}	0.03(2)	0.2(1)	0.3(1)

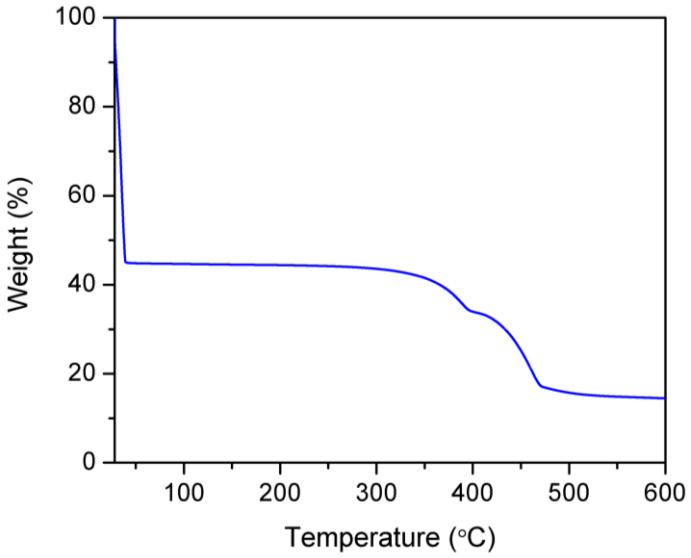

Figure S2.1. Thermogravimetric analysis scan of $Fe(tri)_2(BF_4)_{0.33}$. The initial drop in weight percent is due to evaporation of a hexane matrix used to prevent air exposure during sample loading.

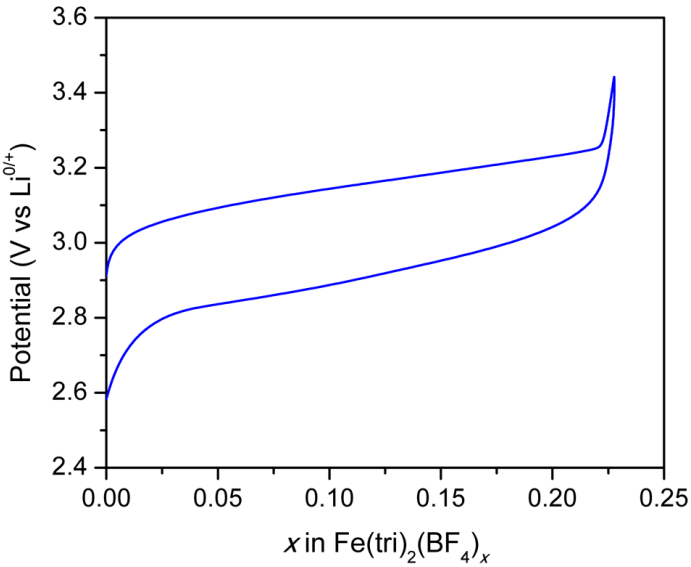

Figure S2.2. Voltage composition profile obtained for $Fe(tri)_2$.

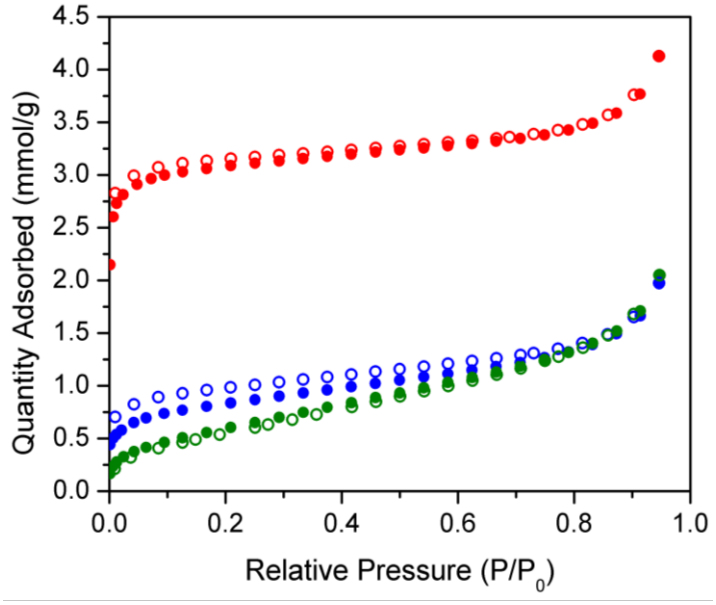

Figure S2.3. N_2 adsorption isotherms for $Fe(tri)_2(BF_4)_x$ for x = 0.09 (red circles), 0.22 (blue circles), and 0.33 (green circles) measured at 77 K. Closed and open data points represent adsorption and desorption, respectively.

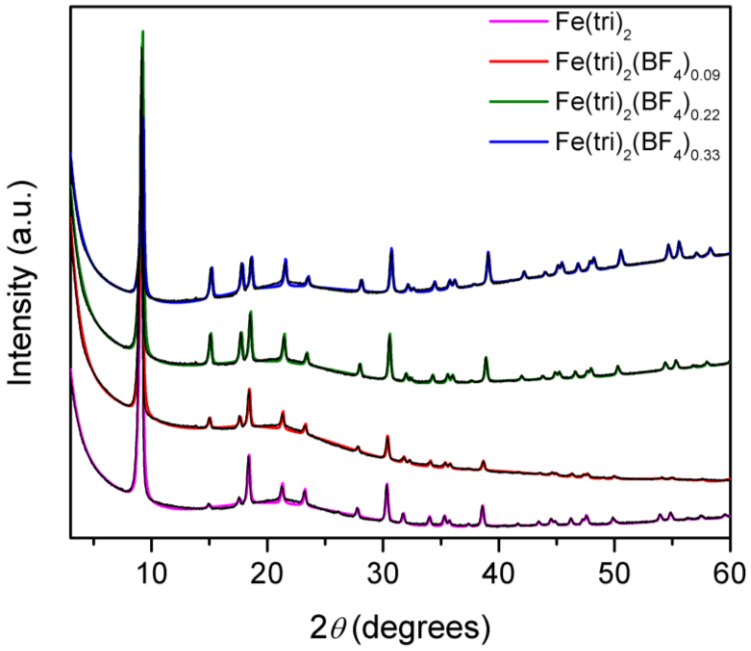

Figure S2.4. Powder X-ray diffraction patterns of $Fe(tri)_2(BF_4)_x$ (x = 0, 0.09, 0.22, and 0.33) with the fit (black) generated from structureless Le Bail refinements. The wavelength was 1.5418 Å.

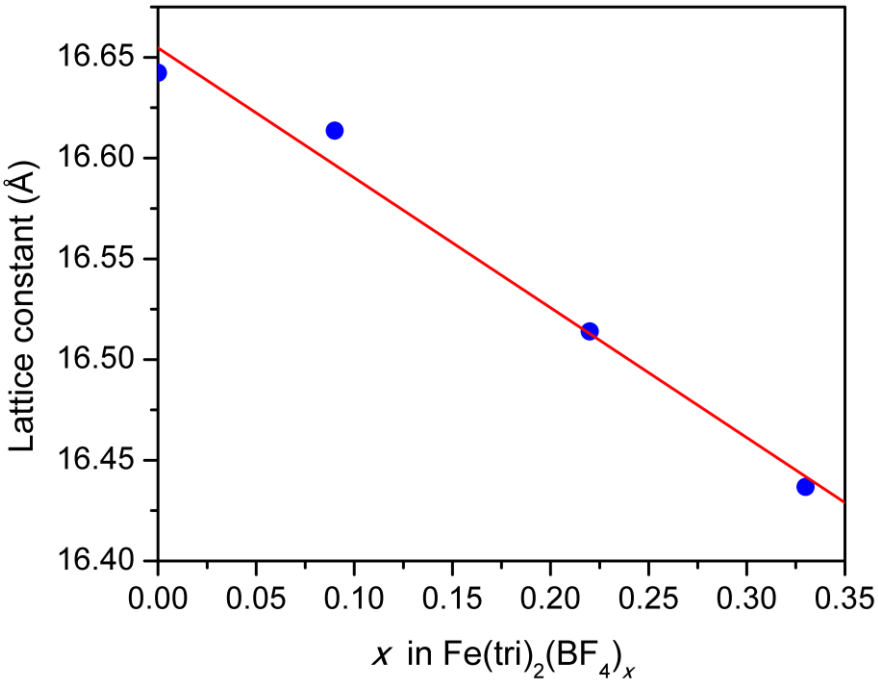

Figure S2.5. Le Bail refinement of the room temperature lattice constant vs x in $Fe(tri)_2(BF_4)_x$ (x = 0, 0.09, 0.22, and 0.33) with a linear fit (red), $a = -0.64(5)x + 16.65(1)$ with $R^2 = 0.983$.

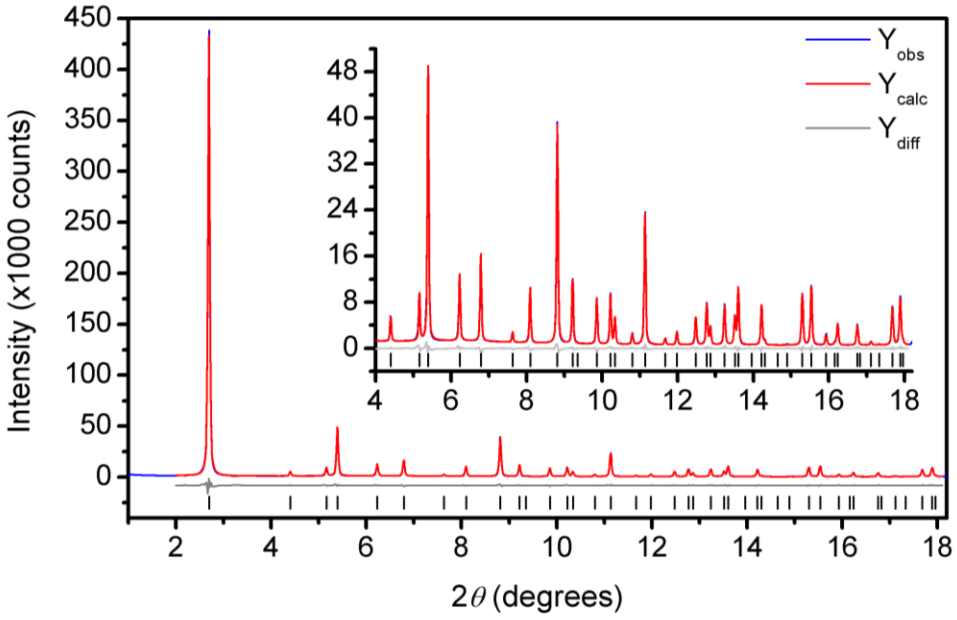

Figure S2.6. Rietveld refinement of powder x-ray diffraction data for activated $Fe(tri)_2$ obtained at 300 K. Measured scattered intensity, best fit, and the difference plot are shown with blue dots and red, gray lines, respectively. Figures-of-merit (as defined by TOPAS): R_{wp} = 3.914%, R_p = 2.731%, GoF = 2.368. The wavelength was 0.45241(4) Å.

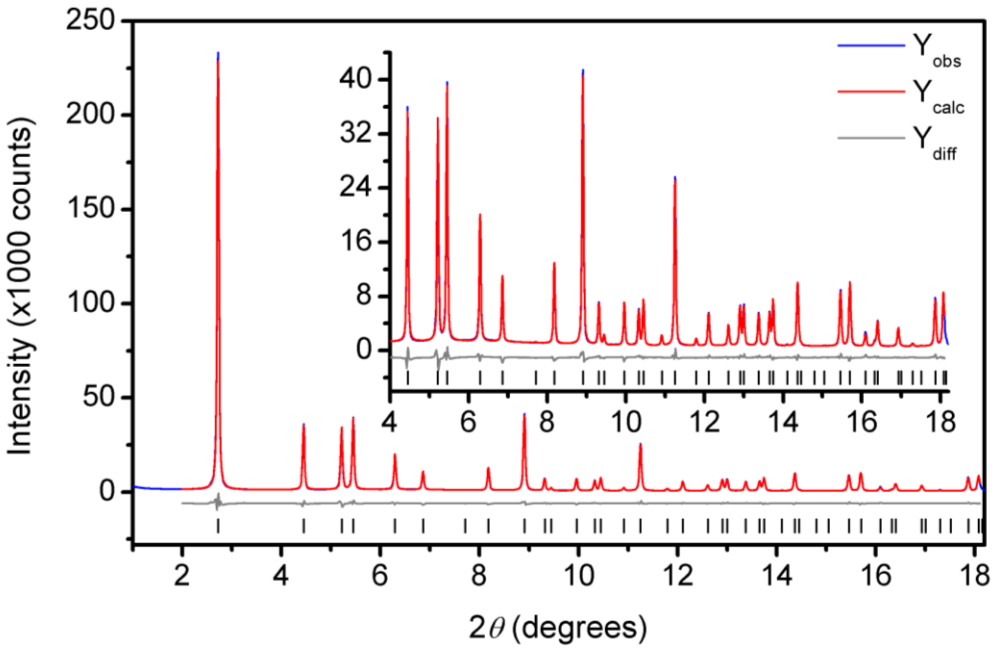

Figure S2.7. Rietveld refinement of powder x-ray diffraction data for activated $Fe(tri)_2(BF_4)_{0.33}$ obtained at 300 K. Measured scattered intensity, best fit, and the difference plot are shown with blue dots and red, gray lines, respectively. Figures-of-merit (as defined by TOPAS): R_{wp} = 6.334%, R_p = 4.325%, GoF = 3.571. The wavelength was 0.45241(4) Å.

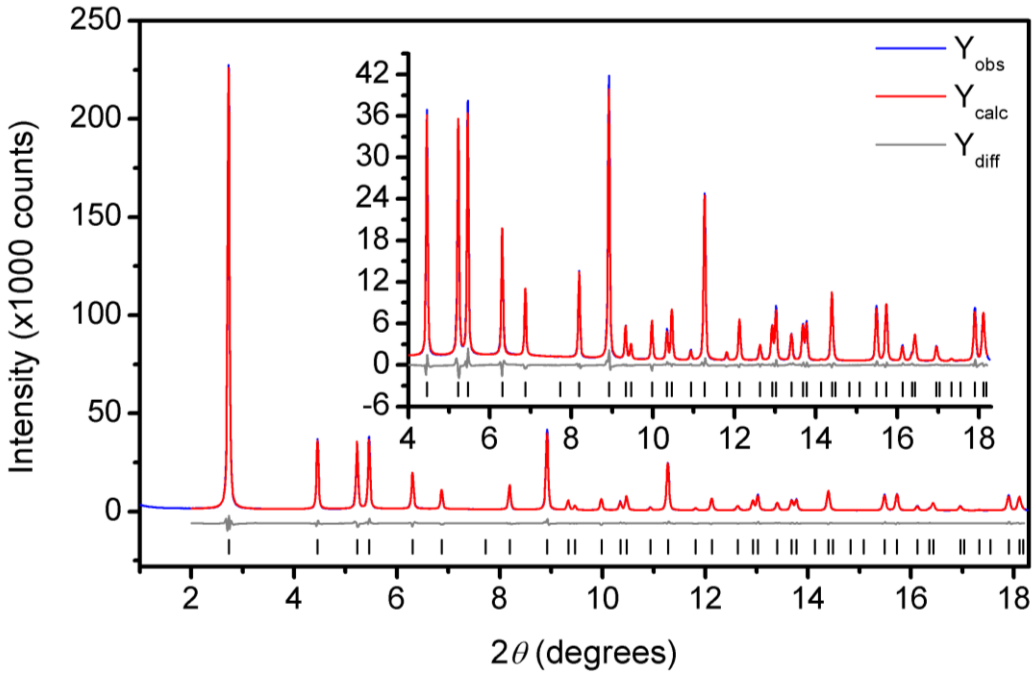

Figure S2.8. Rietveld refinement of powder x-ray diffraction data for activated $Fe(tri)_2(BF_4)_{0.33}$ obtained at 100 K. Measured scattered intensity, best fit, and the difference plot are shown with blue dots and red, gray lines, respectively. Figures-of-merit (as defined by TOPAS): R_{wp} = 6.100%, R_p = 4.286%, GoF = 3.445. The wavelength was 0.45241(4) Å.

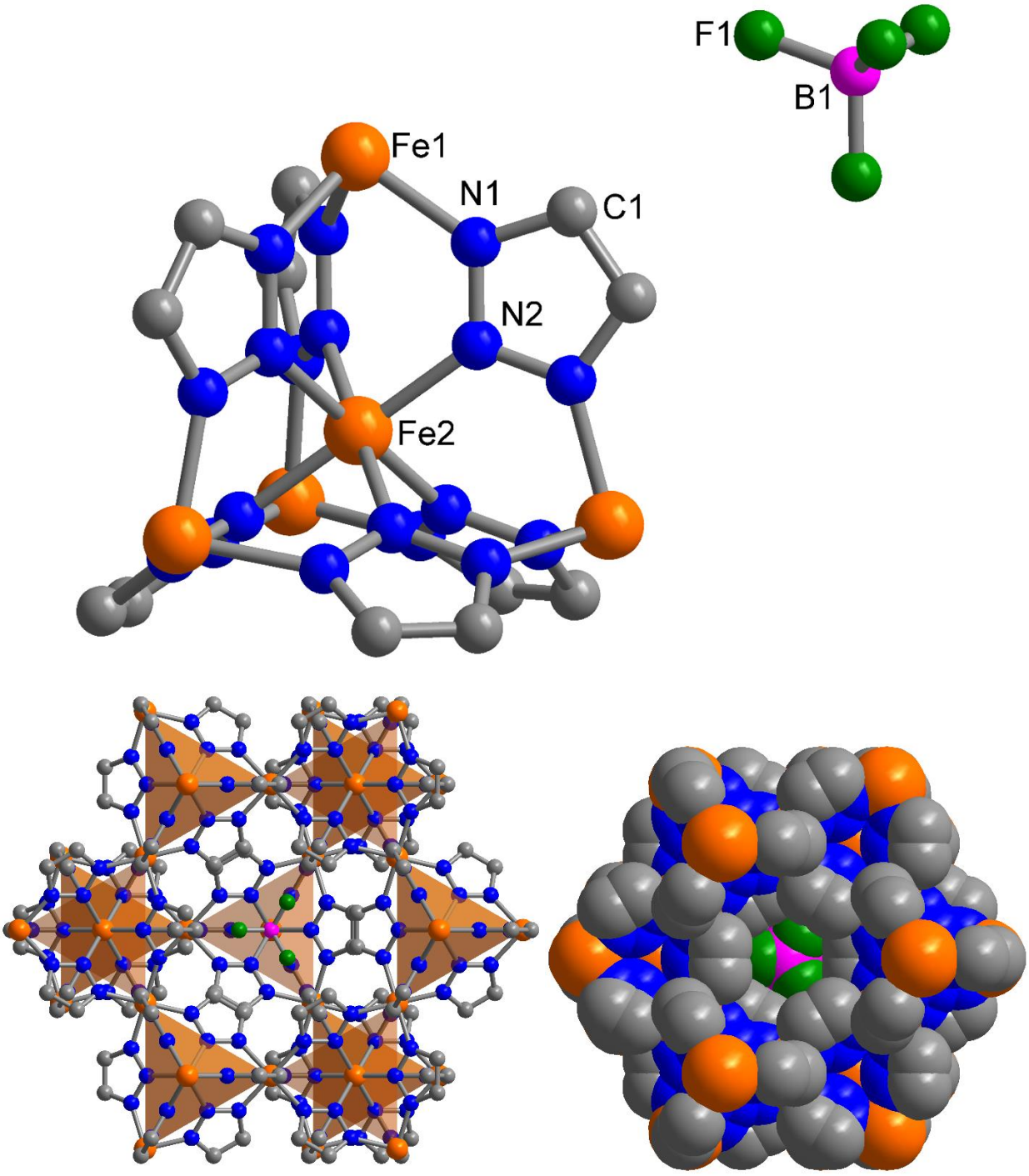

Figure S2.9. Powder X-ray diffraction structures of $Fe(tri)_2(BF_4)_{0.33}$ obtained at 300 K, which display its secondary building unit (top) and pore structure (bottom). Orange, grey, blue, pink, and green spheres represent Fe, C, N, B, and F atoms, respectively. Hydrogen atoms are omitted for clarity.

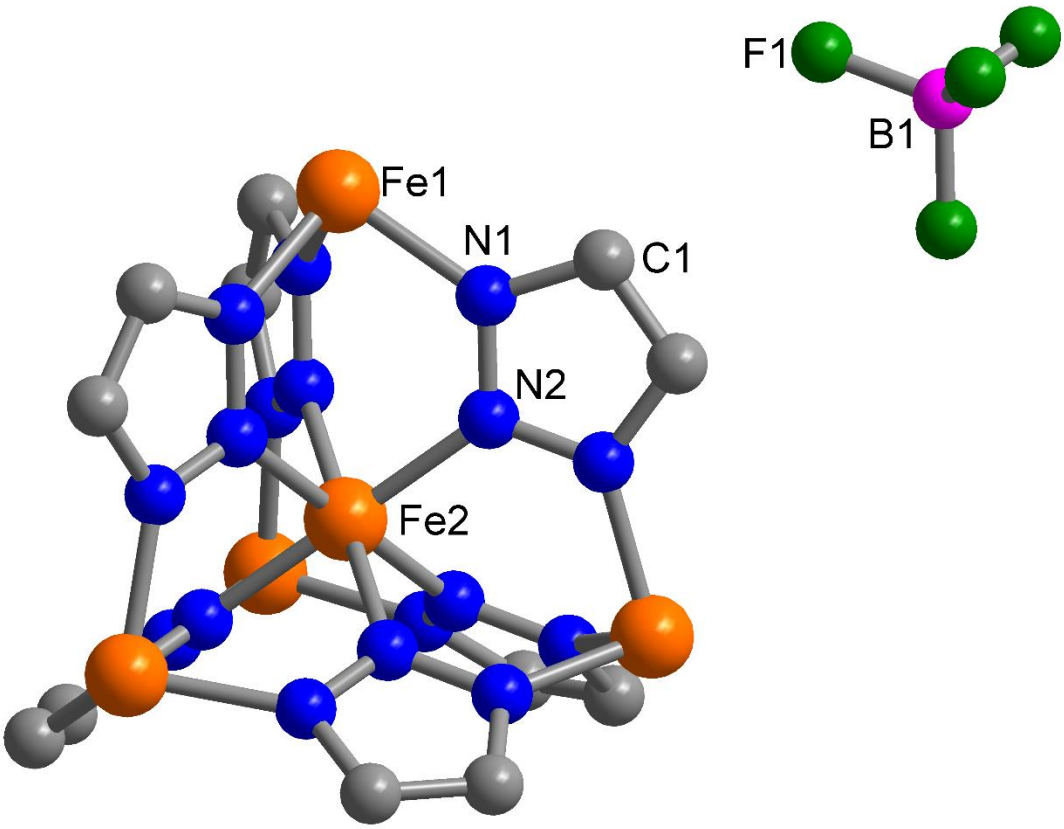

Figure S2.10. Powder X-ray diffraction structures of $Fe(tri)_2(BF_4)_{0.33}$ obtained at 100 K, displaying its secondary secondary building unit. Orange, grey, blue, pink, and green spheres represent Fe, C, N, B, and F atoms, respectively. Hydrogen atoms are omitted for clarity.

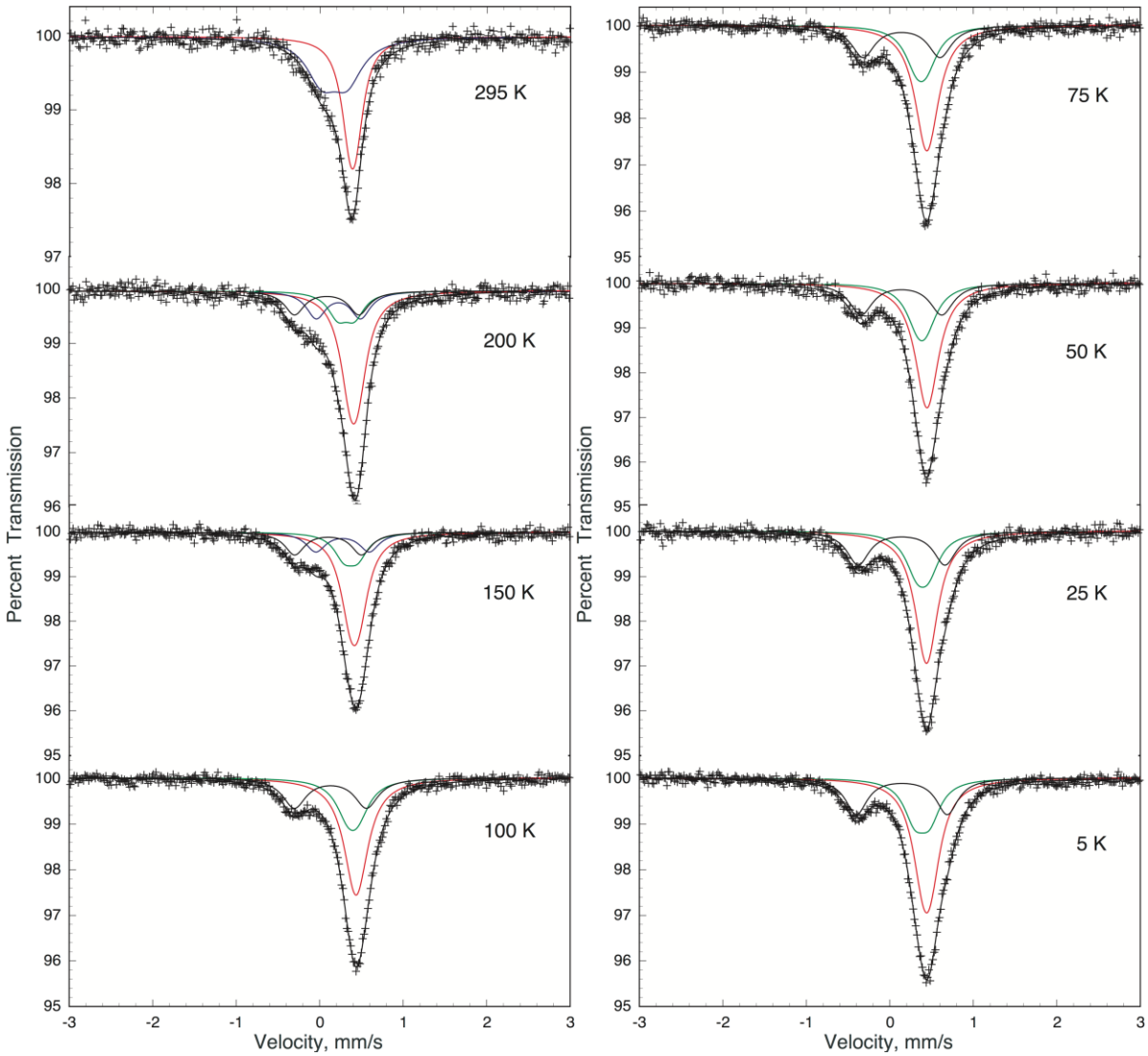

Figure S2.11. Temperature dependence of the Mössbauer spectra of $Fe(tri)_2(BF_4)_{0.22}$.

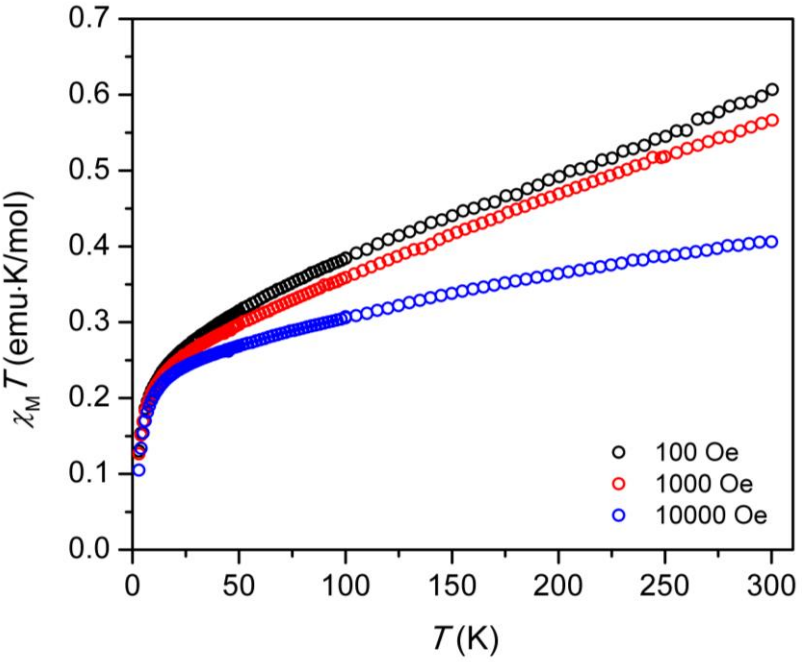

Figure S2.12. Variable-temperature magnetic susceptibility times temperature ($\chi_M T$ versus T) data for $Fe(tri)_2(BF_4)_{0.33}$ collected under variable applied dc fields.

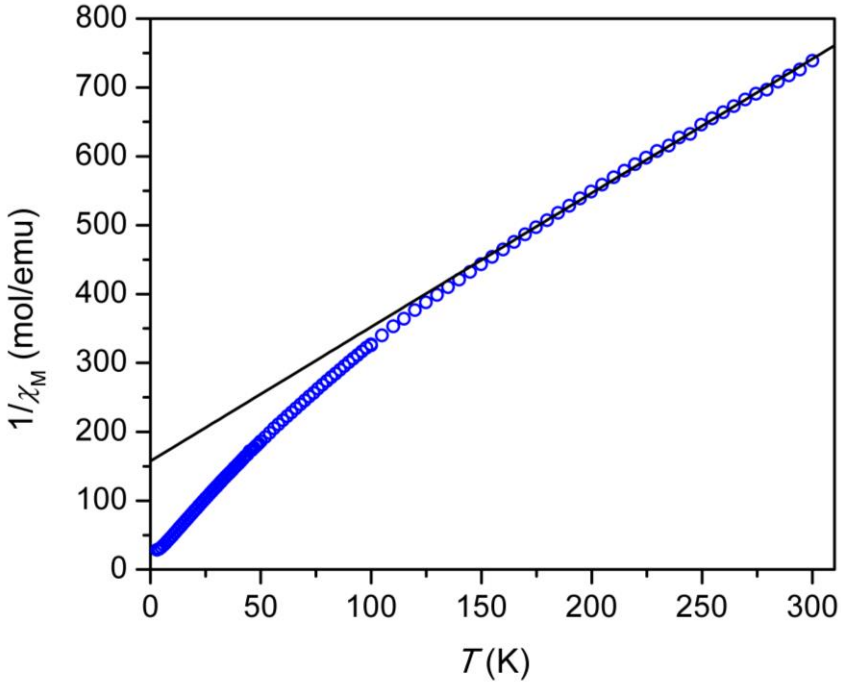

Figure S2.13. Variable-temperature magnetic susceptibility (χ_M) data for $Fe(tri)_2(BF_4)_{0.33}$ collected under the applied dc field of 10000 Oe. Data plotted as $1/\chi_M$ versus temperature. Curie-Weiss fit to the data between 300 and 150 K is shown by a black solid line, with fitting parameters described in the main text.

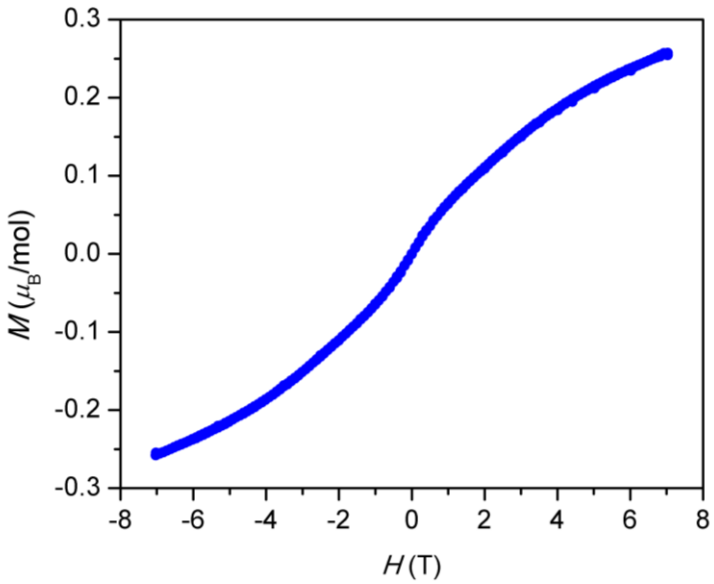

Figure S2.14. Variable-field magnetization for $Fe(tri)_2(BF_4)_{0.33}$ obtained at 3 K.

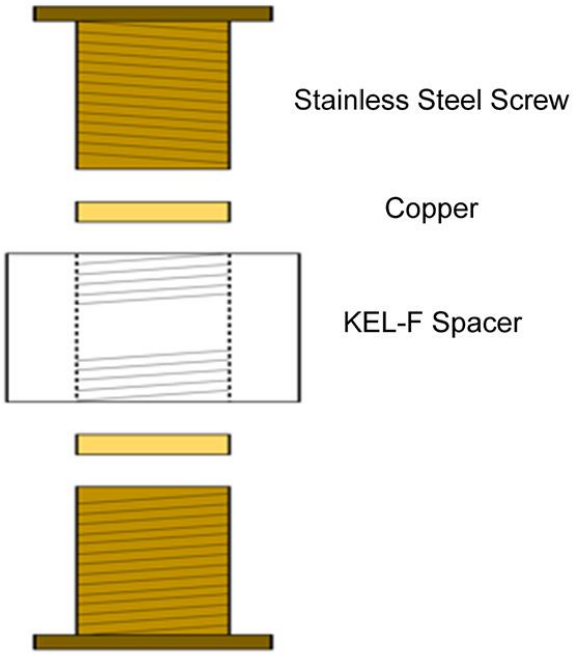

Figure S2.15. Laboratory-constructed two-point conductivity measurement apparatus.

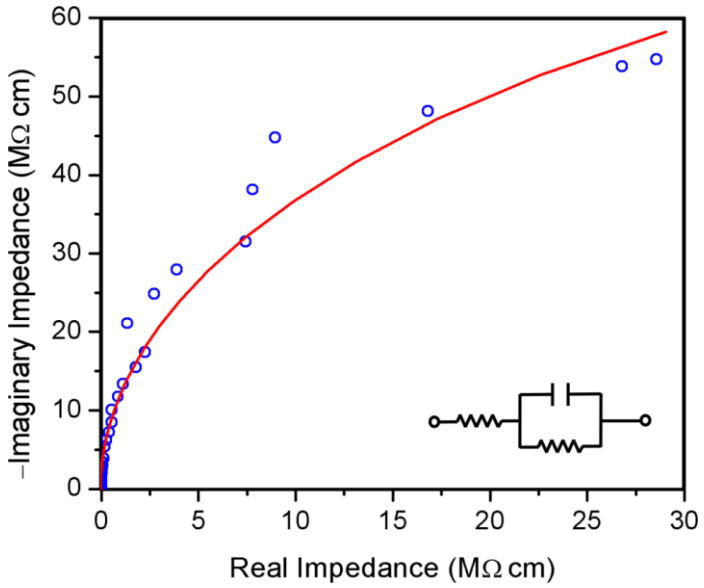

Figure S2.16. Nyquist plot of Fe(tri)$_2$ (blue) and the fit obtained using a model circuit (red). The model circuit assumes that electrons are the only type of mobile species. The deviations observed are due to the instrumental uncertainties at low frequencies.

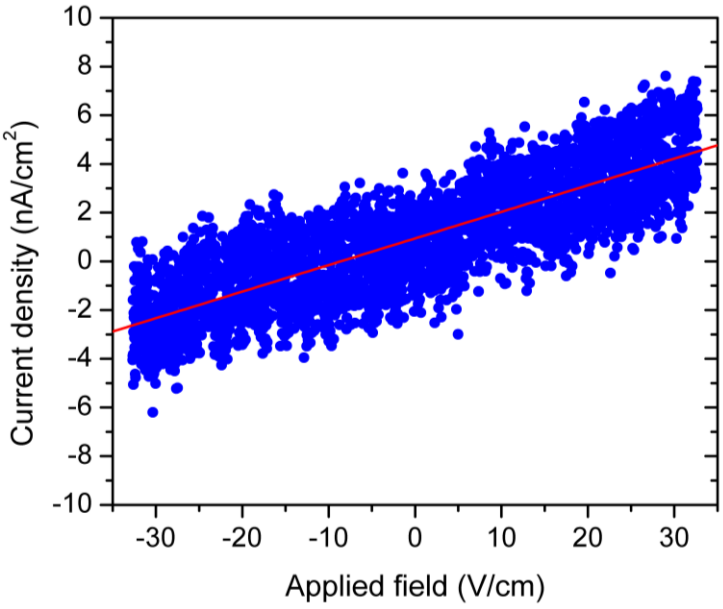

Figure S2.17. Cyclic voltammogram of Fe(tri)$_2$ (blue) and the linear fit (red).

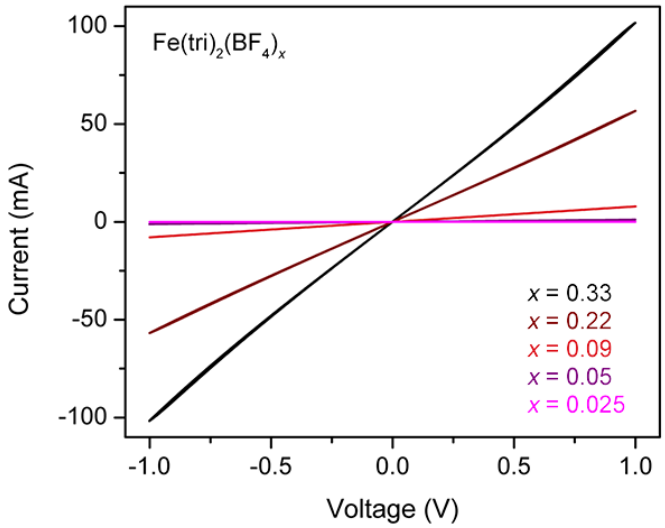

Figure S2.18. *I-V* plots of $Fe(tri)_2(BF_4)_x$ displaying Ohmic response between ±1 V measured at room temperature.

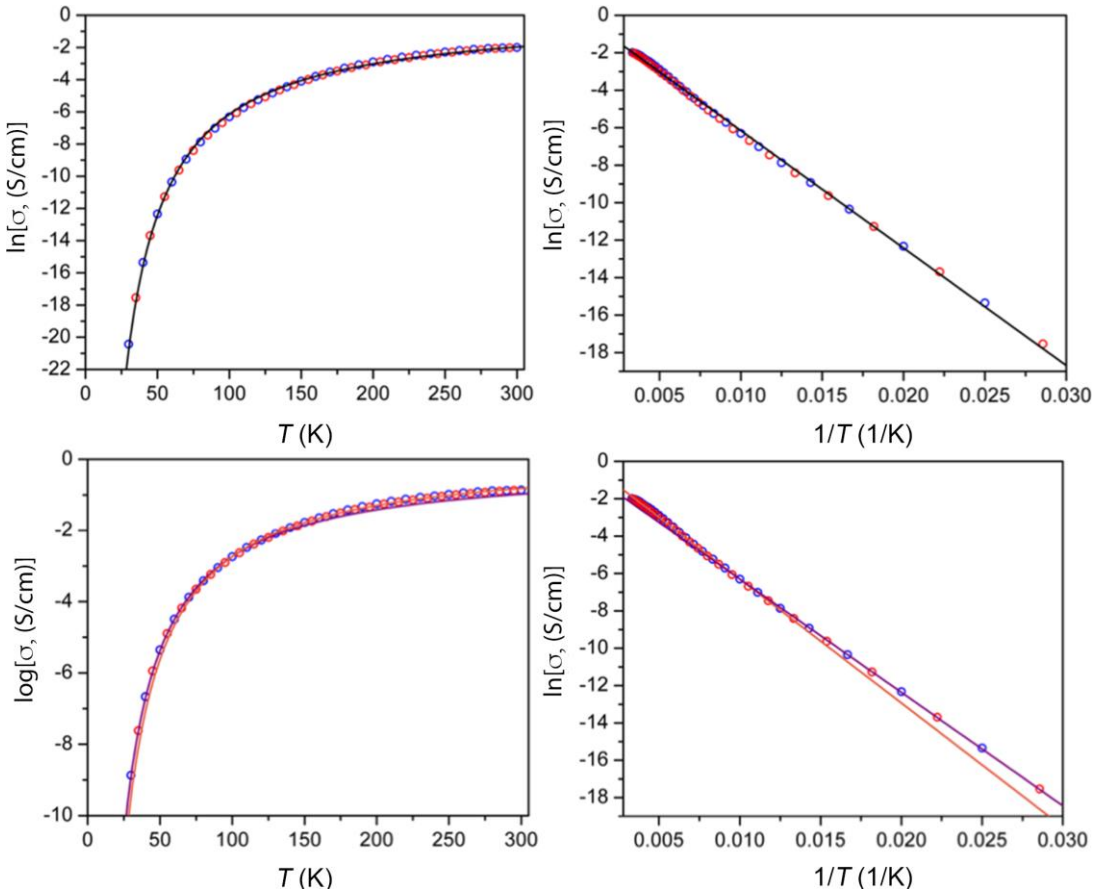

Figure S2.19. Temperature dependence of the conductivity of $Fe(tri)_2(BF_4)_{0.33}$. Blue and red circles represent cooling and warming, respectively. Upper plots correspond to Arrhenius fits of the data from 30 to 300 K and lower plots correspond to fits from 90 to 300 K (orange line) and from 30 to 90 K (purple line).

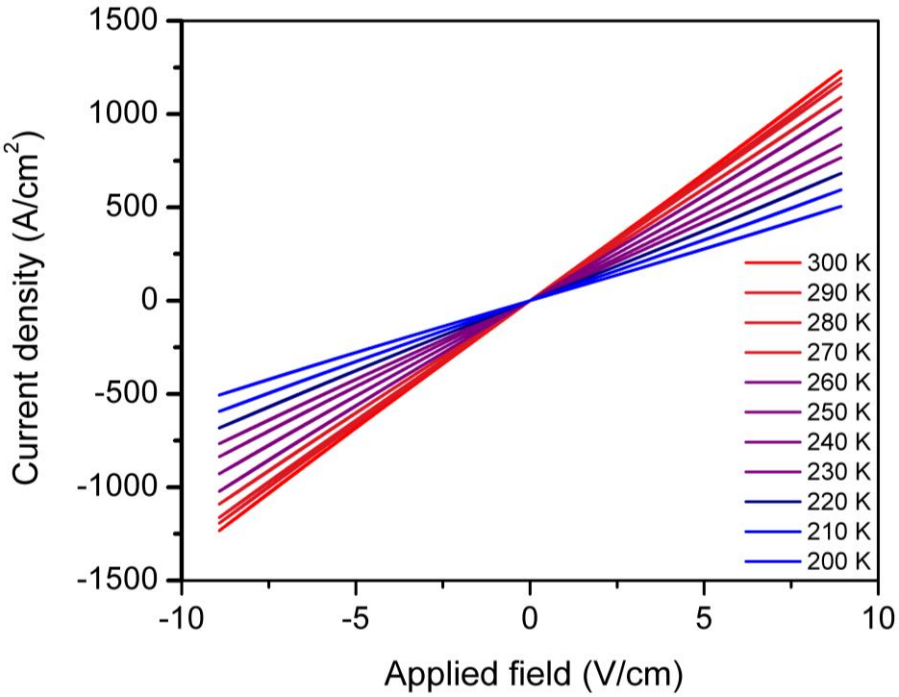

Figure S2.20. Variable temperature *I-V* plots of $Fe(tri)_2(BF_4)_{0.33}$ displaying Ohmic response between ±10 V/cm for selected temperatures. Similar linear behaviors were observed for all investigated temperatures.

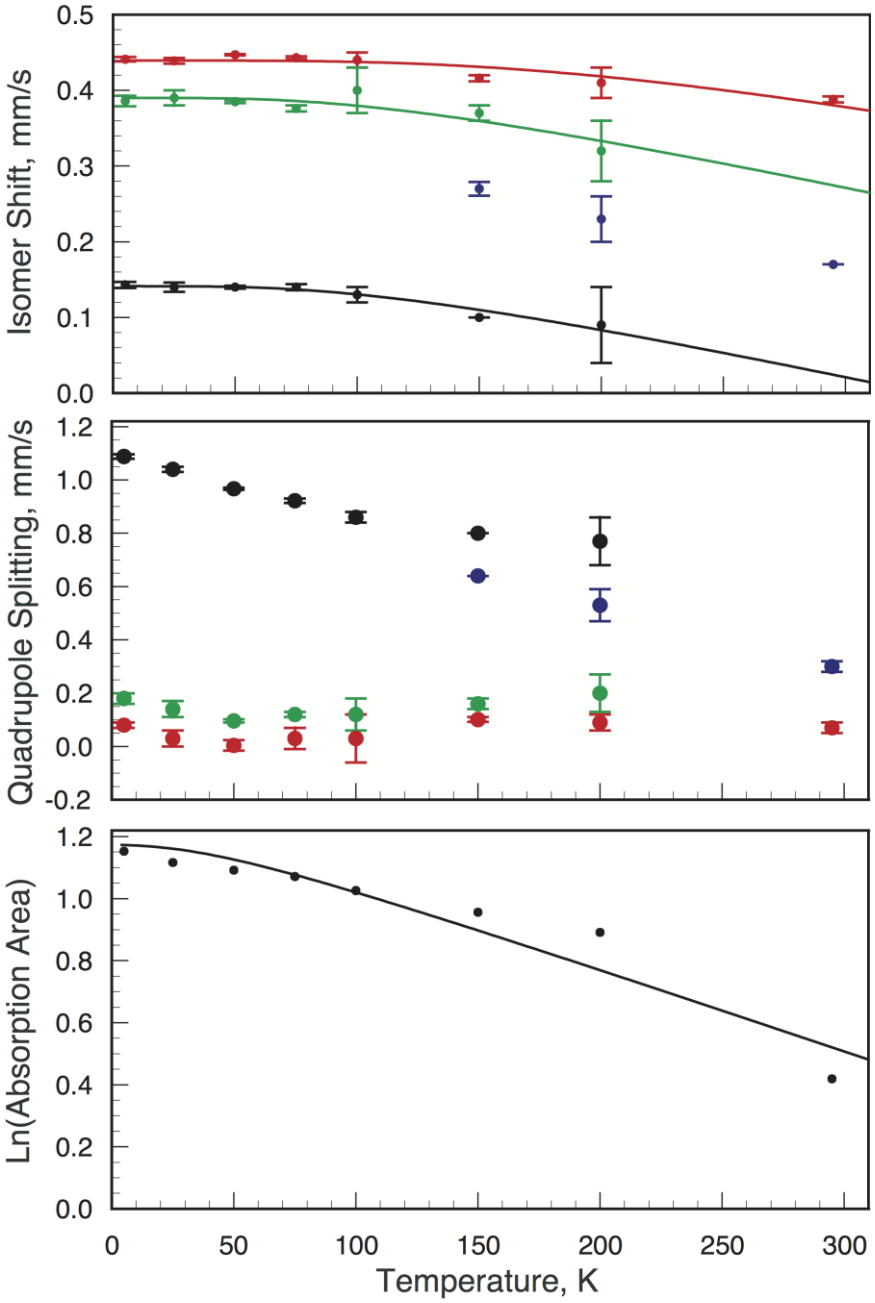

Figure S2.21. Temperature dependence of the Mössbauer spectral parameters of $Fe(tri)_2(BF_4)_{0.22}$.

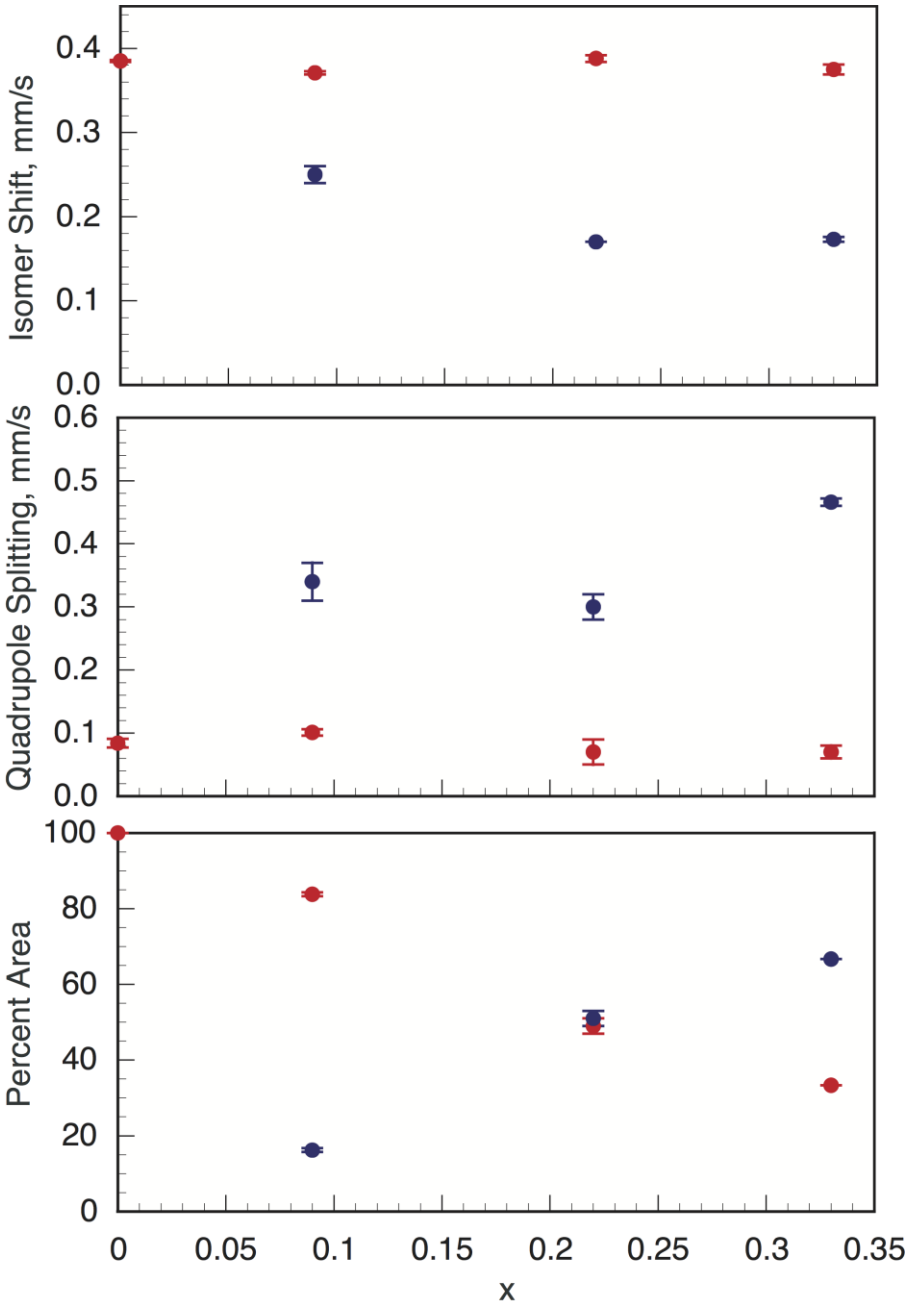

Figure S2.22. Compositional dependence of the 290 K Mössbauer spectral parameters of $Fe(tri)_2(BF_4)_x$.

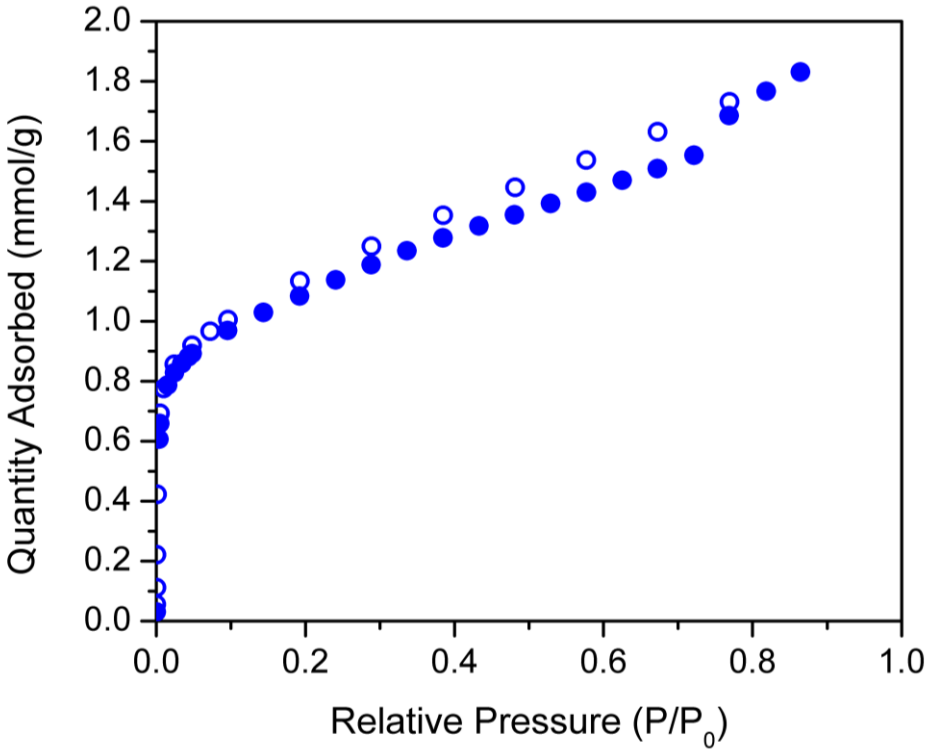

Figure S2.23. CO_2 adsorption isotherm of $Fe(tri)_2(BF_4)_{0.22}$ at 195 K. Closed and open data points represent adsorption and desorption, respectively.

S2.2 References for Chapter 2 Supporting Information

(1) Gándara, F.; Uribe-Romo, F. J.; Britt, D. K.; Furukawa, H.; Lei, L.; Cheng, R.; Duan, X.; O'Keeffe, M.; Yaghi, O. M. Porous, Conductive Metal-Triazolates and Their Structural Elucidation by the Charge-Flipping Method. *Chem. Eur. J.* **2012**, *18*, 10595.
(2) Coelho, A. Indexing of Powder Diffraction Patterns by Iterative Use of Singular Value Decomposition. *Appl. Cryst.* **2003**, *36*, 86.
(3) Coelho, A. TOPAS-Academic, Version 4.1, Coelho Software, Brisbane, 2007.
(4) Zhou, X.; Peng, Y.; Du, X.; Zuo, J.; You, X. Hydrothermal Syntheses and Structures of Three Novel Coordination Polymers Assembled from 1,2,3-Triazolate Ligands. *Cryst. Eng. Comm.* **2009**, *11*, 1964.
(5) Walton, K. S.; Snurr, R. Q. Applicability of the BET Method for Determining Surface Areas of Microporous Metal-Organic Frameworks. *J. Am. Chem. Soc.* **2007**, *129*, 8552.
(6) Willems, T. F.; Rycroft, C. H.; Kazi, M.; Meza, J. C.; Haranczyk, M. Algorithms and Tools for High-Throughput Geometry-Based Analysis of Crystalline Porous Materials. *Micro. Meso. Mater.* **2012**, *149*, 134.
(7) Ingalls, R. Electric-Field Gradient Tensor in Ferrous Compounds. *Phys. Rev.* **1964**, *133*, A787.
(8) Shenoy, G. K.; Wagner, F. E.; Kalvius, G. M. *Mössbauer Isomer Shifts*; Shenoy, G. K.; Wagner, F. E. Ed.; North-Holland: Amsterdam, the Netherlands, **1978**, 49.
(9) Owen, T.; Grandjean, F.; Long, G. J.; Domasevitch, K. V.; Gerasimchuk, N. Synthesis and Characterization of Two Intensely Colored Tris(benzoylcyanoxime)iron(II) Anionic Complexes. *Inorg. Chem.* **2008**, *47*, 8704.
(10) Aubrey, M. L.; Wiers, B. M.; Andrews, S. C.; Sakurai, T.; Reyes-Lillo, S. E.; Hamed, S. M.; Yu, C.-J. Y.; Darago, L. E.; Mason, J. A.; Baeg, J.-O.; Grandjean, F.; Long, G. J.; Seki, S.; Neaton, J. B.; Yang, P.; Long, J. R. Electron Delocalization and Charge Mobility as a Function of Reduction in a Metal-Organic Framework. *Nat. Mater.* [Online early access]. DOI: 10.1038/s41563-018-0098-1. Published Online: June 4, 2018.
(11) (a) Roth, S.; Bleier, H.; Pukachi, W. Charge Transport in Conducting Polymers. *Faraday Discuss. Chem. Soc.* **1989**, 88, 223. (b) Roth, S. *Hopping Transport in Solids*; Pollak, M. Ed.; Elsevier: Amsterdam, **1991**, *3*, 517.

Chapter 3: Tuning Spin Crossover in a Three-Dimensional Metal–Organic Framework via Linker Functionalization

3.1 Introduction

The ability to manipulate electronic structure through synthesis is of fundamental importance for the development of new multifunctional materials. Spin-crossover compounds have attracted much research interest in this regard, owing to proposed applications in spintronics and information storage, as well as in sensors and displays.[1-6] Broadly speaking, these compounds feature octahedral $3d^4$–$3d^7$ metal centers that undergo interconversion from a low-spin to a high-spin electronic state in response to external stimuli, such as temperature, pressure, or light—a conversion accompanied by changes in crystallographic, optical, electronic, and magnetic properties. Importantly, the spin-crossover phenomenon can become cooperative when there is suitable communication between metal centers, giving rise to an abrupt spin transition and, in a number of cases, a pronounced thermal hysteresis.[2,7-14] Initial studies of this thermal memory effect focused on molecular compounds wherein cooperativity is induced by elastic intermolecular interactions,[1,9,15,16] although theoretical and experimental efforts have expanded to include one-, two- and three-dimensional coordination solids,[8,17-19] which can exhibit enhanced cooperativity arising from multiple bridging metal centers in close proximity. For example, one-dimensional iron(II) triazolate chains have been shown to exhibit spin crossover above 300 K with a thermal hysteresis on the order of ~10 K.[8,18-20]

Coordination solids with higher dimensionality can exhibit further enhanced cooperativity and desirable spin-crossover properties. Three-dimensional (3D) systems in particular can support a high concentration of bridging metal centers and provide a relatively rigid matrix that minimizes or even obviates factors responsible for the large variability in the spin-crossover properties in lower dimensional systems, such as sample aging and solvent loss.[13,21-25] A number of 3D solids have been discovered to date that exhibit cooperative spin crossover near or above room-temperature and, in some cases, a large thermal hysteresis with a ΔT as high as 95 K.[17,18,26-35] Many of these systems exhibit guest molecule dependent properties and, as such, are potentially promising for applications as sensors.[17,29-35] However, the same materials are not ideal for applications that require reproducible, consistent spin crossover over a large number of working cycles, such as in displays or switching. Additionally, despite the many conceivable advantages offered by 3D spin-crossover materials, the vast majority of studies to date have focused on Hofmann-type solids of the form $\{Fe(L)_n[M(CN)_4]\}$.[17,18,33-35] The pursuit of novel 3D structure types, for instance featuring all organic bridges, may enable more fine-tuning of the electronic structure and spin-crossover properties.

Metal–organic frameworks (MOFs) are a family of 3D coordination solids that are particularly appealing for the study of the spin-crossover phenomenon. Indeed, MOFs can be prepared using numerous combinations of metal cations and polytopic organic linkers,[36] and their diverse chemical and electronic structures can be further modified via metal or ligand substitution[37-39] and post-synthetic redox chemistry.[40-42] Recently, the framework $Fe(Tri)_2$ (Tri^- = 1,2,3-triazolate)[43,44] was reported to exhibit a spin transition upon warming to around 570 K with an unprecedentedly large thermal hysteresis of $\Delta T \approx 110$ K,[45] highlighting that systems featuring only organic linkers can exhibit even stronger cooperativity than has typically been accessible in Hofmann-type compounds.[35] Herein, we show that simple substitution of the linker in $Fe(Tri)_2$ with 4-methyl-1,2,3-triazolate ($MeTri^-$) affords another example of a MOF exhibiting spin crossover near room temperature, as characterized using *in situ* synchrotron powder X-ray diffraction, optical and Mössbauer spectroscopies, and magnetic susceptibility measurements.

However, cooperativity in $Fe(MeTri)_2$ is substantially diminished, likely the result of steric interactions between methyl groups within the pores of the material.

3.2 Experimental Information

General Considerations. Unless otherwise noted, all manipulations were carried out in an argon atmosphere in an Mbraun MB200MOD glovebox. Glassware was oven-dried at 150 °C for at least 4 h and allowed to cool in an evacuated glovebox antechamber prior to use. *N*,*N*-dimethylformamide (DMF) was dried using a commercial solvent purification system made by JC Meyer Solvent Systems and stored over 3- or 4-Å molecular sieves prior to use. Anhydrous methanol was purchased from EMD Millipore Corporation, sparged with argon and stored over 3-Å molecular sieves prior to use. Anhydrous $FeCl_2$ beads (99.9% purity) were purchased from Sigma-Aldrich. The 4-methyl-1H-1,2,3-triazole ligand (95% purity) was purchased from Enamine ltd, diluted with anhydrous DMF, deoxygenated with three freeze-pump-thaw cycles, and stored over 4-Å molecular sieves prior to use. Carbon, hydrogen, and nitrogen elemental analyses were obtained from the Microanalytical Laboratory at the University of California, Berkeley.

Synthesis of Fe(4-methyl-1,2,3-triazolate)$_2$. To a 20 mL glass scintillation vial containing a solution of $FeCl_2$ (0.256 g, 2.02 mmol) in DMF (5 mL) was added a solution of 4-methyl-1H-1,2,3-triazole (0.503 g, 6.05 mmol) in DMF (5 mL). The vial was sealed with a polytetrafluoroethylene-lined cap and heated at 120 °C for 3 d. The resulting suspension was cooled to 25 °C and filtered with a Nylon membrane filter to yield a light-yellow powder. The powder was washed by soaking in DMF (3 × 15 mL) and then in methanol (4 × 15 mL), and was then dried under dynamic vacuum (<10 μbar) at 130 °C for 48 h to yield 0.257 g (58%) of product as a light yellow powder. Anal. Calcd for $FeC_6H_8N_6$: C, 32.75; H, 3.67; N, 38.20. Found: C, 32.38; H, 3.37; N, 38.07.

Powder X-ray Diffraction Data Collection and Structure Refinement. High-resolution X-ray powder diffraction data was collected on desolvated microcrystals of $Fe(MeTri)_2$ at Beamline 17-BM-B at the Advanced Photon Source (APS) at Argonne National Laboratory. Diffraction patterns were collected between 350 and 100 K with a wavelength of 0.45212 Å. The previously reported crystal structure of the isostructural $Fe(Tri)_2$[44] was used as the initial structural model for the Rietveld refinements of $Fe(MeTri)_2$. Prior to the refinement, accurate unit cell parameters were obtained by Pawley refinement implemented in TOPAS-Academic.[46] During the refinement of the $Fe(MeTri)_2$ diffraction patterns, difference Fourier maps were generated. Positive electron densities were observed in the pores, and a carbon was placed at the corresponding coordinate of the observed electron densities. The chemical occupancy of the carbon was initially allowed to freely refine and was close to 0.5 and was fixed as 0.5 in the subsequent refinements. Hydrogen atoms were placed on calculated positions, assuming a fixed aromatic C–H distance of 1.09 Å. In the final stage of the refinements, all atomic positions (with the exception of special positions and the coordinates of the hydrogen) and thermal and unit cell parameters were fully refined and convoluted with the sample and instrument parameters and Chebyshev background polynomials. Calculated diffraction patterns for the final structural models of $Fe(MeTri)_2$ at 350 and 100 K are in excellent agreement with the experimental diffraction patterns (Figures S3.3 and S3.4, Table S3.1).

For the diffraction patterns collected between 230 and 270 K, in which two distinct phases were observed, multiphase Rietveld analyses were performed by using structural models for the

low- and high-temperature phases at 100 and 350 K, respectively. The analysis enabled determination of percent compositions of the two structural phases (see Figure 3.4). Parameters obtained from Rietveld refinement of the data collected at 350 and 100 K are given in Table S3.1 of the Supporting Information.

Fe(MeTri)$_2$ Surface Area Measurement and Calculation. In an N_2-filled glovebox, a sample was transferred to a pre-weighed analysis tube and capped with a Transeal. The sample was then transferred to a Micromeritics Smart VacPrep instrument, evacuated, and heated to 130 °C at 5 °C/min for 3 d, at which the pressure was stabilized at 1.3 μbar. A N_2 adsorption isotherm at 77 K was measured using UHP-grade gas (Figure S3.7). For the determination of surface area, Langmuir and BET methods were applied using the adsorption branch of the N_2 isotherm, assuming a N_2 cross-sectional area of 16.2 Å^2/molecule; the BET area was calculated in the pressure range with values of $v(P_0-P)$ increasing with P/P_0, according to the method reported by Snurr.[47]

The theoretical surface area of Fe(MeTri)$_2$ was calculated using the open-source software Zeo++ version 0.32[48] accessible through Lawrence Berkeley Laboratory. The structure of Fe(MeTri)$_2$ determined from the Rietveld refinement of the high-resolution powder X-ray diffraction data collected at 350 K exhibits disordered methyl substituents. In an effort to obtain a more realistic crystal structure that better depicts the actual pore structure of Fe(MeTri)$_2$, Materials Studio[49] was used to lower the space group from $Fd\bar{3}$m to $P2_13$, methyl substituents originating from disorder were removed from the asymmetric unit, and hydrogen atoms were added to expected positions. The obtained model structure (Figure S3.8) was used for the theoretical surface area calculation. A probe of radius of 1.2 Å was used to calculate the accessible surface area (Table S3.2). The non-accessible surface area corresponds to the surface area inside inaccessible pockets.

Optical Measurements. Surface reflectivity measurements were performed with a home-built system at the Centre de Recherche Paul Pascal, operating between 10 and 300 K and in a spectrometric range from 400 to 1000 nm. A halogen-tungsten light source (Leica CLS 150 XD tungsten halogen source adjustable from 0.05 mW cm^{-2} to 1 W cm^{-2}) was used as the spectroscopic light. The measurements were calibrated using barium sulfate as a reference sample. The light exposure time was minimized during the experiments keeping the samples in the dark except during the spectra measurements when white light is shined on the sample surface (0.5 mW cm^{-2}). Heating and cooling measurements were carried out at 9 K min^{-1}. Light emitting diodes from Thorlabs operating between 365 and 1050 nm were used for excitation experiments.

Magnetic Measurements. A sample was prepared by adding microcrystalline powder of desolvated Fe(MeTri)$_2$ (12.4 mg) to a 5 mm inner diameter quartz tube containing a raised quartz platform. The sample powder was restrained with a plug of compacted glass wool to prevent crystallite torqueing during measurements. The quartz tube was transferred to a Schlenk line and evacuated until the internal pressure reached 30 mTorr. The tube was then cooled in liquid N_2 and flame-sealed under static vacuum. All magnetic measurements were performed using a Quantum Design MPMS2 SQUID magnetometer from 15 to 320 K using a dc magnetic field of 0.1 T with selected cooling/warming rates between 0.4 and 10 K/min. For sweep rates of 0.4 K/min and above 1 K/min, settle mode and sweep mode in RSO mode were used for temperature variation, respectively. A diamagnetic correction of $\chi_D = -0.00010154$ emu/mol obtained by using Pascal's constants was applied to the molar magnetic susceptibility. Variable temperature magnetic susceptibility data were collected with sweep rates of 1, 5, and 10 K/min using sweep mode and resulted in the temperature lags of 0.4, 4, and 7 K, respectively, as a result of the sample temperature failing to equilibrate with the SQUID chamber temperature. The data were corrected

for the temperature lag using a reported procedure,[50] which removed the artificial scan rate dependent thermal hysteresis (see the Supporting Information for details and Figure S3.12).

Mössbauer Spectroscopy. Zero-field iron-57 Mössbauer spectra were collected for $Fe(MeTri)_2$ using a constant acceleration SEE Co. spectrometer, between 5 and 295 K using a Janis Research Co. cryostat. Prior to the measurement, the spectrometer was calibrated at 295 K with α-iron foil, which also served as reference for the isomer shift. A sample of desolvated, microcrystalline $Fe(MeTri)_2$ was gently ground and mixed homogenously with boron nitride for dilution of the iron concentration to 2 wt%. Approximately 50 mg or 39.5 mg/cm^2 of the resulting powder mixture was placed in a nylon washer and sealed between multiple layers of commercially available Scotch tape under an inert atmosphere, prior to transfer in air into the cryostat of the spectrometer, to avoid oxidation of the air-sensitive $Fe(MeTri)_2$. After the transfer, the absorber was under the He atmosphere of the cryostat. The Mössbauer spectra were fit with a sum of symmetric Lorentzian doublets by using a locally developed program that utilized the Marquardt minimization code. This code was used to generate the statistical uncertainties of any fit parameters as well as their correlation coefficients. The spectral parameters are reported in Table S3.3.

Other Physical Measurements. Thermogravimetric analysis was performed on a Discovery TGA Series from TA Instruments in a flow of dinitrogen at a heating rate of 1.5 °C/min between 25 and 600 °C. A sample powder was transferred to a pre-weighed pan in an argon glovebox. The pan containing the sample was kept inside a sealed vial and taken out of the glovebox. Prior to starting a measurement, the pan containing a sample was quickly transferred to the TGA instrument. Scanning electron microscopy (SEM) images were obtained using a Hitachi S-5000 instrument at 10 keV and 4 nA. The SEM sample was prepared by dispersing a powder microcrystalline sample of $Fe(MeTri)_2$ in dichloromethane followed by drop casting onto a silicon wafer. Infrared spectra were collected on microcrystalline powdered $Fe(MeTri)_2$ using a Perkin Elmer Spectrum FT-IR/FT-FIR spectrometer with an attenuated total reflectance accessory with a home-built N_2 glove bag attachment for air-sensitive compounds.

3.3 Results and Discussion

The material $Fe(MeTri)_2$ was prepared using a modification of the procedure for $Fe(Tri)_2$,[44] by heating a solution of $FeCl_2$ and MeTriH in *N*,*N*-dimethylformamide under an Ar atmosphere. $Fe(MeTri)_2$ was obtained as a microcrystalline yellow powder that is thermally stable up to ~400 °C (Figure S3.1) and consists of heterodisperse, octahedron-shaped crystals less than 0.2 μm in size (Figure S3.2). Elemental analysis data obtained for the desolvated microcrystalline powder is consistent with the formula $Fe(MeTri)_2$. Interestingly, immersing $Fe(MeTri)_2$ in liquid N_2 at 77 K results in a color change from light yellow to orange, potentially indicative of a thermally induced spin-crossover phenomenon.

Powder X-ray Diffraction. *In situ* synchrotron powder X-ray diffraction data were collected on desolvated microcrystals of $Fe(MeTri)_2$ at temperatures ranging from 350 to 100 K (Figure 3.1a). Rietveld refinement of the data obtained at 350 K (Table S3.1 and Figure S3.3) revealed that $Fe(MeTri)_2$ crystallizes in the cubic $Fd\bar{3}m$ space group (no. 227) with a lattice parameter of a = 17.4618(6) Å and a structure analogous to other reported $M(Tri)_2$ (M = Mg, Mn, Fe, Co, Cu, and Zn) compounds.[43-45,51,52] This lattice parameter is significantly larger than that determined for desolvated $Fe(Tri)_2$ at 300 K (a = 16.65075(17) Å),[44] which features low-spin Fe^{II} ions, and is similar to the value reported for the high-spin $Fe(Tri)_2$ phase above 560 K (a = 17.7566(4) Å).[43] Diffraction patterns collected for $Fe(MeTri)_2$ between 350 and 272 K are

indistinguishable, but between 250 and 268 K, the patterns feature additional peaks that coexist with those at higher temperatures, indicative of a structural phase transition. Below 250 K, only the diffraction peaks corresponding to the low-temperature phase persist. Rietveld refinement of data obtained at 100 K (Figure S3.4) revealed that this low-temperature phase adopts the same cubic space group, although with a smaller lattice parameter of a = 16.7790(6) Å (Figure S3.5) that is consistent with that determined for the low-spin Fe(Tri)$_2$ phase.

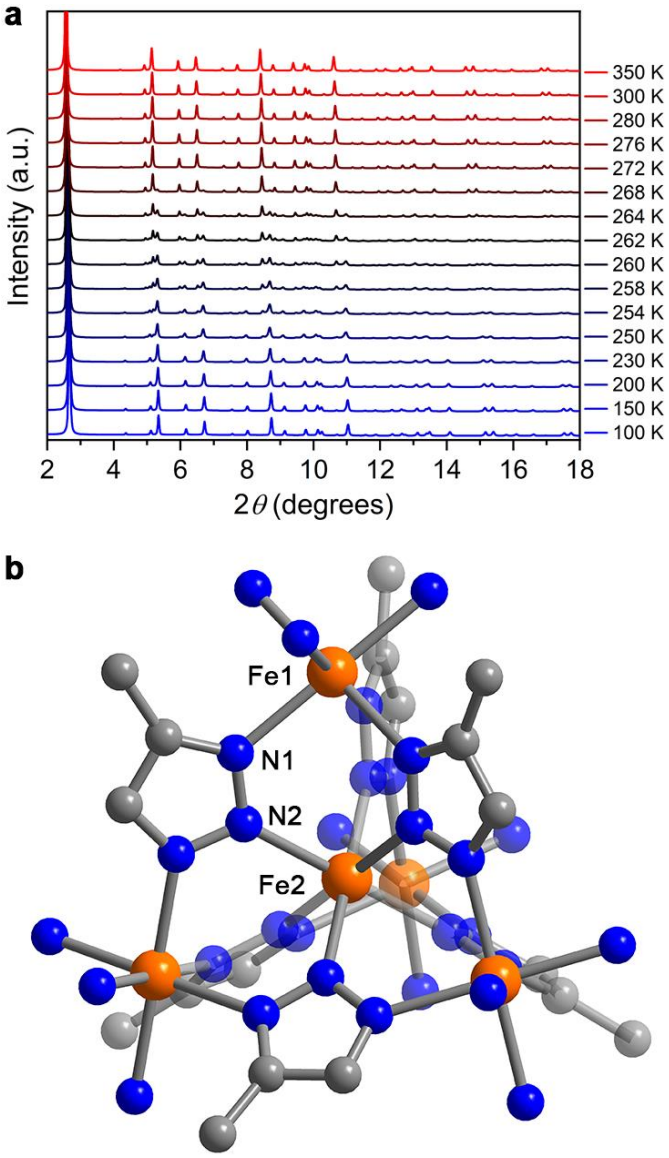

Figure 3.1. X-ray diffraction studies. (a) Temperature-dependent *in situ* synchrotron powder X-ray diffraction patterns for Fe(MeTri)$_2$. (b) The tetrahedral repeat unit of Fe(MeTri)$_2$ at 350 K as determined from Rietveld refinement of the powder X-ray diffraction data. Orange, blue, and grey spheres represent Fe, N, and C atoms, respectively; H atoms have been omitted for clarity.

At 350 K, desolvated Fe(MeTri)$_2$ adopts a diamondoid-type structure built up of pentanuclear, tetrahedral repeat units (Figure 3.1b). Each unit consists of four crystallographically equivalent, corner-sharing Fe^{II} ions (hereafter, Fe1) bridged to a central Fe^{II} ion (hereafter, Fe2)

by six 4-methyl-1,2,3-triazolate linkers. The Fe1–N1 and Fe2–N2 bond distances are 2.176(3) and 2.200(4) Å, respectively, consistent with high-spin Fe^{II} [12,18] and similar to those reported for the high-spin phase of $Fe(Tri)_2$ (Fe1–N1 and Fe2–N2 distances of 2.16(1) and 2.19(2) Å, respectively).[43] Thus, while the ligand field afforded by the Tri^- linker is sufficiently strong to stabilize the low-spin phase of $Fe(Tri)_2$ at room temperature, increased sterics in $Fe(MeTri)_2$ due to the methyl substituents likely favor longer metal–linker bond distances and a high-spin Fe^{II} configuration at a comparable temperature. The methyl substituents on the triazolate linkers are disordered over two positions, each with half occupancy, and a total of six methyl groups point into a single pore (Figure S3.6). While the methyl groups are disordered in the bulk, it is possible that they are ordered within the pores. As a result of the methyl substituents pointing into the cavities of $Fe(MeTri)_2$, the material lacks permanent porosity and has a BET surface area of only 70 m^2/g, as determined from N_2 adsorption data obtained at 77 K (Figure S3.7). In contrast, $Fe(Tri)_2$ exhibits a BET surface area of 370 m^2/g.[44,45] The calculated accessible surface area for $Fe(MeTri)_2$ also supports the lack of permanent porosity (see Table S3.2 and Figure S3.8).

At 100 K, the structure of desolvated $Fe(MeTri)_2$ (Figure S3.9) features Fe1–N1 and Fe2–N2 distances of 2.030(3) and 2.028(4) Å, respectively, consistent with an $^1A_{1g}$ low-spin state for both Fe^{II} sites.[12,18] These distances are shorter than those in the 350 K structure by 0.15–0.17 Å, consistent with bond distance changes observed in other spin-crossover materials.[11,12] Overall, the diffraction data indicate that the phase transition that occurs in $Fe(MeTri)_2$ is driven by a collective spin-crossover phenomenon, albeit at a much lower temperature than characterized for $Fe(Tri)_2$ (between ~250 and 268 K versus >560 K, respectively).[43] The Fe–N distances in $Fe(MeTri)_2$ at 100 K are larger than those for the low-spin structure of $Fe(Tri)_2$ (1.961(2) and 1.977(3) Å[44]), suggesting that the spin crossover in $Fe(MeTri)_2$ is incomplete and that some high-spin Fe^{II} ions remain trapped at 100 K, an observation supported by results from magnetic and Mössbauer experiments (see below).

Optical Spectroscopy. Variable-temperature surface reflectivity spectra collected from 400 to 1000 nm (Figure S3.10) further support spin crossover in $Fe(MeTri)_2$. Upon cooling from 270 to 10 K, the reflectivity gradually decreases between 500 and 1000 nm, and particularly around 560 nm. This change, representing an increase in absorption at these wavelengths, corresponds to the $^1A_{1g}$ to $^1T_{1g}$ d–d spin-allowed electronic transition typical for low-spin Fe^{II} ions. This reversible change is most prominent between 270 and 180 K, corresponding to the temperature range in which the structural phase transition and spin crossover are evident in the powder X-ray diffraction data.

Magnetic Measurements. Variable-temperature dc magnetic susceptibility data were collected for desolvated $Fe(MeTri)_2$ upon warming from 15 to 320 K under a dc field of 0.1 T. The data are plotted in Figure 3.2 (red symbols) as $\chi_M T$ versus T, where χ_M is the molar magnetic susceptibility. At 320 K, the magnitude of $\chi_M T$ is 3.14 emu K/mol, which is consistent with the presence of high-spin $S = 2$ Fe^{II} ions with $g = 2.05$. Below ~285 K, the magnitude of $\chi_M T$ decreases sharply until it reaches a value of 1.23 emu K/mol at ~250 K. This decrease is characteristic of a spin crossover and consistent with the onset of the phase change observed over a similar temperature range in the powder X-ray diffraction patterns. In contrast, magnetic susceptibility data obtained for $Fe(Tri)_2$ upon warming revealed spin crossover at approximately 570 K.[43] These results highlight the power of simple linker functionalization for fine-tuning the properties of metal–organic frameworks for applications near ambient temperature. Below 250 K, the $\chi_M T$ value for $Fe(MeTri)_2$ decreases gradually with decreasing temperature down to ~40 K, suggesting that spin crossover is not complete and that residual Fe^{II} ions remain thermally or structurally trapped

in the high-spin state. Below ~40 K, the slight downturn in $\chi_M T$ is most likely due to zero-field splitting or weak antiferromagnetic interactions between the remaining high-spin Fe^{II} ions. Similarly, the $\chi_M T$ value at 320 K is clearly not saturated, suggesting that some Fe^{II} ions remain trapped in the low-spin state. Fits to the magnetic susceptibility data obtained at a scan rate of 0.4 K/min (see Figures S3.11–S3.12 and the Supporting Information for details) and Mössbauer spectra (see below) support an incomplete spin crossover.

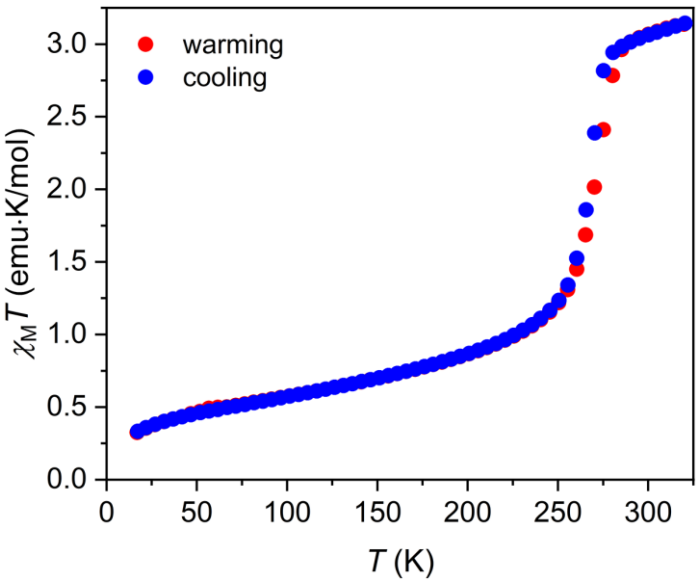

Figure 3.2. Magnetic measurements. Temperature-dependent dc magnetic susceptibility data for $Fe(MeTri)_2$ collected under a field of 0.1 T upon warming from 15 to 320 K (red symbols) and subsequently cooling from 320 to 15 K (blue symbols). Both sets of data were collected using a scan rate of 1 K/min with sweep mode. See Figure S3.11 for data collected using a scan rate of 0.4 K/min with settle mode.

Magnetic susceptibility data collected upon cooling $Fe(MeTri)_2$ from 320 K after initial warming (Figure 3.2, blue circles) revealed a small hysteresis with $\Delta T \approx 4(1)$ K (see the Experimental Section). The hysteresis occurs within a relatively narrow temperature range between 285 and 250 K, and these results, together with the structural phase transition characterized via powder X-ray diffraction, suggest a cooperative spin crossover in $Fe(MeTri)_2$.[50] However, the thermal hysteresis loop is quite narrow compared to that reported for $Fe(Tri)_2$ ($\Delta T \approx$ 110 K), suggesting that the cooperativity is much weaker in $Fe(MeTri)_2$.[2,11,12,14,50] This reduced cooperativity is also supported by the incomplete low-spin to high-spin conversion in this system. One explanation for the weaker cooperativity is that steric interactions between the methyl groups in the framework cavities prevent facile framework expansion and contraction during spin-crossover. Indeed, this observation may be supported by the smaller lattice parameter for the high-temperature phase of $Fe(MeTri)_2$ relative to that for $Fe(Tri)_2$, and further physical and structural studies are necessary to fully understand this difference.

Mössbauer Spectroscopy. ^{57}Fe Mössbauer spectra were collected for desolvated $Fe(MeTri)_2$ at several temperatures ranging from 5 to 295 K to more directly probe the change in the electronic configuration of the Fe^{II} ions with temperature (see Figures 3.3 and S3.14 and the Supporting Information for details). Mössbauer spectra collected at 5 and 295 K are dramatically different. At 5 K, the major absorption is localized at ~0.5 mm/s, an isomer shift that is

characteristic of low-spin Fe^{II}. A minor spectral absorption also occurs at −0.5 and 2.5 mm/s. At 295 K, the low-spin Fe^{II} feature persists and two new major spectral absorptions are present, the first at approximately −0.5 and +2.5 mm/s and the second at 0.7 and 1.3 mm/s, both with isomer shifts of ~1.0 mm/s that are characteristic of high-spin Fe^{II}. Thus, as the temperature increases from 5 to 295 K, it is apparent that a large fraction of the Fe^{II} ions in $Fe(MeTri)_2$ undergo a spin-state change from the low-spin $^1A_{1g}$ to the high-spin $^5T_{2g}$ state. The presence of two quadrupole doublets for high-spin Fe^{II} (and low-spin Fe^{II}, see below) is consistent with the presence of two crystallographically inequivalent Fe^{II} sites in the structure of $Fe(MeTri)_2$, as characterized via powder X-ray diffraction. The major absorption at 5 K with 87.7(2)% area was fit with one singlet and one doublet with a quadrupole splitting, ΔE_Q, of 0.344(3) mm/s (red components in Figure 3.3). These features were assigned to the $^1A_{1g}$ low-spin Fe^{II} ions on the Fe2 and Fe1 sites, respectively, based on the local symmetry of each iron site. Briefly, the Fe2 site is assumed to be in a strictly octahedral coordination environment, while the Fe1 site may experience distortion from octahedral symmetry due to the positional disorder of the methyl groups oriented into the framework cavities. The ^{57}Fe quadrupole splitting is proportional to the electric field gradient at the nucleus, $V_{zz} = eq$, which can be expressed as $eq = eq_{val} \pm eq_{lat}$, where e is the proton charge, q_{val} is the valence contribution, and q_{lat} is the lattice contribution.[53] Low-spin Fe^{II} ions located at the Fe2 site are expected to have $eq \approx 0$ and thus $\Delta E_Q \approx 0$, due to their site symmetry ($eq_{lat} \approx 0$) and spin state ($eq_{val} = 0$). In contrast, q_{lat} is non-zero for low-spin ions at the Fe1 site and gives rise to a small quadrupole splitting (see Table S3.3 and Figure S3.15). Based on the 2:1 ratio of the Fe1:Fe2 sites in $Fe(MeTri)_2$, the percent area of the Fe2 site singlet was constrained to be 33.3%. The Fe1 site then contributes to 66.7% of the total 5 K spectral area, 54.4(2)% of which was assigned to low-spin Fe1 (see Table S3.3 and the Supporting Information for details). The remaining Fe1 percent area of 12.3(2)% was fit with three doublets assigned to $^5T_{2g}$ high-spin Fe^{II} ion sites. The assignment to Fe1 rather than Fe2 ions is supported by the temperature dependence of the spectra.

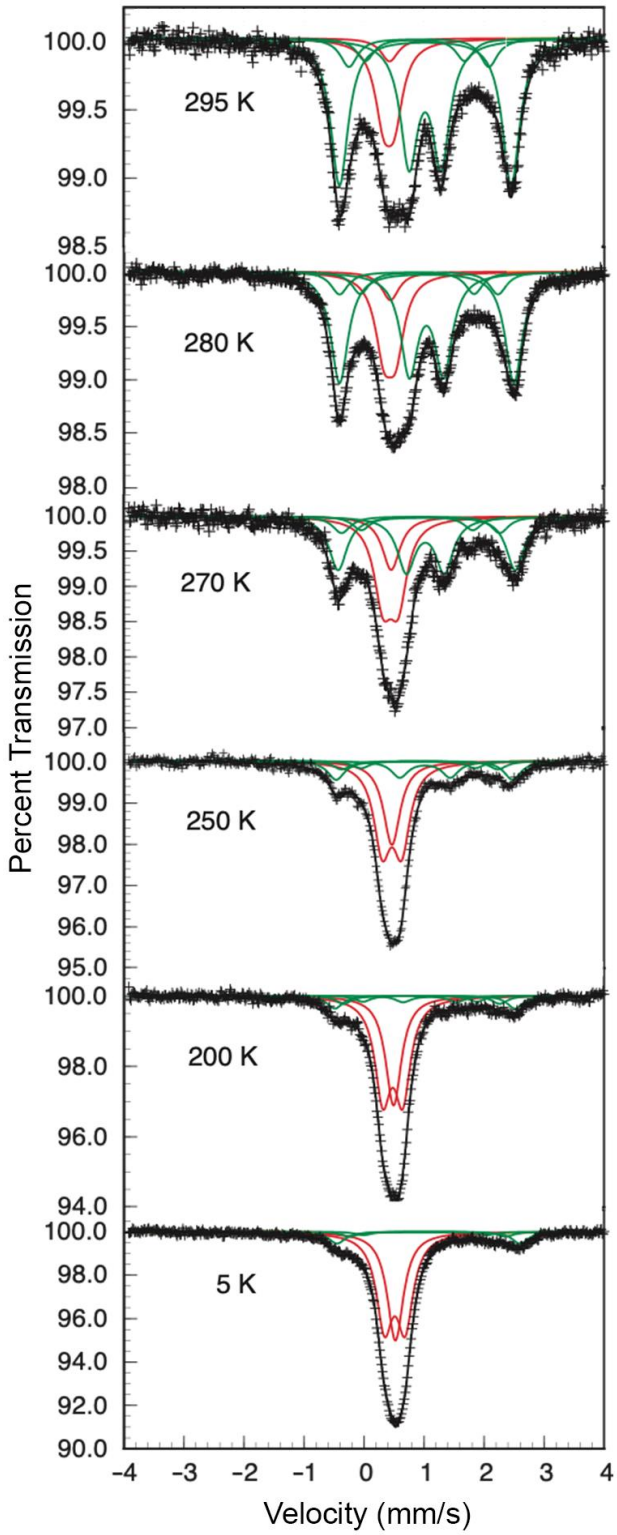

Figure 3.3. Mössbauer spectroscopy. Mössbauer spectra of $Fe(MeTri)_2$ obtained at the indicated temperatures. Red and green solid lines correspond to fits to the low-spin and high-spin Fe^{II} spectral components, respectively, and the total fits are shown as black solid lines.

The minor spectral absorption present at −0.5 and 2.5 mm/s in the 5 K spectrum is the same at 100 K, but at and above 200 K, this absorption gradually increases as a consequence of the increasing population of high-spin Fe^{II} ions at the Fe1 site. Additionally, at 250 K a new doublet is clearly visible at approximately 0.7 and 1.3 mm/s, assigned to high-spin Fe^{II} at the Fe2 site. The percent area of these high-spin components increases with temperature up to 295 K, and the percent area of the low-spin Fe^{II} components decreases. This abrupt change in the population of high- and low-spin Fe^{II} ions (see Figure S3.15) is consistent with the transition observed in the magnetic and variable-temperature powder X-ray diffraction data. However, based on the 295 K Mössbauer spectrum, ~20% of all Fe^{II} ions remain trapped in the low-spin state. Further study will be necessary to determine if all the Fe^{II} ions convert to a high-spin electronic configuration under sufficiently elevated temperatures. We note that the isomer shifts determined for the remaining low-spin Fe^{II} sites at 295 K (0.418(1) and 0.428(1) mm/s) are larger than the 290 K isomer shift observed for low-spin Fe^{II} in $Fe(Tri)_2$ (0.385(1) mm/s).[44] The larger values in the case of $Fe(MeTri)_2$ derive from the larger lattice parameter and Fe–N bond distances resulting from the pore-dwelling methyl groups. The quadrupole splitting determined for the low-spin Fe^{II} in $Fe(MeTri)_2$ at 295 K (ΔE_Q = 0.18(1) mm/s, Table S3.3) is consistent with the value for low-spin Fe^{II} in $Fe(Tri)_2$ at 290 K (ΔE_Q = 0.084(7) mm/s),[44] as expected given the similar octahedral environment of the Fe^{II} ions.

At all temperatures, the high-spin Fe^{II} ions exhibit larger quadrupole splittings than the low-spin ions, due to the non-zero eq_{val} contribution to ΔE_Q (Table S3.3). Interestingly, the quadrupole splitting values for high-spin Fe^{II} at site Fe1 are significantly larger than those for high-spin Fe^{II} at site Fe2 (e.g., ~1.6–2.9 mm/s versus ~0.5–0.8 mm/s, respectively, between 295 and 250 K). We note that, if the Fe2 site was in a strictly cubic environment, even the $^5T_{2g}$ electronic state would yield ΔE_Q = 0,[54] but this is clearly not the case. Presumably, these non-zero Fe2 quadrupole splitting values arise from the presence of disorder introduced into the structure as residual low-spin Fe^{II} ions undergo spin crossover. Additionally, the non-cubic distribution of the near-neighbor high-spin Fe1 sites within the lattice may yield non-zero values for eq_{val} and eq_{lat} for the Fe2 site.

The results from the powder X-ray diffraction and Mössbauer data are summarized in Figure 3.4 and inset, where the high- and low-spin phase compositions and populations of high- and low-spin Fe^{II} sites in $Fe(MeTri)_2$ are plotted as a function of temperature. Between 250 and 270 K, $Fe(MeTri)_2$ is expected to feature equal populations of high- and low-spin ions, which indicates that the spin crossover is centered around 265 K, consistent with results from magnetic measurements (see Figures S3.15 and S3.16).

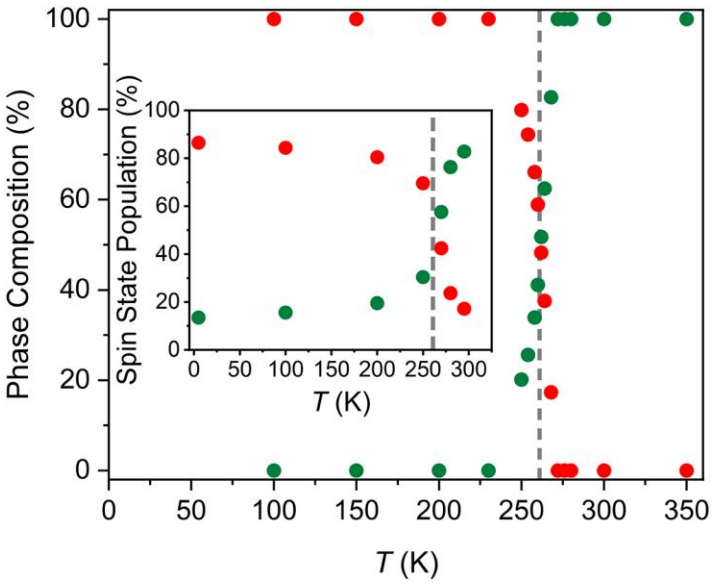

Figure 3.4. Phase composition analysis. Temperature-dependent structural phase composition determined from variable-temperature synchrotron powder X-ray diffraction data (main plot) and Fe^{II} spin state populations determined from Mössbauer spectroscopy (inset). Red and green circles correspond to contributions from low-spin and high-spin Fe^{II}, respectively. The grey dashed lines show the consistent spin crossover temperature obtained from these two methods.

3.4 Conclusions and Outlook

We have shown that the metal–organic framework $Fe(MeTri)_2$ undergoes a structural phase transition driven by spin crossover near room temperature, joining one of only a small number of 3D spin-crossover solids not based on classical Hofmann-type compounds. Interestingly, while the parent material $Fe(Tri)_2$ undergoes a low-to-high-spin transition above 450 K, linker substitution in $Fe(MeTri)_2$ favors elongated metal–ligand bonds and stabilizes the high-spin electronic configuration of Fe^{II} at much lower temperature, significantly decreasing the low- to high-spin crossover temperature in this material. Spin-crossover cooperativity in $Fe(MeTri)_2$ is diminished relative to that in $Fe(Tri)_2$, as evidenced by X-ray diffraction, magnetic measurements, and Mössbauer spectroscopy. Additional studies will focus on further modifications of the linker in $Fe(Tri)_2$, e.g., via expansion, to tune the spin-crossover properties as well as access new materials with intrinsic porosity, which will introduce the possibility of using post-synthetic redox chemistry to probe spin-state dependence of the electronic conductivity.[44]

3.5 Acknowledgement

This research was supported by NSF award number DMR-1611525, with the exception of the measurement and analysis of the magnetic data, which were supported by the Nanoporous Materials Genome Center of the U.S. Department of Energy, Office of Basic Energy Sciences, Division of Chemical Sciences, Geo-sciences and Biosciences under Award No. DE-FG02-17ER16362. Powder X-ray diffraction data were collected at Beamline 17-BM at the Advanced Photon Source, a U.S. Department of Energy Office of Science User Facility, operated by Argonne National Laboratory. Use of the Advanced Photon Source at Argonne National Laboratory was supported by the U.S. Department of Energy, Office of Science, Office of Basic Energy Sciences,

under Contract No. De-AC02-06CH11357. We thank the National Science Foundation Graduate Research Fellowship Program for providing support for J.G.P. and E.O.V. R.C. thanks the University of Bordeaux, the Centre National de la Recherche Scientifique (CNRS), Quantum Matter Bordeaux, and the Conseil Régional de Nouvelle-Aquitaine for financial support. In addition, we thank Dr. Julia Oktawiec and Dr. T. David Harris for helpful discussions and experimental assistance, and Dr. Katie R. Meihaus for editorial assistance.

3.6 References

(1) Cambi, L.; Gagnasso, A. Iron dithiocarbamates and nitrosodithiocarbamates. *Atti. Accad. Naz. Lincei* **1931**, *13*, 809-813.
(2) Halcrow, M. A. *Spin-Crossover Materials: Properties and Applications*; John Wiley and Sons, Ltd.: Oxford, U.K., 2013.
(3) Ohkoshi, S.-I.; Imoto, K.; Tsunobuchi, Y.; Takano, S.; Tokoro, H. Light-induced spin-crossover magnet. *Nat. Chem.* **2011**, *3*, 564-569.
(4) Miyamachi, T.; Gruber, M.; Davesne, V.; Bowen, M.; Boukari, S.; Joly, J.; Scheurer, F.; Rogez, G.; Yamada, T. K.; Ohresser, P.; Beaurepaire, E.; Wulfhekel, W. Robust spin crossover and memristance across a single molecule. *Nat. Commun.* **2012**, *3*, 938.
(5) Lefter, C.; Rat, S.; Costa, J. S.; Manrique-Juárez, M. D.; Quintero, C. M.; Salmon, L.; Séguy, I.; Leichle, T.; Nicu, L.; Demont, P.; Rotaru, A.; Molnár, G.; Bousseksou, A. Current Switching Coupled to Molecular Spin-States in Large-Area Junctions. *Adv. Mater.* **2016**, *28*, 7508-7514.
(6) Sanvito, S. Molecular spintronics. *Chem. Soc. Rev.* **2011**, *40*, 3336-3355.
(7) Kröber, J.; Codjovi, E.; Kahn, O.; Grolière, F.; Jay, C. A Spin Transition System with a Thermal Hysteresis at Room Temperature. *J. Am. Chem. Soc.* **1993**, *115*, 9810-9811.
(8) Kahn, O.; Martinez, C. J. Spin-Transition Polymers: From Molecular Materials Toward Memory Devices. *Science* **1998**, *279*, 44-48.
(9) Létard, J.-F.; Guionneau, P.; Goux-Capes, L. Towards Spin Crossover Applications. *Top. Curr. Chem.* **2004**, *235*, 221-249.
(10) Kumar, K. S.; Ruben, M. Emerging trends in spin crossover (SCO) based functional materials and devices. *Coord. Chem. Rev.* **2017**, *346*, 176-205.
(11) Gütlich, P.; Garcia, Y.; Goodwin H. A. Spin crossover phenomena in Fe(II) complexes. *Chem Soc. Rev.* **2000**, *29*, 419-427.
(12) Gülich, P.; Hauser, A.; Spiering, H. Thermal and Optical Switching of Iron(II) Complexes. *Angew. Chem. Int. Ed.* **1994**, *33*, 2024-2054.
(13) Vela, S.; Paulsen, H. Cooperativity in Spin Crossover Systems. An Atomistic Perspective on the Devil's Staircase. *Inorg. Chem.* **2018**, *57*, 9478-9488.
(14) Nicolazzi, W., Bousseksou, A. Thermodynamical aspects of the spin crossover phenomenon. *C. R. Chim.* **2018**, *21*, 1060-1074.
(15) Baker, W. A.; Bohonich, H. M. Magnetic Properties of Some High-Spin Complexes of Iron(II). *Inorg. Chem.* **1964**, *3*, 1184-1188.
(16) Jeon, I.-R.; Jeannin, O.; Clérac, R.; Rouzières, M.; Fourmigué, M. Spin-state modulation of molecular Fe^{III} complexes via inclusion in halogen-bonded supramolecular networks. *Chem. Commun.* **2017**, *53*, 4989-4992.
(17) Murray, K. S.; Kepert, C. J. Cooperativity in Spin Crossover Systems: Memory, Magnetism and Microporosity. *Top. Curr. Chem.* **2004**, *233*, 195-228.

(18) Garcia, Y.; Niel, V.; Muñoz, M. C.; Real, J. A. Spin Crossover in 1D, 2D, and 3D Polymeric Fe(II) Networks. *Top. Curr. Chem.* **2004**, *233*, 229-257.
(19) Kröber, J.; Audière, J.-P.; Claude, R.; Codjovi, E.; Kahn, O.; Haasnoot, J. G.; Grolière, F.; Jay, C.; Bousseksou, A.; Linarès, J.; Varret, F. Spin Transitions and Thermal Hysteresis in the Molecular-Based Materials $[Fe(Htrz)_2(trz)](BF_4)$ and $[Fe(Htrz)_3](BF_4)_2 \bullet H_2O$ (Htrz = 1,2,4-4*H*-triazole; trz = 1,2,4-triazolato). *Chem. Mater.* **1994**, *6*, 1404-1412.
(20) Haasnoot, J. G.; Vos, G.; Groeneveld, W. L. 1,2,4-Triazole Complexes, III* Complexes of Transition Metal(II) Nitrates and Fluoroborates. *Z. Naturforsch.* **1977**, *32b*, 1421-1430.
(21) Garcia, Y.; Van Konigsbruggen, P. J.; Lapouyade, R.; Fournès, L.; Rabardel, L.; Kahn, O.; Ksenofontov, V.; Levchenko, G.; Gütlich, P. Influences of Temperature, Pressure, and Lattice Solvents on the Spin Transition Regime of the Polymeric Compound $[Fe(hyetrz)_3]A_2 \bullet 3H_2O$ (hyetrz = 4-(2'-hydroxyethyl)-1,2,4-triazole and A^- = 3-nitrophenylsulfonate) *Chem. Mater.* **1998**, *10*, 2426-2433.
(22) Garcia, Y.; Van Koningsbruggen, P. J.; Codjovi, E.; Lapouyade, R.; Kahn, O.; Rabardel, L. Non-classical Fe^{II} spin-crossover behavior leading to an unprecedented extremely large apparent thermal hysteresis of 270 K: application for displays. *J. Mater. Chem.* **1997**, *7*, 857-858.
(23) Roubeau, O.; Haasnoot, J. G.; Codjovi, E.; Varret, F.; Reedijk, J. Spin Transition Regime in New One-Dimensional Polymeric Iron(II) Compounds. Importance of the Water Content for the Thermal and Optical Properties. *Chem. Mater.* **2002**, *14*, 2559-2566.
(24) Weber, B. Spin crossover complexes with N_4O_2 coordination sphere—The influence of covalent linkers on cooperative interactions. *Coord. Chem. Rev.* **2009**, *253*, 2432-2449.
(25) Quesada, M.; de la Pena-O'Shea, V. A.; Aromi, G.; Geremia, S.; Massera, C.; Roubeau, O.; Gamez, P.; Reedijk, J. A Molecule-Based Nanoporous Material Showing Tuneable Spin-Crossover Behavior near Room Temperature. *Adv. Mater.* **2007**, *19*, 1397-1402.
(26) Garcia, Y.; Kahn, O.; Rabardel, L.; Chansou, B.; Salmon, L.; Tuchagues, J. P. Two-Step Spin Conversion for the Three-Dimensional Compound Tris(4,4'-bis-1,2,4-triazole)iron(II) Diperchlorate. *Inorg. Chem.* **1999**, *38*, 21, 4663-4670.
(27) Van Koningsbruggen, P. J.; Garcia, Y.; Kooijman, H.; Spek, A. L.; Haasnoot, J. G.; Kahn, O.; Linares, J.; Codjovi, E.; Varret, F. A new 3-D polymeric spin transition compound: [tris(1,4-bis-(tetrazol-1-yl)butane-*N*1,*N*1')iron(II)] bis(perchlorate). *J. Chem. Soc., Dalton Trans.* **2001**, 466-471.
(28) Moliner, N.; Muñoz, C.; Létard, S.; Solans, X.; Menéndez, N.; Goujon, A.; Varret, F.; Real, J. A. Spin Crossover Bistability in Three Mutually Perpendicular Interpenetrated (4,4) Nets. *Inorg. Chem.* **2000**, *39*, 5390-5393.
(29) Halder, G. J.; Kepert, C. J.; Moubaraki, B.; Murray, K. S.; Cashion, J. D. Guest-Dependent Spin Crossover in a Nanoporous Molecular Framework Material. *Science* **2002**, *298*, 1762-1765.
(30) Southon, P. D.; Liu, L.; Fellows, E. A.; Price, D. J.; Halder, G. J.; Chapman, K. W.; Moubaraki, B.; Murray, K. S.; Létard, J.-F.; Kepert, C. J. Dynamic Interplay between Spin-Crossover and Host–Guest Function in a Nanoporous Metal–Organic Framework Material. *J. Am. Chem. Soc.* **2009**, *131*, 10998-11009.
(31) Agustí, G.; Ohtani, R.; Yoneda, K.; Gaspar, A. B.; Ohba, M.; Sánchez-Royo, J. F.; Muñoz, M. C.; Kitagawa, S.; Real, J. A. Oxidative Addition of Halogens on Open Metal Sites in a Microporous Spin-Crossover Coordination Polymer. *Angew. Chem. Int. Ed.* **2009**, *48*, 8944-8947.
(32) Ohba, M.; Yoneda, K.; Agustí, G.; Muñoz, M. C.; Gaspar, A. B.; Real, J. A.; Yamasaki, M.; Ando, H.; Nakao, Y.; Sakaki, S.; Kitagawa, S. Bidirectional Chemo-Switching of Spin State in a Microporous Framework. *Angew. Chem. Int. Ed.* **2009**, *48*, 4767-4771.

(33) Niel, V.; Martinez-Agudo, J. M.; Muñoz, M. C., Gaspar, A. B.; Real, J. A. Cooperative Spin Crossover Behavior in Cyanide-Bridged Fe(II)-M(II) Bimetallic 3D Hofmann-like Networks (M = Ni, Pd, and Pt). *Inorg. Chem.* **2001**, *40*, 3838-3839.
(34) Niel, V.; Muñoz, M. C.; Gaspar, A. B.; Galet, A.; Levchenko, G.; Real, J. A. Thermal-, Pressure-, and Light-Induced Spin Transition in Novel Cyanide-Bridged Fe^{II}–Ag^{I} Bimetallic Compounds with Three-Dimensional Interpenetrating Double Structures $\{Fe^{II}L_x[Ag(CN)_2]_2\}$•G. *Chem. Eur. J.* **2002**, *8*, 2446-2453.
(35) Ni, Z.-P.; Liu, J.-L.; Hoque, M. N.; Liu, W.; Li, J.-Y.; Chen, Y.-C.; Tong, M.-L. Recent advances in guest effects on spin-crossover behavior in Hofmann-type metal-organic frameworks. *Coord. Chem. Rev.* **2017**, *335*, 28-43.
(36) Furukawa, H.; Cordova, K. E.; O'Keeffe, M.; Yaghi, O. M. The Chemistry and Applications of Metal-Organic Frameworks. *Science*, **2013**, *341*. 1230444.
(37) Brozek, C. K.; Dincă M. Cation exchange at the secondary building units of metal-organic frameworks. *Chem. Soc. Rev.* **2014**, *43*, 5456-5467.
(38) Yin, Z.; Wan, S.; Yang, J.; Kurmoo, M.; Zeng, M.-H. Recent advances in post-synthetic modification of metal-organic frameworks: New types and tandem reactions. *Coord. Chem. Rev.* **2019**, *378*, 500–512.
(39) Liu, L.; Li, L.; Ziebel, M. E.; Harris, T. D. Metal-Diamidobenzoquinone Frameworks via Post-Synthetic Linker Exchange. *J. Am. Chem. Soc.* **2020**, *142*, 4705–4713.
(40) Kobayashi, Y.; Jacobs, B.; Allendorf, M. D.; Long, J. R. Conductivity, Doping, and Redox Chemistry of a Microporous Dithiolene-Based Metal-Organic Framework. *Chem. Mater.* **2010**, *22*, 4120-4122.
(41) D'Alessandro, D. M. Exploiting redox activity in metal-organic frameworks: concepts, trends and perspectives. *Chem. Commun.* **2016**, *52*, 8957-8971.
(42) Perlepe, P.; Oyarzabal, I.; Mailman, A.; Yquel, M.; Platunov, M.; Dovgaliuk, I.; Rouzières, M.; Négrier, P.; Mondieig, D.; Suturina, E. A.; Dourges, M.-A.; Bonhommeau, S.; Musgrave, R. A.; Pedersen, K. S.; Chernyshov, D.; Wilhelm, F.; Rogalev, A.; Mathonière, C.; Clérac, R. Metal-organic magnets with large coercivity and ordering temperatures up to 242°C. *Science* **2020**, *370*, 587-592.
(43) Grzywa, M.; Röß-Ohlenroth, R.; Muschielok, C.; Oberhofer, H.; Blachowski, A.; Żukrowski, J.; Vieweg, D.; Krug von Nidda, H.-A.; Volkmer, D. Cooperative Large-Hysteresis Spin-Crossover Transition in the Iron(II) Triazolate $[Fe(ta)_2]$ Metal–Organic Framework. *Inorg. Chem.* **2020**, *59*, 10501-10511.
(44) Park, J. G.; Aubrey, M. L.; Oktawiec, J.; Chakarawet, K.; Darago, L. E.; Grandjean, F.; Long, G. J.; Long, J. R. Charge Delocalization and Bulk Electronic Conductivity in the Mixed-Valence Metal–Organic Framework Fe(1,2,3-triazolate)$_2(BF_4)_x$. *J. Am. Chem. Soc.* **2018**, *140*, 8526-8534.
(45) Gándara, F.; Uribe-Romo, F. J.; Britt, D. K.; Furukawa, H.; Lei, L.; Cheng, R.; Duan, X.; O'Keeffe, M.; Yaghi, O. M. Porous, conductive metal-triazolates and their structural elucidation by the charge-flipping method. *Chem. Eur. J.* **2012**, *18*, 10595-10601.
(46) Coelho, A. TOPAS-Academic, Version 4.1, Coelho Software, Brisbane, 2007.
(47) Gómez-Gualdrón, D. A.; Moghadam, P. Z.; Hupp, J. T.; Farha, O. K.; Snurr, R. Q. Application of Consistency Criteria To Calculate BET Areas of Micro- and Mesoporous Metal–Organic Frameworks. *J. Am. Chem. Soc.* **2016**, *138*, 215.

(48) Willems, T. F.; Rycroft, C. H.; Kazi, M.; Meza, J. C.; Haranczyk, M. Algorithms and Tools for High-Throughput Geometry-Based Analysis of Crystalline Porous Materials. *Micro. Meso. Mater.* **2012**, *149*, 134.
(49) BIOVIA, Dassault Systèmes, Materials Studio, version 18.1.0.2017, San Diego: Dassault Systèmes, 2018.
(50) Brooker, S. Spin crossover with thermal hysteresis: practicalities and lessons learnt. *Chem. Soc. Rev.* **2015**, *44*, 2880-2892.
(51) Zhou, X.-H.; Peng, Y.-H.; Du, X.-D.; Zuo, J.-L.; You, X.-Z. Hydrothermal syntheses and structures of three novel coordination polymers assembled from 1,2,3-triazolate ligands. *Cryst. Eng. Comm.* **2009**, *11*, 1964-1970.
(52) Grzywa, M.; Denysenko, D.; Hanss, J.; Scheidt, E.-W.; Scherer, W.; Weil, M.; Volkmer, D. CuN_6 Jahn-Teller centers in coordination frameworks comprising fully condensed Kuratowski-type secondary building units: Phase transitions and magneto-structural correlations. *Dalton Trans.* **2012**, *41*, 4239-4248.
(53) Long, G. J. Basic Concepts of Mössbauer Spectroscopy in *Mössbauer Spectroscopy Applied to Inorganic Chemistry*; Ed., Springer-Science, New York, 1984, pp. 7-26.
(54) Ingalls, R. Electric-Field Gradient Tensor in Ferrous Compounds. *Phys. Rev.* **1964**, *133*, A787-A795.

Chapter 3 Supporting Information

S3.1 Additional Experimental Data

Magnetic Data Analysis and Discussion. Temperature dependent magnetic susceptibility data were collected for $Fe(MeTri)_2$ under an applied dc field of 0.1 T with a scan rate of 0.4 K/min during warming from 30 to 320 K and subsequent cooling from 320 to 30 K (Figure S3.11). The data are plotted as $\chi_M T$ and χ_M versus T in Figure S3.12. The warming/cooling average data collected between 30 and 200 K were fit using the following equations,

$$\chi_M T = N\alpha T + 3.001 p_{HS},$$

and

$$\chi_M = N\alpha + \frac{3.001 p_{HS}}{T},$$

where Na is the temperature-independent paramagnetic contribution to the molar magnetic susceptibility and p_{HS} is the fraction of $S = 2$ and $g = 2$ high-spin iron(II) ions. Fits of $\chi_M T$ versus T and χ_M versus T yielded Na / p_{HS} values of 0.00260(2) emu/mol / 0.106(1) and 0.00257(2) emu/mol / 0.107(1), respectively. The relatively large values of Na are likely due to a temperature independent contribution from low-lying excited states; further investigation would be needed for confirmation of this contribution.

In addition, the $\chi_M T$ data between 30 and 320 K were used to obtain the temperature-dependent population of high-spin iron(II) ions by using the following rearranged equation,

$$p_{HS} = \frac{\chi_M T - N\alpha T}{3.001},$$

where Na was fixed to 0.00260(2) emu/mol as determined above. The temperature dependence of the high-spin iron(II) percentages obtained from analysis of X-ray diffraction, Mössbauer spectroscopy, and magnetic data are shown in Figure S3.16.

The results from the magnetic and Mössbauer experiments are in reasonable agreement and reveal incomplete spin-state crossover, with approximately 10% high-spin iron(II) at 30 and 5 K and approximately 80% at 320 K. In contrast, the powder X-ray diffraction data suggest a complete spin-state crossover with only the low-temperature and high-temperature spin-states present below 230 and above 270 K, respectively. Of course, the X-ray diffraction measurements provide average, long-range order information only if there is coherent long-range scattering, whereas both magnetic and Mössbauer spectral measurements yield local information. As a result, if at low temperature a small fraction of high-spin iron(II) ions are trapped on either the Fe1 or Fe2 site, perhaps because of a peculiar distribution of the methyl groups in an adjacent pore, these ions will contribute to the magnetic and Mössbauer spectral signals but will not contribute to coherent long-range X-ray diffraction scattering, because of the absence of long-range order. The same explanation would apply to the magnetic and Mössbauer spectral observation of approximately 20% of trapped low-spin iron(II) ions at 295 K.

Mössbauer Spectral Analysis. The Mössbauer spectra were fit with the minimum number of symmetric Lorentzian quadrupole doublets, namely five at 5 K and six for the remaining temperatures. All of the doublets at a given temperature were fit with a single linewidth ranging from 0.32 to 0.36 mm/s. The quality of the fits was judged by their statistical c^2 values, the randomness of the fit residuals, and the values of the correlation coefficients between the various fit parameters. The spectra and fits are shown in Figure 3.3 in the main text and the resulting spectral fit parameters are given in Table S3.1.

Because the iron(II) cations occupy two inequivalent crystallographic sites in $Fe(MeTri)_2$ and further may be in the low- or high-spin state, at least four different contributions, likely quadrupole doublets, to the Mössbauer spectra may be expected. The random distribution of the methyl groups in the pores of the structure may also give rise to additional contributions, most likely through the broadening of the various spectral components.

At 5 K, the temperature at which the recoil-free fractions of the two inequivalent crystallographic sites, Fe1 and Fe2, are expected to be equal, the absorption areas of the contributions from these two sites are thus expected to be in a ratio of 2:1. Fits of the major absorption centered at 0.5 mm/s with one doublet clearly showed systematic misfits in the fit residual plots. Hence, the major absorption was fit with two contributions (red lines in Figure 3.3 and S3.13): a singlet (or a doublet with a nearly zero quadrupole splitting) assigned to low-spin iron(II) at site Fe2, and a doublet with a quadrupole splitting of 0.34 mm/s assigned to low-spin iron(II) at site Fe1, as discussed in the main text. Based on these assignments, the absorption area of the Fe2 component was constrained to 33.3% of the total absorption area. The remaining 66.7% of the absorption area consists of 54.4(2)% of the low-spin iron(II) ions located at site Fe1 and 12.3(2)% of high-spin iron(II) ions also at the Fe1 site, assigned on the basis of their large positive isomer shifts (green lines). The use of three high-spin iron(II) doublets is justified by the asymmetric broadening of the absorption centered at ~2.5 mm/s, and the different quadrupole splittings associated with these doublets (see Table S3.1) most likely represent a distribution of near-neighbor environments at the Fe1 sites, resulting from the disordered methyl groups in the pores. The fit results for the 100 and 200 K Mössbauer spectra are similar to those found for the 5 K spectrum, as shown in Figure 3.3 and Table S3.1. We also attempted to unconstrain the quadrupole splitting of the low-spin Fe2 component at 5 K, and this fitting yielded a non-zero value of at most $\Delta E_Q = 0.05$ mm/s (see 5 K* fit in Table S3.3 and Figure S3.14). This 5 K* fit is consistent with the spectral profile yet statistically indistinguishable from the 5 K fit using the constrained quadrupole splitting value of $\Delta E_Q = 0$ mm/s. To prevent overparameterization, the quadrupole splitting value of all low-spin Fe2 components have been constrained to $\Delta E_Q = 0$ mm/s.

At and above 250 K, there is an additional absorption at ~1.3 mm/s that increases with increasing temperature, while the central absorption also broadens with increasing temperature. The additional absorption was assigned to a high-spin iron(II) quadrupole doublet for the Fe2 site. Hence, between 250 and 295 K, the red singlet and one green doublet with a total percent area of 33.3% were assigned to the Fe2 sites; the relative area of the red singlet decreases with increasing temperature. The remaining red doublet and three green doublets with a total percent area of 66.7% were assigned to the Fe1 sites; the relative area of the red doublet decreases with increasing temperature.

The fitting model described above assumes that the recoil-free fractions of the Fe1 and Fe2 sites are equal at all temperatures. In an attempt to check this assumption at 270 K, the percent area of the Fe2 components was refined, and a fit with a quality similar to that shown in Figure 3.3 was obtained. The resulting Fe2 area was found to be 33.6(1.0)%, slightly larger than the value of

33.3% assigned as described above. Thus, the assumption of equivalent recoil-free fractions is valid.

There is a second assumption in the above fitting model; at 5 K the Fe2 iron(II) ions are assumed to be 100% low-spin, whereas the Fe1 iron(II) ions are only 87.7% low-spin. Because only 1% high-spin Fe2 is fitted at 100 K (Table S3.1), no more is expected at 5 K, and the high-velocity line of this contribution is expected at ~1.6 mm/s. Neither the fit nor the residuals indicate that there is any unaccounted absorption at this velocity. If the constraint on the Fe2 percent area of 33.3% is released, the percent area refines to 32(1)%; the c^2 of this fit with one additional parameter is not significantly smaller than that of the constrained fit, the linewidth increases (which is not a good sign for this fit), and the low-spin Fe1 quadrupole splitting decreases and is highly positively correlated with the Fe2 percent area. Hence, the analysis of the 5 K Mössbauer spectrum rules out the presence of more than one percent of high-spin Fe2, i.e., an amount that is comparable to the statistical uncertainty on the measured percent area.

Under the above assumptions, the Mössbauer spectra indicate that the Fe2 iron(II) ions undergo a facile, complete spin-state crossover at a higher temperature than the Fe1 iron(II) ions. We believe that this different behavior has its origin in the "protected" environment of the Fe2 iron(II) ions in the tetrahedron of four Fe1 iron(II) ions and in the larger change in Fe2–N bond distance at the transition.

The isomer shifts of the singlet and doublet assigned to the low-spin iron(II) ions on the Fe2 and Fe1 sites, respectively, decrease with increasing temperature, as expected from the second-order Doppler shift. The isomer shifts of the green doublets assigned to the high-spin iron(II) ions on the Fe1 and Fe2 sites decrease from 5 to 250 K, as expected, but slightly increase at 270, 280, and 295 K. This increase most likely is associated with the structural transition that is complete at 268 K and is accompanied by an increase in lattice parameter and Fe–N bond distances.

The quadrupole splitting of the red doublet assigned to low-spin iron(II) ions on the Fe1 sites decreases with increasing temperature, as is usually observed. The quadrupole splitting of the green doublet assigned to high-spin iron(II) ions on the Fe2 sites decreases with increasing temperature, in agreement with the Ingalls model.[1] The weighted average quadrupole splitting of the green doublets assigned to high-spin iron(II) ions on the Fe1 sites decreases with increasing temperature from 5 to 250 K but slightly increases at 270, 280, and 295 K. This increase most likely is associated with the structural transition which is complete at 268 K.

Table S3.1. Rietveld structural refinement parameters to variable-temperature high resolution powder X-ray diffraction patterns of $Fe(MeTri)_2$.

Compound	**$Fe(Tri)_2$[2]**	**$Fe(MeTri)_2$**	
Temperature	300 K	100 K	350 K
Crystal system	Cubic	Cubic	Cubic
Space group	*Fd*–3*m*	*Fd*–3*m*	*Fd*–3*m*
***V* / Å^3**	4616.38(14)	4723.9(5)	5324.3(6)
***a* / Å**	16.65075(17)	16.7790(6)	17.4618(6)
R_p / %	2.731	3.009	3.039
R_{wp} / %	3.914	3.958	4.086
GOF	2.368	1.902	2.056

Table S3.2. Calculated surface areas of $Fe(Tri)_2$[2] from and $Fe(MeTri)_2$ from 77 K N_2 adsorption isotherm data and crystal structures.

Surface Area	**$Fe(Tri)_2$[2]**	**$Fe(MeTri)_2$**
Langmuir / m^2g^{-1}	560	170
BET / m^2g^{-1}	370	70
Calculated Accessible / m^2g^{-1}	557	0

Table S3.3. Complete Mössbauer Spectral Parameters for $Fe(MeTri)_2$[a]

T, K	δ, mm/s[b]	ΔE_Q, mm/s	Γ, mm/s	*Area*, %	*Area*, (%ε)(mm/s)	Site Assignment
295	1.023(2)	2.858(5)	0.353(5)	36.8(4)	3.24(3)	Fe1, HS Fe(II)
	0.92(1)	2.33(3)	0.353(5)	7.1(5)	-	Fe1, HS Fe(II)
	0.85(2)	1.65(3)	0.353(5)	5.7(4)	-	Fe1, HS Fe(II)
	1.020(3)	0.532(5)	0.353(5)	30.4	-	Fe2, HS Fe(II)
	0.418(1)	0.18(1)	0.353(5)	17.1(1.0)	-	Fe1, LS Fe(II)
	0.428(1)	0.00	0.353(5)	2.9	-	Fe2, LS Fe(II)
280	1.042(3)	2.904(7)	0.351(3)	32.8(3)	3.52(1)	Fe1, HS Fe(II)
	0.91(2)	2.64(3)	0.351(3)	6.7(3)	-	Fe1, HS Fe(II)
	0.89(1)	1.89(2)	0.351(3)	5.7(3)	-	Fe1, HS Fe(II)
	1.039(2)	0.570(4)	0.351(3)	29.1	-	Fe2, HS Fe(II)
	0.427(2)	0.198(6)	0.351(3)	21.5(9)	-	Fe1, LS Fe(II)
	0.437(2)	0.00	0.351(3)	4.2	-	Fe2, LS Fe(II)
270	1.04(1)	2.95(2)	0.36(1)	22(2)	3.90(4)	Fe1, HS Fe(II)
	0.94(2)	2.63(8)	0.36(1)	7(2)	-	Fe1, HS Fe(II)
	0.88(2)	1.86(5)	0.36(1)	5.7(7)	-	Fe1, HS Fe(II)
	1.023(7)	0.63(1)	0.36(1)	22.2	-	Fe2, HS Fe(II)
	0.444(3)	0.253(9)	0.36(1)	32(1)	-	Fe1, LS Fe(II)
	0.454(3)	0.00	0.36(1)	11.1	-	Fe2, LS Fe(II)
250	1.006(9)	2.94(2)	0.343(7)	10.8(7)	4.54(4)	Fe1, HS Fe(II)
	0.93	2.6	0.343(7)	4.8(8)	-	Fe1, HS Fe(II)
	0.901	1.9	0.343(7)	4.0(6)	-	Fe1, HS Fe(II)
	1.03(5)	0.8(1)	0.343(7)	9.3	-	Fe2, HS Fe(II)
	0.46(1)	0.32(2)	0.343(7)	47.1(1.0)	-	Fe1, LS Fe(II)
	0.468(3)	0.00	0.343(7)	24.0	-	Fe2, LS Fe(II)
200	1.015(8)	3.00(2)	0.319(2)	7.0(2)	5.24(1)	Fe1, HS Fe(II)
	0.96	2.6	0.319(2)	4.4(2)	-	Fe1, HS Fe(II)
	0.931	1.9	0.319(2)	3.3(2)	-	Fe1, HS Fe(II)
	1.10(2)	0.89(3)	0.319(2)	3.5	-	Fe2, HS Fe(II)
	0.479(1)	0.331(2)	0.319(2)	52.0(6)	-	Fe1, LS Fe(II)
	0.492(2)	0.00	0.319(2)	29.8	-	Fe2, LS Fe(II)
100	1.080(9)	3.07(2)	0.340(5)	7.8(3)	6.65(4)	Fe1, HS Fe(II)
	1.01	2.6	0.340(5)	3.00	-	Fe1, HS Fe(II)
	0.98	2.1	0.340(5)	2.4	-	Fe1, HS Fe(II)
	1.11	1.0	0.340(5)	1.0	-	Fe2, HS Fe(II)
	0.506(2)	0.336(4)	0.340(5)	53.5(3)	-	Fe1, LS Fe(II)
	0.520(2)	0.00	0.340(5)	32.3	-	Fe2, LS Fe(II)
5	1.075(8)	3.05(2)	0.329(4)	7.3(2)	7.75(4)	Fe1, HS Fe(II)
	1.06	2.6	0.329(4)	3.00	-	Fe1, HS Fe(II)
	1.02	2.06	0.329(4)	2.00	-	Fe1, HS Fe(II)
	0.513(1)	0.344(3)	0.329(4)	54.4(2)	-	Fe1, LS Fe(II)
	0.523(1)	0.00	0.329(4)	33.3	-	Fe2, LS Fe(II)
5* [c]	1.06(1)	2.78(2)	0.329(3)	12.3(2)		Fe1, HS Fe(II)
	0.513(1)	0.340(3)	0.329(3)	54(1)		Fe1, LS Fe(II)
	0.523(1)	0.05(1)	0.329(3)	33.33		Fe2, LS Fe(II)

[a] Statistical fitting uncertainties are given in parentheses; actual uncertainties may be twice as large. The absence of an uncertainty indicates that the parameter was constrained to the value given. [b] Isomer shifts are given relative to α-iron foil measured at 295 K. [c] Parameters corresponding to the fit at the bottom of Figure S3.14, in which the uncertainties on the two low-spin quadrupole splittings and the linewidth have been determined through individual fits as discussed in the Mössbauer section above.

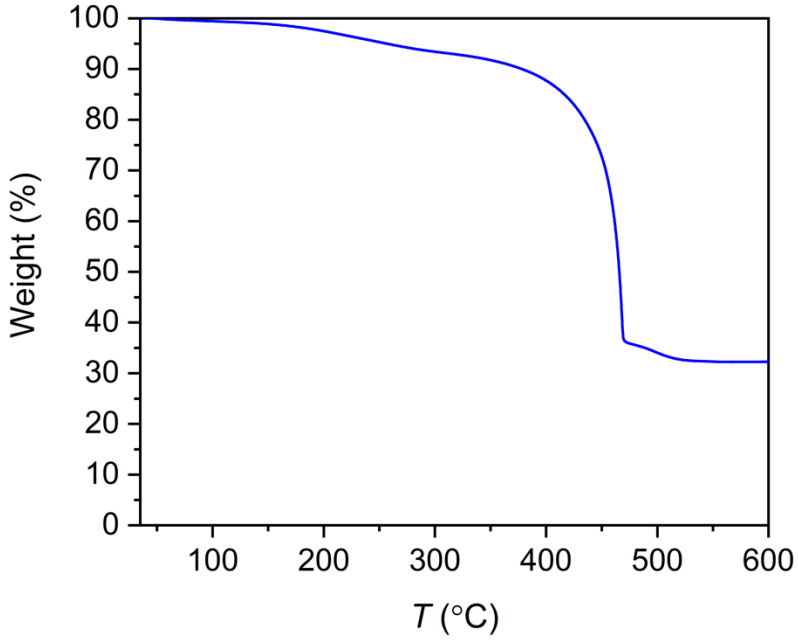

Figure S3.1. Thermogravimetric analysis results obtained for as-synthesized $Fe(MeTri)_2$, measured with a scan rate of 1.5 °C/min. The initial decrease in weight percent likely corresponds to evaporation of *N*,*N*-dimethylformamide from the crystallite surface and a small amount of water introduced during the sample loading.

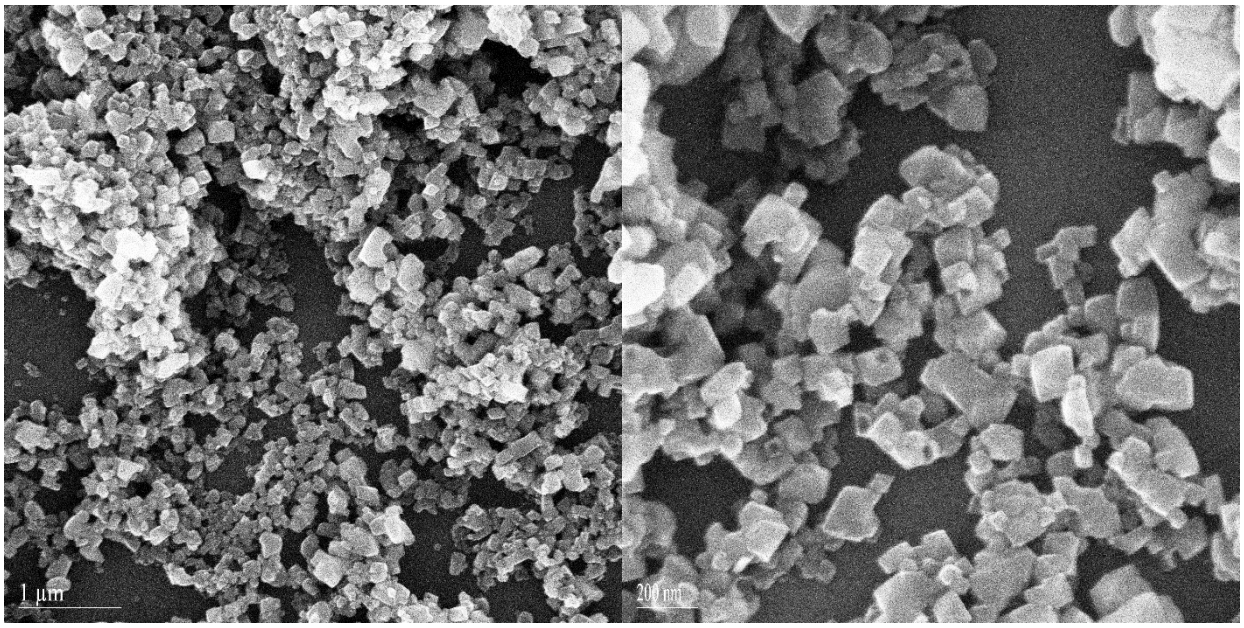

Figure S3.2. Scanning electron microscopy images of $Fe(MeTri)_2$ crystals obtained at a magnification of 1 µm (left) and 200 nm (right).

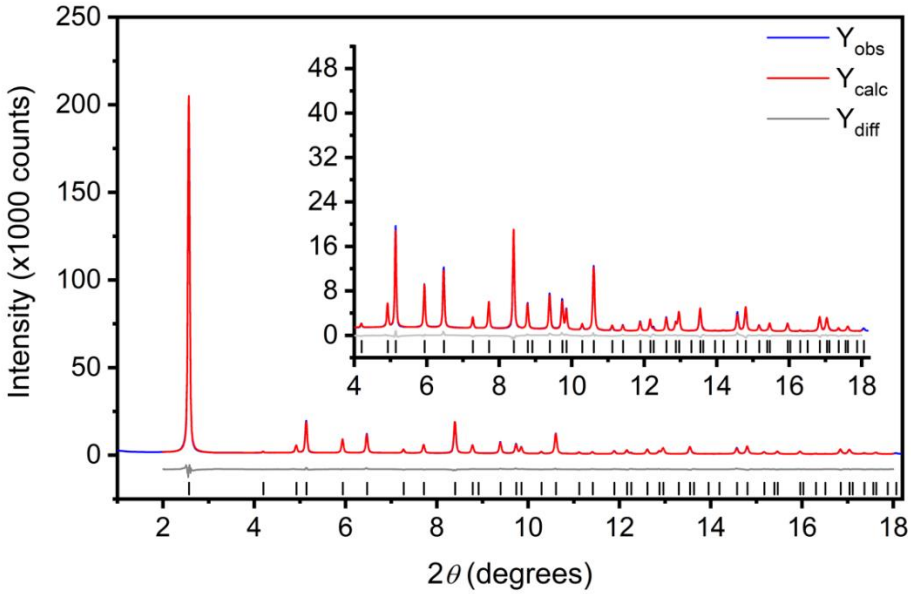

Figure S3.3. Rietveld refinement of powder X-ray diffraction data for desolvated Fe(MeTri)$_2$ obtained at 350 K. Measured scattered intensity, best fit, and the difference plot are shown with blue dots and red, gray lines, respectively. Figures-of-merit (as defined by TOPAS[3]): R_{wp} = 4.086%, R_p = 3.039%, GoF = 2.056. The wavelength was 0.45212 Å.

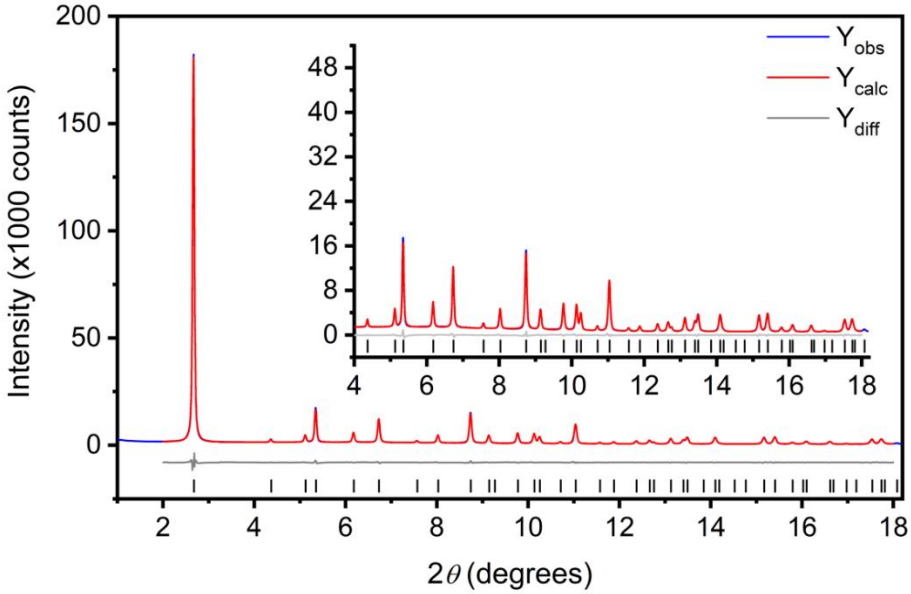

Figure S3.4. Rietveld refinement of powder X-ray diffraction data for desolvated Fe(MeTri)$_2$ obtained at 100 K. Measured scattered intensity, best fit, and the difference plot are shown with blue dots and red, gray lines, respectively. Figures-of-merit (as defined by TOPAS[3]): R_{wp} = 3.958%, R_p = 3.009%, GoF = 1.902. The wavelength was 0.45212 Å.

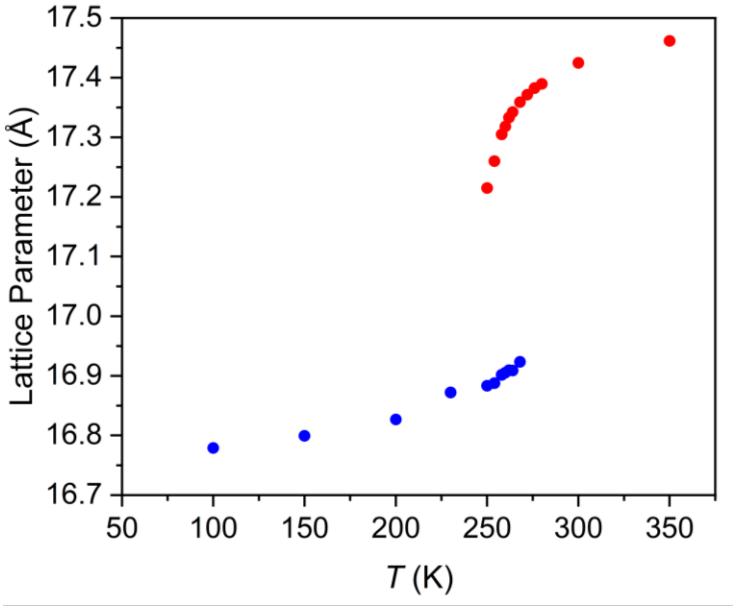

Figure S3.5. Temperature dependence of unit cell lattice parameter obtained from Pawley refinements of variable-temperature powder X-ray diffraction data. Red and blue points correspond to lattice parameters determined for the high- and low-temperature structural phases.

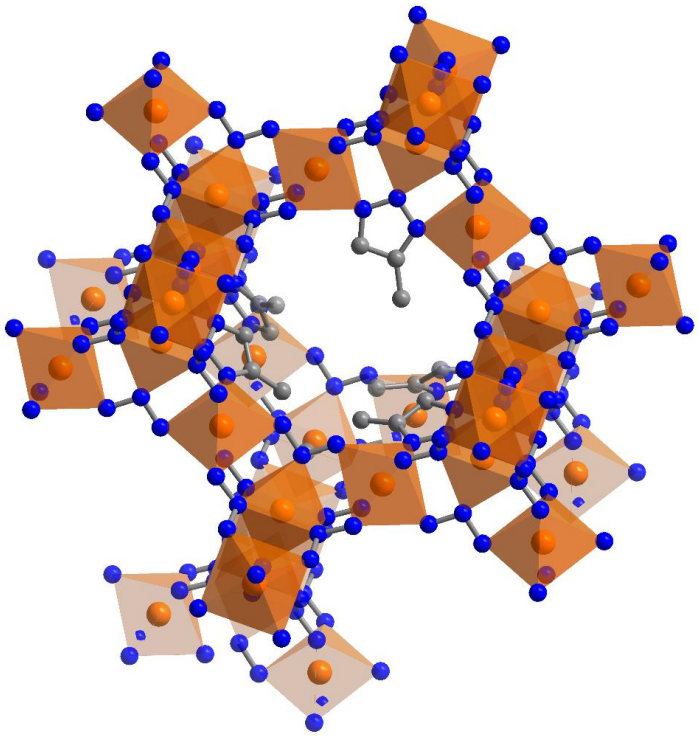

Figure S3.6. Structural model of desolvated $Fe(MeTri)_2$ obtained from Rietveld refinement of powder X-ray diffraction data obtained at 350 K, illustrating a view down the framework pore.

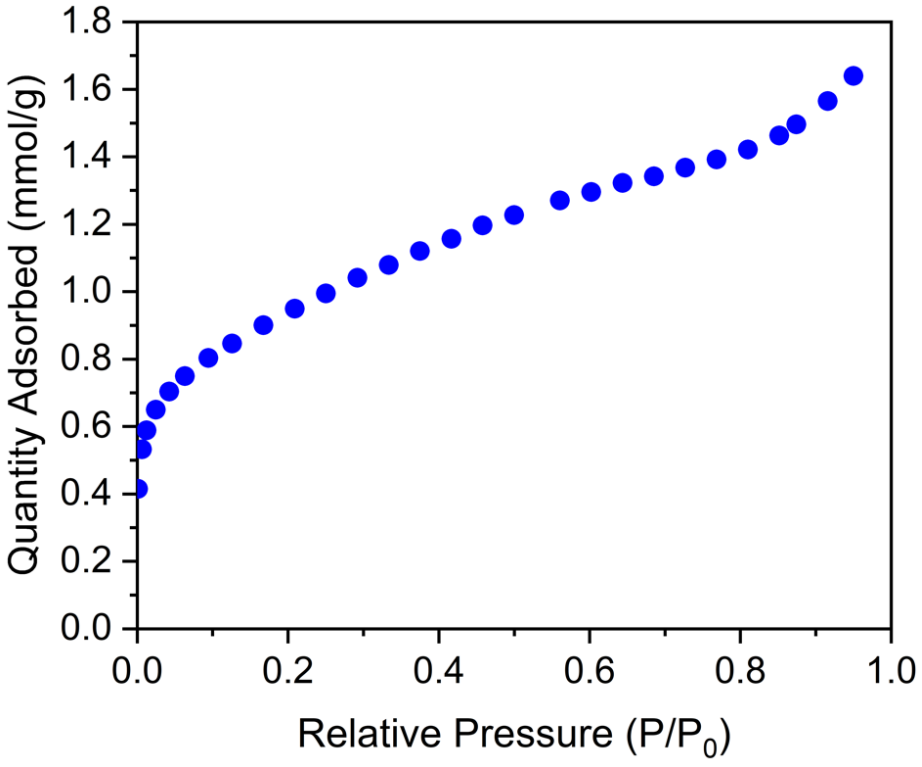

Figure S3.7. N_2 adsorption isotherm of $Fe(MeTri)_2$ measured at 77 K.

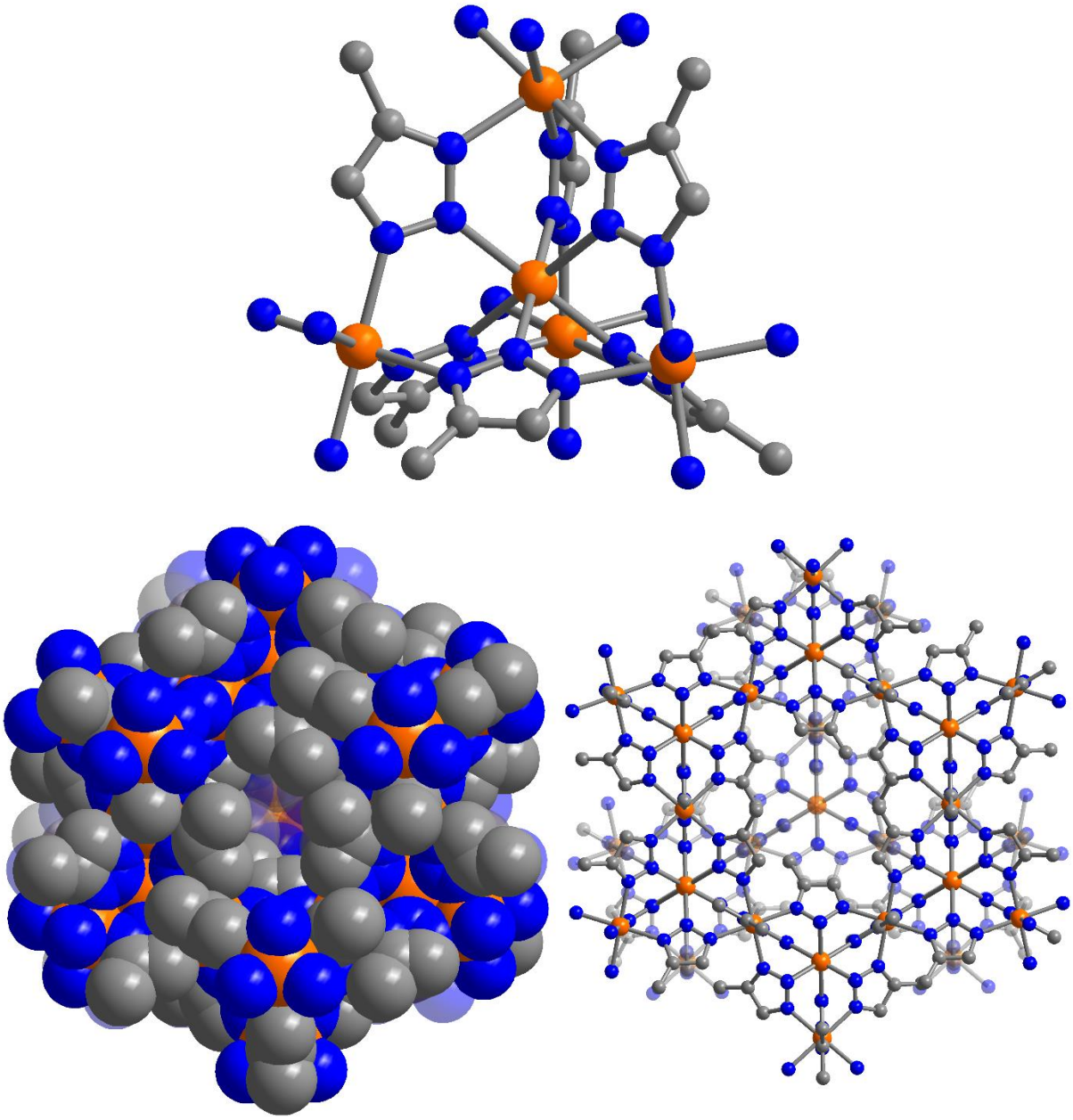

Figure S3.8. Structural model of desolvated Fe(MeTri)$_2$ at 350 K obtained using Materials Studio, as described in the Additional Experimental Details above. The model structure was assigned a space group of $P2_13$ (lowered from the experimental $Fd\bar{3}m$ space group) and methyl groups originating from disorder were removed. This structure was then used for the calculation of theoretical surface area. Tetrahedral building unit (top) and pore structure (bottom) are shown. Orange, grey, and blue spheres represent Fe, C, and N ions or atoms, respectively. Hydrogen atoms are omitted for clarity.

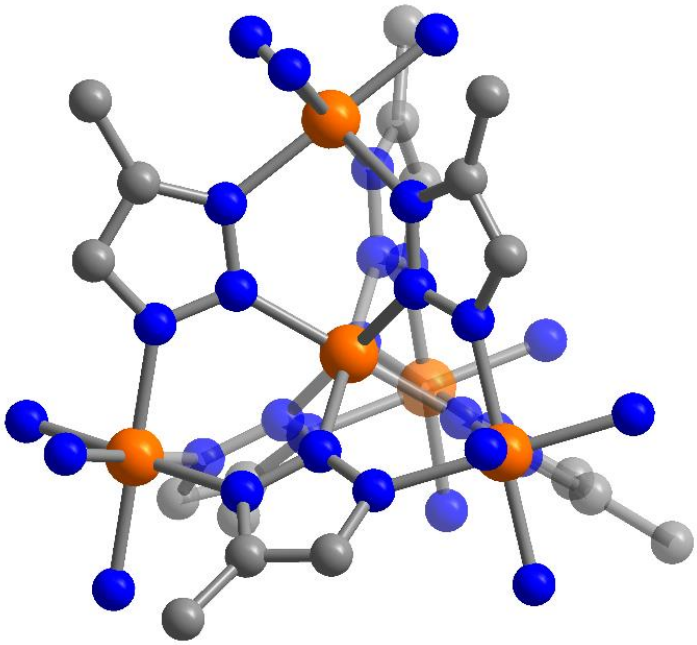

Figure S3.9. Structural model from Rietveld refinement of powder X-ray diffraction data obtained at 100 K, displaying the tetrahedral repeat unit. Orange, grey, and blue spheres represent Fe, C, and N ions or atoms, respectively. Hydrogen atoms are omitted for clarity. One of the two disordered methyl groups per triazolate was omitted for clarity.

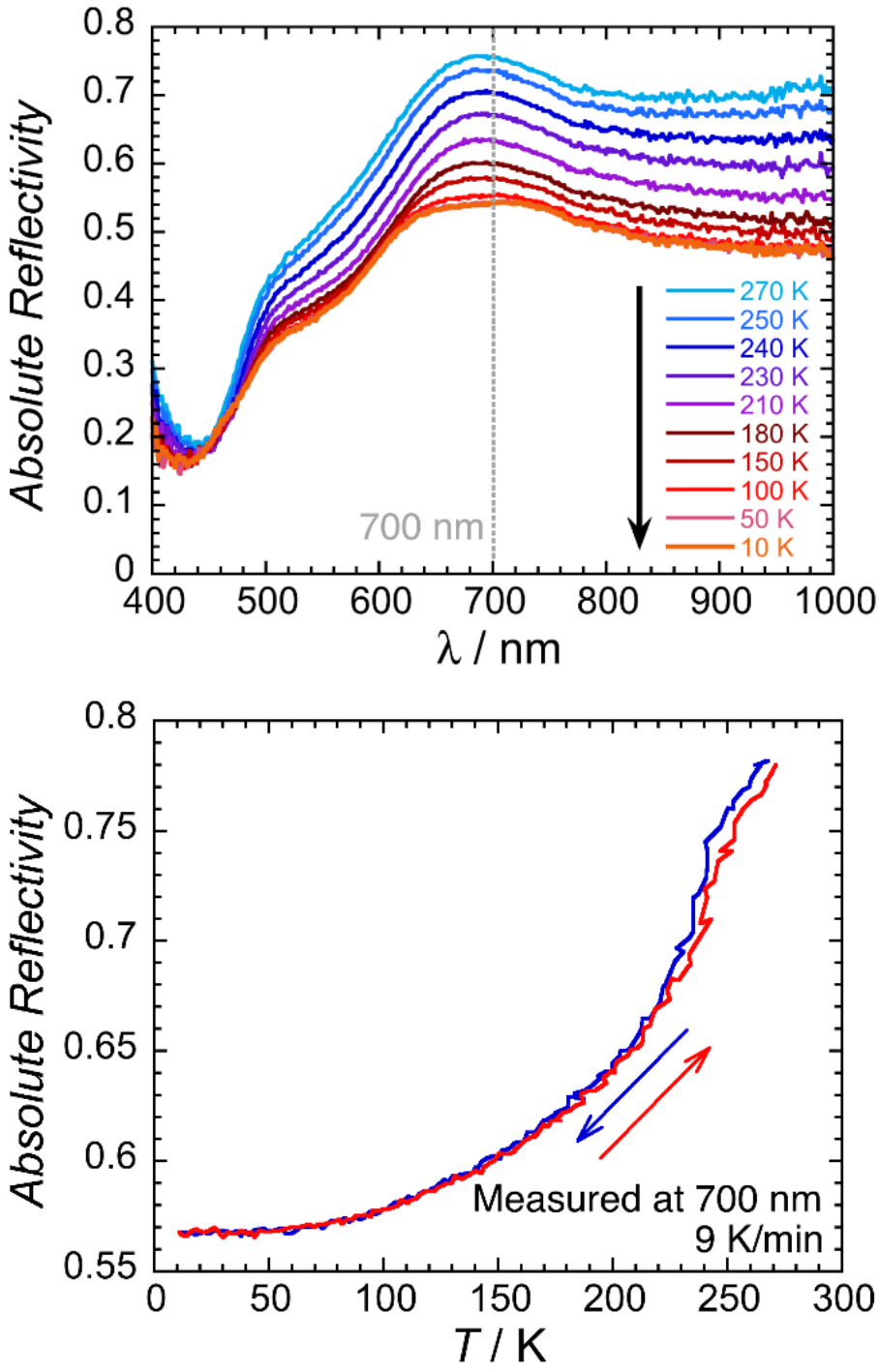

Figure S3.10. Optical reflectivity spectra (upper) and the absolute reflectivity recorded at 700 nm (lower) for $Fe(MeTri)_2$, measured at selected temperatures between 10 and 270 K. A spectroscopic white light of 0.5 mW cm^{-2} was used for the measurements. The absolute reflectivity (lower) plot suggests the thermal hysteresis of around 4 K, consistent with the magnetic data.

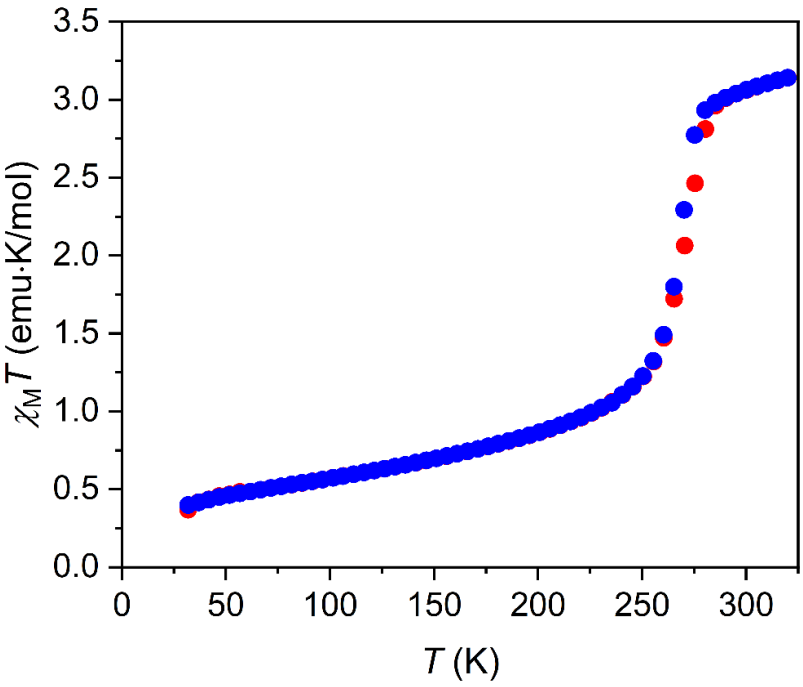

Figure S3.11. Temperature-dependent dc magnetic susceptibility data for $Fe(MeTri)_2$ collected under a field of 0.1 T upon warming from 30 to 320 K (red circles) and subsequently cooling from 320 to 30 K (blue circles). Both sets of data were collected using a scan rate of 0.4 K/min in settle mode.

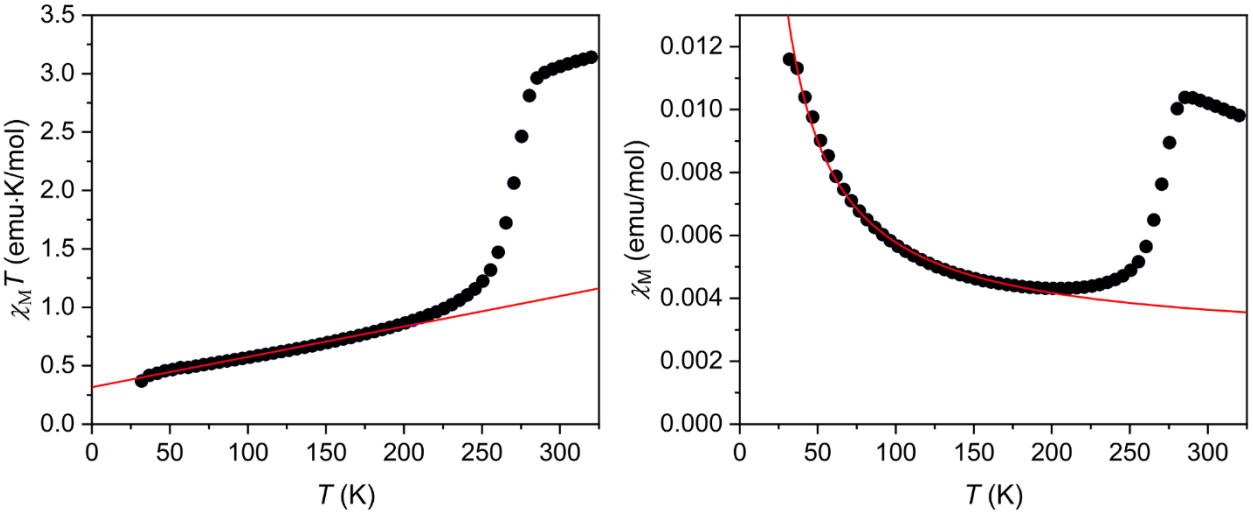

Figure S3.12. Plot of the temperature dependence of $\chi_M T$ (left) and χ_M (right) for $Fe(MeTri)_2$ collected at a scan rate of 0.4 K/min. The plotted data points are an average of data from cooling and warming sweeps, as shown above. Fits between 30 and 200 K, as described above, are shown as solid red lines.

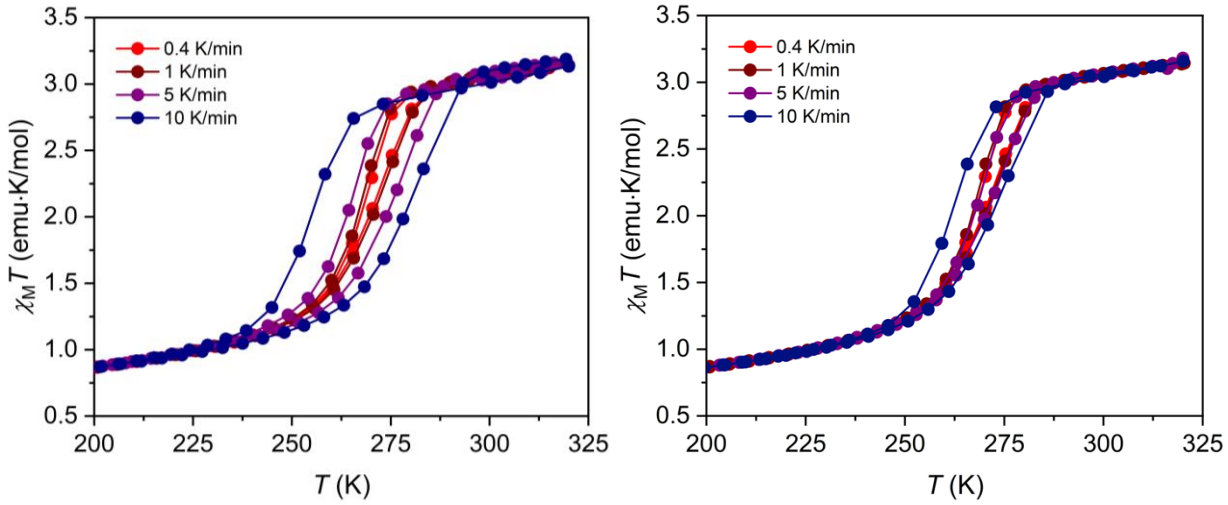

Figure S3.13. Variable temperature dc magnetic susceptibility data collected at the indicated scan rates before (left) and after (right) temperature lag correction of 0.4, 4, and 7 K for the 1, 5, and 10 K/min data sets, respectively. Whereas the 0.4, 1, and 5 K/min data sets show the same 4(1) K hysteresis at ~265 K, a larger thermal hysteresis of 10 K remains for the highest scan rate of 10 K/min. This larger hysteresis may be real or may be from an insufficient temperature lag correction.

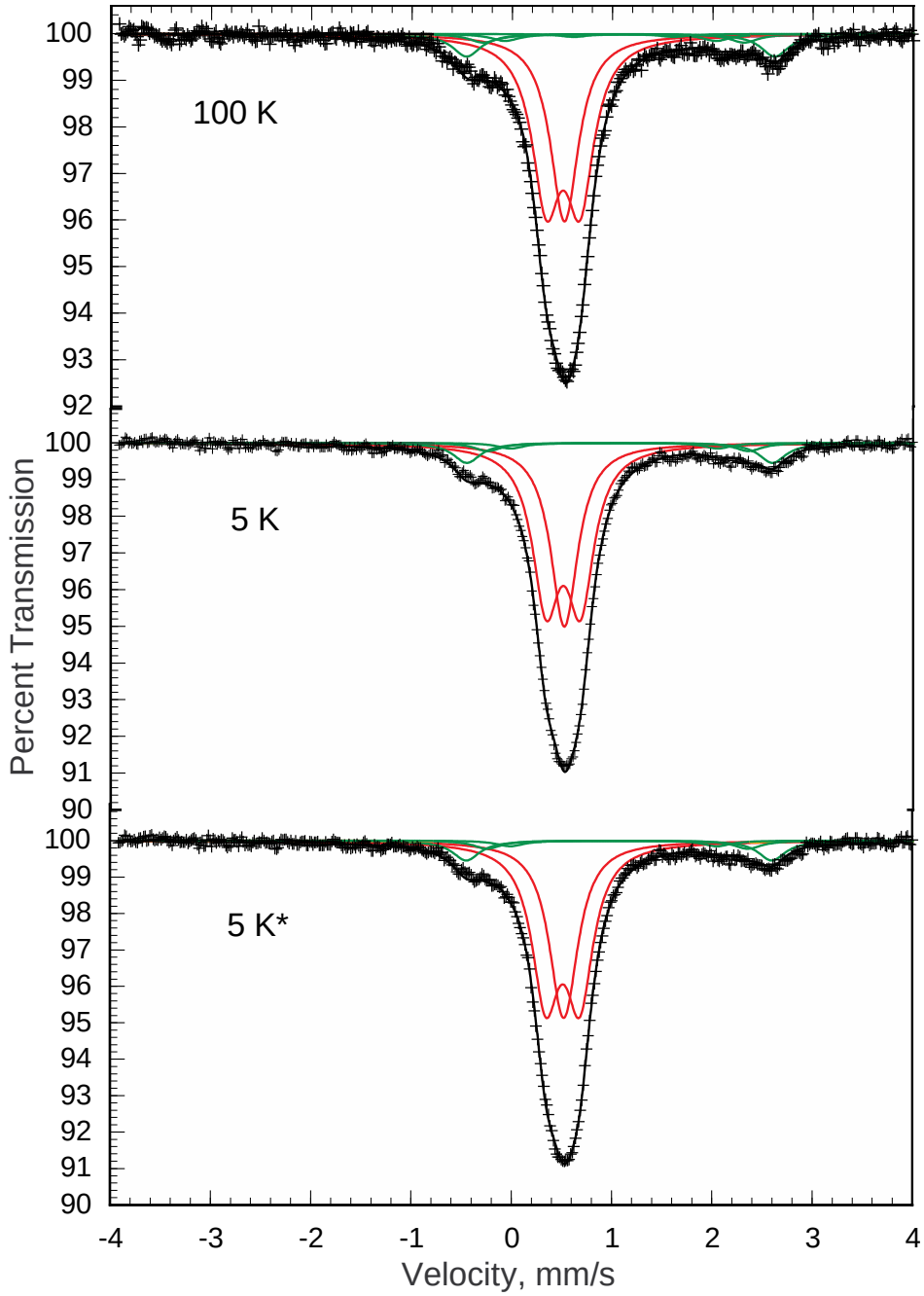

Figure S3.14. The upper 100 and 5 K Mössbauer spectra of Fe(MeTri)$_2$ correspond to the spectral parameters given in Table S3.3. The lower 5 K* spectral fit corresponds to the parameters given at the bottom of Table S3.3. The red and green solid lines correspond to the low- and high-spin iron(II) ions, respectively.

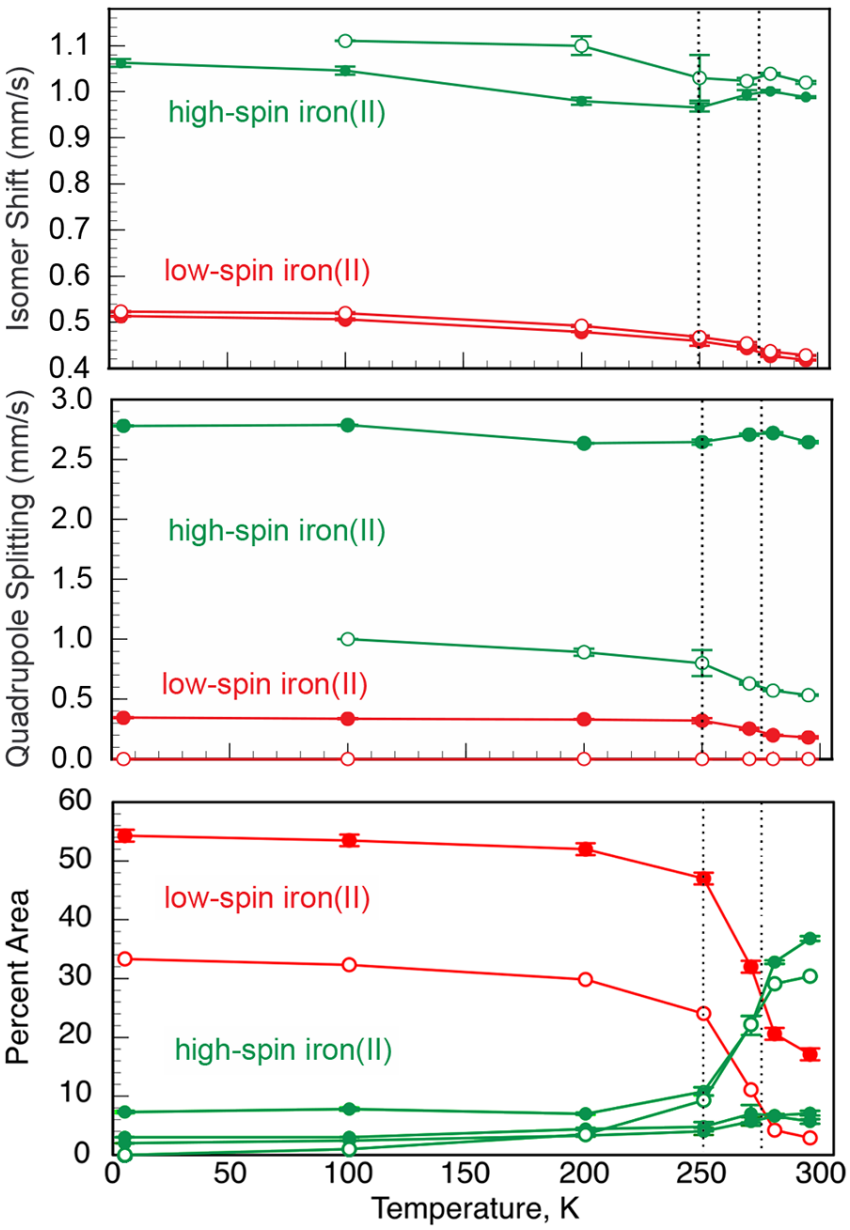

Figure S3.15. Temperature dependence of the weighted average hyperfine parameters and the percent area of high-spin and low-spin sites obtained from fits of the Mössbauer spectra of $Fe(MeTri)_2$. The closed and open symbols correspond to the Fe1 and Fe2 crystallographic sites, respectively, and the dotted lines indicate the temperature region, over which the low- and high-temperature crystallographic phases coexist. In many cases, the uncertainties are smaller than the size of the data points. From the Percent Area plot, it is clear that at 5 K, the central Fe2 ions are fully LS and ca. 10% of the corner Fe1 sites are HS. As temperature increases, both Fe1 and Fe2 ions follow rather parallel curves, suggesting good communication between the iron sites.

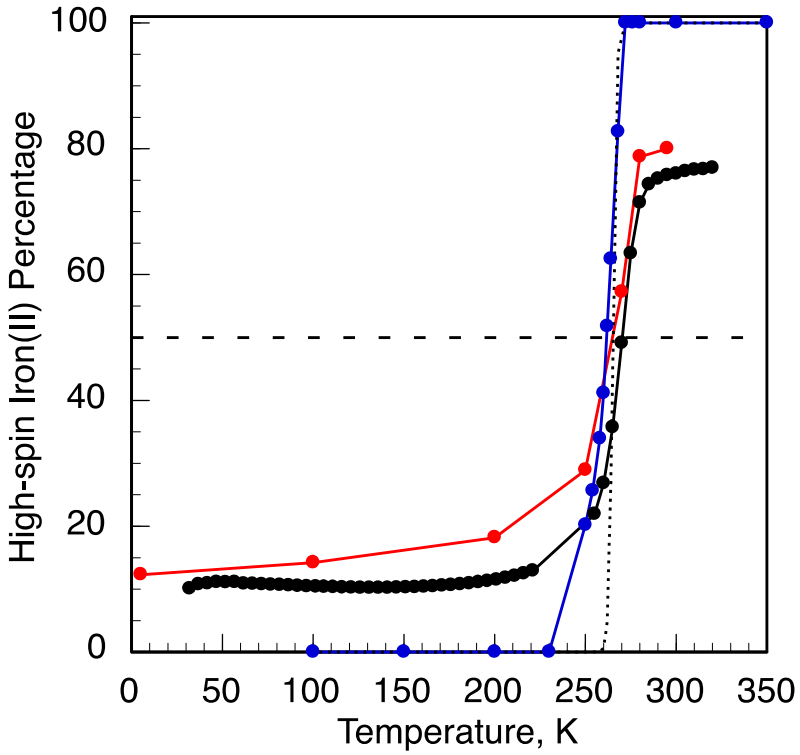

Figure S3.16. The temperature dependence of the high-spin iron(II) percentage obtained from the variable temperature magnetic susceptibility data collected at 0.4 K/min (black), from the Mössbauer results (red), and from the powder X-ray diffraction results (blue). The dotted curve is the sigmoid function $p_{HS} = 100 \frac{1}{1+e^{-T+255}}$.

S3.2 References for Chapter 3 Supporting Information

(1) Ingalls, R. Electric-Field Gradient Tensor in Ferrous Compounds. *Phys. Rev.* **1964**, *133*, A787.
(2) Park, J. G.; Aubrey, M. L.; Oktawiec, J.; Chakarawet, K.; Darago, L. E.; Grandjean, F.; Long, G. J.; Long, J. R. Charge Delocalization and Bulk Electronic Conductivity in the Mixed-Valence Metal–Organic Framework Fe(1,2,3-triazolate)$_2$(BF_4)$_x$. *J. Am. Chem. Soc.* **2018**, *140*, 8526.
(3) Coelho, A. TOPAS-Academic, Version 4.1, Coelho Software, Brisbane, 2007.

Chapter 4: Magnetic Ordering through Itinerant Ferromagnetism in a Metal–Organic Framework

This chapter includes published contents

4.1 Introduction

The development of multifunctional magnets with optimized magnetic properties in concert with other physical properties such as porosity and high magnetoresistance remains a daunting challenge, with promise to enable new applications in green technologies[1] and next-generation data processing and storage.[2,3] For realization of commercial applications, it is crucial for a magnet to exhibit a high magnetic ordering temperature beyond potentially elevated operating temperatures. The vast majority of solid-state permanent magnets with high ordering temperatures are based on itinerant magnetism.[4] In particular, a specific form of itinerant magnetism, known as a double-exchange mechanism, was discovered by Zener in 1951 to explain the coexistence of metallic conductivity and high-temperature ferromagnetism in perovskite mixed-valence manganites, which contain Mn^{III} and Mn^{IV} ions connected by bridging O^{2-} ions.[5] Here, an itinerant electron is delocalized between e_g orbitals of neighboring Mn ions and consequently promotes a parallel alignment of spins for the localized electrons in t_{2g} orbitals, in accordance with Hund's rules. Many such double-exchange solid-state materials, including cobaltites and Heusler alloys, have since been discovered and investigated for applications in spintronics devices.[2,6,7]

As an alternative to traditional solid-state materials, metal–organic frameworks, a subclass of coordination solids, are composed of inorganic building units connected by polytopic organic linkers. Compared to solid-state materials, metal–organic frameworks can offer tremendous synthetic versatility for fine-tuning their chemical and physical properties. For instance, organic linkers with predictable binding modes can be utilized to yield frameworks with unique crystal structures and physical properties, which are easily modified through methods including substitution of electron donating/withdrawing substituents on the ligand, post-synthetic redox chemistry, and metal or linker exchange.[8-10] Furthermore, a combination of a long-range magnetic order and porosity in framework materials could lead to the realization of lightweight permanent magnets and magnetic separation media.[11-13] Nevertheless, the overwhelming majority of framework materials are not permanent magnets, owing primarily to the inability of diamagnetic organic linkers to mediate the strong magnetic coupling requisite for long-range order. Indeed, only a few strategies have been developed to synthesize coordination solids with high magnetic ordering temperatures, including the employment of short diamagnetic inorganic ligands or organic radical ligands, as exemplified by Prussian blue analogues and the amorphous material V(tetracyanoethylene)$_{\sim 2}$, respectively.[11,12,14–18] Alternatively, a potentially powerful, yet unrealized strategy involves the utilization of itinerant charge carriers via a double exchange mechanism. In addition to achieving high ordering temperatures in metal–organic magnets containing diamagnetic linkers, this approach may further provide a means of introducing metallic electronic conductivity.

While double exchange is a recognized phenomenon in solid-state materials,[5–7] examples in coordination solids with organic ligands are limited to molecular compounds.[19,20] Azolate ligands have strong σ-donating and π-accepting abilities, and when coordinated to octahedral metal ions with diffuse d_π orbitals of favorable energies, strong π-*d* conjugation between ligand and metal orbitals may arise.[19,20,21] Furthermore, compact, symmetrical azolate ligands can support crystal structures consisting of infinite metal–azolate chains with short metal–metal distances and an octahedral coordination environment around metal ions, providing efficient pathways for long-range charge transport and magnetic interaction.[23-25] Herein, we report the mixed-valence framework material $Cr(tri)_2(CF_3SO_3)_{0.33}$, which exhibits itinerant ferromagnetism with T_C = 225 K via a double-exchange mechanism.

4.2 Results and discussion

Synthesis and spectroscopic properties. The compound $Cr(tri)_2(CF_3SO_3)_{0.33}$ (Htri = 1*H*-1,2,3-triazole) is formed through a solvothermal reaction between anhydrous $Cr(CF_3SO_3)_2$ and 1*H*-1,2,3-triazole in *N*,*N*-dimethylformamide (see Methods and Supporting Information). The resulting purple solid consists of octahedron-shaped crystals with an edge dimension of ~0.5 μm (Fig. S4.1) and is structurally analogous to reported $M(tri)_2$ (M = Mg, Mn, Fe, Co, Cu, Zn, Cd) materials.[24,26,27] The material has a diamondoid-type structure formed by corner-sharing tetrahedral pentanuclear repeating units (Fig. 1a), where each unit comprises two crystallographically distinct Cr ions bridged by a 1,2,3-triazolate ligand with Cr1-N1 and Cr2-N2 distances of 2.067(4) and 2.031(6) Å, respectively (Fig. 1b). In addition, the pores of the framework are occupied by disordered $CF_3SO_3^-$ ions. A careful analysis of the refined chemical occupancies reveals the presence of 0.34 $CF_3SO_3^-$ ions per Cr ion, which is close to the expected chemical formula of $Cr(tri)_2(CF_3SO_3)_{0.33}$ if each pore within the framework is filled with a single $CF_3SO_3^-$ ion. The presence of inserted $CF_3SO_3^-$ ions was further confirmed by the low BET surface area of 80 $m^2\ g^{-1}$ calculated from an N_2 adsorption isotherm (Fig. S4.2) and elemental analysis for C, H, and N that is consistent with the formula $Cr(tri)_2(CF_3SO_3)_{0.33}$ (see Methods). The presence of charge-balancing $CF_3SO_3^-$ ions in the pores of the framework indicates that the material contains mixed-valence $Cr^{II/III}$ centers (see Supporting Information).

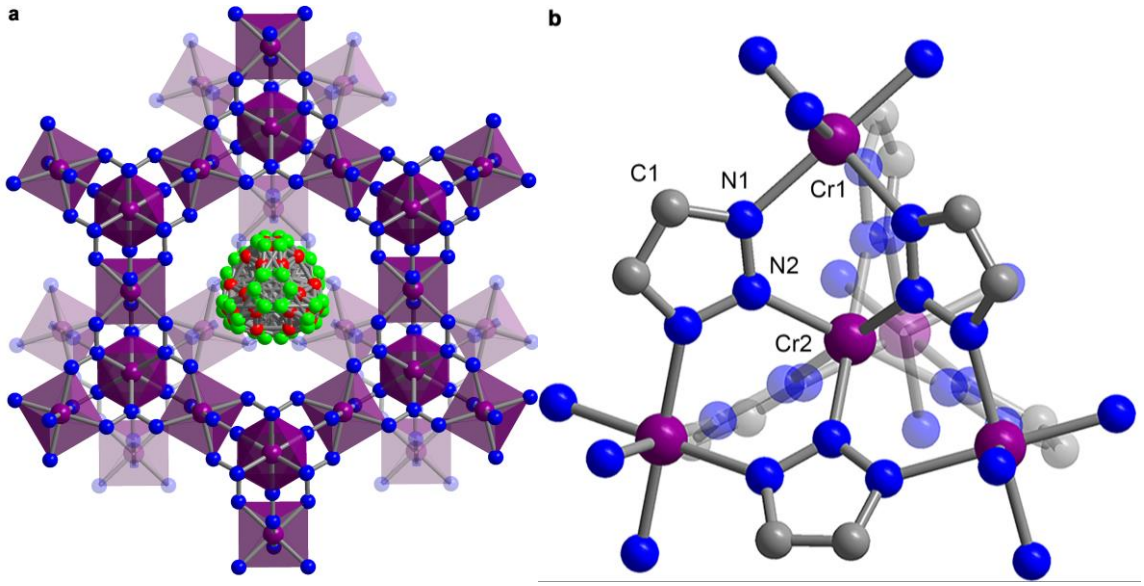

Figure 4.1. Solid-state structures. a, Portions of the Cr–N sublattice of the $Cr(tri)_2(CF_3SO_3)_{0.33}$ structure determined from analysis of powder X-ray diffraction data collected at 360 K, showing continuous chromium-triazolate chains forming a diamondoid-type lattice and a disordered, charge-balancing trifluoromethanesulfonate anion in the pore cavity. **b**, A tetrahedral, pentanuclear repeating unit. Cr, purple; S, yellow; F, green; O, red; N, blue and C, grey; H atoms are omitted for clarity.

A diffuse reflectance UV–vis–near-IR spectrum of $Cr(tri)_2(CF_3SO_3)_{0.33}$ was obtained to confirm and further probe the mixed-valence electronic structure (Fig. 2a). Notably, the spectrum exhibits an intense absorption band in the near-IR region between 5,000 and 12,000 cm^{-1}, with the absorbance increasing continuously to lower energies. We assign the observed band to an intervalence charge-transfer transition between mixed-valence $Cr^{II/III}$ centers. Furthermore, the IR spectrum of $Cr(tri)_2(CF_3SO_3)_{0.33}$ exhibits a broad absorption between 1,500 and 6,000 cm^{-1}, owing to extension of the intervalence charge-transfer transition band into the mid-IR region (Fig. 2b). The absorption band masks most of the expected vibrational modes, leaving few detectable, sharp features. Indeed, absorption bands of similar energies have also been reported for other mixed-valence coordination solids and charge transfer salts.[21,24,28,29] We note that the presence of such low-energy transitions suggests a negligible optical band gap stemming from a near-continuous distribution of mid-gap states.

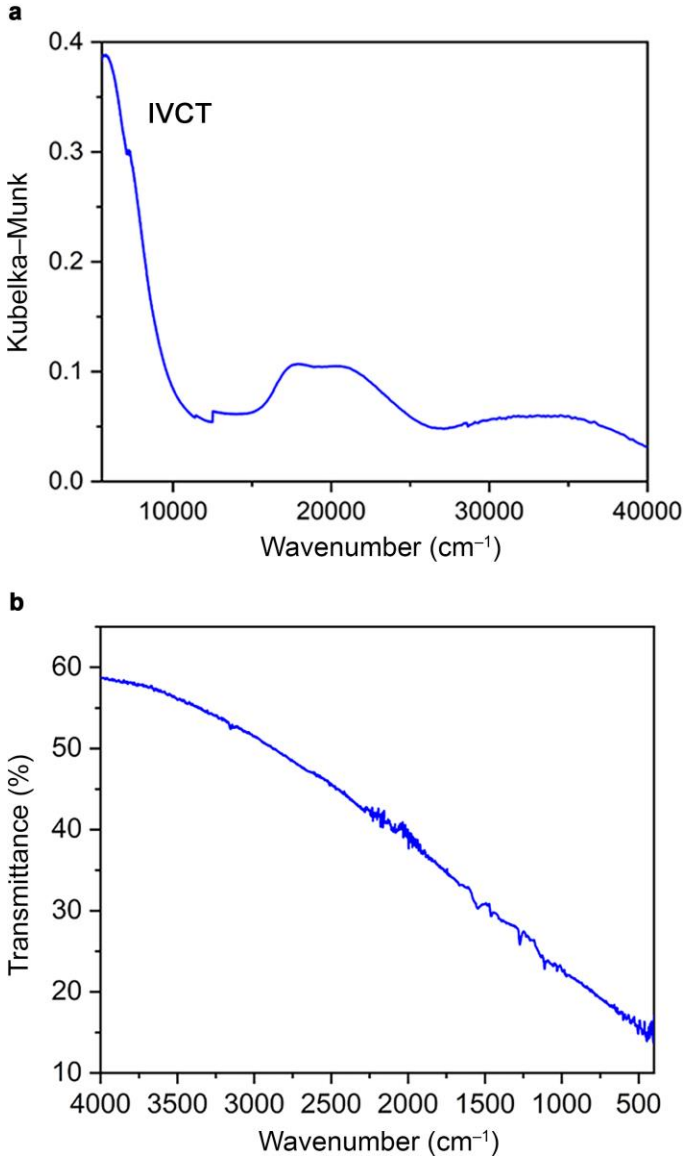

Figure 4.2. Spectroscopic characterization. a, **b**, Diffuse reflectance UV-vis-NIR (**a**) and infrared (**b**) spectra of $Cr(tri)_2(CF_3SO_3)_{0.33}$ collected at 300 K. Intense absorption band below 12,000 cm^{-1} extending to mid-IR region is due to intervalence charge-transfer transition from mixed-valence Cr ions.

Magnetic Properties. Variable-temperature dc magnetic susceptibility measurements were performed to investigate the magnetic properties of $Cr(tri)_2(CF_3SO_3)_{0.33}$, (Fig. 3a). The plot of magnetization versus temperature features a gradual increase in magnetization upon decreasing the temperature from 350 K, followed by a sudden increase below ~250 K. This sharp rise indicates a magnetic phase transition accompanied by an increased magnetic correlation length within the system. The plot exhibits bifurcation of field-cooled and zero-field-cooled curves below the transition temperature, indicative of spontaneous magnetization. Furthermore, a Curie-Weiss fit to the inverse dc susceptibility data from 300 to 350 K affords θ_{CW} = 268 K, with the positive Curie-Weiss temperature suggesting dominant ferromagnetism, consistent with double exchange (see Supporting Information and Fig. S4.3a). The presence of magnetic order was confirmed by ac magnetic susceptibility measurements (Fig. S4.3b-f), which show sharp increases in both the in-phase (χ_M') and the out-of-phase (χ_M'') susceptibilities below 250 K. A precise magnetic ordering temperature was determined as T_C = 225 K by locating the temperature at which χ_M'' undergoes a sharp increase from zero. To the best of our knowledge, $Cr(tri)_2(CF_3SO_3)_{0.33}$ exhibits the highest ferromagnetic ordering temperature among all coordination solids and the highest temperature for any type of magnetic order among structurally characterized metal–organic frameworks, with the previous records being T_C = 107 K for [{Ru_2(*m*-fluorobenzoate)$_4$}$_2$(BTDA-TCNQ)] (BTDA-TCNQ = bis(1,2,5-thiadiazolo)tetracyanoquinodimethane) and T_N = 171 K for $Mn(TCNE)_{3/2}(I_3)_{1/2}$ (TCNE = tetracyanoethylene), respectively.[11,12,30,31] The variable-field magnetization data collected between 3 and 270 K exhibit an S-shaped curve that quickly saturates at a magnetization of 2.39 μ_B mol^{-1} at 3 K, close to the expected value of 2.33 μ_B mol^{-1} for ferromagnetically coupled low-spin Cr^{II} and Cr^{III} centers present in a 2:1 ratio (Fig. 3c). We note that the presence of mixed-valence low-spin $Cr^{II/III}$ ions suggests that the itinerant electrons are housed in the t_{2g} orbitals. The magnetization data do not exhibit a significant hysteresis, with only a small remnant magnetization at all temperatures below T_C, indicating that $Cr(tri)_2(CF_3SO_3)_{0.33}$ is a soft magnet. We note that the cubic crystal structure of the compound, which results in a clear lack of bulk magnetocrystalline anisotropy, is one of the dominant contributors to the observed magnetic behavior with small hysteresis.

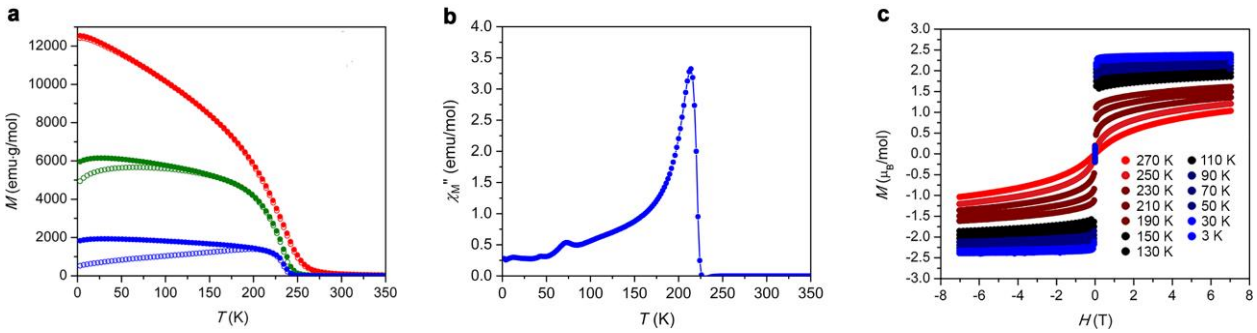

Figure 3.1. Magnetic properties of $Cr(tri)_2(CF_3SO_3)_{0.33}$. a, Variable-temperature zero-field-cooled (open circles) and field-cooled (closed circles) magnetic susceptibility data collected at selected dc magnetic fields of 1000 (red), 100 (green), and 25 Oe (blue). **b**, Variable-temperature out-of-phase ac magnetic susceptibility (χ_M'') collected with ac oscillating magnetic field of 4 Oe at a frequency of 10 Hz and under zero dc magnetic field. The sharp increase of χ_M'' suggests magnetic ordering temperature of T_C = 225 K. **c**, Variable-field magnetization data collected at selected temperatures with a sweep rate of 33 Oe s^{-1}. Saturation magnetization value of 2.39 μ_B mol^{-1} at 3 K consistent with ferromagnetically coupled mixed-valence low-spin $Cr^{II/III}$ ions.

Electronic structure calculations. Insights into the electronic structure of $Cr(tri)_2(CF_3SO_3)_{0.33}$ were obtained using Density Functional Theory (DFT) (see Supporting Information for full computational details). Calculations were performed on the full three-dimensional unit cell, which contains 24 Cr atoms, 48 triazolate ligands, and 8 triflate anions. The results suggest that the ferromagnetic state is lower in energy compared to the antiferromagnetic state by 0.127 eV/Cr atom, in agreement with the magnetic measurements. In the ferromagnetic state, the calculated saturation magnetic moment is 2.41 μ_B, which is in excellent agreement with the experimentally measured value of 2.39 μ_B. The band structure of $Cr(tri)_2(CF_3SO_3)_{0.33}$ (Fig. 4a) near the Fermi energy predominantly consists of spin-down bands with a large density of states and a band dispersion of ~1 eV, suggesting significant spin-polarization. Here, spin polarization is defined as the extent to which the spin is aligned in a particular direction.[32] The projected band structure (Fig. 4b) and projected density of states (Fig. 4d) show that both Cr *d* orbitals and N *p* orbitals of the triazolate ligands contribute to the valence band maximum and the conduction band minimum. Near the Fermi energy, the frontier orbitals of the bands are dominated by the Cr d_π orbitals and N *p* orbitals, with approximately 32% hybridization between them, indicating a strong hybridization between the Cr *d* and N *p* orbitals and π-*d* conjugation. Fig. 4d also highlights spin polarization as illustrated by the substantial peak in the spin-down density at the Fermi energy for both the total and the Cr *d* orbitals. This shows that the Cr d orbitals are primarily contributing to the spin polarized state. The localized charge density (Fig. S4.4) shows alternating high and low charge Cr centers. The Cr centers of lower and higher charges exhibit lower and higher magnetic moments, respectively, consistent with the mixed-valence low-spin $Cr^{II/III}$ centers. Notably, the charge density and projected density of states both indicate spin-polarization. Taken together, these computational results demonstrate a ferromagnetic ground state for $Cr(tri)_2(CF_3SO_3)_{0.33}$, and the high density of spin-polarized bands near the Fermi energy arising from a strong π-*d* hybridization suggests delocalization of electrons in the valence band maximum, consistent with double exchange stemming from the mixed-valence metal centers.

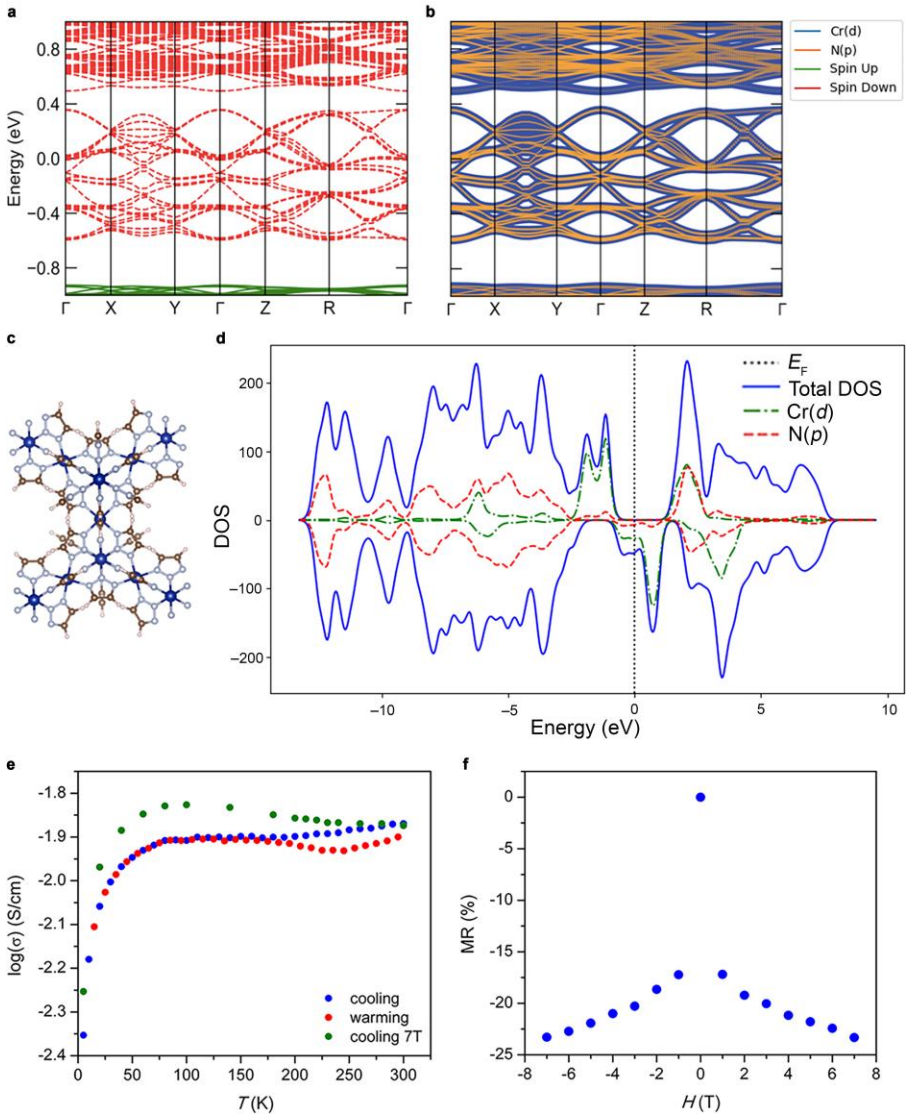

Figure 4.4. Electronic structure calculations and electronic conductivity of $Cr(tri)_2(CF_3SO_3)_{0.33}$. a,b, Total (**a**) and projected (**b**) band structure for the ferromagnetic state, calculated using the Perdew-Burke-Brnzerhof (PBE) functional. The zero of energy is set to the highest occupied state. The symmetry points correspond to Γ = (0,0,0), X = (0.5,0,0), Y = (0,0.5,0), Z = (0,0,0.5), and R = (0.5,0.5,0.5). Dense spin-down bands near the Fermi energy with dominant contributions from strongly hybridized Cr d_π and N *p* orbitals. **c**, The geometry-optimized structure of $Cr(tri)_2(CF_3SO_3)_{0.33}$. Blue, light blue, brown, and white spheres represent Cr, N, C, and H atoms, respectively; $CF_3SO_3^-$ ion has been omitted for clarity. **d**, Partial density of states (pDOS) in arbitrary units for the ferromagnetic state. The zero of energy is set to the highest occupied state denoted by the dotted vertical line. **e**, Variable-temperature conductivity data of $Cr(tri)_2(CF_3SO_3)_{0.33}$. Blue and red spheres represent measurements taken during cooling and warming, respectively. Green spheres represent data collected while cooling under an applied magnetic field of 7 T. The increased conductivity under a magnetic field below T_C consistent with negative magnetoresistance. **f**, Magnetoresistance data of $Cr(tri)_2(CF_3SO_3)_{0.33}$ collected at 5 K under selected dc magnetic fields with maximum negative magnetoresistance of ~23 % at 7 T.

Electronic conductivity and magnetoresistance. Variable-temperature conductivity measurements were performed to investigate the charge transport properties associated with double exchange in $Cr(tri)_2(CF_3SO_3)_{0.33}$ (Fig. 4e and Fig. S4.5). Upon cooling from 300 to 200 K, the conductivity decreases very slightly from $\sigma = 1.4(1) \times 10^{-2}$ to $1.3(1) \times 10^{-2}$ S cm^{-1}. Despite the presence of a slight hysteresis between data measured upon cooling vs warming the sample, the cooling data above 200 K could be fit using the three-dimensional variable-range hopping model (see Supporting Information). Below T_C and down to 80 K, the compound exhibits a conductivity that is nearly temperature-independent, with $\sigma \approx 1.2(1) \times 10^{-2}$ S cm^{-1}. An Arrhenius fit to the data in this temperature range yields a small activation energy of 0.14 meV, suggestive of highly delocalized charge carriers. Upon cooling below 80 K, we observed a decrease in conductivity to $\sigma = 4.4(1) \times 10^{-3}$ S cm^{-1} at 5 K. The low-temperature data are best fit with the Efros–Shklovskii variable-range hopping model, highlighting a transition back to localized small polarons (see Supporting Information).[33] Next, conductivity measurements were performed on the same sample pellet while cooling the cell under an applied field of 7 T. Strikingly, the conductivity increases as the temperature is lowered from 225 to 80 K. At 5 K, $Cr(tri)_2(CF_3SO_3)_{0.33}$ exhibits a maximum negative magnetoresistance of ~23 % (Fig. 4f), representing one of the highest values for any coordination solid.[34–37] The observed barrier-less transport behavior in conjunction with the large negative magnetoresistance is consistent with a double exchange mechanism in $Cr(tri)_2(CF_3SO_3)_{0.33}$. The computational results suggest that the partially filled spin-down bands near the Fermi level give rise to a current density that is carried mainly by spin-down charge carriers. Due to the spin-polarized current, the presence of any tunneling junctions consisting of ferromagnetic domains/layers can yield large magnetoresistance. As $Cr(tri)_2(CF_3SO_3)_{0.33}$ is a soft ferromagnet, the material most likely consists of randomly aligned ferromagnetic domains under zero applied magnetic field. Under an applied magnetic field, the ferromagnetic domains can align parallel to each other, allowing a facile transport of spin-polarized currents. Indeed, large negative magnetoresistance has commonly been observed in solid-state materials with itinerant ferromagnetism.[38,39]

4.3 Conclusions

The foregoing results demonstrate the observation of itinerant ferromagnetism in a metal–organic framework, which gives rise to an magnetic ordering temperature of T_C = 225 K and high magnetoresistance. Importantly, the employed synthetic approach of utilizing π-d conjugation between organic linkers and mixed-valence metal centers with diffuse d_π orbitals provides a general blueprint from which to design materials with enhanced magnetic and charge transport properties, given the vast chemical versatility offered by metal–organic frameworks.

4.4 Methods

Synthesis of $Cr(tri)_2(CF_3SO_3)_{0.33}$. All handling of $Cr(tri)_2(CF_3SO_3)_{0.33}$ was performed under a dry N_2 or Ar atmosphere. Liquid 1*H*-1,2,3-triazole (1.04 g, 15.0 mmol) was added to a 20-mL glass scintillation vial containing a solution of $Cr(CF_3SO_3)_2$ (1.75 g, 5.00 mmol) in 10 mL of DMF. The vial was sealed with a polytetrafluoroethylene-lined cap and heated at 120 °C for 3 days. The resulting suspension was cooled to 25 °C and filtered with a Nylon membrane filter to yield a dark purple powder. The powder was washed by soaking in DMF (3 × 15 mL) and then in

dichloromethane (4 × 15 mL), and was dried under dynamic vacuum (<10 μbar) at 130 °C for 48 h to afford 0.356 g (30%) of product as a purple microcrystalline powder. Anal. Calcd for $CrC_{4.33}H_4N_6FS_{0.33}O$: C, 21.91; H, 1.70; N, 35.41. Found: C, 22.24; H, 1.44; N, 35.21.

Magnetic measurements. In a glovebox under an N_2 atmosphere, a sample was prepared by adding an activated powder into a 5-mm-inner-diameter quartz tube containing a raised quartz platform. The sample powder was restrained with a plug of compacted glass wool to prevent crystallite torqueing during measurements. The quartz tube was transferred to a Schlenk line and evacuated until the internal pressure reached 30 mTorr. The tube was cooled in liquid N_2 and flame-sealed under static vacuum. All magnetic measurements were performed using a Quantum Design MPMS2 SQUID magnetometer from 3 to 350 K at applied magnetic fields ranging from 0 to ±7 T. The ac susceptibility measurements were performed with an oscillating field of 4 Oe with a frequency from 1 to 100 Hz. Diamagnetic corrections were applied to the data using Pascal's constants to give $\chi_D = -0.00009744$ emu mol^{-1}.

Electrical conductivity measurements. Conductivity measurements were performed using a home-built four-contact cell (Fig. S4.10a). In a glovebox under an Ar atmosphere, a sample pellet was manually pressed in a cell with a known inner cell diameter. While pressed, the cell was sealed with Torr Seal® low-vapor-pressure epoxy. When the epoxy dried completely, the cell was removed from the press for the sample pellet thickness to be measured using a caliper. Room temperature conductivity measurement was performed using a Bio-Logic VMP-3 multipotentiostat fitted to the Ar glovebox. Variable-temperature conductivity measurements were performed in a Quantum Design MPMS2 SQUID magnetometer with a modified sample rod that accommodates ten 26 AWG silver coated copper cables sealed at the top of the rod with an air tight Swagelock fitting and Torr Seal® low-vapor-pressure epoxy. The airtight sample cell was attached to the SQUID sample rod and inserted into the cryostat-equipped SQUID chamber at 300 K. *I*-*V* profiles between 5 and 300 K were collected with a Bio-Logic SP200 potentiostat by scanning current between ±50 μA and the sample cell allowed to equilibrate for at least 30 min between each measured temperature. All data collected were ohmic within a ±50 μA window and were then modelled with Ohm's Law, $E \times \sigma = j$, where E is the applied electric field and j is the current density, to determine the sample conductivity with σ with the units of S cm^{-1}. Magnetoresistance measurements were performed by applying magnetic fields ranging from 0 to ±7 T during *I*-*V* profile collections. Data were fitted to charge-transport models as described in the Supporting Information.

High-resolution powder X-ray diffraction. The powder sample was packed into a 1.0-mm boron-rich glass capillary tube inside a glovebox under an N_2 atmosphere. The capillary was flame-sealed and placed inside a Kapton tube that was sealed on both ends with epoxy. High-resolution synchrotron X-ray powder diffraction data were collected at Beamline 11-BM at the Advanced Photon Source (APS) at Argonne National Laboratory. Diffraction patterns were collected at 360, 220, and 120 K with a wavelength of 0.412685 Å. Discrete detectors covering an angular range from −6 to 16° in 2θ were scanned over a 34° range of 2θ, with data points collected every 0.001° in 2θ and at scan speed of 0.01° s^{-1}. For all diffraction data from Beamline 11-BM, precise unit-cell dimensions were determined by performing Pawley refinements, after which Rietveld refinements were performed using the software package TOPAS-Academic[40]. High-resolution synchrotron X-ray powder diffraction data between 270 and 5 K (Fig. S4.12a) were collected at Beamline BM31 at the European Synchrotron Radiation Facility (ESRF) with the wavelength of 0.49754758 Å.

Powder neutron diffraction. Powder neutron diffraction data were collected on the POWGEN instrument at the Spallation Neutron Source (SNS) at Oak Ridge National Laboratory (ORNL). Approximately one gram of sample was loaded into a vanadium POWGEN Automatic Changer can in an He-filled glovebox. Data were collected at the selected temperatures of 300, 150, and 10 K in the high-resolution mode[41].

4.5 Acknowledgements

This research was supported by National Science Foundation (NSF) Award No. DMR-1611525, with the exception of the measurement and analysis of the magnetic data, which were supported by the Nanoporous Materials Genome Center of the U.S. Department of Energy, Office of Basic Energy Sciences, Division of Chemical Sciences, Geosciences and Biosciences under Award No. DE-FG02-17ER16362. Powder X-ray diffraction data were collected at Beamline 11-BM at the Advanced Photon Source, operated by Argonne National Laboratory, and beamline BM31 at the European Synchrotron Radiation Facility (ESRF), Grenoble, France. We are grateful to Local Contact at the ESRF for providing assistance in using beamline BM31. Use of the Advanced Photon Source at Argonne National Laboratory was supported by U.S. Department of Energy, Office of Science, Office of Basic Energy Sciences, under Contract No. DE-AC02-06CH11357. Data from Beamline 11-BM were collected as part of the 2018 Modern Methods in Rietveld Refinement and Structural Analysis workshop, a school supported by the US national Committee for Crystallography and the American Crystallographic Association. Neutron diffraction data were collected at the POWGEN beamline at the Spallation Neutron Source, a DOE Office of Science User Facility operated by the Oak Ridge National Laboratory. Soft X-ray absorption spectroscopy data were collected at Beamline 8.0.1 at the Advanced Light Source of Lawrence Berkeley National Laboratory, a Department of Energy Office of Science User Facility under contract no. DE-AC02-05CH11231. Electronic structure calculations utilized an award of computer time provided by ASCR Leadership Computing Challenge (ALCC) program and resources of the National Energy Research Scientific Computing Center (NERSC), a U.S. Department of Energy Office of Science User Facility operated under Contract No. DE-AC02-05CH11231. Additional computation resources were provided by the Minnesota Supercomputing Institute (MSI) at the University of Minnesota. T.R. thanks the Welch Foundation (Grant No. N-2012-20190330) for funding. In addition, we thank J. Oktawiec, S. H. Lapidus, X. Wenqian, P. Khalifah, Q. Zhang, M. J. Kirkham, Y.-S. Liu, and G. Ren for discussions and experimental assistance, and Prof. T. D. Harris for editorial assistance. We also thank the National Science Foundation and National GEM Consortium for providing graduate fellowship supports for J.G.P and B.A.C, respectively.

4.6 References

(1) Gutfleicsch, O. et al. Magnetic materials and devices for the 21st century: stronger, lighter and more energy efficient. *Adv. Mater.* **23**, 821-842 (2011).
(2) Felser, C., Fecher, G. H. & Balke, B. Spintronics: a challenge for materials science and solid-state chemistry. *Angew. Chem. Int. Ed.* **46**, 668-699 (2007).
(3) Coronado, E., Palacio, F. & Veciana, J. Molecule-based magnetic materials. *Angew. Chem. Int. Ed.* **42**, 2570-2572 (2003).
(4) Kübler, J. *Theory of itinerant electron magnetism* (Oxford Univ. Press, 2000).
(5) Zener, C. Interaction between the *d*-shells in the transition metals. II. Ferromagnetic compounds of manganese with perovskite structure. *Phys. Rev.* **82**, 403-405 (1951).
(6) Briceño, G., Chang, H., Sun, X., Schultz, P. G. & Xiang, X.-D. A Class of Cobalt Oxide Magnetoresistance Materials Discovered with Combinatorial Synthesis. *Science* **270**, 273-275 (1995).
(7) Şaşıoğlu, E., Sandratskii, L. M. & Bruno, P. Role of conduction electrons in mediating exchange interactions in Mn-based Heusler alloys. *Phys. Rev. B* **77**, 064417 (2008).
(8) Yaghi, O. M. et al. Reticular synthesis and the design of new materials. *Nature* **423**, 705-714 (2003).
(9) Calbo, J., Golomb, M. J. & Walsh, A. Redox-active metalo-organic frameworks for energy conversion and storage. *J. Mater. Chem. A* **7**, 16571-16597 (2019).
(10) Yin, Z., Wan, S., Yang, J., Kurmoo, M. & Zeng, M.-H. Recent advances in post-synthetic modification of metal–organic frameworks: New types and tendem reactions. *Coord. Chem. Rev.* **378**, 500-512 (2019).
(11) Dechambenoit, P. & Long, J. R. Microporous magnets. *Chem. Soc. Rev.* **40**, 3249-3265 (2011).
(12) Thorarinsdottir, A. E. & Harris, T. D. Metal–Organic Framework Magnets. *Chem. Rev.* **120**, 8716-8789 (2020).
(13) Kosaka, W. et al. Gas-responsive porous magnet distinguishes the electron spin of molecular oxygen. *Nat. Commun.* **9**, 5420 (2018).
(14) Ruiz, E., Rodríguez-Fortea, A., Alvarez, S. & Verdaguer, M. Is it possible to get high T_c magnets with Prussian blue analogues? A theoretical prospect. *Chem Eur. J.* **11**, 2135-2144 (2005).
(15) Mallah, T., Thiébaut, S., Verdaguer, M., Veillet, P. High-Tc Molecular-Based Magnets: Ferrimagnetic Mixed-Valence Chromium(III)-Chromium(II) Cyanide with Tc at 240 and 190 Kelvin. *Science* **262**, 1554-1557 (1993).
(16) Ferlay, S., Mallah, T., Ouahès, R., Veillet, P., Verdaguer, M. A room-temperature organometallic magnet based on Prussian blue. *Nature* **378**, 701-703 (1995).
(17) Holmes, S. M., Girolami, G. S. Sol-Gel Synthesis of $KV^{II}[Cr^{III}(CN)_6]\cdot 2H_2O$: A Crystalline Molecule-Based Magnet with a Magnetic Ordering above 100 °C. *J. Am. Chem. Soc.* **121**, 5593-5594 (1999).
(18) Manriquez, J. M., Yee, G. T., McLean, R. S., Epstein, A. J. & Miller, J. S. A room-temperature molecular/organic-based magnet. *Science* **252**, 1415-1417 (1991).
(19) Bechlar, B. et al. High-spin ground states via electron delocalization in mixed-valence imidazolate-bridged divanadium complexes. *Nat. Chem.* **2**, 362-368 (2010).

(20) Gaudette, A. I. et al. Electron hopping through double-exchange coupling in a mixed-valence diiminobenzoquinone-bridged Fe2 complex. *J. Am. Chem. Soc.* **137,** 12617-12626 (2015).
(21) Schulze, B. & Schubert, U. S. Beyond click chemistry – supramolecular interactions of 1,2,3-triazoles. *Chem. Soc. Rev.* **43**, 2522-2571 (2014).
(22) Aubrey, M. L. et al. Electron delocalization and charge mobility as a function of reduction in a metal–organic framework. *Nat. Mater.* **17**, 625-632 (2018).
(23) Zhang, J. P., Zhang, Y. B., Lin, J. B. & Chen, X. M. Metal azolate frameworks: from crystal engineering to functional materials. *Chem. Rev.* **112**, 1001-1033 (2012).
(24) Park, J. G. et al. Charge delocalization and bulk electronic conductivity in the mixed-valence metal–organic framework Fe(1,2,3-triazolate)$_2$(BF_4)$_x$. *J. Am. Chem. Soc.* **140**, 8526-8534 (2018).
(25) Brunschwig, B. S., Creutz, C. & Sutin, N. Optical transitions of symmetrical mixed-valence systems in the class II-III transition regime. *Chem Soc. Rev.* **31**, 168-184 (2002).
(26) Gándara, F. et al. Porous, conductive metal–triazolates and their structural elucidation by the charge-flipping method. *Chem. Eur. J.* **18**, 10595-10601 (2012).
(27) Zhou, X.-H., Peng, Y.-H., Du, X.-D., Zuo, J.-L. & You, X.-Z. Hydrothermal syntheses and structures of three novel coordination polymers assembled from 1,2,3-triazolate ligands. *Cryst. Eng. Comm.* **11**, 1964-1970 (2009).
(28) Collman, J. P. et al. Synthetic, electrochemical, optical, and conductivity studies of coordination polymers of iron, ruthenium, and osmium octaethylporphyrin. *J. Am. Chem. Soc.* **109**, 4606-4614 (1987).
(29) Tanner, D. B., Jacobsen, C. S., Garito, A. F. & Heeger, A. J. Infrared studies of the energy gap in tetrathiofulvalene-tetracyanoquinodimethane (TTF-TCNQ). *Phys. Rev. B* **13**, 3381-3404 (1976).
(30) Motokawa, N., Miyasaka, H., Yamashita, M. & Dunbar, K. R. An Electron-Transfer Ferromagnet with T_c=107 K Based on a Three-Dimensional $[Ru_2]_2$/TCNQ System. *Angew. Chem. Int. Ed.* **47**, 7760-7763 (2008).
(31) Stone, K. H. et al. $Mn^{II}(TCNE)_{3/2}(I_3)_{1/2}$–A 3D Network-Structured Organic-Based Magnet and Comparison to a 2D Analog. *Adv. Mater.* **22**, 2514-2519 (2010).
(32) Kessler, J. *Polarized Electrons* (Springer-Verlag Berlin Heidelberg, 1985).
(33) Efros, A. L. & Shklovskii, B. I. Coulomb gap and low temperature conductivity of disordered systems. *J. Phys. C: Solid State Phys.* **8**, L49-56 (1975).
(34) Raju, N. P. et al. Anomalous magnetoresistance in high-temperature organic-based magnetic semiconducting V(TCNE)$_x$ films. *J. Appl. Phys.* **93**, 6799 (2003).
(35) Coronado, E., Prieto-Ruiz, J. P. & Prima-Garcia, H. Spin polarization in electrodeposited thin films of the molecule-based magnetic semiconductor $Cr_{5.5}(CN)_{12}\cdot 11.5H_2O$. *Chem. Commun.* **49**, 10145-10147 (2013).
(36) Lu, Y. et al. Thin-film deposition of an organic magnet based on vanadium methyl tricyanoethylenecarboxylate. *Adv. Mater.* **26**, 7632-7636 (2014).
(37) Black, N. et al. Giant negative magnetoresistance in Ni(quinoline-8-selenoate)$_2$. *Phys. Chem. Chem. Phys.* **20**, 514-519 (2018).
(38) Coey, J. M. D. & Venkatesan, M. Half-metallic ferromagnetism: Example of CrO_2. *J. Appl. Phys.* **91**, 8345-8350 (2002)
(39) Xiao, J. Q., Jian, J. S. & Chien, C. L. Giant magnetoresistance in nonmultilayer magnetic systems. *Phys. Rev. Lett.* **68**, 3749-3752 (1992).

(40) Coelho, A. A. TOPAS-Academic, version 5 (Coelho Software, 2017)
(41) Huq, A. et al. POWGEN: rebuild of a third-generation powder diffractometer at the Spallation Neutron Source. *J. Appl. Cryst.* **52**, 1199-1201 (2019).

Chapter 4 Supporting Information

S4.1 Definition of compound

$Cr(tri)_2(CF_3SO_3)_{0.33}$ (Htri = 1*H*-1,2,3-triazole)

S4.2 Additional Methods

Materials. All manipulations were performed under an Ar atmosphere in an Mbraun glovebox or using standard Schlenk techniques. Anhydrous *N*,*N*-dimethylformamide (DMF) and dichloromethane were obtained from a JC Meyer solvent system and stored over 3- or 4-Å molecular sieves prior to use. The molecule 1*H*-1,2,3-triazole (98% purity) was purchased from VWR International LLC, deoxygenated with three successive freeze-pump-thaw cycles, and dried over 4-Å molecular sieves before use. Anhydrous $Cr(CF_3SO_3)_2$ was prepared according to a previously reported procedure.[1] Elemental analyses for C, H, and N were obtained from the Microanalytical Laboratory at the University of California, Berkeley.

Soft X-ray Absorption Spectroscopy. In an Ar atmosphere glovebox, samples of $Fe(tri)_2$ (prepared according to a previously reported procedure[2]) and $Cr(tri)_2(CF_3SO_3)_{0.33}$ were loaded on carbon tape on a Cu sample puck. Samples were transferred to an airtight sample holder, transferred to the end station of beamline 8.0.1 of the Advanced Light Source at Lawrence Berkeley National Laboratory, and evacuated to ultrahigh vacuum (10^{-9} torr). Spectra were collected in both total-electron-yield (TEY) and total-fluorescence-yield (TFY) mode. TFY data are presented here to ensure the spectra are reflective of the bulk sample. Reference spectra were collected on samples of hexagonal boron nitride before and after each measurement to calibrate the monochromator energy. XAS spectra were collected at room temperature from energies well-below to well-above the region of interest. Data were collected on three different spots on the samples and combined prior to normalization. Normalization was performed according to an established procedure: (1) The sample signal was divided by the incident intensity measured from the sample drain current from a freshly coated gold mesh inserted into the beam path before the X-rays interact with the sample; (2) A linear background is removed from the collected data by fitting a line to the featureless, low-energy data region of the spectrum; (3) The spectrum is normalized by setting the low-energy region to 0 and the linear, high-energy region to unity.

Surface area measurement. Gas adsorption isotherms for pressures in the range of 0-1 bar were measured using a Micrometrics ASAP2020 gas adsorption analyser instrument. In an N_2-filled glovebox, the samples were transferred to a pre-weighted analysis tube and capped with a Micrometrics TranSeal. The analysis tube containing the sample was transferred to a Micrometrics Smart VacPrep instrument and evacuated by heating to 130 °C with a ramp rate of 2 °C min^{-1} under dynamic vacuum for 48 h, until an outgas rate of <3 μbar min^{-1} was achieved. The evacuated tube was carefully transferred to an electronic balance and weighed to determine the sample mass. The analysis tube was then transferred to an analysis port of the Micrometrics ASAP2020 instrument. An N_2 isotherm at 77 K was measured using a UHP-grade gas source. For the determination of surface areas, the Langmuir and BET methods were applied using Micrometrics software, assuming an N_2 cross-sectional area of 16.2 $Å^2$ $molecule^{-1}$.

Infrared spectroscopy. Room temperature infrared spectrum was collected using a Perkin Elmer Spectrum FT-IR/FT-FIR spectrometer with an attenuated total reflectance accessory (ATR) with a home-built N_2 glove bag attachment for air-sensitive compounds. For variable-temperature measurements, infrared spectra were collected using a Bruker Vertex 70 spectrometer equipped with a glowbar source, KBr beamsplitter, and a liquid nitrogen cooled mercury-cadmium-telluride detector. A custom-built diffuse reflectance system was used for all measurements. Sample temperature was controlled by an Oxford Instruments OptistatDry TLEX cryostat, and sample atmosphere was controlled by a Micromeritics ASAP 2020Plus gas sorption analyzer. In a typical experiment, material was dispersed in dry KBr (10 wt %) in an Ar-filled glovebox and evacuated under turbovac. Spectra were collected at various temperatures until no further changes were observed.

UV-visible-NIR diffuse reflectance spectroscopy. UV-vis-NIR diffuse reflectance spectra were collected using a CARY 5000 spectrophotometer interfaced with Varian Win UV software. The sample was prepared in an Ar-filled glovebox and held in a Praying Mantis air-free diffuse reflectance cell. Barium sulfate powder was used as a non-abosrbing matrix. The spectrum was collected in $F(R)$ vs wavenumber, where $F(R)$ is the Kublelka-Munk conversion $F(R) = (1 - R)^2/2R$ of the raw diffuse reflectance, R.

Scanning electron microscopy. The sample for scanning electron microscopy (SEM) imaging was prepared by dispersing a powder sample of $Cr(tri)_2(CF_3SO_3)_{0.33}$ in dichloromethane followed by drop casting onto a silicon wafer. SEM images were obtained using a Hitachi S-5000 instrument at 10 keV and 4 nA.

S4.3 Additional Discussion

Synthesis of $Cr(tri)_2(CF_3SO_3)_{0.33}$. For a successful synthesis of $Cr(tri)_2(CF_3SO_3)_{0.33}$ with high crystallinity, a careful choice of Cr^{II} salt was found to be crucial. For instance, a presence of any coordinating anions during reaction resulted in the formation of different phase or defects. Among Cr^{II} salts screened, the weakly coordinating trifluoromethanesulfonate anion with high thermal stability yielded the best result. Despite reactions under a rigorously air free condition, spontaneous oxidation of some Cr^{II} ions resulted in mixed-valence $Cr(tri)_2(CF_3SO_3)_{0.33}$ material. This is could be due to reduction of protons on 1*H*-1,2,3-triazole ligands, forming H_2 gas. Though unsuccessful, among numerous attempts to isolate valence-pure $Cr(tri)_2$ include using bulky anions such as tetraphenylborate to prevent insertion into the pores of the framework,[3] using Cr^0 sources to maintain a reducing chemical environment during reactions,[4] and post-synthetic reduction of mixed-valence $Cr(tri)_2(CF_3SO_3)_{0.33}$ material.[5]

Structure solution and Rietveld refinement. The data analysis was performed with the TOPAS software.[6] In the Rietveld refinements,[7] the MOF was described using the published cubic structure (space group *Fd*-3*m*, a = 16.65075(17) Å).[2] The triflate anion was found to be disordered in the pore of the MOF. To model the structure, one triflate anion was placed on a general position (with site multiplicity of 192), described as a rigid body in *Z*-matrix notation, and the fractional coordinates and one general site occupancy factor were freely refined with the simulated annealing algorithm.[8] Once a global minimum was reached, the crystal structures were subjected to Rietveld refinement, in which the fractional coordinates and one general site occupancy factor were refined together with all profile and lattice parameters. For the 360 K pattern, the refinement resulted in site occupancy of 0.34 that corresponds to 0.33 anions to one Cr atom (see Supplementary Table S4.2).

Magnetic measurements and powder neutron diffraction data. At 350 K, $Cr(tri)_2(CF_3SO_3)_{0.33}$ exhibits the magnetic susceptibility-temperature product, $\chi_M T$, of 10.7 emu·K/mol, which is larger than the expected value of 1.29 emu·K/mol for uncoupled S = 3/2 Cr^{3+} and S = 1 low-spin Cr^{2+} with 1:2 ratio. Furthermore, $\chi_M T$ value increases significantly with decreasing temperature. This high temperature behavior is indicative of a strong magnetic interaction between paramagnetic centers. Indeed, high temperature region of inverse dc susceptibility data is poorly described by Curie-Weiss law (Fig. S4.3a). Thus, magnetic susceptibility data from 300 to 350 K was used for a Curie-Weiss fit to yield C = 2.55 emu K mol^{-1} and θ_{CW} = 268 K with R^2 = 0.994. We note that the Curie-Weiss fits on the magnetic data of many radical-bridged metal-organic ferrimagnets also yield positive θ_{CW} values, and that Cr^{II} ions are known to reduce redox-active ligands, such as pyrazine, in framework materials. We believe this scenario is not a possibility in $Cr(tri)_2(CF_3SO_3)_{0.33}$. Nitrogen–nitrogen and carbon–nitrogen bond distances in the ligands of the framework (Supplementary Table S4.2) are similar to those found in other triazolate-based materials, though we note that full metal-to-ligand electron transfer in $Cr(tri)_2(CF_3SO_3)_{0.33}$ would likely result in only partial reduction of each ligand, suggesting that bond distances are not completely conclusive of the redox state of the triazolate ligands. However, direct evidence for the absence of organic radical character in $Cr(tri)_2(CF_3SO_3)_{0.33}$ is provided by nitrogen K-edge X-ray absorption spectroscopy (Figure S4.11), which probes excitations from nitrogen 1s to 2p orbitals. A comparison of nitrogen K-edge XAS data for $Fe(tri)_2$ (for which Mössbauer and EPR spectroscopy provide no evidence of ligand-centered radicals) and $Cr(tri)_2(CF_3SO_3)_{0.33}$ indicate no

change in the primary transition at 401.2 eV. A metal-to-ligand electron transfer in $Cr(tri)_2(CF_3SO_3)_{0.33}$ would result in population of a ligand π^* orbital, which would result in a suppression of this transition intensity and/or a shift to lower energies. As such, nitrogen K-edge XAS support an assignment of Cr mixed-valency, rather than ligand reduction. Consequently, the observed positive θ_{CW} value in $Cr(tri)_2(CF_3SO_3)_{0.33}$ arise from the ferromagnetic double-exchange contribution.

Upon the onset of magnetic ordering, variable-temperature ac magnetic susceptibility data exhibits a strong peak in in-phase (χ_M') and out-of-phase (χ_M'') susceptibilities (Fig. S4.3b-f). Both χ_M' and χ_M'' susceptibility plots display small frequency dependencies, with the maximum peak positions shifting to higher temperatures with increasing ac frequencies. Such frequency dependent ac susceptibility peaks are often attributed to glassy magnetic behavior from spin frustration. For quantifying glassiness, Mydosh parameter, φ, may be calculated, defined as the slope in T_f vs log(ν) curve normalized at $T_f(0)$, where T_f is the freezing temperature defined as the peak maximum in χ_M' at each frequency, $T_f(0)$ is the freezing temperature defined as the peak maximum in χ_M' extrapolated at log(ν) = 0, and log(ν) is the logarithm of the ac frequency.[9] For $Cr(tri)_2(CF_3SO_3)_{0.33}$, ac susceptibility data at 1, 10, 100 Hz were used to estimate the Mydosh parameter, yielding φ = 0.01. The estimate Mydosh parameter indicates that $Cr(tri)_2(CF_3SO_3)_{0.33}$ may be classified as a spin glass rather than a superparamagnet or a cluster glass. However, unlike in most frustrated spin-glass materials, $Cr(tri)_2(CF_3SO_3)_{0.33}$ exhibits a variable-field magnetization data with a magnetization moment that quickly saturates at a small applied field (Fig. 3b). Also, a small frustration parameter $f = |\theta_{CW}|/T_C$ ~1.2 indicates that the spin frustration in $Cr(tri)_2(CF_3SO_3)_{0.33}$ is negligible and long-ranged magnetic ordering is feasible. Indeed, the neutron diffraction data (Fig. S4.8b) at 150 K exhibit a notable increase in the diffraction peak intensities from magnetic scattering, supporting a long-ranged magnetic ordering. We note that a χ_M'' susceptibility data exhibits a smaller peak at a lower temperature ~75 K, which exhibits a larger frequency dependence with φ = 0.11. Furthermore, the neutron diffraction data suggest disappearance of magnetic scattering at 10 K, with nearly overlapping 300 and 10 K diffraction patterns. While we have not investigated further, the low-temperature frequency-dependent χ_M'' peak and neutron diffraction data suggest a magnetic phase transition such as re-entrant spin glass, as observed in some double-exchange solids at intermediate doping levels.[10,11] Investigation of the magnetic domain size and redox dependent magnetism in $Cr(tri)_2(CF_3SO_3)_{0.33}$ presents an intriguing area for further study.

Electrical conductivity measurements and charge transport mechanisms. For investigation of temperature-dependent charge transport mechanism, variable-temperature conductivity data was plotted as Fig. S4.5. Log(σ) data for polaronic nearest-neighbor hopping (Eqn 1), Efros-Shklovskii variable-range hopping (Eqn 2), and three-dimensional variable-range hopping (Eqn 3) models are expected to follow linear T^{-1}, $T^{-\frac{1}{2}}$, and $T^{-\frac{1}{4}}$ temperature dependences, respectively.

(1) $$\sigma T = \sigma_0 e^{-\frac{E_A}{k_B T}}$$

(2) $$\sigma = \sigma_0 e^{-(\frac{T_0}{T})^{\frac{1}{2}}}$$

(3) $$\sigma = \sigma_0 e^{-(\frac{T_0}{T})^{\frac{1}{4}}}$$

In Eqn 1, 2, and 3, σ is the conductivity, T is temperature, σ_0 is the pre-exponential factor, E_A is the thermal energy barrier to hopping, k_B is the Boltzmann constant, and T_0 is the characteristic temperature.

Notably, variable-temperature conductivity data of $Cr(tri)_2(CF_3SO_3)_{0.33}$ exhibits distinct temperature dependences at high, intermediate, and low temperature regimes for $T > 200$ K, 200 K $> T >$ 80 K, and $T < 80$ K. Prior to the discussion, we note that variable-temperature synchrotron powder X-ray diffraction measurements was performed between 5 and 270 K to investigate potential structural phase transitions between three temperature regimes (Fig. S4.8a). However, $Cr(tri)_2(CF_3SO_3)_{0.33}$ maintains a cubic $Fd\bar{3}m$ space group at all investigated temperatures without any noticeable indication of a structural phase change.

For high temperature regime, although a precise determination of charge transport mechanism is challenging due to the presence of hysteresis, three-dimensional variable-range hopping model on the data collected while cooling the sample yielded a satisfactory fit. An Arrhenius fit to the data yields an activation energy of 4.2 meV. We believe the observed hysteresis is an intrinsic property of $Cr(tri)_2(CF_3SO_3)_{0.33}$. The conductivity at 300 K measured before and after the measurement was reversible. To maintain a constant pressure on the pallet at all measured temperatures, conductivity measurement cell was designed using a material with a low coefficient of thermal expansion. We note that the observed hysteresis could be due to magnetic polaron formation near magnetic ordering temperature and needs further study.[12]

At the intermediate temperature regime, conductivity data exhibits a weak temperature dependence. To approximate the activation energy for charge hopping, data was tentatively fitted using an Arrhenius equation, yielding a small value of 0.14 meV. We highlight that a notable decrease in activation energy from 4.2 meV to 0.14 meV and a crossover in charge transport mechanism occur near the ferromagnetic ordering temperature, strongly indicating double exchange in $Cr(tri)_2(CF_3SO_3)_{0.33}$.

For the low temperature regime, data is best fitted to Efros-Shklovskii variable-range hopping model. We note that the temperature at which the observed transition in charge transport mechanism occurs is similar to that of the second magnetic phase transition at ~75 K observed through ac magnetic susceptibility measurements. Further study on identification of the low temperature magnetic phase transition and the corresponding magnetic structure may yield a better understanding on the physical reasoning behind the low temperature Efros-Shklovskii variable-range transport mechanism in $Cr(tri)_2(CF_3SO_3)_{0.33}$.

Electronic structure calculations. Spin-Polarized Density functional theory (DFT) calculations were performed using the Vienna *ab*-initio Simulation Package (VASP) version 5.3.5.[13] The electronic wave-functions were expanded in a plane-wave basis set with an energy cutoff of 400 eV. Electron-ion interactions were described using the projector augmented wave (PAW) method in the form of pseudopotentials found in the VASP library.[14] All structures were fully relaxed using the ISIF = 3 tag in VASP at a 1×1×1 Monkhorst-pack k-point mesh and a force tolerance of 0.02 eV/Å using the Perdew-Burke-Ernzerhof (PBE) functional.[15] The low k-point sampling for geometry optimizations was required due to the large unit cell; however, subsequent self-consistent calculations for the energies and charge densities were performed at a 3×3×3 Monkhorst-pack k-point mesh and the Perdew-Burke-Ernzerhof functional with an energy tolerance of 10^{-5}. The charge analysis was performed using the Chargemol DDEC6 scheme.[16,17,18] The resultant structures with magnetic moment and atomic charge color gradients were constructed in Jmol

using the information from the DDEC6 calculations.[19] All additional visualization of the systems was done in Visualization for Electronic and Structural Analysis (VESTA).[20]

We generated the geometry to use for our DFT calculations starting from the crystal structure of $Cr(tri)_2(CF_3SO_3)_{0.33}$. The crystal structure was disordered around the counterions, therefore the initial position of the counterions were estimated and hydrogen atoms were added to fill missing valencies. The resultant structure has 424 atoms. The counterions were kept in all calculations. Experimental data suggest disordered triflate anions. We only tested a limited number of triflate configurations. Our results suggested that there was not a large impact on the magnetic state; however, the exact impact on anion configuration on the magnetic state requires further study. The PBE functional was used for the optimization and subsequent calculations because this functional is free of empirical parameters and gives good results for the structure of densely packed solids.[15] Although previous work on magnetic metal-organic frameworks used the HSE functional,[4] this would have been too computationally expensive for a system of this size. Furthermore, we did not include a U parameter correction in our calculations. A U parameter is frequently included to correct over-delocalization seen in DFT calculations.[21] However, such a correction is typically not included for systems with delocalized electrons, such as metals and conductors. Experimentally, $Cr(tri)_2(CF_3SO_3)_{0.33}$ shows high conductivity at low temperatures; therefore, a U parameter is not required. We did test applying the U parameter, and we found a decrease in the mixed-valent character, with less charge difference between different Cr centers. Additionally, applying a U value increases the magnetic moment of our calculations with high values of U (8.0 eV) approaching 2.66 μ_B, while omitting a U value gives 2.41 μ_B, in good agreement with the experimentally observed value of 2.39 μ_B.

The Fig. S4.9 exhibits the convergence of the energy with respect to the plane-wave energy cutoff and irreducible k-points. We find that a plane-wave cutoff of 400 eV is sufficient with less than 0.1 eV energy change compared to 425 eV. Additionally, we find that 3×3×3 k-point sampling to be sufficient. The energetics taken from subsequent self-consistent energy calculations suggest that the ferromagnetic state is lower in energy than the antiferromagnetic state by 0.127 eV/Cr atom. In all calculations, the Fermi smearing technique was used to determine orbital occupancy with a width of 0.1 eV. This leads to a broadening of the DOS compared to the band structure by approximately 0.1 eV.

The pDOS (Fig. 4d) and Fig. S4.4 were obtained using data that was parsed using Pymatgen (Python Materials Genomics), which is an open-source Python library for materials analysis, and then plotted using Matplotlib.[22,23] The band structures (Fig. 4a,b) were obtained using Sumo, a Python toolkit for plotting and analysis of ab initio solid-state calculation data.[24]

The Fig. S4.4 shows the net atomic charge and the even-tempered magnetic moments as a function of color gradient from blue and white to red for the ferromagnetic (Fig. S4.4a,b) and the antiferromagnetic states (Fig. S4.4c,d), respectively. In the Fig. 4.4a,b, there is a clear evidence that the state captured is ferromagnetic and that the distribution of magnetic moments on the Cr atoms ranges from around two to three unpaired electrons, which is consistent with experimental evidences for mixed-valence low-spin $Cr^{II/III}$. The same conclusions can be drawn from the net atomic charges. The Fig. S4.4c,d also distinctly displays confirmation that the state captured is antiferromagnetic while the net atomic charges show the expected mixed-valency between $Cr^{II/III}$. These findings are consistent with the experimental evidences for the $Cr(tri)_2(CF_3SO_3)_{0.33}$ and support double-exchange phenomenon.

Interestingly, the Fig. S4.4c shows that the antiferromagnetic state consists not of alternating spin orientations between nearest-neighbor Cr atoms but of several spin-up and spin-

down ‘domains’ within a unit cell. The projected density of states (pDOS) for the antiferromagnetic state is shown in The Fig. S4.5. Similar to the ferromagnetic state, the antiferromagnetic state also exhibits significant hybridization between the Cr *d* and N *p* orbitals.

S4.4 Supplementary Tables

Supplementary Table S4.1. Experimental conditions and refinement parameters resulting from Rietveld refinements of powder X-ray diffraction patterns of $Cr(tri)_2(CF_3SO_3)_{0.33}$

	$Cr(tri)_2(CF_3SO_3)_{0.33}$		
Wavelength (Å)	0.412685	0.412685	0.412685
T (K)	360	220	120
Space Group	$Fd\bar{3}m$:2	$Fd\bar{3}m$:2	$Fd\bar{3}m$:2
a, b, c (Å)	16.98035(14)	16.95402(17)	16.93708(17)
V (Å^3)	4896.0(1)	4873.2(1)	4858.6(2)
R_{wp}	6.76%	6.97%	6.76%
R_{exp}	7.85%	7.92%	7.87%
R_{Bragg}	1.73%	1.78%	1.75%
R_p	5.20%	5.40%	5.20%
$R_{wp(Rietveld)}/R_{wp(Pawley)}$	1.01	1.04	1.00

Supplementary Table S4.2. Deduced chemical formula and selected interatomic distances (Å) from Rietveld refinements of powder X-ray diffraction patterns of $Cr(tri)_2(CF_3SO_3)_{0.33}$

	$Cr(tri)_2(CF_3SO_3)_{0.33}$		
T (K)	360	220	120
Deduced Formula	$Cr(tri)_2(CF_3SO_3)_{0.34}$	$Cr(tri)_2(CF_3SO_3)_{0.35}$	$Cr(tri)_2(CF_3SO_3)_{0.35}$
Cr1–N1	2.067(4)	2.074(4)	2.063(5)
Cr2–N2	2.031(6)	2.018(7)	2.037(7)
N1–N2	1.334(5)	1.321(6)	1.318(6)
C1–N1	1.353(7)	1.353(8)	1.350(8)
C1–C1	1.350(10)	1.350(11)	1.350(11)

S4.5 Supplementary Figures

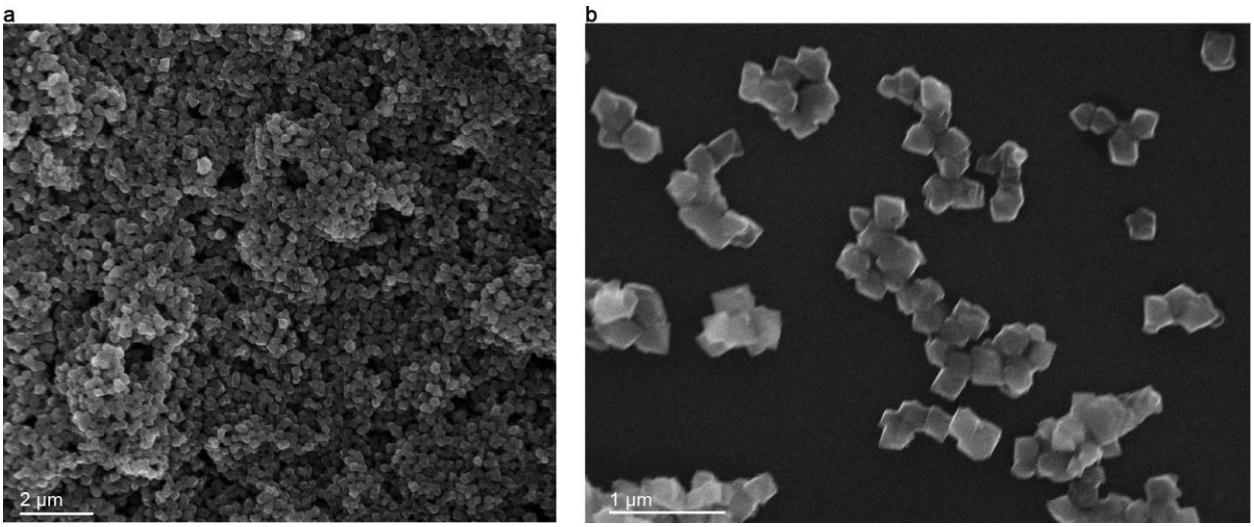

Fig. S4.1. Scanning electron microscopy images of $Cr(tri)_2(CF_3SO_3)_{0.33}$ crystals. a,b Scanning electron microscopy images of microcrystalline $Cr(tri)_2(CF_3SO_3)_{0.33}$ powder. Octahedron-shaped crystals have an average edge dimension of ~0.5 µm. Scale bars 2 µm **(a)** and 1 µm **(b)**.

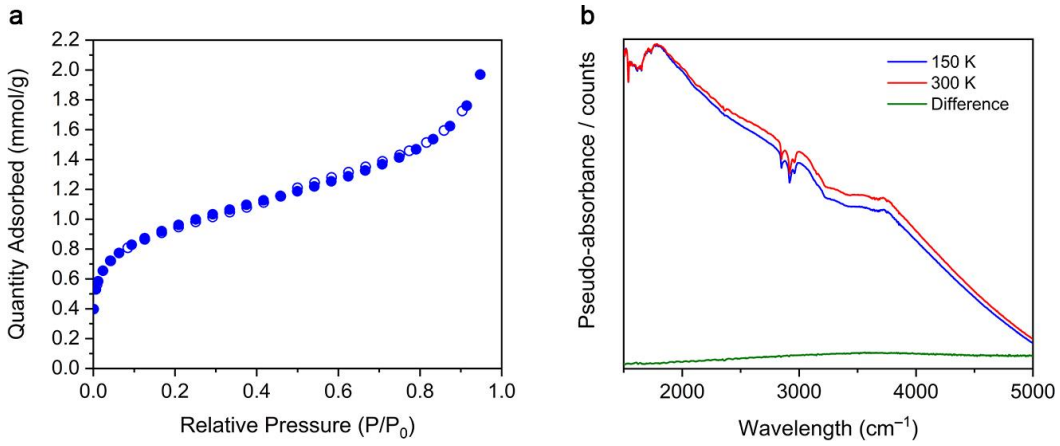

Fig. S4.2. Analyses of the Cr mixed-valency. a, N_2 adsorption isotherm collected at 77 K for $Cr(tri)_2(CF_3SO_3)_{0.33}$. Closed and open data points represent adsorption and desorption, respectively. **b**, Infrared data collected at 150 K (blue) and 300 K (red) and the difference plot (green) for $Cr(tri)_2(CF_3SO_3)_{0.33}$.

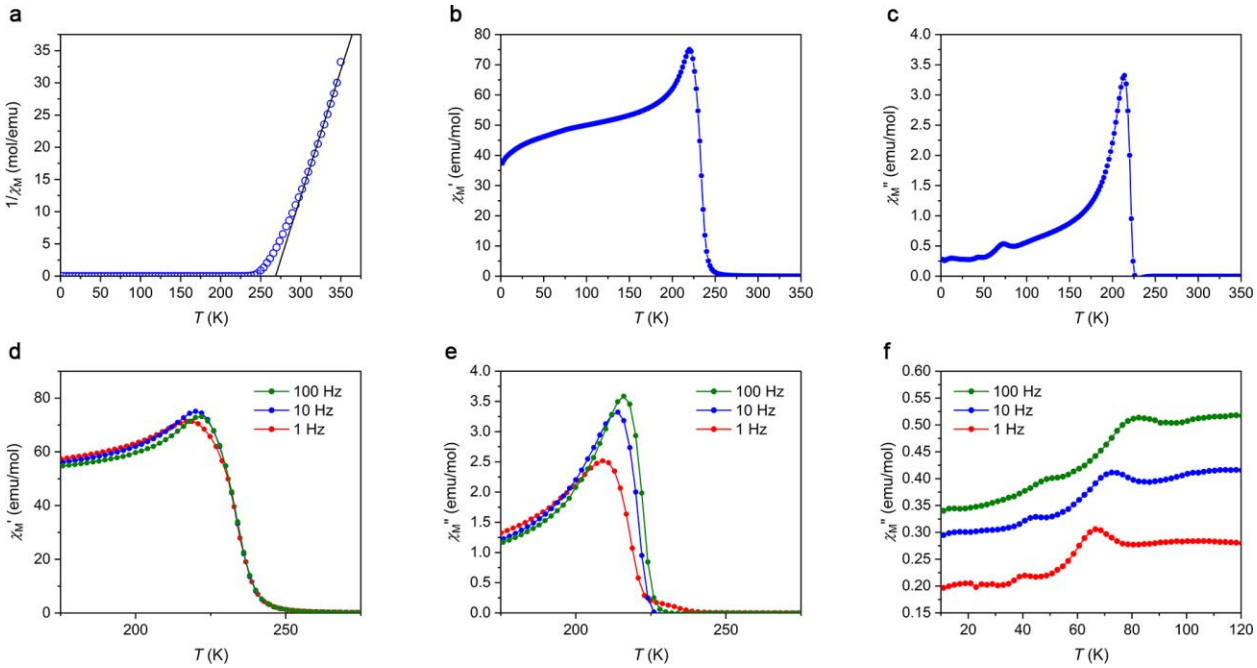

Fig. S4.3. Magnetic data. a, Variable-temperature magnetic susceptibility data (χ_M) for $Cr(tri)_2(CF_3SO_3)_{0.33}$ collected under the applied dc field of 25 Oe. Data plotted as $1/\chi_M$ versus temperature. Curie-Weiss fit to the data between 300 K and 350 K is shown by a black solid line, with fitting parameters described in the main text. **b-f**, Variable-temperature in-phase (χ') and out-of-phase (χ'') ac magnetic susceptibility of $Cr(tri)_2(CF_3SO_3)_{0.33}$. at selected frequencies of 4 Oe ac oscillating magnetic field and zero dc magnetic field.

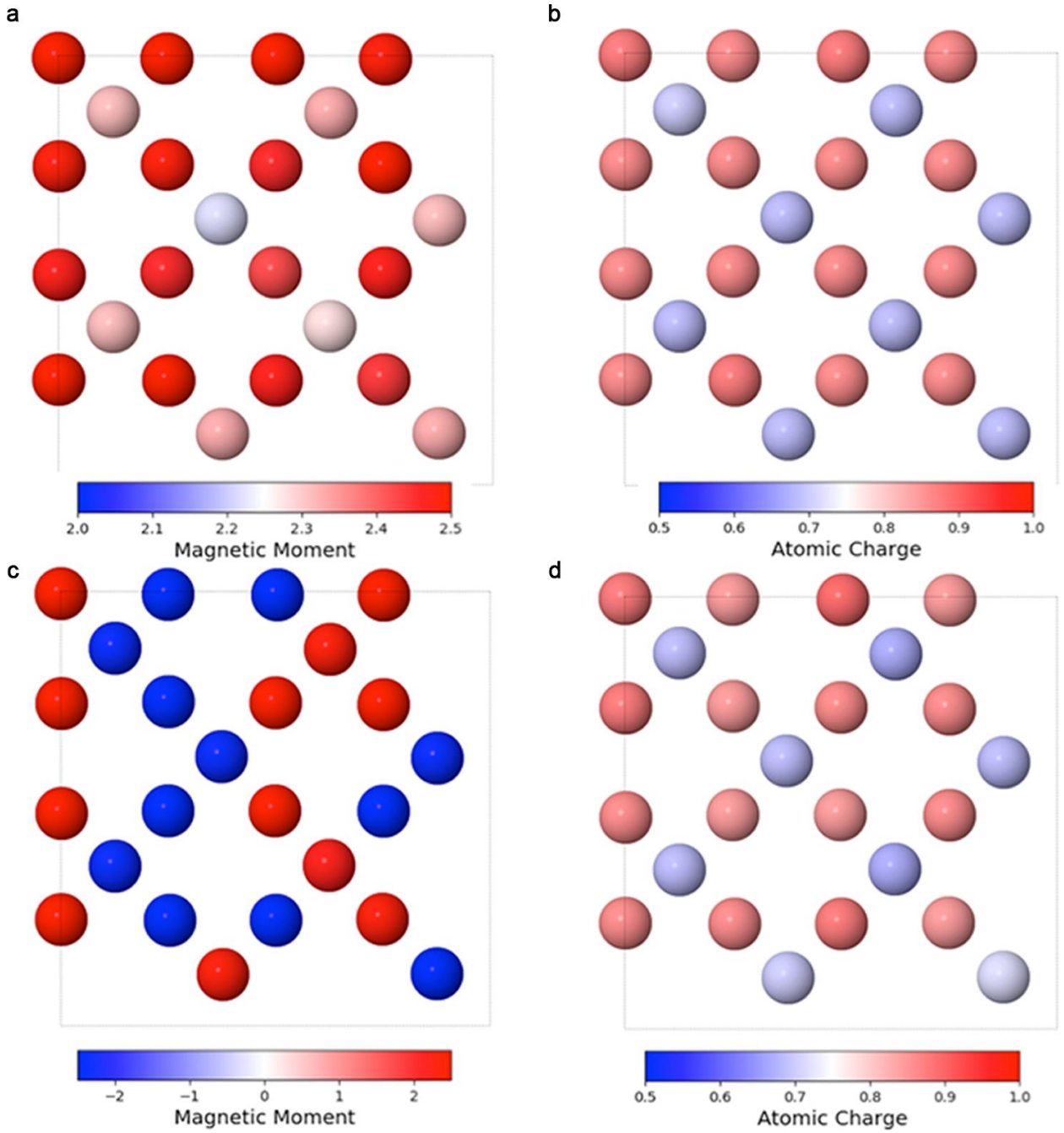

Fig. S4.4. Charge analysis. a, Magnetic moments (μ_B mol^{-1}) for the ferromagnetic state. **b**, Atomic charge for the ferromagnetic state in atomic units. **c**, Magnetic moments (μ_B mol^{-1}) for the antiferromagnetic state. **d**, Atomic charge for the antiferromagnetic state in atomic units. Atomic properties shown as a gradient from blue to white to red. Negative magnetic moments indicate spin-down contributions.

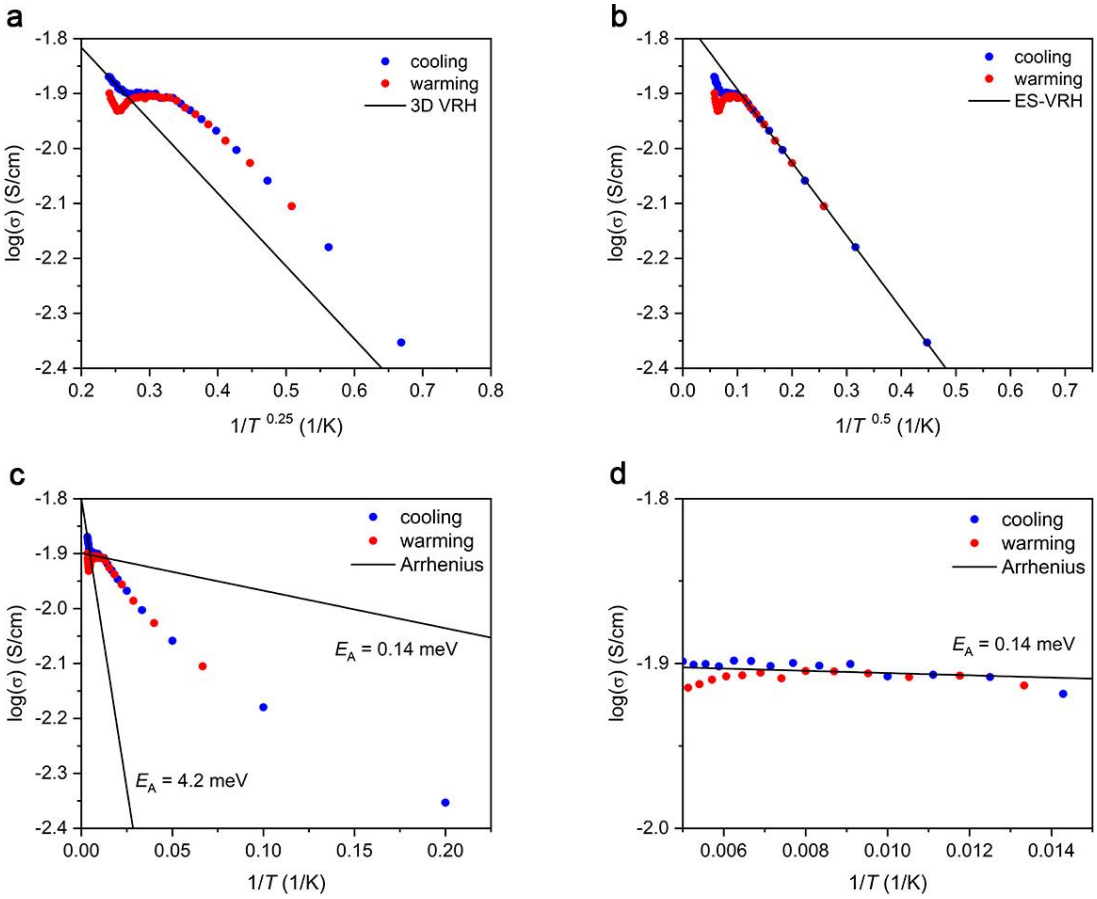

Fig. S4.5. Variable temperature conductivity data modeling. a-d, Variable-temperature log(σ) data of $Cr(tri)_2(CF_3SO_3)_{0.33}$ plotted versus (**a**) $1/T^{0.25}$, (**b**) $1/T^{0.5}$, and (**c**, **d**) $1/T$ and fitted with three-dimensional variable-range hopping, Efros-Shklovskii variable-range hopping, and Arrhenius models, respectively. For clarity, log(σ) versus $1/T$ plot (**c**) has been zoomed-in to the intermediate temperature region (**d**) where conductivity exhibits a weak temperature dependence.

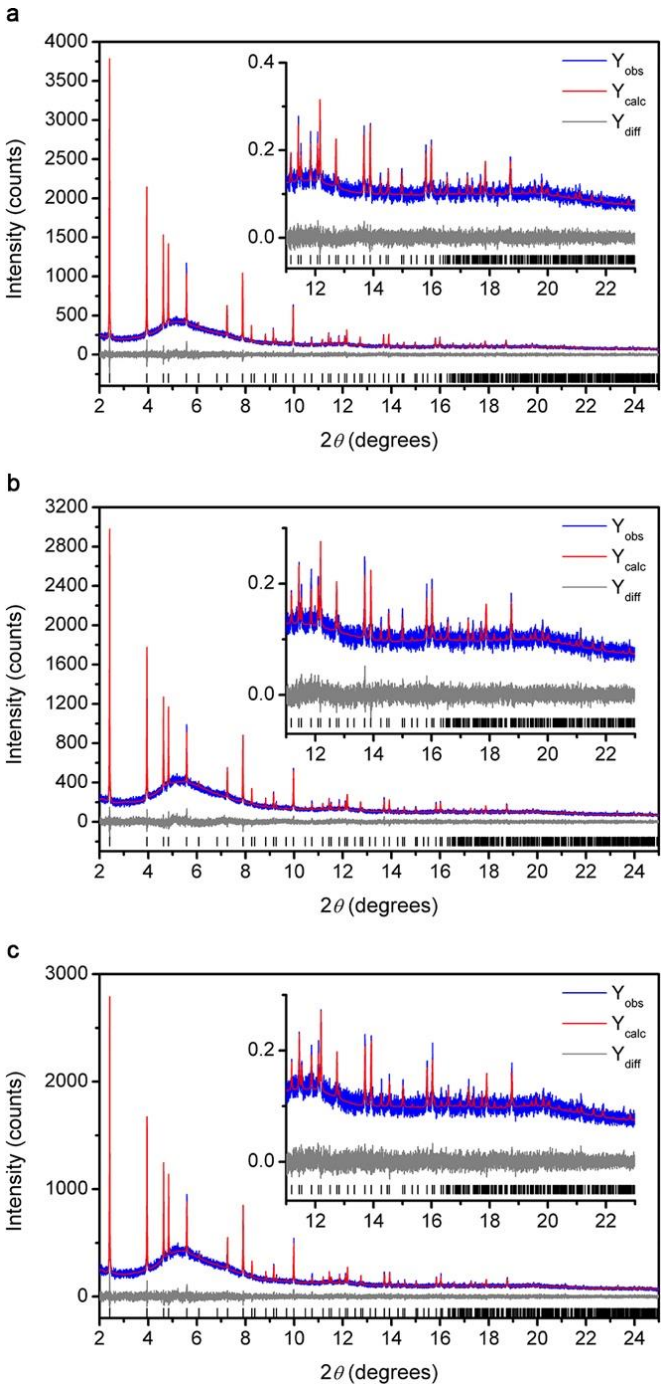

Fig. S4.6. Rietveld refinements. a-c, Rietveld refinements performed on the synchrotron powder X-ray diffraction patterns of $Cr(tri)_2(CF_3SO_3)_{0.33}$ at (**a**) 360, (**b**) 220, and (**c**) 120 K from 2° to 25°. Blue and red lines represent the observed and calculated diffraction patterns, respectively. The gray line represents the difference between observed and calculated patterns, and the black tick marks indicate calculated Bragg peak positions. The inset shows the high angle region at a magnified scale. The wavelength was 0.412685 Å. Figure-of-merit (as defined by TOPAS): (**a**) R_{wp} = 6.76%, R_p = 5.20%, R_{bragg} = 1.73%, $R_{wp(Rietveld)}/R_{wp(Pawley)}$ = 1.01; (**b**) R_{wp} = 6.97%, R_p = 5.40%, R_{bragg} = 1.78%, $R_{wp(Rietveld)}/R_{wp(Pawley)}$ = 1.04; (**c**) R_{wp} = 6.76%, R_p = 5.20%, R_{bragg} = 1.75%, $R_{wp(Rietveld)}/R_{wp(Pawley)}$ = 1.00.

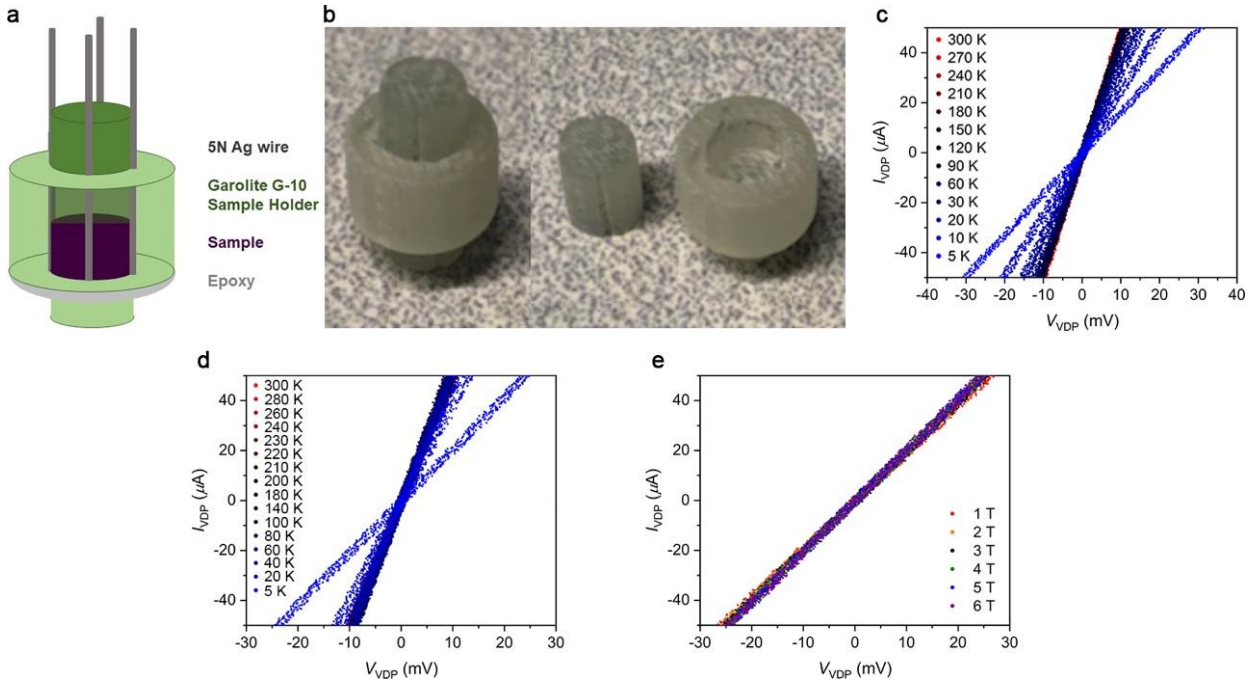

Fig. S4.7. Variable-temperature conductivity. a, **b**, Laboratory-constructed four-contact conductivity measurement apparatus. **c**, Variable-temperature *I*-*V* plots measured under zero applied magnetic field. **d**, Variable-temperature *I*-*V* plots measured under applied magnetic field of 7 T. **e**, *I*-*V* plots measured at 5 K under selected applied magnetic fields. All *I*-*V* profiles exhibited Ohmic response between ±50 μA.

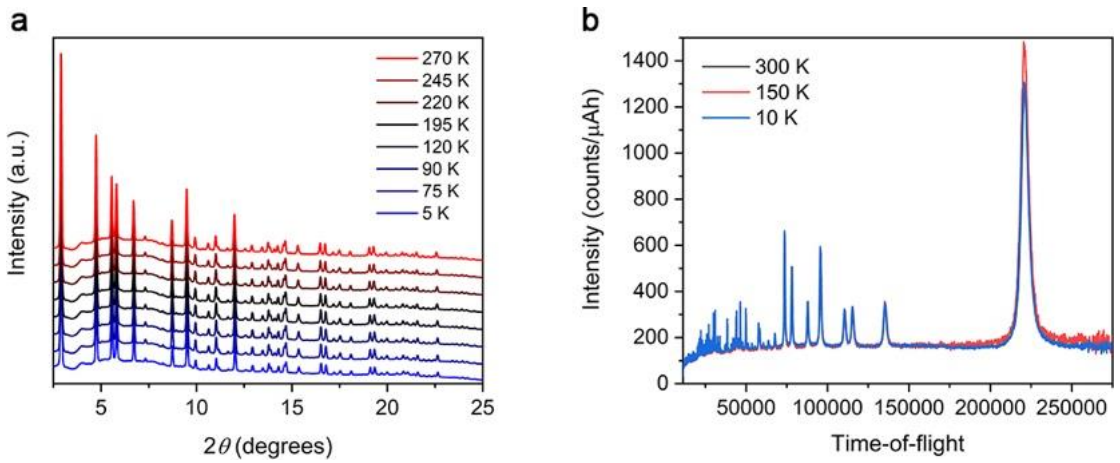

Fig. S4.8. Further diffraction studies. a, Variable-temperature synchrotron powder X-ray diffraction patterns of $Cr(tri)_2(CF_3SO_3)_{0.33}$ collected at selected temperatures between 5 and 270 K. The wavelength was 0.49754758 Å. **b**, Powder neutron diffraction data collected at 10, 150, and 300 K. To clarify, 10 and 300 K diffraction patterns nearly overlap with similar peak intensities and positions.

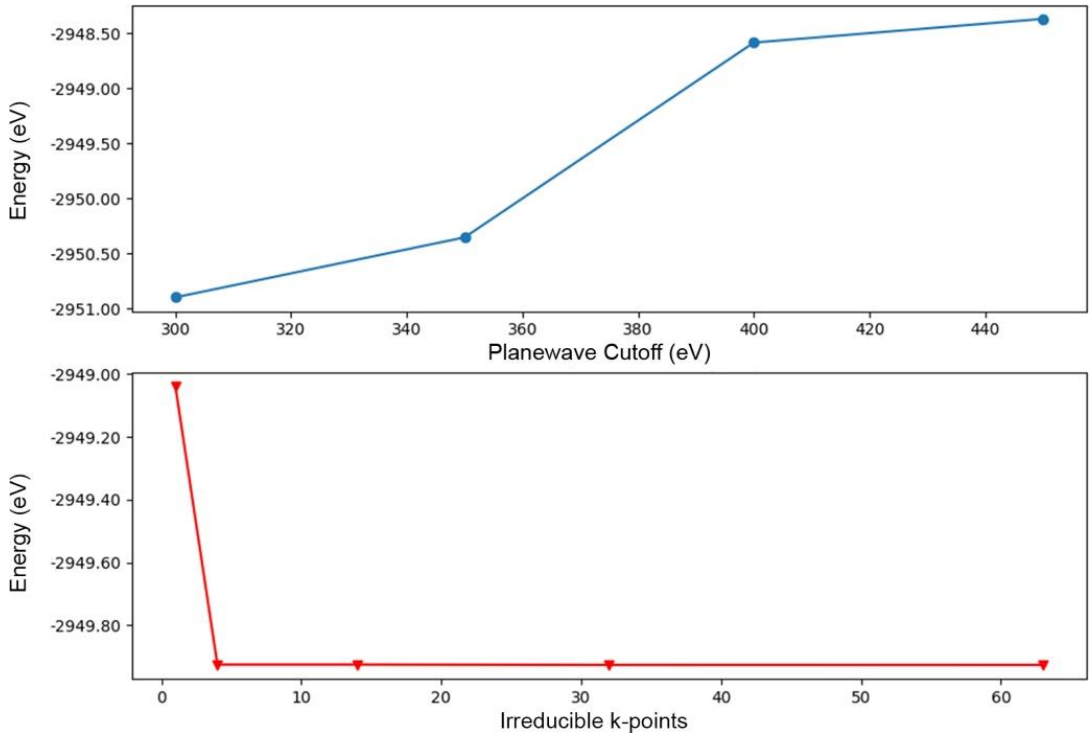

Fig. S4.9. Energy calculations. The energy of the optimized system is shown with respect to planewave cutoff and number of irreducible k-points. The calculations done varying planewave cutoff include 14 irreducible k-points.

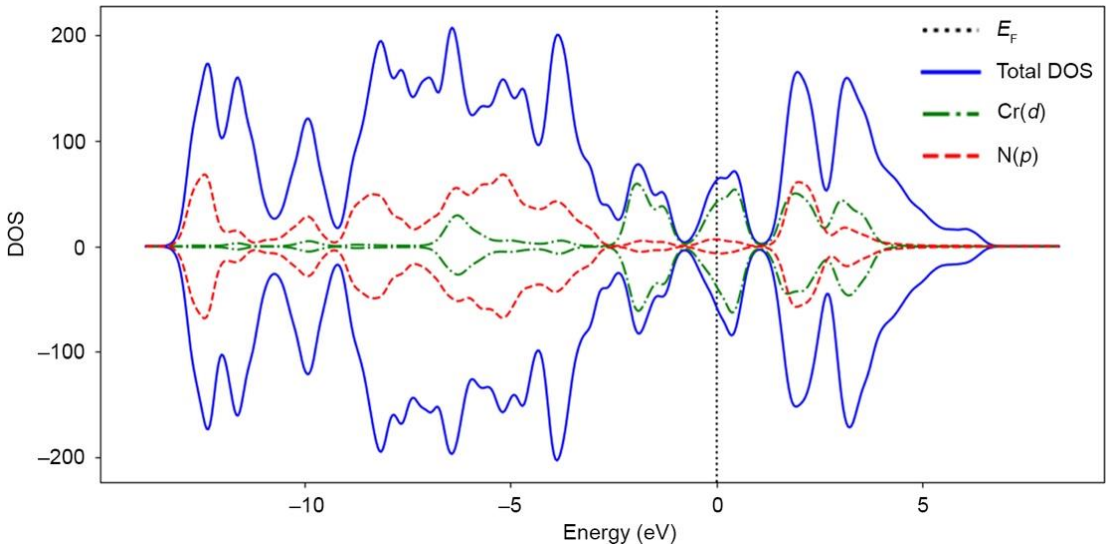

Fig. S4.10. Partial density of states (pDOS) of the antiferromagnetic state. Partial density of states (pDOS) in arbitrary units for the antiferromagnetic system. Blue, green, and red denote the

total, Cr *d*, and N *p*, respectively. The zero of energy is set to the highest occupied state denoted by the dotted vertical line which has an energy of 2.60 eV.

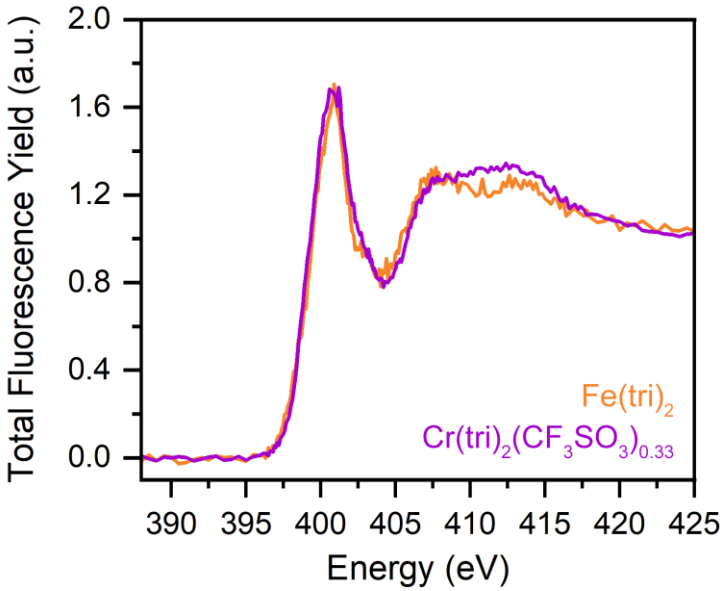

Fig. S4.11. X-ray absorption spectroscopy. Nitrogen K-edge X-ray absorption spectroscopy data of $Fe(tri)_2$ and $Cr(tri)_2(CF_3SO_3)_{0.33}$ represented by orange and purple lines, respectively.

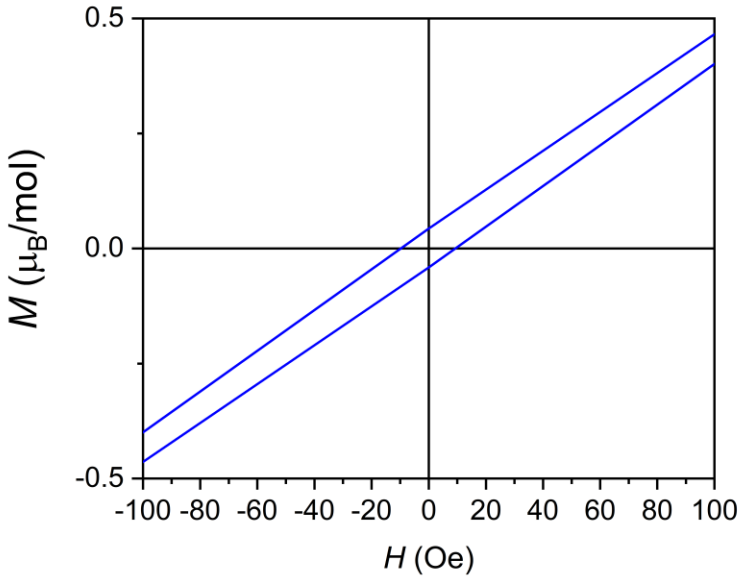

Fig. S4.12. Variable-field magnetization data. Variable-field magnetization data of $Cr(tri)_2(CF_3SO_3)_{0.33}$ collected at 3 K. Data is expanded in the region of interest, showing a small hysteresis and non-negligible coercivity of ~10 Oe.

S4.6 References for Chapter 4 Supporting Information

(1) Dixon, N. E., Lawrance, G. A., Lay, P. A., Sargeson, A. M. & Taube, H. Trifluoromethanesulfonates and trifluoromethanesulfonato-o complexes. *Inorg. Synth.* **28**, 70-76 (1990).

(2) Park, J. G. et al. Charge delocalization and bulk electronic conductivity in the mixed-valence metal-organic framework Fe(1,2,3-triazolate)$_2$(BF$_4$)$_x$. *J. Am. Chem. Soc.* **140**, 8526-8534 (2018).

(3) Thangavel, A., Wieliczko, M., Scarborough, C., Dittrich, S. & Bacsa, J. An investigation of the electron density of a Jahn–Teller-distorted Cr^{II} cation: the crystal structure and charge density of hexakis(acetonitrile-*κN*)chromium(II) bis(tetraphenylborate) acetonitrile disolvate. *Acta Cryst*. **C71**, 936-943 (2015).

(4) Murray, L. J. et al. Highly-Selective and Reversible O_2 Binding in Cr$_3$(1,3,5-benzenetricarboxylate)$_2$. *J. Am. Chem. Soc.* **132**, 7856-7857 (2010).

(5) Aubrey, M. L. et al. Electron delocalization and charge mobility as a function of reduction in a metal-organic framework. *Nat. Mater.* **17**, 625-632 (2018).

(6) Coelho, A. A. TOPAS-Academic, Version 5 (Coelho Software, 2017).

(7) Rietveld, H. M. A profile refinement method for nuclear and magnetic structures. *J. Appl. Crystallogr*. **2**, 65-71 (1969).

(8) Andreev, Y. G., MacGlashan, G. S. & Bruce, P. G. Ab initio solution of a complex crystal structure from powder-diffraction data using simulated-annealing method and a high degree of molecular flexibility. *Phys. Rev. B* **55**, 12011-12017 (1997).

(9) Mydosh, J. A. *Spin glasses* (Taylor & Francis, 1993).

(10) Wu, J. & Leighton, C. Glassy ferromagnetism and magnetic phase separation in La$_{1-x}$Sr$_x$CoO$_3$. *Phys. Rev. B* **67**, 174408 (2003).

(11) Chun, S. H. et al. Reentrant spin glass behavior in layered manganite La$_{1.2}$Sr$_{1.8}$Mn$_2$O$_7$ single crystals. *J. Appl. Phys.* **90**, 6307-6311 (2001).

(12) Nagaev, E. L. *Physics of magnetic semiconductors* (Mir, 1983).

(13) Kresse, G. & Furthmüller, J. Efficiency of *ab*-initio total energy calculations for metals and semiconductors using a plane-wave basis set. *Comput. Mater. Sci.* **6**, 15-50 (1996).

(14) Perdew, J. P. et al. Atoms, molecules, solids, and surfaces: Applications of the generalized gradient approximation for exchange and correlation. *Phys. Rev. B* **46**, 6671-6687 (1992).

(15) Perdew, J. P., Burke, K. & Ernzerhof, M. Generalized gradient approximation made simple. *Phys. Rev. Lett.* **77**, 3865-3868 (1996).

(16) Manz, T. A. & Sholl, D. S. Methods for computing accurate atomic spin moments for collinear and noncollinear magnetism in periodic and nonperiodic materials. *J. Chem. Theory Comput*. **7**, 4146-4164 (2011).

(17) Manz, T. A. & Sholl, D. S. Improved atoms-in-molecule charge partitioning functional for simultaneously reproducing the electrostatic potential and chemical states in periodic and non-periodic materials. *J. Chem. Theory Comput*. 8, 2844-2867 (2012).

(18) Manz, T. A. & Sholl, D. S. Chemically meaningful atomic charges that reproduce the electrostatic potential in periodic and nonperiodic materials. *J. Chem. Theory Comput.* **6**, 2455-2468 (2010).

(19) Jmol: an open-source Java viewer for chemical structures in 3D. http://www.jmol.org/

(20) Momma, K. & Izumi, F. VESTA: a three-dimensional visualization for electronic and structural analysis. *J. Appl. Cryst*. **41**, 653-658 (2008).
(21) Kulik, H. J. Perspective: Treating electron over-delocalization with the DFT+U method. *J. Chem. Phys.* **142**, 240901 (2015).
(22) Ong, S. P. et al. Python Materials Genomics (pymatgen): a robust, open-source python library for materials analysis. *Comput. Mater. Sci.* **68**, 314-319 (2013).
(23) Hunter, J. D. Matplotlib: a 2D graphics environment. *Comput. Sci. Eng.* ***9***, 90–95 (2007).
(24) Ganose, A. M., Jackson, A. J. & Scanlon, D. O. Sumo: command-line tools for plotting and analysis of periodic ab initio calculations. *J. Open Source Soft.* **3**, 717 (2018).